



JOURNÉES SCIENTIFIQUES, *WORKSHOP*

## RÉSEAUX DU FUTUR : 5G ET AU-DELÀ

### *FUTURE NETWORKS: 5G AND BEYOND*

**11 / 13 MARS, 2020**

**TELECOM PARIS, INSTITUT POLYTECHNIQUE DE PARIS, PALAISEAU**



**ACTES *PROCEEDINGS***

Crédit illustration de couverture : Atelier Isatis – Dijon  
*Cover image Crédit: Atelier Isatis - Dijon*

## EDITORIAL

Les Journées scientifiques 2020 d'URSI-France, sous l'égide de l'Académie des sciences, ont eu pour thème les « Réseaux du futur : 5G et au-delà ».

L'année 2020 sera celle de l'ouverture au grand public de la « 5G ». Cette nouvelle génération de systèmes de communication sans fil va être, comme les précédentes, la concrétisation d'études commencées il y a 10 ans et le début de recherches qui vont paver la voie pour les systèmes futurs. Quel chemin parcouru depuis 1794 et le télégraphe optique de Claude Chappe ! Que de recherches nous ayant permis de découvrir l'existence des ondes électromagnétiques puis de les apprivoiser ! Le monde d'aujourd'hui est devenu sans fil, le téléphone et l'ordinateur se sont, en grande partie, débarrassés de ce lien mécanique pour devenir mobile ou portable et leurs usages en ont été fondamentalement modifiés. Ainsi, en 2019, sur les 7,7 milliards d'humains dans le monde, 4,4 milliards utilisaient Internet, 5,1 milliards possédaient un téléphone mobile. Ces chiffres montrent que les systèmes de communication sans fil font de plus en plus partie de notre vie quotidienne, même s'il existe des différences géographiques comme en Afrique centrale où les utilisateurs d'internet ne représentent que 12%, et même si la perception du risque complexifie parfois le déploiement des infrastructures. Ces réseaux s'appuient sur des technologies dont l'usage est de plus en plus simple, mais cela masque en fait une complexité croissante nécessitant de gros efforts de R&D. Avec les réseaux du futur, l'internet des objets devrait continuer à se développer, se diffuser, et alimenter de nouveaux secteurs comme la domotique, la santé connectée, l'usine du futur et les véhicules autonomes.

Les thèmes retenus pour ces Journées ont été développés au cours de 4 exposés invités qui présenteront l'état de la technique et des développements récents, de 30 communications orales et 9 posters couvrant diverses questions scientifiques posées par les réseaux du futur. Dans le but constant de développer les échanges et la coopération entre les différents comités européens de l'URSI, nous eûmes également le plaisir d'accueillir plusieurs conférenciers provenant de pays voisins.

Comme chaque année, les Journées scientifiques furent l'occasion de la tenue de l'Assemblée générale d'URSI-France. Ce moment annuel essentiel dans la vie de l'association est le point de rencontre de ses membres. Il permet notamment des échanges entre les dix commissions et favorise leur dimension transdisciplinaire, qui est probablement la valeur principale de cette organisation scientifique centenaire qu'est l'URSI.

Les Journées scientifiques 2020 ont été, comme de coutume, ponctuées par la remise de la Médaille du CNFRS (URSI-France), honorant une personnalité qui a contribué de façon remarquable aux progrès dans le domaine des radiosciences et à l'animation de la communauté scientifique. Le récipiendaire en fut cette année Jacques Palicot, Professeur émérite à CentraleSupélec Rennes et la Médaille lui fut remise par Maurice Bellenger, Membre de l'Académie des Technologies.

De même, le « Prix de thèse en radiosciences », fut attribué cette année à Frédéric Challita, pour « Caractérisation des Canaux Massive MIMO et Stratégies de Sélection d'Antennes : Application pour la 5G et l'Industrie 4.0 »

Joe Wiart, Président des Journées scientifiques 2020 d'URSI-France

*The URSI-France 2020 Workshop, being held under the sponsoring of the French Academy of Sciences was dedicated to "Future Networks: 5G and beyond".*

*The year 2020 will see the opening of 5G to commercial service. This new generation of wireless communication systems, like the previous ones, will result from studies started a decade ago and, at the same time, will be the germ for future systems. How long was the route since Claude Chappe invented optical telegraphy! How numerous were the research works that allowed us to discover the existence of EM waves, then to master them! Today's world has become wireless, the voice phone and the computer got largely rid of the mechanical link to become mobile and portable and their uses have greatly changed. Thus, in 2019, out of the 7.7 billion humans in the world, 4.4 made use of internet and 5.5 billion owned a mobile phone. These numbers demonstrate that wireless communication systems are more and more intimately part of our daily lives, even though strong differences exist, such as in central Africa where internet users do not exceed 12% and even though the risk perception makes deployment uneasy. These networks rest on technologies whose use is simpler and simpler, although this hides an underlying increasing complexity requiring enormous efforts in R&D. Through future networks, the internet of things should further expand, spread and feed new sectors such as home automation, connected health, factory 4.0 and autonomous vehicles.*

*The topics selected for 2020 URSI-France Workshop were developed during 4 invited lectures, 30 oral presentations and 9 posters, addressing various scientific issues raised by future networks. With the constant aim of developing exchanges and cooperation between the various European URSI committees, we were pleased to welcome several speakers from neighboring countries.*

*As usual, the URSI-France General Assembly was held during the Workshop. This essential yearly moment in the life of URSI-France indeed is the meeting point of its members; it allows exchanges between the ten commissions, favoring their transdisciplinary dimension, which is probably the main value of this century old scientific organization that is URSI.*

*As usual, the URSI-France 2020 Workshop will see the CNFRS (URSI-France) Medal award, honoring a personality who has made a remarkable contribution to the progress in the field of radiosciences and to the animation of the scientific community. The recipient was this year Jacques Palicot, Professor Emeritus at CentraleSupélec Rennes and the Medal was awarded by Maurice Bellenger, Member of the French Academy of Technologies.*

*Similarly, the "Radioscience PhD Award" was given to Frédéric Challita, for "Characterization of Massive MIMO Channels and Antenna Selection Strategies: Application for 5G and 4.0 Industry".*

*Joe Wiart, Chairman of the URSI-France 2020 annual scientific workshop*

## **CONFÉRENCES INVITÉES, *INVITED TALKS***

- « **LA 5G, LE CADRE RÉGLEMENTAIRE** » PAR **GILLES BRÉGANT (ANFR DIRECTEUR GÉNÉRAL)** : <https://youtu.be/hcjmQC1So9s>
- « **LA 5G, CHALLENGES ET PERSPECTIVES** » PAR **PHILIPPE LUCAS (ORANGE, VICE-PRÉSIDENT PRINCIPAL, STRATÉGIE, ARCHITECTURE ET NORMALISATION)** : <https://youtu.be/EtxKG5qVfAE>
- « **LA 5G, UN SURVOL** » PAR **PHILIPPE SEHIER (NOKIA, MOBILE STRATEGY)** : <https://youtu.be/PcIoPmxduRc>
- « **AU-DELÀ DE LA 5G, AU CŒUR DE LA TRANSFORMATION NUMÉRIQUE** » PAR **DANIEL KOFMAN (TELECOM PARIS, PROFESSEUR)** : <https://youtu.be/LBzchWs4lAw>



# Table of contents

<b>Introduction</b>	<b>1</b>
<b>Author Index</b>	<b>7</b>
<b>5G Antennas</b>	<b>1</b>
Statistical study of the matching properties and radiation pattern distortion of high density randomly distributed dipoles, Adjali Imad [et al.] . . . . .	1
Conversion of a Pulsed Source Using a Multiband Frequency Selective Surface for HPM Applications, Albarracin-Vargas Fernando [et al.] . . . . .	6
Conception et synthèse d'un réseau d'antennes parcimonieux en bande C (3,4 – 3,8 GHz), Fofana Seydouba [et al.] . . . . .	11
Surface rayonnante à agilité de faisceaux versus réseaux d'antennes agiles, Jecko Bernard [et al.] . . . . .	17
Antenne ultra-large bande avec polarisation circulaire pour des applications 5G, Mantash Mohamad . . . . .	24
Observatoire des Ondes, une réponse au débat sociétal, Pinel Philippe [et al.] . .	27
Métasurfaces à faible densité d'éléments : Application aux antennes, Popov Vladislav [et al.] . . . . .	34
Multi-beam Modulated Metasurface Antenna for Backhaul Applications at K-band, Ruiz Jorge [et al.] . . . . .	36
Passive reconstruction of the impulse response between two antennas in a reverberation chamber, Tamart Meriem [et al.] . . . . .	40
Antenne 3D filaire miniature pour les systèmes 5G, Benamahmoud Fateh [et al.]	44

<b>Propagation and physical layer</b>	<b>50</b>
---------------------------------------	-----------

Sécurité à la Couche Physique pour une Communication SISO MROF dans le Domaine Fréquentiel avec Renversement Temporel, Golstein Sidney [et al.] . . . . .	50
Investigating Sub-THz PHY Layer for Future High-data-rate Wireless Backhaul, Gougeon Grégory [et al.] . . . . .	54
Power and Delay performance of Optical Wireless Communication inside Aircraft Cockpit, Joumessi Steve [et al.] . . . . .	60
IQ Based Direct Sequence Spread Spectrum Spatial Data Focusing implemented over a 6 Ray Urban Canyon Channel Model, Odhiambo Michael [et al.] . . . . .	68
An adaptive Uplink SCMA Scheme Based on Channel State Information, Rebhi Manel [et al.] . . . . .	76
Capteur communicant par rétro-modulation dans la bande 5G, Samat Neel [et al.]	83
A light neural network for modulation detection under impairments, Du Mas Des Bourboux Hélion . . . . .	89

<b>Dimensioning and Optimization of 5G systems</b>	<b>97</b>
--	-----------

Wireless communication in presence of digitally controllable scatterers: channel decomposition and capacity analysis, Buccelli Juan Carlos [et al.] . . . . .	97
Performances des techniques de diversité de polarisation dans les systèmes MIMO massifs, Challita Frederic [et al.] . . . . .	102
Path-Loss Modeling of Reconfigurable Intelligent Surfaces – Mirror or Diffuser?, Di Renzo Marco . . . . .	106
Optimization and Analysis of Deep Unfolding Based Double Loop Turbo Equalizers, Sahin Serdar [et al.] . . . . .	107
Performance Evaluation of SWIPT-enabled Cellular Networks with Adaptive Modulation - A Stochastic Geometry Approach, Tu Lam Thanh [et al.] . . . . .	114

<b>Electromagnetic Compatibility Issues</b>	<b>122</b>
---	------------

Dielectric material characterization up to 330 GHz : a free space S-parameter measurement technique without time domain gating, Bourreau Daniel [et al.] . . .	122
--	-----

Statistique de l'efficacité de blindage de matériaux composites pour la 5G: méthodes avancées d'échantillonnage, Lallechere Sébastien [et al.] . . . . .	127
Design of 3.6-GHz 5G NGD passive circuit, Ravello Blaise [et al.] . . . . .	131
<b>Exposition and Dosimetry in the 5G context</b>	<b>135</b>
Massive MIMO Network Downlink Exposure Evaluation Using Stochastic Geometry, Al Hajj Maarouf [et al.] . . . . .	135
Proposal for simplified RF exposure assessment formula updates for millimetre wave small cells using beamforming, Bechta Kamil [et al.] . . . . .	140
RF-EMF exposure assessment in the new incoming 5G indoor exposure scenarios, Bonato Marta [et al.] . . . . .	145
Artificial Neural Networks for Uncertainty Quantification in RF Radiation Modeling, Cheng Xi [et al.] . . . . .	148
Assessment Of Temporal Uplink Emitted Power Variation For VoLTE Calls, Chobineh Amirreza [et al.] . . . . .	149
Evaluation of exposure induced by a 5G antenna in the 3,4 – 3,8 GHz band., Conil Emmanuelle [et al.] . . . . .	152
On the use of ERCs for 5G measurements, Fichte Lars Ole [et al.] . . . . .	156
Estimation of network densification impact on EMF exposure using stochastic geometry, Gontier Quentin [et al.] . . . . .	160
Numerical dosimetry in human model for 5G and beyond, Ijjeh Abdelrahman [et al.] . . . . .	163
Study of estimation accuracy of fast SAR measurement systems, Liu Zicheng [et al.] . . . . .	170
Numerical modeling of downlink electromagnetic wave exposure generated by 5G beamforming antennas, Noe Nicolas . . . . .	171
Sur les procédures de mesure pour l'évaluation du débit d'absorption spécifique (DAS) des équipements cellulaires MIMO ayant des variations rapides des phases relatives, Teniou Mounir [et al.] . . . . .	177
Assessment of MaMIMO beamwidth using measurements and raytracing, Velghe Maarten [et al.] . . . . .	186

Reconstruction of EMF Exposure in Cellular Networks from Sensor Measurements  
by Using Artificial Neural Network, Wang Shanshan [et al.] . . . . . 189

**Organisation** **192**

# Author Index

- Aberbour Lyazid, 177–185  
Adjali Imad, 2–5  
Agnani Jean-Benoît, 152–155  
Al Hajj Maarouf, 136–139  
Albarracin-Vargas Fernando, 6–10  
Alyafei Fahad, 6–10  
Andriulli Francesco, 148  
Aslam Mohammed Zahid, 54–59  
Aveneau Lilian, 60–67
- Bechta Kamil, 140–144  
Benamahmoud Fateh, 44–49  
Bicaïs Simon, 54–59  
Boeglen Hervé, 60–67  
Bonato Marta, 145–147  
Bourreau Daniel, 123–126  
Boust Fabrice, 34, 35  
Bradai Abbas, 114–121  
Buccelli Juan Carlos, 98–101  
Burokur Shah Nawaz, 34, 35
- Challita Frederic, 102–105  
Chargé Pascal, 76–82  
Cheng Xi, 148  
Chiaramello Emma, 145–147  
Chobineh Amirreza, 149–151  
Cipriano Antonio, 107–113  
Clément Gilles, 127–130  
Combeau Pierre, 60–67  
Conil Emmanuelle, 149–155  
Corre Yoann, 54–59  
Cueille Marylene, 163–169
- Davy Matthieu, 40–43  
De Doncker Philippe, 51–53, 68–75, 136–139, 160–162  
De Rosny Julien, 40–43  
Degauque Pierre, 102–105  
Di Renzo Marco, 106  
Doré Jean-Baptiste, 54–59  
Dossi Laura, 145–147  
Du Mas Des Bourboux Hélion, 89–96  
Dubard Jean-Lou, 163–169
- Ettorre Mauro, 36–39
- Faenzi Marco, 36–39  
Fichte Lars Ole, 156–159  
Fichte Lars-Ole, 6–10  
Fiocchi Serena, 145–147  
Fofana Seydouba, 11–16  
Fuchs Benjamin, 11–16
- Gaillot Davy, 102–105  
Gallucci Silvia, 145–147  
Girard Sébastien, 127–130  
Golstein Sidney, 51–53, 68–75  
Gontier Quentin, 160–162  
Gonzalez Ovejero David, 36–39  
Gougeon Grégory, 54–59  
Grangeat Christophe, 140–144
- Hassan Kais, 76–82  
Henry Clément, 148  
Horlin François, 51–53
- Ijjeh Abdelrahman, 163–169
- Jawad Ourouk, 177–185  
Jecko Bernard, 17–23  
Joseph Wout, 102–105, 186–188  
Joumessi Steve, 60–67  
Julien Thomas, 177–185  
Julien-Vergonjanne Anne, 60–67
- Kamoun Mohamed, 98–101  
Kasmi Chaouki, 6–10, 156–159
- Laheurte Jean-Marc, 2–5  
Lalléchère Sébastien, 156–159  
Lallechere Sébastien, 127–134  
Laly Pierre, 102–105  
Lemaître-Auger Pierre, 44–49  
Lienard Martine, 102–105  
Liu Zicheng, 170
- Mahmoud Adham, 36–39  
Majed Mohamad, 17–23  
Mantash Mohamad, 24–26  
Martens Luc, 186–188  
Martinez David, 6–10  
Molineaux Guylian, 68–75

- Mostarshedi Shermila, 2–5  
Ney Michel, 163–169  
Nguyen Trung-Hien, 51–53, 160–162  
Noe Nicolas, 171–176  
Odhiambo Michael, 68–75  
Oestges Claude, 136–139, 160–162  
Ourak Lamine, 27–33  
Péden Alain, 123–126  
Pannetrat Stephane, 177–185  
Parazzini Marta, 145–147  
Person Christian, 148  
Petrillo Luca, 160–162  
Pinel Philippe, 27–33  
Podlecki Jean, 83–88  
Poiré Yannick, 27–33  
Popov Vladislav, 34, 35  
Potier Patrick, 36–39  
Pouliguen Philippe, 36–39  
Poulliat Charly, 107–113  
Pousset Yannis, 114–121  
Poussot Benoit, 2–5  
  
Ramdani Mehdi, 177–185  
Raoof Kosai, 76–82  
Ratni Badreddine, 34, 35  
Ravazzani Paolo, 145–147  
Ravello Blaise, 131–134  
Rebhi Manel, 76–82  
Richalot Elodie, 40–43  
Rossignol Jérôme, 127–130  
Ruiz Jorge, 36–39  
  
Sahin Serdar, 107–113  
Sahuguède Stéphanie, 60–67  
Samat Neel, 83–88  
Sarrazin Francois, 40–43  
Sarrazin Julien, 51–53, 68–75  
Sauveau Ronan, 36–39  
Sauveron Damien, 60–67  
Shikhantsov Sergei, 186–188  
Sibille Alain, 98–101  
Sorli Brice, 83–88  
Stiemer Marcus, 156–159  
Stuerga Didier, 127–130  
  
Tajan Pascal, 27–33  
Tamat Meriem, 40–43  
Tanghe Emmeric, 102–105  
Tedjini Smail, 44–49  
Teniou Mounir, 177–185
- Thielens Arno, 186–188  
Tognola Gabriella, 145–147  
Tu Lam Thanh, 114–121  
Vega Felix, 6–10  
Velghe Maarten, 186–188  
Vena Arnaud, 83–88  
Wang Shanshan, 136–139, 189–191  
Wiart Joe, 136–139, 148–151, 160–162, 170, 189–191  
Yusuf Marwan, 102–105

# **5G Antennas**

# Statistical study of the matching properties and radiation pattern distortion of high density randomly distributed dipoles

*Étude statique de l'adaptation et de la distorsion du diagramme de rayonnement des dipôles couplés aléatoirement répartis*

**I. Adjali<sup>1</sup>, S. Mostarshedi<sup>1</sup>, B. Poussot<sup>1</sup>, and J-M. Lheureurte<sup>1</sup>**

<sup>1</sup>ESYCOM, Université Gustave Eiffel, CNRS UMR 9007, F-77454 Marne-la-Vallée, France, imad.adjali@u-pem.fr

**Keywords:** Electromagnetic coupling, highly coupled dipoles, random distribution, statistical study

**Mots clés:** Couplage électromagnétique, dipôles couplés, distribution aléatoire, étude statistique

## Abstract:

A statistical analysis of the coupling in a set of thin and thick randomly distributed dipoles is presented. The reflection coefficient and the radiation pattern of surrounded dipoles are calculated for a few loads of the surrounding dipoles. The cumulative distributed functions are presented for different dipole densities.

## Résumé:

Une analyse statistique du couplage d'un ensemble de dipôles fins et épais aléatoirement répartis est présentée. Le coefficient de réflexion ainsi que le diagramme de rayonnement des dipôles environnés sont calculés pour quelques valeurs de charge sur les dipôles environnants. Les fonctions de répartition sont présentées pour différentes densités de dipôles.

## 1 Introduction

UHF RFID (Radio Frequency IDentification) technologies have a long established role for tracking and identification of objects and persons. With the growth of the Internet of Thing (IoT), the RFID technology becomes more pervasive and omnipresent. In some applications the density of RFID tags is high, this can give rise to an important electromagnetic coupling between tag antennas which modifies antenna's key parameters, i.e. matching properties and radiation pattern. These electromagnetic modifications can alter and degrade the communication links between devices, e.g. reduced read-range or read-rate.

Despite an initial description of the mutual coupling between RFID tags [1], the statistical modelling of the impact of the mutual coupling for high densities of RFID tags is still a new topic [2]. In these series of research studies, we assume that a dipole-like RFID tag antenna can be modeled by a simple wire dipole antenna. Consequently, we use the IEMF (Induced Electromotive Force) technique [3] and we extend this technique to estimate the impedance matrix of a set of thin dipoles in any orientation and position in a plane [4]. Using this impedance matrix we can calculate the input impedance (or reflection coefficient) and the radiation pattern of a surrounded dipole.

This article aims to study statistically the group behaviour of a set of randomly distributed thin dipoles and to compare the results with the statistical behaviour of thick dipoles for different density and load of surrounding dipoles.

## 2 Statistical assessment

In order to proceed to the statistical assessment, the same number of half-wave dipoles are distributed randomly in  $zOy$  plane over a surface of  $n\lambda \times n\lambda$  as shown in figure 1. The observation point is in far-field and located by  $\theta$  and  $\varphi$  angles. In this study, the experimental design consists in 10 identical thin and thick dipoles distributed over surfaces of dimensions  $4\lambda \times 4\lambda$ ,  $3\lambda \times 3\lambda$ ,  $2\lambda \times 2\lambda$  and  $1\lambda \times 1\lambda$ . For each density, 200 random configurations have been generated using Monte Carlo method, which corresponds to 2000 samples. This number of samples has been chosen according to the convergence of the mean, the variance and the coefficient of variation for the worst case of the largest distribution surface.

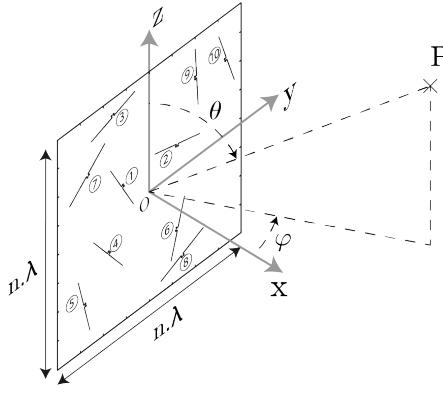


Figure 1 – A generated random configuration of dipoles and the observation point

## 2.1 Reflection coefficient

In order to statistically assess the mismatch of a surrounded dipole in different random configurations, the reflection coefficient  $\Gamma_{ini}$  for the  $i^{th}$  surrounded dipole is defined as follows [5]:

$$\Gamma_{ini} = \frac{Z_{ini} - Z_{ref}^*}{Z_{ini} + Z_{ref}} \quad (1)$$

where the reference impedance  $Z_{ref}$  is the complex conjugate of the self-impedance of an isolated dipole. Table 1 summarizes the self impedance of thin and thick dipoles obtained by IEMF and NEC at the working frequency (892 MHz).

	IEMF	NEC
Thin dipole $\oslash 10^{-6}\lambda$	$73 + j42.5$	$77 + j44.5$
Thick dipole $\oslash 10^{-3}\lambda$	-	$81.5 + j39.3$

Table 1 – Self-impedance of dipoles

The magnitude of the input reflection coefficient ( $|\Gamma_{in}|$ ) of each dipole has been calculated in dB when all other dipoles are short-circuited or matched. The cumulative distribution functions are presented in figure 2. An excellent agreement is observed between the four series of CDF obtained by extended IEMF and NEC (thin and thick dipoles). Table 2 summarizes the empirical statistical moments of the study. For each density and loading conditions, we observe that the empirical mean ( $|\mu|$ ) and standard deviation ( $\sigma$ ) present very close values for thin and thick dipoles, regardless of the simulation method.

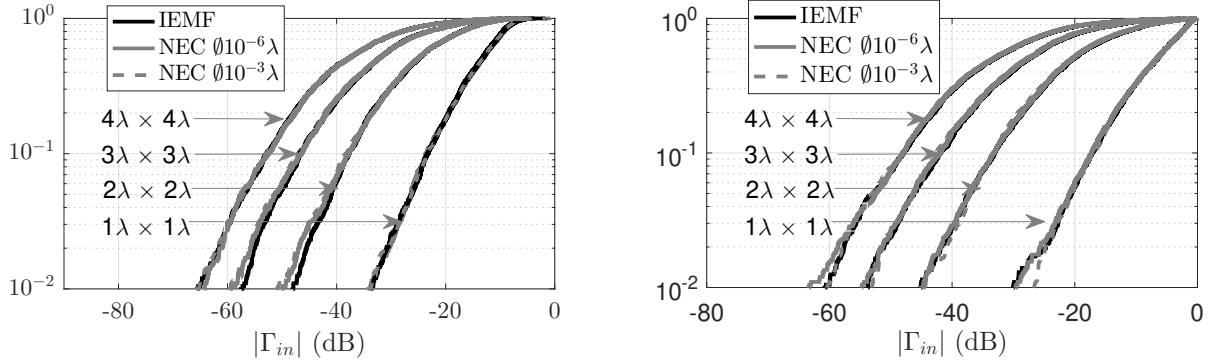


Figure 2 – CDF of the input reflection coefficient of a dipole surrounded by matched (left) and short-circuited (right) dipoles as a function of different densities obtained by extended IEMF and NEC

It is important to note that neither the visual inspection of the CDF in figure 2 nor the close values of the two statistical moments in table 2 do not allow to conclude on the identical behaviour of each group of CDF. For that reason, the Kolmogorov–Smirnov test [6] associated with a level of signification equal to  $\alpha = 10\%$  was used in order to check the goodness of fit. For each density and loads, the KS test has been applied to each pair of simulation conditions (e.g. IEMF and NEC  $\oslash 10^{-3}\lambda$ ) and for each pair the test validates the goodness of fit with a high level of reliability reflected by the p-value larger than  $\alpha$ . According to this test, we can conclude

Density	Load	Simulation condition	Statistical moments	
			$ \mu $	$\sigma$
$1\lambda \times 1\lambda$	Matched	1	11.42	6.99
		2	11.50	7.05
		3	11.57	7.02
	Short-circuited	1	8.27	6.60
		2	8.33	6.62
		3	8.55	6.65
$2\lambda \times 2\lambda$	Matched	1	22.81	9.83
		2	22.94	9.80
		3	23.23	9.72
	Short-circuited	1	20.41	9.80
		2	20.59	9.79
		3	20.98	9.76
$3\lambda \times 3\lambda$	Matched	1	30.11	11.27
		2	30.26	11.20
		3	30.40	11.19
	Short-circuited	1	27.69	11.06
		2	27.94	11.12
		3	28.16	11.08
$4\lambda \times 4\lambda$	Matched	1	35.37	11.82
		2	35.55	11.88
		3	35.87	12.13
	Short-circuited	1	33.13	11.85
		2	33.37	11.94
		3	33.71	11.96

Table 2 – Statistical moments of reflection coefficient ( $|\Gamma_{in}|$ ) of surrounded dipoles, where the numbers present the simulation condition: 1 : IEMF, 2 : NEC  $\otimes 10^{-6}\lambda$  et 3 : NEC  $\otimes 10^{-3}\lambda$ .

that the statistical behaviour of the thick and thin dipoles are the same even if the intrinsic values of their input impedances and thus their reflection coefficients are quite different.

Figure 2 also shows that for a given mismatch level, the number of dipoles presenting better matching properties increases as the distribution surface increases (or the density decreases). In the case of short-circuit load the percentage of dipoles presenting a smaller reflection coefficient than  $|\Gamma_{in}| = -10$  dB, is equal to 33% for the highest density ( $1\lambda \times 1\lambda$ ) and reaches 99.6% for the lowest density ( $4\lambda \times 4\lambda$ ) as presented in the table 3. It is also observed that for a given density of tags, the loads of the surrounding dipoles have a very important influence on the reflection coefficient of a surrounded dipole. For  $1\lambda \times 1\lambda$  surface, the percentage of dipoles having  $|\Gamma_{in}| \leq -10$  dB increases from 33% with short-circuited surrounding dipoles to 75% with matched surrounding dipoles.

Load	$1\lambda \times 1\lambda$	$2\lambda \times 2\lambda$	$3\lambda \times 3\lambda$	$4\lambda \times 4\lambda$
Matched	75.35%	96.65%	98.7%	99.6%
Short-circuited	32.7%	84.05%	94.55%	97.3%

Table 3 – Percentage of matched dipoles

## 2.2 Radiation pattern

A method for estimating the radiation pattern of a driven antenna surrounded by a set of dipoles was initially developed in [7]. This method consists in determining the radiation pattern of a driven dipole by using the field radiated by each isolated element and the impedance matrix of the network. For a given direction of observation, the radiation field of a surrounded dipole is compared to the radiation field of the same dipole when isolated. For this direction, we calculate the ratio between these two field quantities as follows:

$$g_{\text{norm}} = \frac{|E_{\text{surrounded}}|}{|E_{\text{isolated}}|} \quad (2)$$

where  $E_{\text{surrounded}}$  is the electric field of the surrounded dipole and  $E_{\text{isolated}}$  is the electric field of the same dipole, when this latter is isolated.

According to the position and the orientation of the surrounded dipole and the density and the load of surrounding dipoles, the mutual coupling may have a positive impact on dipole radiation ( $g_{\text{norm}} > 1$ ), or may degrade the radiation of the isolated dipole ( $g_{\text{norm}} < 1$ ). Figure 3 shows the cumulative distribution functions of  $g_{\text{norm}}$  for the surrounded dipoles whose radiation is degraded compared to the radiation of the isolated dipole at the observation point  $\theta = 90^\circ$  and  $\varphi = 0^\circ$ . We can see that for a threshold of  $g_{\text{norm}} \leq 0.8$  which represent a

degradation higher than 20%, by increasing the density of the dipoles the percentage of dipoles having  $g_{\text{norm}}$  less than or equal to the threshold also increases. We can also observe in table 4 that the load of the surrounding dipoles has an important influence on the percentage of the degraded dipoles.

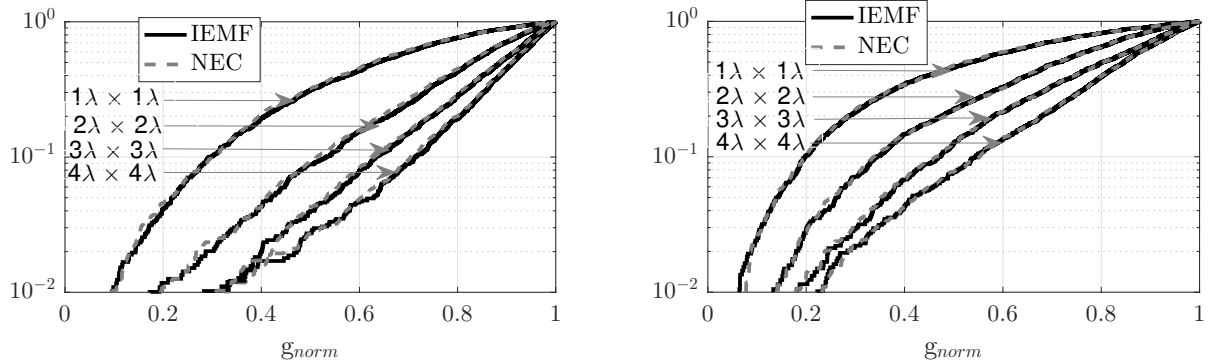


Figure 3 – CDF of  $g_{\text{norm}}$  for the set of surrounded dipoles whose radiation is degraded compared to the isolated dipole in the presence of matched (left) and short-circuited (right) dipoles as a function of different densities obtained by extended IEMF and NEC

Load	$1\lambda \times 1\lambda$	$2\lambda \times 2\lambda$	$3\lambda \times 3\lambda$	$4\lambda \times 4\lambda$
Matched	78%	44%	29%	20%
Short-circuited	82%	65%	49%	40%

Table 4 – Percentage of dipoles presenting a degradation higher than 20%

### 3 Conclusion

A set of tag antennas has been modeled by thin arbitrary distributed and oriented dipoles. In this paper, the input reflection coefficient and the radiation pattern of a surrounded dipole are calculated for different configurations of surrounding dipoles. The statistical assessment provides interesting conclusions about the percentage of mismatched dipoles as well as the distorted radiation pattern in the direction of the reader. The influence of the density, the loads and the thickness of the dipoles on the results have also been quantified. The results of the statistical study show also a similar group behaviour between thin and thick dipoles.

### 4 References

- [1] G. Marrocco, “RFID Grids: Part I Electromagnetic Theory,” *IEEE Transactions on Antennas and Propagation*, vol. 59, pp. 1019–1026, March 2011.
- [2] I. Adjali, A. Gueye, B. Poussot, S. Mostarshedi, F. Nadal, and J. Laheurte, “Statistical study of coupling in randomly distributed dipole sets,” in *12th European Conference on Antennas and Propagation (EuCAP 2018)*, pp. 1–5, April 2018.
- [3] H. Baker and A. LaGrone, “Digital computation of the mutual independance between thin dipoles,” *IRE Transactions on Antennas and Propagation*, vol. 10, no. 2, pp. 172–178, 1962.
- [4] I. Adjali, A. Gueye, S. Mostarshedi, B. Poussot, F. Nadal, and J. Laheurte, “Matching evaluation of highly coupled dipoles quantified by a statistical approach,” *IEEE Transactions on Antennas and Propagation*, accepted to be published.
- [5] K. Kurokawa, “Power waves and the scattering matrix,” *IEEE Transactions on Microwave Theory and Techniques*, vol. 13, pp. 194–202, March 1965.
- [6] A. Papoulis and S. U. Pillai, *Probability, Random Variables, and Stochastic Processes*. Tata McGraw-Hill Education, 2002.
- [7] I. Gupta and A. Ksieński, “Effect of mutual coupling on the performance of adaptive arrays,” *IEEE Transactions on Antennas and Propagation*, vol. 31, no. 5, pp. 785–791, 1983.

## **Conversion of a Pulsed Source Using a Multiband Frequency Selective Surface for HPM Applications**

### ***Modification d'une Source Impulsionnelle via Surface Sélective en Fréquence Multibande pour des Applications HPM***

***Fernando Albarracín-Vargas<sup>1</sup>, Félix Vega<sup>1,2</sup>, Chaouki Kasmi<sup>1,3</sup>, David Martínez<sup>1</sup>, Fahad Alyafei<sup>1</sup>, Lars-Ole Fichte<sup>2</sup>***

<sup>1</sup> *Directed Energy Research Centre, TII, Abu Dhabi, United Arab Emirates, fernando.albarracin@tii.ae*

<sup>2</sup> *Universidad Nacional de Colombia - Sede Bogotá, Bogotá, Colombia, jfvegas@unal.edu.co*

<sup>3</sup> *Faculty of Electrical Engineering, Helmut Schmidt University, Hamburg, Germany, lo.fichte@hsu-hh.de*

**Keywords (in English and French): frequency selective surface, impulse radiating antenna, complementary split-ring resonator/surface sélective en fréquence, antenne à rayonnement impulsif, résonateur à anneau fendu complémentaire.**

#### **Abstract/Résumé**

This paper presents a new contribution to a recently introduced type of resonant radiator, obtained as a combination of a Frequency Selective Surface (FSS) and an Impulse Radiating Antenna. The effects of a multiband FSS is studied and verified via simulations. A multiband radiator is obtained, enabling the capability of modifying the emitted signal for multiple applications, like EMI testing, or development of hardening modules that could be integrated into facilities. / Cet article présente une nouvelle méthode permettant la création d'une source micro-onde obtenu en combinant une surface sélective en fréquence (FSS) et une antenne à rayonnement impulsif. Les effets d'une FSS multibande sont étudiés et vérifiés via des simulations. Cette combinaison permet de modifier le signal émis par une source impulsionnelle résultant en une source micro-onde de forte puissance.

#### **1 Introduction**

The radiation of high-power electromagnetic pulses (EMP), produced by High Power Microwave (HPM) sources, is a topic of significant interest for the academic community and defense industry. It is related to the potential disruption of electrical systems and high technology microcircuits, both part of the critical infrastructure of a country. The characterization of such disruptions is subject to the Intentional Electromagnetic Interference (IEMI) studies. A key part of the design of a high-power EMP radiator is the antenna system [1], which involves the use of radiators with both broad bandwidth and high-voltage handling capabilities. The Impulse Radiating Antenna (IRA), first proposed by Baum and Farr [2]–[4], is one of the most representative types of high-power pulsed radiators for IEMI tests, due to its hyper-band response and high-power capability.

Both components mentioned so far, the antenna and the HPM pulsed source, share two important characteristics: high cost and fixed working bandwidth. In this context, the use of a frequency selective planar structure arises as a strategy to add frequency agility to the complete system antenna+EMP source. The ability to radiate over multiple bands is possible by arranging multiple resonating unit-cell types/dimensions into the Frequency Selective Surfaces (FSS). A thorough study regarding the band-stop effect from the metal-based grid of building walls, when illuminated with a hyper-band radiator, has been reported in [5]. The attenuation effect, due to reinforced concrete walls, in the downlink bands of actual mobile communication systems, is studied in [6]. A low-pass FSS that can be integrated into an ultra-wideband radiator was presented in [7]. Other alternatives, like the use of self-actuated surfaces, using arrays of nonlinear devices are described in [8], [9]. Voltage-controlled piezoelectric actuators are used to tune an FSS in [10].

FSS are narrowband passive structures that expose interesting properties when illuminated by electromagnetic fields. In their more usual form, the FSSs are implemented as resonant metal elements, or apertures, electrically small as compared with its resonance frequency, placed periodically over a containing surface or substrate [11]. The well-known Split Ring Resonators (SRR) proposed in [12] and its complementary version (i.e., CSRR), have been studied and characterized in the last years as a compact structure to compose an FSS [11], [13]. Frequency Selective Surfaces (FSS) are narrowband passive structures. In their more usual form, the FSSs are

implemented as resonant metal elements, or apertures, electrically small with respect to its resonance frequency, placed periodically over a containing surface or substrate [11]. To avoid diffractive effects and grating-lobes on the intended radiated beam, both the unit cell size and the periodicity separation shall be smaller than the wavelength of the incident radiation.

The well-known Split Ring Resonators (SRR) proposed in [12] and its complementary version (i.e. CSRR), have been studied and characterized in the last years as a compact structure to compose an FSS [13]. A very relevant characteristic of this resonators, for the sake of this work, is the capability of being cross-polarized. Thus, for the case of the SRR, a polarizing surface results by either the E- or the H- field (or both) polarized in a certain direction [11], a band-stop response of the FSS is obtained. Similarly, an electric dipole is induced from the excitation of a CSRR with an incident wave with the E-field component parallel to the rings' gaps, resulting in a bandpass filter surface. Marques et al. [11] presented an analytical solution for the behavior of the SRR- and CSRR-based FSS. Although restricted to the infinitesimally thin perfect conductor in free space, the analytical approach gives a first approximation to the response of a band-pass-type FSS.

This work presents an integrated multiband radiator by locating a CSRR-FSS in the near-field of an IRA as a strategy to add waveform and frequency agility to the EMP source. The ability to radiate over multiple bands is possible by arranging multiple-size resonating unit-cell into the FSS.

## 2 Multiband FSS Design

### 2.1 Unit Cell Design

The proposed unit cell is to be supported by a low relative permittivity substrate, (ideally  $\epsilon_r = 1$ ), simulated as losses free as a first approximation. It is composed of two different CSRRs, oriented as shown in Figure 1b. Since the intended response of the FSS is multiband, each band shall be tuned according to the resonant frequency of each unit-cell size. Only waves whose E-field is aligned to the gaps in the rings ( $y$ -axis in Figure 1a) will be able to pass through the FSS, at frequencies slightly higher than the resonant frequencies of the composing CSRR sizes. Figure 2 shows the reflection and the transmission parameter, respectively, for the unconnected CSRR-based FSS presented in this work. An additional resonant frequency is observed at 2.6 GHz in Figure 2b. This is associated with a high-frequency resonance of the 1.5 GHz unit cell. This additional passband is expected to be overlapped with the response from the 2.4 GHz unit cell.

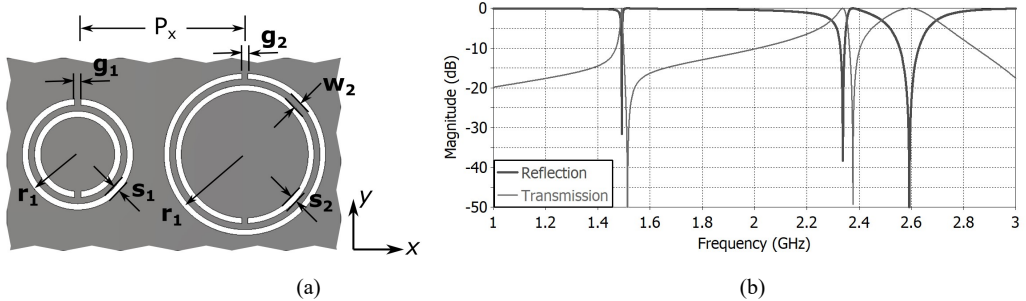


Figure 1: (a) Sketch of the two CSRR unit cells geometry. Unit cell 1, on the left, is associated with a passband frequency of 2.4 GHz. The unit cell on the right is resonant at 1.5 GHz. The dimensions are (all in mm)  $P_x = 26.5$ ,  $P_y = 26.5$ ,  $r_1 = 8.5$ ,  $r_2 = 12.65$ ,  $g_1 = g_2 = 1$ ,  $s_1 = s_2 = 1$ ,  $w_1 = w_2 = 1$ . (b) FSS response, simulated as an infinite periodic structure

### 2.2 Reflector Based IRA

The sketch of a two-arm IRA is shown in Figure 2a. When connected to a pulsed voltage source, the IRA radiates an impulse-like waveform over a narrow beam in the boresight direction ( $z$ -axis in Figure 2a). The electric field related to the waveform radiated by the IRA can be described as:

$$E_t(t, r) = f_1 \frac{1}{2\pi f_g} \left( \begin{array}{l} \frac{V(t-r/c)}{r} \frac{\sin(\beta)}{1+\cos(\beta)} - \frac{V(t-l/c-R_2/c)}{R_2} \frac{\sin(\beta)+\sin(\gamma)}{1+\cos(\beta-\gamma)} \\ - \frac{4}{D} V(t-2F/c-r/c) + (2+2\cos(\gamma)) \frac{V(t-l/c-R_2/c)}{D} \end{array} \right) (V / m) \quad (1)$$

where:  $V(t)$  is the feeding voltage,  $c$  is the speed of light and  $r$  is the distance between the focal point and the measurement point. The geometric impedance factor,  $f_g = Z_{\text{IRA}}/120\pi$ , is a reference parameter related to the feeder geometry that transmits the quasi-spherical TEM wave into the reflector.  $Z_{\text{IRA}}$  is the input impedance of the antenna.  $D$ ,  $F$ ,  $l$ ,  $\beta$ ,  $\gamma$ , and  $R_2$ , are described in Figure 2a. The two-arm coplanar feeder IRA presented in this paper is designed with the following parameters:  $D= 1(\text{m})$ ,  $F/D = 0.4$ ,  $Z_{\text{IRA}}= 400 (\Omega)$ .

### 2.3 Radiator Integration

The multiband radiator proposed here is depicted in Figure 2b. The FSS acts as a passband filter with a high-Q factor response. As mentioned before, the FSS is acting as a bandpass filter, modifying the impulse-like waveform propagating from the IRA by converting it into a damped sinusoidal, with two different frequency components. Only the E-field components aligned with the  $y$ -axis, and around the resonant frequency of each unit cell, will effectively pass through the FSS. Unit cells of the same size are aligned along the  $y$ -axis, in order to align each resonant polarization with the incoming wideband transient wave from the IRA.

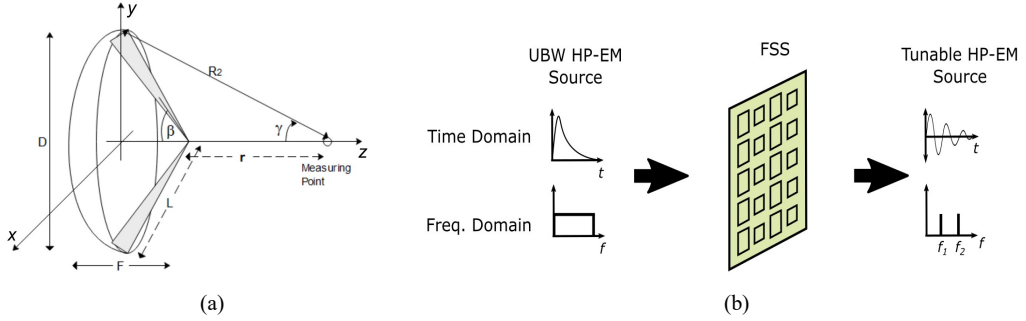


Figure 2: (a) Reflector-based IRA geometry. (b) Multiband HMP Radiator scenario

## 3 Results

The proposed integrated multiband radiator is modeled in a commercial full-wave simulator. The FSS is located 10 cm away from the focal point of the IRA. Although a large separation between FSS and antenna would minimize multiple reflections, diffracted waves from the perimeter of the FSS structure will have a more significant effect in the filtered pulse.

The E-field has been computed 5 m away from the focal point of the IRA, in broadside ( $z$ -axis). The time-domain response of the radiated E-field is shown in Figure 3a. The field radiated by a conventional two-arm unloaded IRA, with the same dimensions, is also shown as a reference. In both cases, a Gaussian pulse, with spectral content ranging from 0 to 3.5 GHz and unity amplitude is used as the driving signal.

It is observed the damped-like sinusoidal response of the proposed design, as expected. The passband filter behavior of the FSS loading the IRA is seen in the frequency domain response of the electric field, as shown in Figure 3b. The ideal filtering response of the IRA+FSS system can be computed as a cascaded product of the transfer functions, in the frequency domain, of the IRA and the FSS. This is possible by applying the *chain parameters* approach [6], as

$$T_A(f) = E_{\text{IRA}}(f)/V_{in}(f) \quad (2)$$

$$\begin{aligned} T_{\text{Total}}(f) &= T_A(f)T_{\text{FSS}}(f) \\ E_{\text{IRA+FSS}}(f) &= T_{\text{Total}}(f)V_{in}(f) \end{aligned} \quad (3)$$

where  $V_{in}(f)$  and  $E_{IRA}(f)$  are the Fourier transform of the voltage driving the IRA, and the radiated field, respectively.  $T_{FSS}(f)$  can be computed from the  $S$ -parameters of the FSS. Note that the  $E_{IRA}(f)$  does not necessarily have to be computed in the far-field region.

Despite the amplitude drop in the full-wave simulated IRA+FSS response, the intended passband effect holds around the resonant frequency of each unit-cell size, as can be seen in Figure 3b. Ideally, the impulse-like radiated pulse shall be converted into a signal with two different frequency components. However, harmonic resonances from the unit cells limit the bandwidth operation of the integrated radiator.

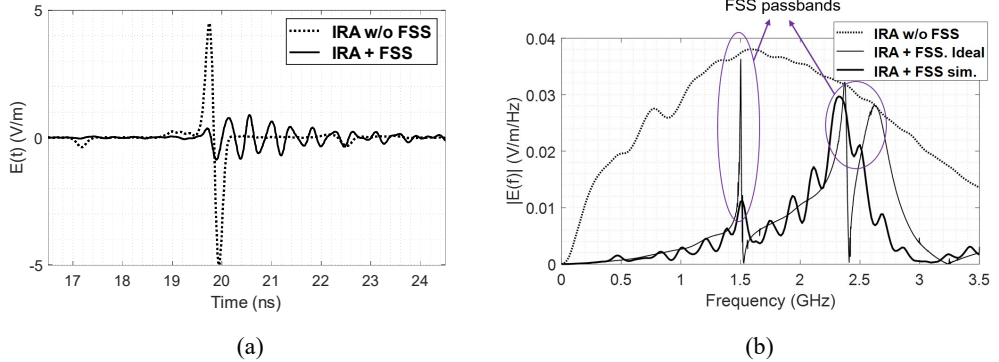


Figure 3: IRA vs. IRA+FSS: (a) time-domain and (b) spectral magnitude response in farfield, on boresight.

Since the proposed multiband FSS presents bilateral symmetry with respect to the main planes around the axis of the IRA, i.e.,  $xz$ -plane and  $yz$ -plane in Figure 2a, a symmetric and still directive radiation pattern can be expected, as it is shown in Figure 4. Significant degradation in the SLL ratio is observed in both frequency bands, especially in the  $E$ -plane. This can be associated with the limited size of the FSS ( $1 \times 1 \text{ m}^2$ ) that was finally integrated into the radiator. Thus, the effects of diffraction due to the FSS edge are evident. At higher frequencies (i.e. 2.4 GHz) this phenomenon is less arresting but still significant. One possible solution for this problem can be simply increasing the total area of the FSS, at the expense of affecting the manageability of the radiator. The maximum directivity is decreased from 18 dBi to 11 dBi at 1.5 GHz, while remained 22 dBi at 2.4 GHz. This response is in accordance with the higher field strength around 2.4 GHz, once the wave passes through the FSS (see Figure 3b).

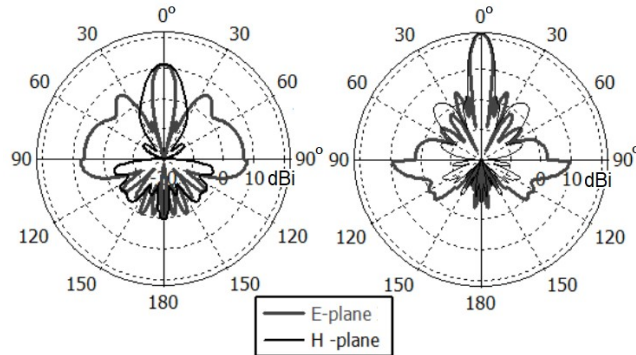


Figure 4: Radiation response of the integrated radiator, IRA+FSS. (a) At 1.5 GHz, (b) at 2.4 GHz.

An integrated multiband radiator has been presented. Multiband high-power radiation is enabled by adding frequency-selective planar structures to hyper-band radiators, like the two-arm IRA. Computed results in terms of the field strength, spectral density of the electric field, and the radiation pattern of the integrated antenna system have been obtained. The implementation of a prototype to verify the design is under process.

## References

- [1] F. Vega, N. Mora, F. Rachidi, N. Pena, and F. Roman, "Design, Construction and Test of a Half Impulse Radiating Antenna (HIRA)Canada," in *American Electromagnetics Conference [AMEREM]*, Ottawa, 2010.
- [2] C. E. Baum, "Radiation of Impulse-Like Transient Fields," *Sens. Simul. Notes*, vol. 321, no. USAF Phillips Lab, p. 28, Nov. 1989.
- [3] C. E. Baum and E. G. Farr, "Impulse Radiating Antennas," in *Ultra-Wideband, Short-Pulse Electromagnetics 2*, H. L. Bertoni, L. Carin, and L. B. Felsen, Eds. Boston, MA: Springer US, 1993, pp. 139–147.
- [4] C. E. Baum, "Aperture Efficiencies for IRAs," *Sens. Simul. Notes*, no. 328, Jun. 1991.
- [5] F. M. Tesche and D. V. Giri, "Modification of Impulse-Radiating Antenna Waveforms for Infrastructure Element Testing," *Sens. Simul. Notes*, vol. 572, p. 25.
- [6] G. Antonini, A. Orlandi, and S. D'elia, "Shielding effects of reinforced concrete structures to electromagnetic fields due to GSM and UMTS systems," *IEEE Trans. Magn.*, vol. 39, no. 3, pp. 1582–1585, May 2003, doi: 10.1109/TMAG.2003.810327.
- [7] W. Bigelow, E. G. Farr, and J. S. Tyo, "A Frequency Selective Surface Used as a Broadband Filter to Pass Low-Frequency UWB while Reflecting X-Band Radar," *Sens. Simul. Notes*, no. 506, 2006.
- [8] C. Yang, P.-G. Liu, and X.-J. Huang, "A Novel Method of Energy Selective Surface for Adaptive HPM/EMP Protection," *IEEE Antennas Wirel. Propag. Lett.*, vol. 12, pp. 112–115, 2013, doi: 10.1109/LAWP.2013.2243105.
- [9] S. Monni *et al.*, "Limiting frequency selective surfaces," in *2009 European Microwave Conference (EuMC)*, 2009, pp. 606–609, doi: 10.23919/EUMC.2009.5296360.
- [10] M. Mavridou, K. Konstantinidis, A. Feresidis, and P. Gardner, "Novel tunable frequency selective metasurfaces," in *2016 46th European Microwave Conference (EuMC)*, 2016, pp. 301–304, doi: 10.1109/EuMC.2016.7824338.
- [11] R. Marques *et al.*, "Ab initio analysis of frequency selective surfaces based on conventional and complementary split ring resonators," 2005, doi: 10.1088/1464-4258/7/2/005.
- [12] J. B. Pendry, A. J. Holden, D. J. Robbins, and W. J. Stewart, "Magnetism from conductors and enhanced nonlinear phenomena," *IEEE Trans. Microw. Theory Tech.*, vol. 47, no. 11, pp. 2075–2084, Nov. 1999, doi: 10.1109/22.798002.
- [13] J. D. Ortiz, J. D. Baena, V. Losada, F. Medina, and J. L. Araque, "Spatial Angular Filtering by FSSs Made of Chains of Interconnected SRRs and CSRRs," *IEEE Microw. Wirel. Compon. Lett.*, vol. 23, no. 9, pp. 477–479, Sep. 2013, doi: 10.1109/LMWC.2013.2274997.

# Conception et synthèse d'un réseau d'antennes parcimonieux dans la bande 3,4 – 3,8 GHz

S. FOFANA<sup>1,2</sup>, B. FUCHS<sup>1</sup>, F. COLOMBEL<sup>1</sup>, S. AVRILLON<sup>1</sup>, S. PALUD<sup>2</sup>

<sup>1</sup> IETR UMR 6164, 263 Av du Général Leclerc, 35000 Rennes,

{seydouba.fofana, benjamin.fuchs, franck.colombel, stephane.avrillon}@univ-rennes1.fr

<sup>2</sup>TDF, Centre de Mesures d'Antennes, La haute Galesnais, 35340 Liffré,

{ seydouba.fofana, sebastien.palud}@tdf.fr

*Mots clés (en français et en anglais) : 5G, réseau, synthèse, parcimonieux, reconfigurable*

## Résumé/Abstract

Ce papier présente le résultat de la conception d'un réseau linéaire d'antennes espacées de  $0,5\lambda_0$  à 3,6 GHz, puis une méthode de synthèse de réseau parcimonieux. L'antenne élémentaire est constituée de deux dipôles croisés à  $\pm 45^\circ$ , son design est réalisé avec le logiciel CST MWS. Le réseau d'antennes fonctionne dans la bande 3,4 -3,8 GHz et est alimenté par une architecture de beamforming numérique. Les diagrammes de rayonnement environnés des antennes sont introduits dans la méthode de synthèse. On démontre qu'avec la méthode de synthèse parcimonieuse, il est possible de réduire le nombre d'antennes utilisées pour une configuration de rayonnement donnée.

This paper presents the result of the design of a linear array of antennas spaced  $0,5\lambda_0$ , then a method to synthesize sparse arrays. The elementary antenna consists of two crossed dipoles at  $\pm 45^\circ$ , its design is made with CST MWS software. The antenna array operates in the 3.4-3.8 GHz band and is powered by a digital beamforming architecture. The embedded patterns of the antennas of the network are taken into account in the synthesis procedure. We show that with the sparse synthesis method, it is possible to reduce the number of antennas used for a given radiation configuration.

## 1 Introduction

La 5G se présente comme un réseau hétérogène et dense qui nécessite des infrastructures performantes et intelligentes [1]. Les infrastructures radio telles que les stations de base seront équipées de réseaux d'antennes reconfigurables qui rendront les couvertures radios plus flexibles, augmentant ainsi les performances en termes de débit et de capacité [2, 3]. Ce type de réseau est constitué de plusieurs amplificateurs de puissance (PA), or les amplificateurs de puissances font partie des composants qui consomme le plus d'énergie dans les stations de base, en particulier dans les macrocellules [4, 5]. Par conséquent, la consommation d'énergétique des stations de base pourrait considérablement augmenter.

Dans ce papier, on propose donc une solution qui consiste à minimiser le nombre d'antennes tout en respectant le gabarit de rayonnement nécessaire à une bonne couverture radio. On vous présente dans un premier temps la méthode de synthèse utilisée, puis dans un second la conception du réseau d'antennes. Ensuite des résultats de mesures de rayonnement et de consommation seront présentés avant de conclure.

## 2 Synthèse de réseau parcimonieux par la méthode d'optimisation convexe

Le problème consiste à déterminer une solution de pondération amplitude et phase parcimonieuse, qui respecte le gabarit de rayonnement défini dans le plan azimutal du réseau. Avec cette méthode, nous cherchons à réduire au maximum possible le nombre d'antennes puis de contrôler les excitations d'amplitudes et de phases des sources utilisées afin d'améliorer la consommation du réseau. Les problèmes seront formulés sous la forme d'un problème d'optimisation convexe [6]. Pour résoudre ces problèmes, nous utilisons CVX [7], qui est une bibliothèque permettant d'utiliser Matlab comme langage de modélisation.

Considérons un réseau linéaire de N antennes espacées de  $d_i$ . Chaque antenne rayonne un diagramme de rayonnement environné  $E_i$ , ce diagramme de rayonnement nous permet de prendre en compte les effets du couplage sur le rayonnement des antennes au sein du réseau. L'angle du plan azimutal est représenté par  $\varphi$  pour un niveau d'élévation  $\theta = \theta_o$ . Le champ électrique  $E(\varphi)$  rayonné par le réseau dans le plan azimutal s'exprime :

$$E(\varphi) = \mathbf{a}^H(\varphi)\mathbf{x} \quad (1)$$

$$\text{avec le vecteur directionnel } \mathbf{a}(\varphi) = [E_1(\varphi)e^{j\left(\frac{2\pi}{\lambda}\right)d_1 \sin \varphi}, \dots, E_N(\varphi)e^{j\left(\frac{2\pi}{\lambda}\right)d_N \sin \varphi}] \quad (2)$$

Où  $\mathbf{x}$  est le vecteur d'excitation complexe pour générer un diagramme de rayonnement à la fréquence  $f$  correspondant à la longueur  $\lambda$ . Le vecteur  $\mathbf{x}$  représente la variable d'optimisation du problème.

Le problème d'optimisation convexe consiste à trouver le vecteur d'excitation  $\mathbf{x}$  afin d'émettre un diagramme de rayonnement directif dans une direction  $\varphi_{max}$ . Cependant, nous voulons réduire au maximum le nombre d'excitations. Une excitation nulle signifie que l'antenne correspondante n'est pas utilisée, et par conséquent l'amplificateur associé est éteint. Pour cela, minimiser la norme  $l_1$ , c'est-à-dire la somme des valeurs absolues des excitations se révèle être une approche efficace. Le problème s'écrit :

$$\min_{\mathbf{x}} \sum_{n=1}^N |x_n| \quad \text{sous} \quad C(\mathbf{x}) = \begin{cases} Re(\mathbf{a}^H(\varphi_{max})\mathbf{x}) \geq \beta \\ \max(|\mathbf{a}^H(\varphi)\mathbf{x}|) \leq \frac{\beta}{\sqrt{2}}, \quad \varphi \notin \varphi_{HPBW} \\ \max(|\mathbf{a}^H(\varphi)\mathbf{x}|) \leq \frac{\beta}{\rho}, \quad \varphi \in \varphi_{SLL} \end{cases} \quad (3)$$

Où l'angle  $\varphi_{max}$  représente la direction du lobe principal et  $\rho$  est le rapport entre le niveau maximal du lobe principal et celui des lobes secondaires. Les domaines angulaires  $\varphi_{HPBW}$  et  $\varphi_{SLL}$  sont respectivement les domaines définis pour la contrainte liée à l'ouverture à mi-puissance (HPBW) et celle liée au niveau des lobes secondaires (SLL). De plus,  $\beta$  représente, le champ électrique rayonné par le réseau à une distance  $R$  de celui-ci. Il existe une relation entre  $\beta$  et la puissance isotopique rayonnée équivalente PIRE [8], cela permet donc de dimensionner le réseau par rapport à la puissance d'émission souhaitée. La relation s'écrit :

$$\beta = \frac{\sqrt{30 * \text{PIRE}}}{R} \quad (4)$$

Pour augmenter la parcimonie de la solution (3), on peut appliquer la norme  $l_1$  pondérée tel que décrit dans [9].

## 1 Réseau de 16 antennes reconfigurables

Pour nos travaux, nous avons réalisé uniquement les chaines d'émission, tel que décrit sur la figure 1. Les chaines d'émission alimentent 16 dipôles ayant la même polarisation, à priori ceux orientés à  $-45^\circ$  par rapport au plan du réseau (voir figure 2). Dans l'idéal, ce réseau doit être en mesure de générer un diagramme qui dépointe jusqu'à  $\pm 45^\circ$  dans son plan azimutal.

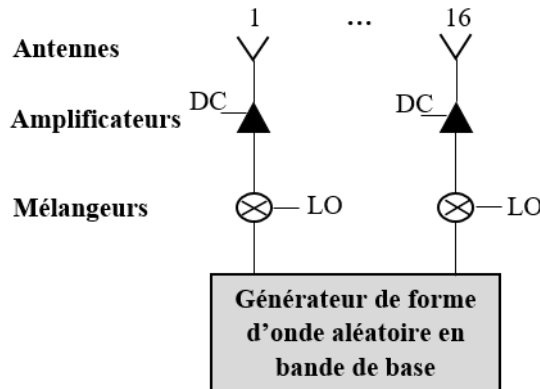


Figure 1 : Architecture du réseau d'antennes reconfigurables

### 1.1. Architecture

L'architecture du réseau choisie est celle d'un réseau d'antennes actives composé d'un générateur de signaux à 16 voix reliés à 16 chaines d'émission. C'est une architecture de formation de faisceau numérique communément appelé beamforming numérique, le déphasage et les pondérations amplitude et phase sont réalisés en bande de base.

Pour la génération des signaux en bande de base, nous avons utilisé un générateur de forme d'onde aléatoire DN6.662-16 de la compagnie d'instrumentation SPECTRUM [10]. Cet appareil a une fréquence d'échantillonnage maximale de 625 MS/s et il est capable de générer des signaux dont les amplitudes et les phases peuvent être contrôlés par logiciel. Il peut générer des signaux en bande de base de 0 à 200 MHz entre  $\pm 2,5$  V.

Les signaux en bande de base sont transposés dans la bande 3,4 – 3,8 GHz grâce aux 16 mélangeurs [11]. Chaque mélangeur comporte 2 entrées, une entrée pour le signal en bande de base et une autre pour le signal de l'oscillateur local OL dont la fréquence  $f_{OL}$  fixée à 3,57 GHz, constitue la fréquence de transposition. Les signaux OL proviennent de la même source à l'aide d'un jeu de 5 répartiteurs de puissance à 4 sorties. Tel que décrit par le fabricant, pour garantir un bon fonctionnement du mélangeur, la puissance des signaux OL doivent être environ de 13 dBm et celle des signaux en bande de base ne doit pas excéder 10 dBm (soit une amplitude maximale de 1 V) pour éviter la saturation du mélangeur. Dans le cadre des mesures en chambre anéchoïque, les signaux en bande de base sont des porteuses pures à 10 MHz (ou à 50 MHz) avec une différence d'amplitudes et de phases, après transposition on obtient des signaux hautes fréquences à 3,58 GHz (ou 3,62 GHz).

Les signaux transposés sont ensuite amplifiés avant d'être émis par le réseau. Nous avons utilisé pour cela 16 amplificateurs du commerce dénommés BMT352 [12], dédiés aux applications de transmission. Un circuit d'alimentation à polarisation unique incluant des interrupteurs a été conçu pour permettre d'alimenter ou d'éteindre indépendamment chaque amplificateur. Après la mise en place des amplificateurs et leur circuit d'alimentation, ils ont un point de compression d'environ 30 dBm.

Afin de bien dimensionner le réseau, une étape de calibration a été nécessaire. L'étape de calibration a consisté à mesurer, à l'aide d'un analyseur de réseau, le gain associé à chaque chaîne d'émission et leurs différences de phase par rapport à une chaîne RF de référence. Les résultats des mesures sont ensuite intégrés dans l'outil de synthèse pour déterminer directement l'amplitude en tension et la phase du signal que doit générer sur chacune des 16 voix du générateur.

## 1.2. Conception du réseau d'antennes

Le réseau est composé de 16 antennes espacées de  $0,5\lambda_0$  correspondant à la fréquence  $f_0 = 3,6$  GHz. Chaque antenne est constituée de deux dipôles croisés à  $\pm 45^\circ$ , pour notre étude nous considérons uniquement une des dipôles. Le choix de ce type d'antenne répond aux exigences des antennes de station de base, qui doivent être de faible coût, robuste et facile à reproduire [13].

Ces dipôles sont en technologie imprimée, ils ont été conçus à l'aide du logiciel CST MWS (cf. Figure 2). Les dimensions des dipôles et des baluns ont été prédefinis suivant le modèle théorique décrit dans [14]. Avec l'antenne seule, nous obtenons une bonne adaptation dans la bande 3,4 – 3,8 GHz, à savoir un coefficient de réflexion  $|S_{ii}|$  inférieur à -15 dB et un niveau de découplage  $|S_{ji}|$  inférieur à -38 dB.

Cependant, une fois les 16 antennes mise en réseau (voir figure 2), les performances radioélectriques ont été impactées par le biais des phénomènes de couplage inter-élément et de réflexions aux alentours des antennes. Comme on peut le voir sur un extrait des résultats de la simulation présenté sur la figure 3a, nous obtenons finalement un niveau maximum de couplage de -15 dB et une adaptation qui reste inférieur à -15 dB. De plus, les diagrammes des antennes sont différents et ne sont plus identiques à celui d'une antenne isolée, on parle de diagramme de rayonnement environné (figure 3b). Pour la formulation du problème (3), ces diagrammes sont extraits de CST MWS pour un niveau de champ (en volt par mètre) correspondant à une distance de  $R = 100$  m du réseau.

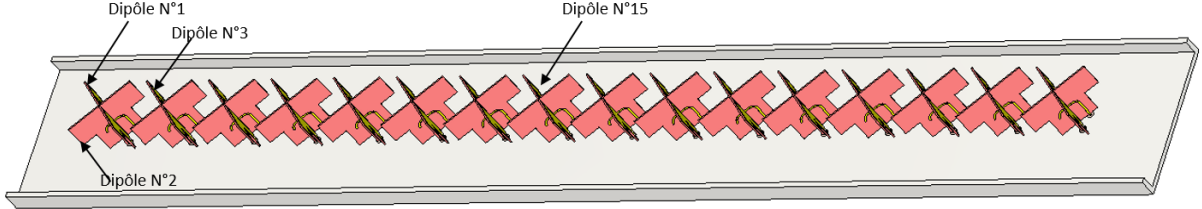


Figure 2: Réseau linéaire de 16 antennes à base de 2 dipôles croisés ( $\pm 45^\circ$ )

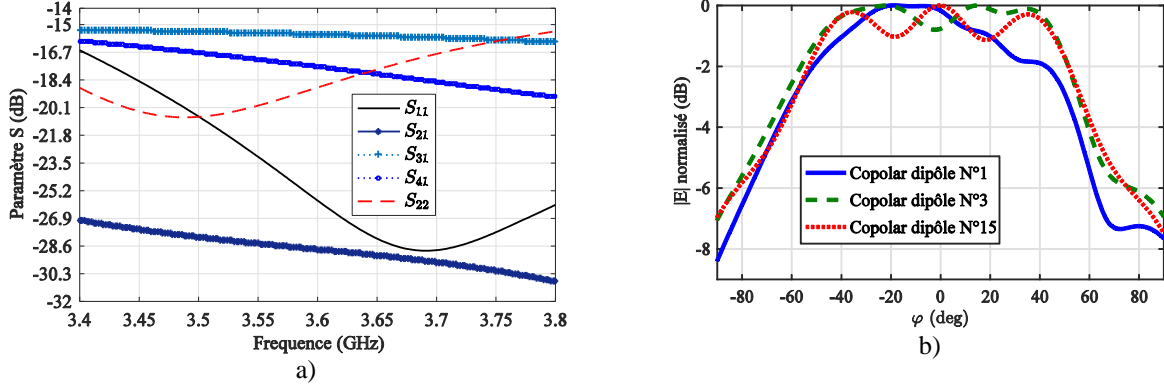


Figure 3: Extrait du paramètre S des 2 premiers dipôles du réseau (a) et exemples de diagrammes environnés (simulés) de dipôles dans le réseau (b). Ces diagrammes sont représentatifs des diagrammes de rayonnement des dipôles situés à l'extrémité et au centre du réseau.

## 2 Mesures

Les mesures sont réalisées en chambre anéchoïque au centre de mesure d'antennes de TDF. L'objectif est de valider la méthode de synthèse et d'évaluer la consommation énergétique. Pour cela, on analyse les performances de rayonnement en termes de diagramme et de puissance d'émission (PIRE). Les mesures de consommation sont collectées à l'aide d'un microcontrôleur relié au circuit d'alimentation des amplificateurs.

Pour le scenario, deux exemples de faisceaux seront présentés, l'un pour  $\varphi_{\max} = 0^\circ$  à 3,58 GHz (figure 4a) et l'autre pour  $\varphi_{\max} = +30^\circ$  à 3,62 GHz (figure 5a). Pour chacune de ces exemples, le gabarit se résume à une PIRE de 48 dBm, une ouverture à mi-puissance (HPBW) inférieur à  $10^\circ$  et un niveau maximal des lobes secondaires (SLL) de -15 dB en dessous du lobe principal. Connaissant la PIRE, et la distance  $R = 100$  m, on déduit la contrainte  $\beta$  à l'aide de l'équation (4).

### 2.1. Performance en rayonnement

Les jeux de pondération (figure 4b et 5b) pour les 2 exemples cités sont déterminés en résolvant l'équation (3). Dans le premier cas, nous avons 3 sources éteintes contre 2 sources éteintes dans le second cas, car plus on dépointe plus il devient difficile de respecter les contraintes avec moins de sources allumées. Après mesure, nous obtenons les diagrammes représentés sur les figures 4a et 5a. Les diagrammes mesurés sont assez proches des résultats de simulation avec des valeurs de PIRE respectives de 47,25 dBm et 47,5 dBm. De plus les écarts entre la composante co-polarisation et cross-polarisation restent correctes.

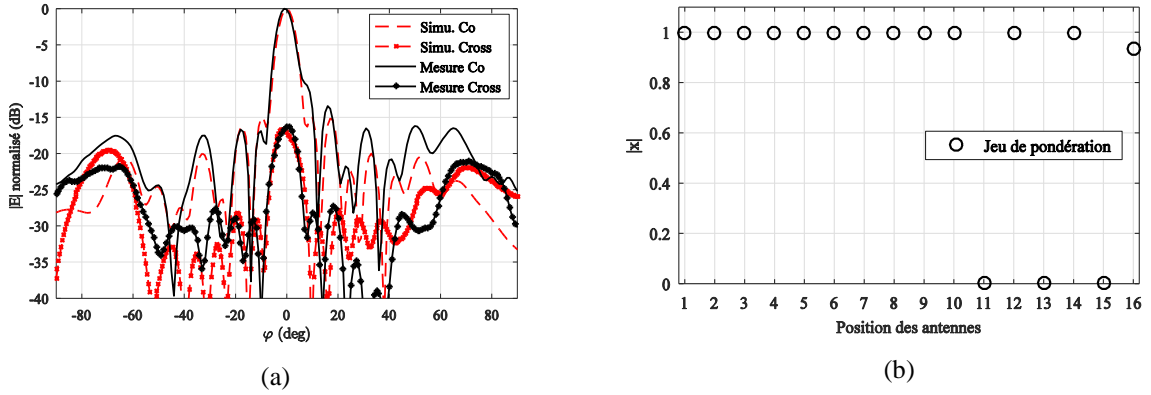


Figure 4: Résultat de la synthèse de réseau (a) et le jeu de pondération en amplitude associé (b) pour un rayonnement à 3,58 GHz et un dépointage à 0°. Comparaison entre simulation et mesures des composantes co- et cross-polarisation du champ électrique rayonné par le réseau.

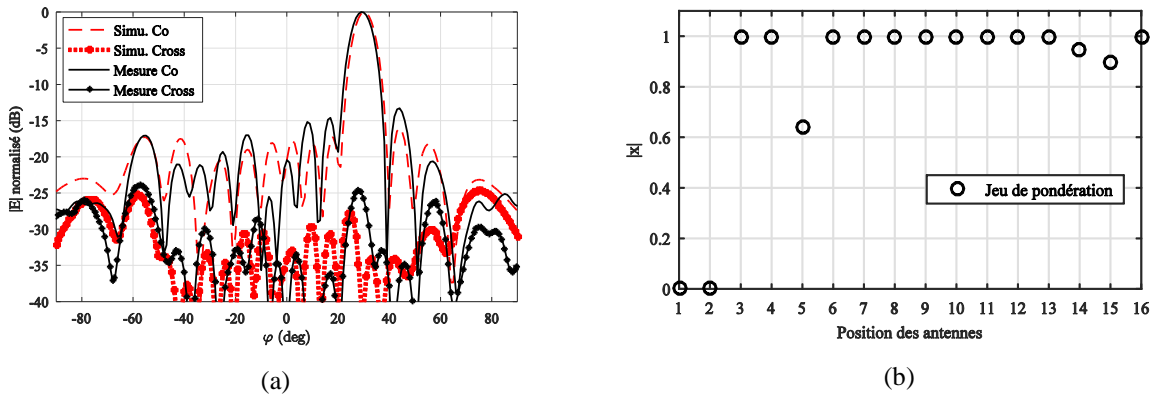


Figure 5: Résultat de la synthèse de réseau (a) et le jeu de pondération en amplitude associé (b) pour un rayonnement à 3,62 GHz et un dépointage à +30°. Comparaison entre simulation et mesures des composantes co- et cross-polarisation du champ électrique rayonné par le réseau.

D'après une étude qui n'est pas présenté dans ce document, les écarts seraient liés en partie, à l'influence de l'impédance active des amplificateurs éteints sur les diagrammes environnés des antennes allumées. Cette influence est plus importante lorsque les sources éteintes sont entourées de sources allumées, comme dans l'exemple de la figure 4b. Au cours de cette étude nous avons constaté que, en prenant en compte l'impédance active des amplificateurs éteints et allumés, nous obtenons un jeu d'excitation différent et donc de meilleurs résultats.

## 2.2. Reduction de la consommation

Afin d'évaluer la réduction de consommation en énergie, nous comparons notre méthode de synthèse avec une autre solution qui utiliserait toutes les sources du réseau. Cette autre solution est obtenue en résolvant l'équation (3) sans appliquer la norme  $l_1$ , on obtient un jeu de pondération tapérisé. D'après les résultats de mesures présentés dans le Tableau 1, nous constatons une réduction de la consommation d'au moins 4 %. Il faut retenir que plus il y a de sources éteintes, plus la consommation est réduite.

De surcroit, en mettant en place un circuit d'alimentation permettant de changer la polarisation des amplificateurs, pour baisser leur point de compression en fonction de la puissance nécessaire en sortie, nous parviendrons à réduire davantage la consommation des amplificateurs et améliorer leur rendement. Après avoir obtenu des résultats convainquant à travers la simulation, ceci constitue la prochaine étape qui démontrerait l'efficacité énergétique d'un réseau d'antenne parcimonieux alimenté par des amplificateurs à polarisation variables.

Type de réseau	$\varphi^{max}$	P <sub>Dc</sub> (W)	Sources éteintes	Pourcentage de réduction
Solution proposée	0°	21,3	3	10 %
Sans sources éteintes	0°	23,7	0	
Solution proposée	+ 30 °	22,0	2	4,3 %
Sans sources éteintes	+ 30 °	23,0	0	

Tableau 1 : Consommation des amplificateurs

### 3 Conclusion

Dans ce papier, nous avons présenté la conception d'un réseau d'antennes reconfigurables dans la bande 3,4 – 3,8 GHz, et la méthode de synthèse de réseau parcimonieux associée. D'après les bonnes performances de rayonnement et de réduction énergétique obtenues, nous concluons que ce procédé d'utilisation des réseaux reconfigurables peut être un bon atout pour les stations de base 5G.

### Références bibliographiques

- [1] GSMA Intelligence, «Understandig 5G: Perspectives on future technological advancements in mobile», Dec. 2014
- [2] ICT-317669 METIS project, “Final report on the METIS 5G system concept and technology roadmap,” 30 Apr. 2015.
- [3] Ericsson, «5G Radio Access,» *Ericsson White paper*, Apr. 2016.
- [4] S. K. Bhondge, D. B. Bhowar and S. Mohad, “Strategy for Power Consumption Management at Base Transceiver Station,” *IEEE Word Conference on Futuristic Trends in Research and Innovation for Social Welfare*, 2016.
- [5] M. H. Alsharif, M. Ismail and R. Nordin, “Survey of Green Radio Communications Networks: Techniques and Recent,” *Journal of Computer Networks and Communications*, Dec. 2013.
- [6] H. Lebret and S. Boyd, "Antenna pattern synthesis via convex optimization," *IEEE Trans. Signal Proc.*, vol. 45, no. 3, pp. 526-531, March 1997.
- [7] CVX Research, Inc. (Sep. 2012). CVX: Matlab Software for Disciplined Convex Programming, Version 2.0 Beta. [Online]. Available: <http://cvxr.com/cvx>
- [8] T. A. Milligan, *Modern Antennas Design*, A JOHN WILEY & SONS, 2nd ed., 2005.
- [9] B. Fuchs, "Synthesis of Sparse Arrays With Focused or Shaped Beampattern via Sequential Convex Optimizations," *IEEE*, vol. 60, pp. 3499 - 3503, July 2012.
- [10] Spectrum, 16 bit Arbitrary Waveform Generator, <https://spectrum-instrumentation.com/en/dn6662-16>.
- [11] Mini-Circuits, Double Balanced Mixer: RF/LO Freq 2300 –7600 MHz, Available: <https://www.minicircuits.com/WebStore/dashboard.html?model=ZX05-762H-S%2B>.
- [12] BEREX, High Power Amplifier, Available: <https://www.berex.com/Products/HighPowerAmplifier.aspx>.
- [13] Z. N. Chen and K.-M. Luk, *Antennas for base stations in wireless communications*, The McGraw-Hill Companies, 2009.
- [14] B. Edward and D. Rees, “A broadband printed dipole with integrated balun”, *Microwave journal*, pp. 339-344, May 1987

## Surface rayonnante à agilité de faisceaux versus réseaux d'antennes agiles Beamsteering radiating surface vs phased antenna array

Bernard Jecko<sup>1</sup>, Mohamad Majed<sup>1</sup>

<sup>1</sup> XLIM UMR 7252, université de Limoges/CNRS, {bernard.jecko , mohamad.majed}@xlim.fr

*Mots clés:* Antennes à agilité de faisceaux, Matrice rayonnante pixellisée, Agile beam antennas, agile beam radiating matrix antenna, (ARMA).

### Résumé/Abstract

Dans le domaine des télécom (en particulier pour la 5G), des Radars, de la Guerre Electronique, les antennes à agilité de faisceaux sont de plus en plus demandées car elles sont capables d'effectuer la formation de faisceaux ou (et) le balayage électronique. Aujourd'hui, ces fonctions sont essentiellement effectuées par une technique très connue : les Réseaux d'antennes agiles (AESA). Malheureusement cette technique entraîne des limitations intrinsèques que l'on va avoir besoin de dépasser dans un futur proche pour de nouvelles applications. L'objet de cette présentation est d'introduire une nouvelle technique appelée en français MARPEM (Matrice Agile Rayonnante à Pixels Elaborés en Metamatériaux) pour tenter de repousser ces limitations.

In the field of terrestrial or space telecoms, Radars, Electronic Warfare, Beam Agility Antennas are increasingly in demand as they are capable of Beamforming or (and) Beamsteering. Today, these functions are mainly performed by a very well-known technique: phased antenna array (AESA). Unfortunately, this technique leads to intrinsic limitations that we will need to overcome in the near future for new applications. The purpose of this presentation is to introduce a new technique called in English ARMA (Agile Radiating Matrix Antenna) to try to overcome these limitations.

### 1 Le concept MARPEM

Quelle est la meilleure solution pour obtenir un diagramme de rayonnement agile ou non? Pour répondre à une telle question il faut développer une approche rigoureuse au départ: Equations de Maxwell, Equations de Propagation, Fonction de Green de l'espace libre, Principe d'Equivalence (Huygens), Produit de Convolution Fonction de Green par les champs sur la surface S d'Huygens dite Surface Rayonnante.

Dans le cas particulier des antennes planaires (low profile antennas) la surface rayonnante peut être un parallélépipède extra plat ( $\approx \lambda/10$ ) posé sur un plan de masse et réduite à sa surface supérieure S par ou sort l'essentiel de l'énergie. Une approximation analogue est effectuée dans la théorie des ouvertures résonnante qui conduit à la même expression du champ rayonné :

$$\vec{E}(P) = \frac{jk}{4\pi} \psi(R)(1 + \cos\theta)(\cos\phi \vec{e}_\theta - \sin\phi \vec{e}_\phi) SFT = K \cdot SFT \quad (1)$$

Avec :  $SFT = \iint E_s(x, y) e^{j(kx \sin\theta \cos\phi + ky \sin\theta \sin\phi)} ds$  et  $\psi(R) = \frac{e^{jKR}}{R}$

Cette intégrale montre que le champ rayonné  $E(P)$  est pratiquement la transformée de Fourier spatiale du champ sur la surface S notée SFT.

### 2 Introduction de l'agilité

Pour changer de diagramme, il faut pouvoir générer n'importe quel champ ( $E_s, H_s$ ) sur la surface S ; il faut donc échantillonner cette surface, de cette façon on pourra reconstruire n'importe quel champ mais l'approche rigoureuse s'arrête là. La plus simple des techniques d'échantillonnage est l'échantillonnage par Peigne de Dirac 2 D: le plus simple mais le moins précis. L'équation (1) devient :

$$E(P) = K \sum_i \sum_j E_s(x_i, y_j) e^{j(kx \sin\theta \cos\phi + ky \sin\theta \sin\phi)} dx dy$$

Le champ  $E(P)$  est la somme des champs générés par  $N \times M$  sources ponctuelles localisées en  $i, j$  ; c'est la Théorie des Réseaux d'Antennes.

L'approche originale proposée consiste à appliquer un échantillonnage par une fonction porte en  $x$  et une en  $y$  formant un carré.

Cet échantillonnage plus précis conduit à l'expression du champ  $E(P)$  :

$$\vec{E}(P) = K \sum_i \sum_j A_{i,j} \iint_{S_{i,j}} e_{i,j}(x, y) e^{j(kx \sin \theta \cos \phi + ky \sin \theta \sin \phi)} dx dy$$

Avec  $e_{i,j}(x, y)$  : Constante et  $A_{i,j}$ : poids imposés pour in diagramme donné.

Le champ  $E(P)$  est la somme des champs créés par  $N \times M$  éléments de surface  $S_{i,j}$  uniformes jointifs dits «Pixels»[1][2][3].

Pour une antenne planaire de surface  $S$ , la solution revient à considérer la surface comme une matrice de  $N \times M$  pixels, chacun affecté d'un poids particulier (figure 1).

### Matrice planaire

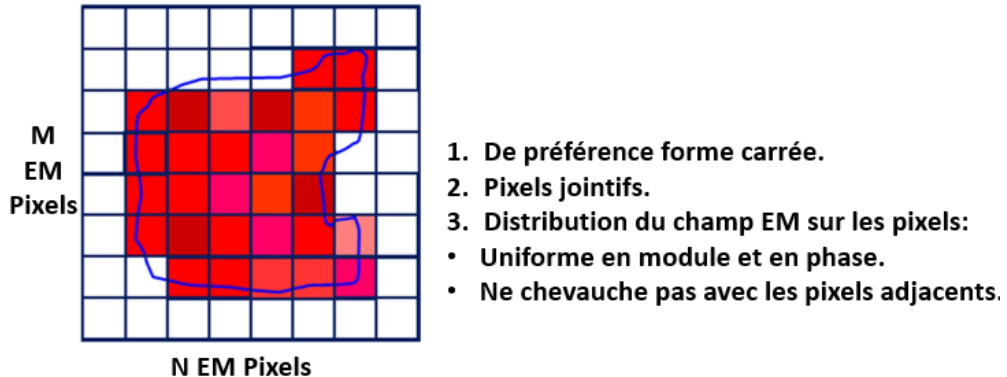


Figure 1 Surface rayonnante échantillonnée par des pixels carrés jointifs.

Il n'y a aucune restriction sur la surface  $S$  et les pixels peuvent avoir n'importe quelle forme, mais ils doivent être jointifs. Comme pour les réseaux agiles, les pixels doivent être alimentés par une électronique de commande des faisceaux (BFN: Beam Forming Network) pour appliquer les poids appropriés[2] afin d'obtenir les diagrammes de rayonnement attendus.

Enfin, toute l'antenne est constituée des nombreux pixels formant une matrice qui s'appelle MARPEM (Matrice Agile Rayonnante à Pixels Elaborés en Metamatériaux) (figure 2).

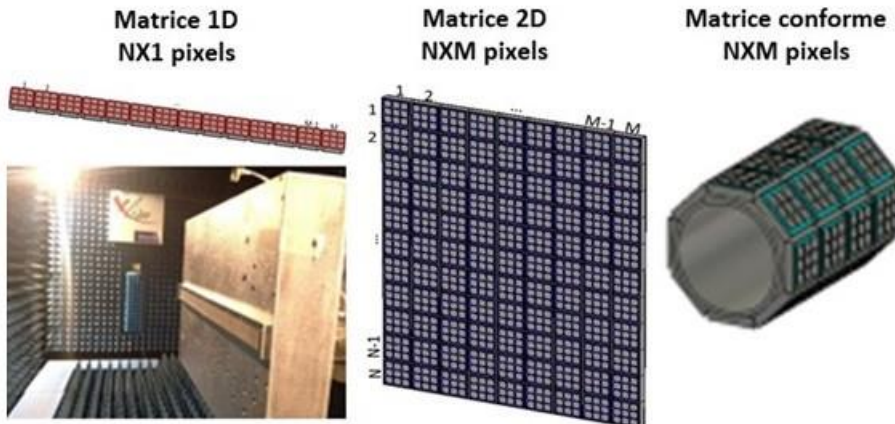


Figure 2 Architectures de MARPEM.

### 3 Design du pixel

Le pixel [2] doit être capable de générer une surface rayonnante uniforme (champs constants sur toute la surface). Sa forme est déduite de celle d'une antenne BIE (à Bande Interdite Electromagnétique) de grande taille (figure 3a) caractérisée par un plan de masse, une cavité à air et une surface semi-réfléchissante (PRS) qui est généralement une surface sélective en fréquence (FSS)[4][5][6][7]. Des murs métalliques (figure 3b) sont introduites autour de la sonde d'alimentation (généralement un patch) de l'antenne BIE [1]. La structure finale est représentée sur les figures 4a et 4b. En raison de l'évanescence radiale du mode dans l'antenne BIE, le champ électromagnétique est presque constant au sommet du pixel figure 4c, générant un diagramme de rayonnement directif [1].

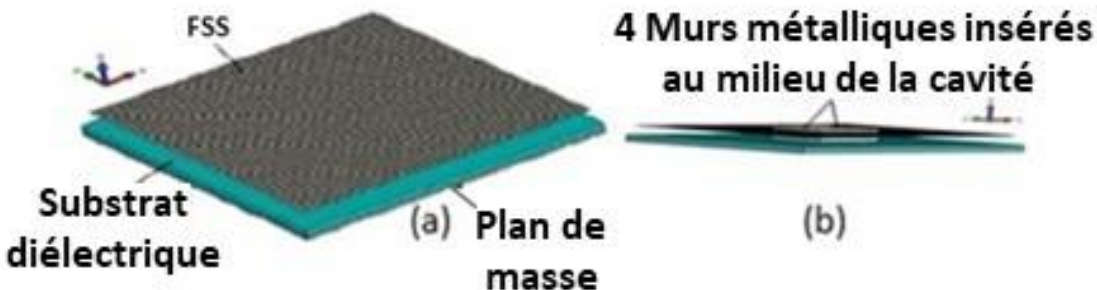


Figure 3 (a) Antenne BIE à grand gain (b) Murs métalliques à l'intérieur de l'antenne BIE.

Les murs électriques peuvent être remplacés par des murs magnétiques ce qui revient à isoler un morceau de l'antenne BIE.

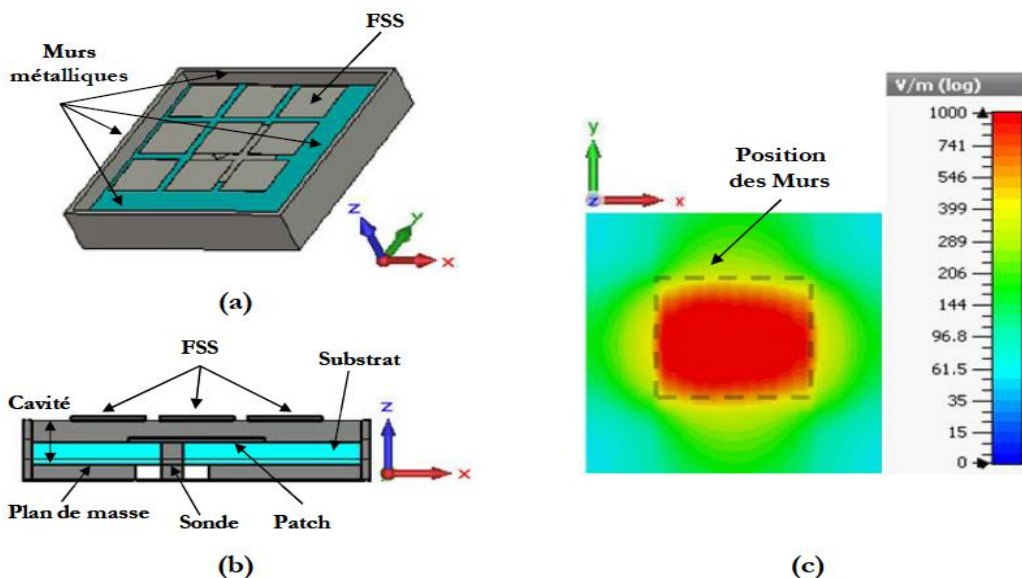


Figure 4 Pixel alimenté par un patch: (a) vue en perspective, (b) vue en coupe selon x, (c) Cartographie du champ  $E$  sur la surface rayonnante du pixel

### 4 Comparaison MARPEM-Réseaux Agiles

#### 4.1 Avantages de la structure

- Les dimensions des pixels dans l'antenne MARPEM peuvent facilement atteindre  $1,2\lambda \times 1,2\lambda$ . Pour une surface d'antenne donnée, le nombre d'éléments (pixels) peut être bien limité, ce qui réduit fortement le coût du BFN. Un réseau avec la même surface a généralement besoin d'environ 4 fois plus d'éléments rayonnants (patches) car la périodicité est limitée à  $0,8\lambda$  pour éviter les lobes de réseau [1].

- Bande de fréquence: en raison des propriétés de l'antenne BIE « low profil » d'origine, la bande passante des pixels peut facilement atteindre 40% [8] et les effets de couplage entre 2 ports sont généralement limités sous -20 dB [9] en polarisation TE. Par conséquent, une antenne MARPEM avec  $14 \times 14$  pixels a approximativement la même bande passante que le pixel seul (figure 5) pour les 196 pixels.

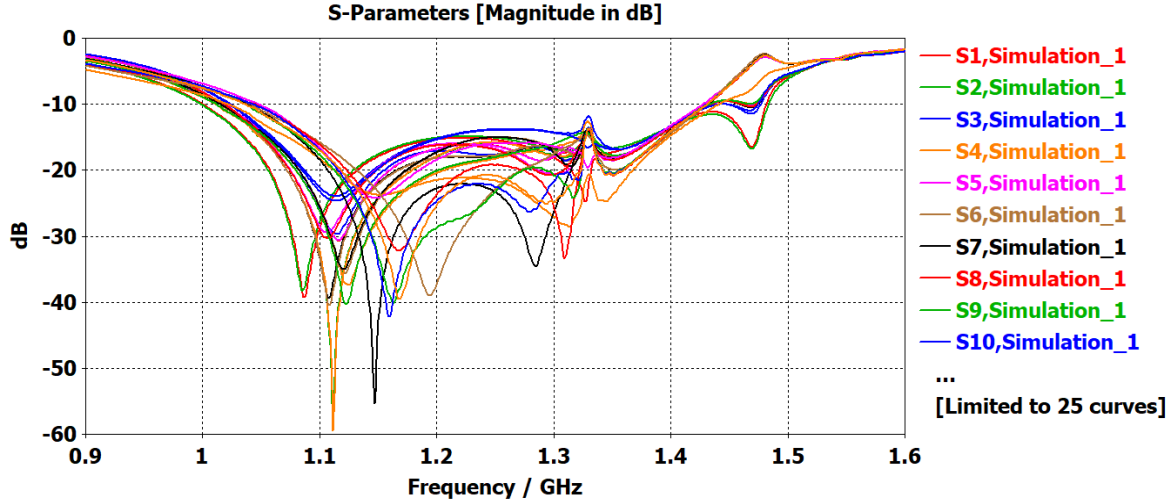


Figure 5 Evolution des paramètres actifs  $S_{ii}$  en fonction de la fréquence pour un ARMA  $14 \times 14$  pixels.

- Dans les fréquences millimétriques (Ku ou Ka), la solution MARPEM peut également être conçue [10] avec les mêmes performances, notamment le même ordre de grandeur de bande passante. Par exemple, un pixel construit avec une PRS (Partially Reflective Surface) très simple constituée d'une plaque de zircone homogène et alimenté par un dipôle large bande (figure 6) donne une bande passante de 47,8%.

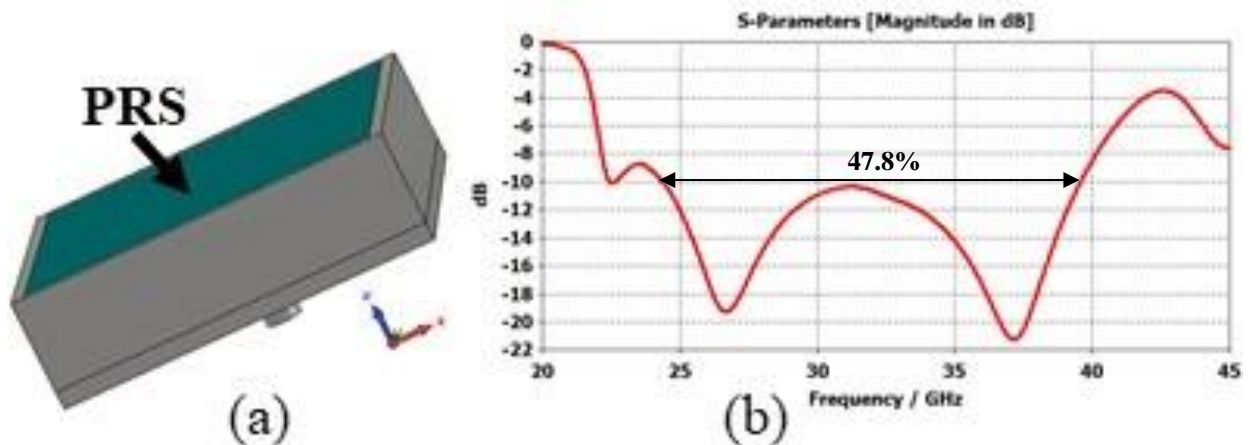


Figure 6 (a) Antenne pixel avec une PRS homogène. (b) Paramètre  $S_{11}$  en fonction de la fréquence.

- La surface MARPEM: Il n'y a pas de restrictions strictes sur la forme des pixels, qui peut être plane ou conformée [11], avec n'importe quelle forme de surface: carrée, rectangulaire, triangulaire, circulaire et trapézoïdale... Par exemple, des pixels circulaires et trapézoïdaux sont combinés (figure 7) pour conserver une bonne symétrie circulaire dans un diagramme de rayonnement isoflux autour de 8,2 GHz.

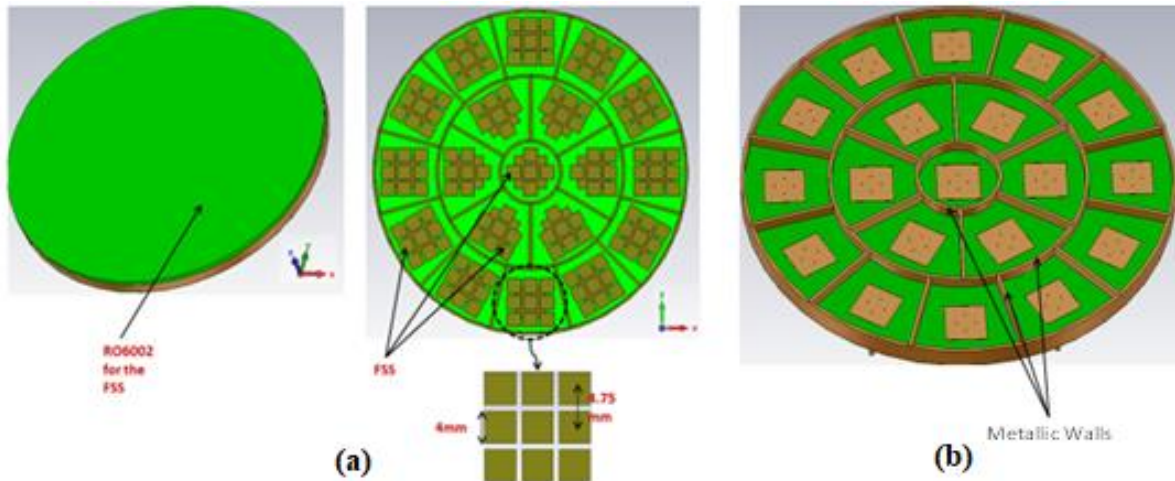


Figure 7 Antenne « low profil » à symétrie de révolution avec pixels alimentés par des patchs à quatre ports (polarisation circulaire): (a) Vues globales avec et sans radôme, (b) sans FSS.

Pour illustrer ce comportement, le diagramme de rayonnement polarisé circulairement obtenu à partir de l'antenne MARPEM à symétrie de révolution (figure 8) est présenté sur la figure 8 et comparé à celui obtenu à partir d'une solution MARPEM carrée [12]. L'antenne MARPEM low profil de forme carrée avec 5X5 pixels [12] montre sur la figure 8a une forte non uniformité du gain d'environ 2,75 dBi, par contre l'antenne MARPEM à symétrie de révolution présente un diagramme (Figure 8b) avec une bonne uniformité (0,7 dBi). Une comparaison avec un réseau de mêmes dimensions n'a pas été réalisée car dans le cas du réseau, il était impossible d'obtenir un maximum de gain proche de  $\theta = 60^\circ$  avec une matrice 5x5 éléments.

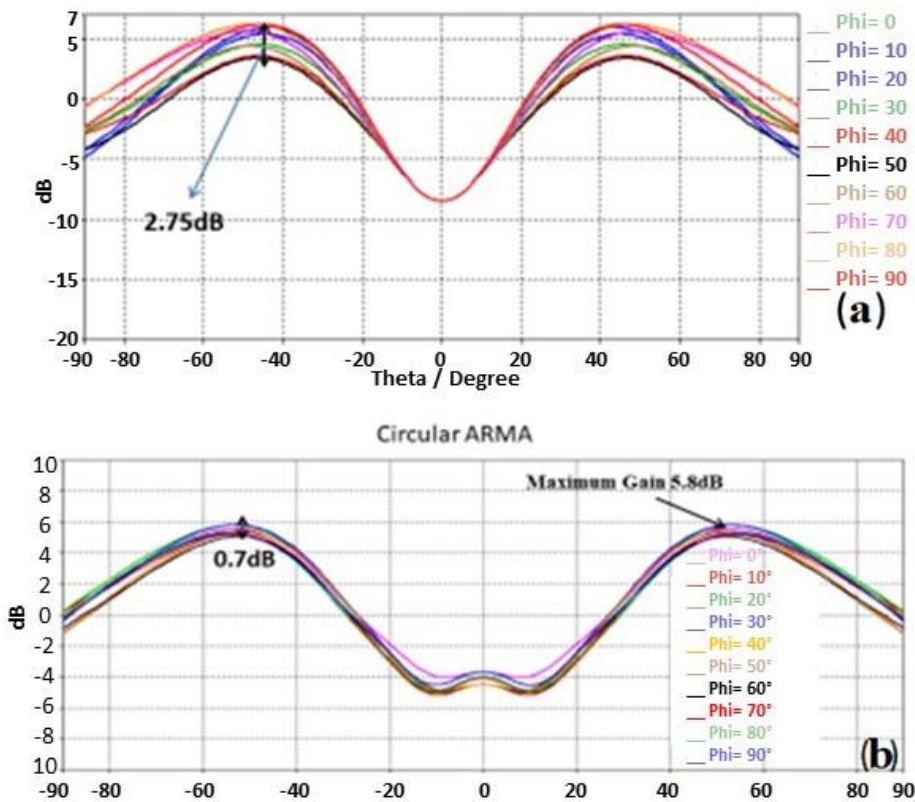


Figure 8 (a) Diagramme de rayonnement obtenu avec un MARPEM carré de 5 x 5 pixels (b) Diagramme de rayonnement isoflux obtenu avec l'antenne MARPEM à symétrie de révolution.

## 4.2 Performances du balayage électronique

Une comparaison [1] a été réalisée entre deux (1D) antennes à faisceaux agiles avec la même surface et la même périodicité: un réseaux d'antenne patches et une antenne MARPEM comme le montre la figure 9.

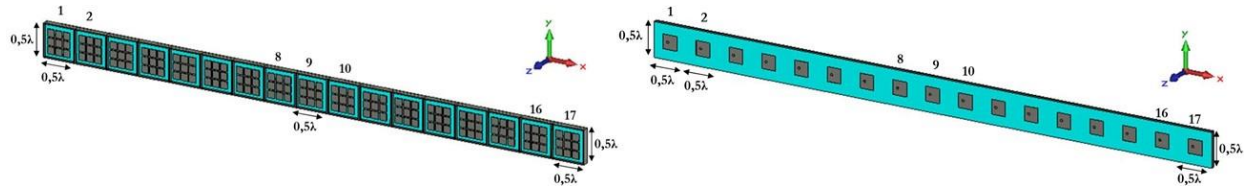


Figure 9 Antennes 1D utilisées pour comparer les performances des réseaux d'antennes et des antennes MARPEM.

Le gain obtenu pour un angle de dépointage  $\theta = 70^\circ$  est beaucoup plus élevé pour MARPEM que pour les réseaux d'antennes (fig 10). Il suit la loi  $(1 + \cos \theta)$  qui apparaît dans l'équation 2 comme le montre la figure 11.

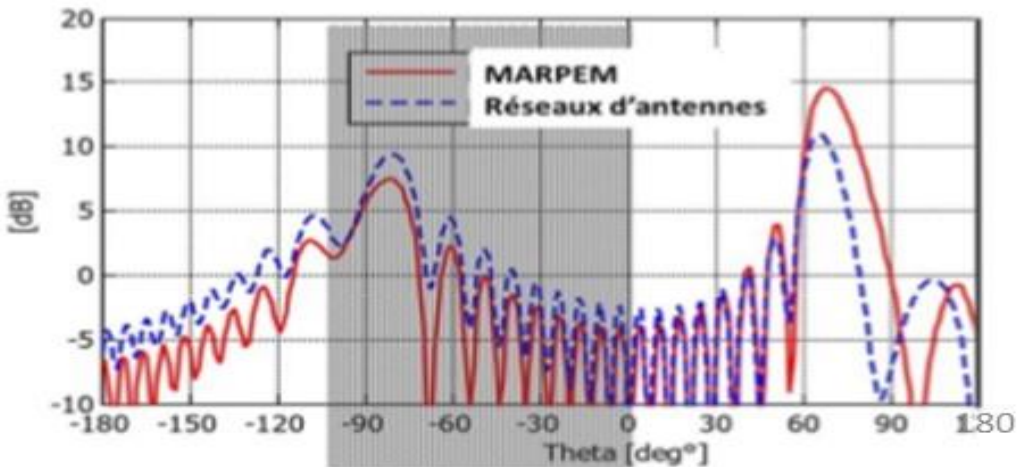


Figure 10 Comparaison des diagrammes de rayonnement des réseaux d'antenne et du MARPEM pour un dépointage  $\theta = 70^\circ$ .

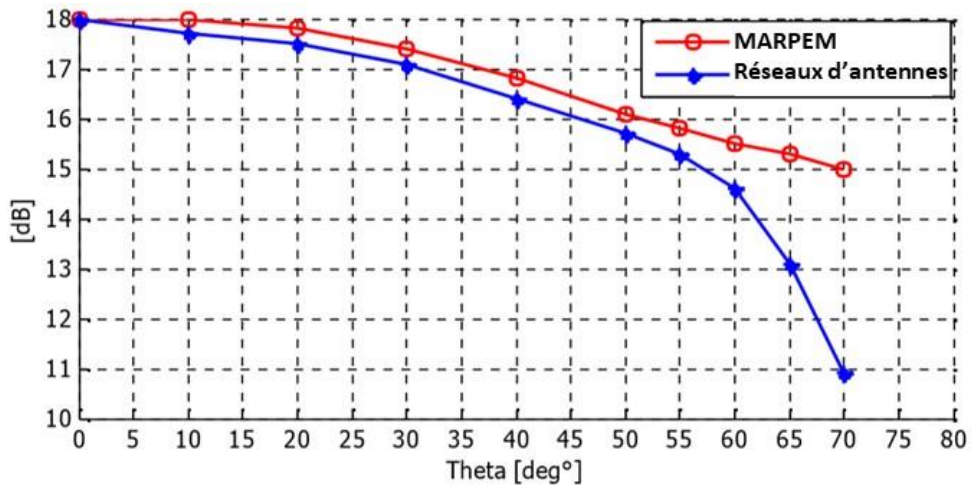


Figure 11 Evolution du gain maximal en fonction de l'angle de pointage

Cet avantage, illustré sur le balayage électronique (Beamsteering), peut être conservé pour la formation du faisceau (Beamforming). Par exemple, une couverture terrestre isoflux en bande X à partir d'un CubeSat situé sur une orbite LEO est possible avec un gain maximum proche de  $\theta = 60^\circ$ [12].

## 5 Conclusion

Cet article présente une nouvelle technique d'antenne à faisceau agile appelée MARPEM qui peut remplacer au prix d'une faible augmentation de la complexité de la structure celle basée sur les réseaux (AESA) lorsque des fortes limitations apparaissent.

Les pixels avec des restrictions sur la forme, les dimensions et la bande passante moins importantes que pour les réseaux, augmentent la flexibilité des applications.

L'avantage de MARPEM est particulièrement important pour la formation et le balayage du faisceau dans de nombreux domaines de recherche: communications terrestres et par satellite, guerre électronique, radars, etc.

## Références bibliographiques

- [1] B. Jecko, E. Arnaud, H. Abou Taam, A. Siblini, "The ARMA concept: Comparison of AESA and ARMA technologies for agile antenna design," Fermat Journal vol 20, 2017.
- [2] H. Abou Taam, G. Zakka El Nashef, E. Arnaud, N. Chevalier, B. Lenoir, B. Jecko, M. Rammal , "Design Development And Experimental Validation Of An EBG Matrix Antenna For Tracking Application," in International Journal of Microwave and Wireless Technology IJMWT, page 1 of 9 Cambridge University Press and European Microwave Association 2015.
- [3] Y.-F. Cheng, X. Ding, W. Shao, M.-X. Yu, B.-Z. Wang, "2-D planar wide-angle scanning-phased array based on wide-beam elements," IEEE Antennas Wireless Propag. Lett., vol. 16, pp. 876–879, 2017.
- [4] C. MENUDIER, M. THEVENOT, T. MONEDIERE, B. JECKO, "EBG Resonator Antennas," State of Art and Prospects». 6th International Conference on Antenna Theory and Techniques ICATT'07, Sevastopol, the Crimea, Ukraine, September 17-21, 2007.
- [5] R.Chantalat, L.Moustapha, M.Thevenot, T.Monediere and B.Jecko, "Low Profile EBG Resonator Antennas," International Journal of Antennas and Propagation. Vol 2009, Article ID 394801, 7Pages.
- [6] S. Palreddy, "WIDEBAND ELECTROMAGNETIC BAND GAP (EBG) STRUCTURES, ANALYSIS AND APPLICATIONS TO ANTENNAS," Dissertation submitted to the faculty of the Virginia Polytechnic Institute and State University in partial fulfillment of the requirements for the degree of Doctor of Philosophy In Electrical Engineering, May 1, 2015.
- [7] M. S. Toubet, M. Hajj, R. Chantalat, E. Arnaud, and B. Jecko, "Wide bandwidth, high-gain, and low-profile EBG prototype for high power applications," IEEE Antennas Wireless Propagation Letters, vol. 10, no. 10, pp. 1362–1365, 2011.
- [8] M. Rammal, M. Majed, E. Arnaud, J. Andrieu, and B. Jecko, "Small-Size Wide-Band Low-Profile "Pixel Antenna": Comparison of Theoretical and Experimental Results in L Band," International Journal of Antennas and Propagation, vol. 2019, Article ID 3653270, 8 pages, 2019.
- [9] H. Abou Taam, M. Salah Toubet, T. Monediere, B. Jecko, M. Rammal and A. Bellion, "Interests of a 1D EBG Matrix Compared to a Patch Array in Terms of Mutual Coupling and Grating Lobes," IEEE, 7th European Conference on Antennas and Propagation EuCAP, 8-12 April 2013, Sweden.
- [10] L. Teng, ZN. Chen, "Shared-Surface Dual-Band Antenna for 5G Applications," IEEE Transactions on Antennas and Propagation (2019).
- [11] B. Jecko, M. Majed, S. Aija, H. Chereim, A. Siblini, H. Abou Taam, J. Andrieu, M. Lalande, E. Martinod, "Agile Beam Radiating Surfaces," Fermat Journal vol 30, 2018.
- [12] A. SIBLINI, B. JECKO, E. ARNAUD, "Multimode Reconfigurable Nano-Satellite Antenna for PDTM Application," EUCAP 2017 Paris.

## **Antenne ultra-large bande avec polarisation circulaire pour des applications 5G**

### ***Ultra-Wideband Circularly Polarized Antenna for 5G Applications***

---

**Mohamad Mantash<sup>1</sup>**

<sup>1</sup>*Microwave Vision Group, 295 Avenue Alexis de Rochon, 29280 Plouzané, mohamad.mantash@mvg-world.com*

---

**Mots clés :** Antenne; polarisation circulaire (CP); ondes millimétrique; ultra large bande (ULB); Antenna; circular polarization (CP); millimeter wave; ultra-wideband (UWB).

---

#### **Résumé/Abstract**

Cet article présente une antenne ultra-large bande pour des ondes millimétriques à polarisation circulaire qui fonctionne dans la bande de fréquences 26 - 37 GHz. Afin de valider l'antenne, des simulations dans CST Microwave Studio ont été réalisées. L'antenne a une bande passante de 11 GHz avec un gain maximum de 10 dB et un rapport axial inférieur à 3 dB dans la bande de fréquences 33,5-37,5 GHz. De plus, l'antenne proposée a un diagramme de rayonnement à polarisation circulaire droite et peut être utilisée pour du balayage de faisceau. Par la suite, l'antenne proposée peut être un bon candidat pour les communications des systèmes à ondes millimétriques.

This paper presents an ultra-wideband circularly polarized millimeter-wave antenna that operates in the 26 – 37 GHz frequency band. In order to validate the antenna, simulations in CST Microwave Studio have been realized. The antenna has a bandwidth of 11 GHz with an achieved maximum gain of 10 dB and an axial ratio lower than 3 dB in the 33.5-37.5 GHz frequency band. Moreover, the proposed antenna has a right-handed circular polarization (RHCP) radiation pattern and can be used for beam scanning. Subsequently, the proposed antenna can be a good candidate for millimeter wave system communications.

#### **1 Introduction**

Nowadays, people prefer wireless devices that are portable, operate on multiple frequency bands, have high speed data rates and are very small. This is why, over the years, designing antennas that operate at millimeter – wave (MM-wave) frequencies have attracted more and more attention among researchers. Furthermore, circularly polarized (CP) antennas offer more advantages than linearly polarized (LP) antennas, such as, lower susceptibility to multipath, more flexibility when orienting the antennas, lower atmospherically absorption and lower reflection effects [1]. Several methods can be used for designing CP antennas: single feeding [2], multi feeding techniques [3] or the usage of polarizers [4]. The single feeding technique has only one feeding port and a compact configuration. Therefore, in this paper, this method is used. The multi feeding technique has two to four feeding ports that are excited with equal amplitude and 90° phase difference and can achieve a wide band with minimum losses [5]-[8]. And finally, the technique that employs polarizers can obtain a wideband configuration, but the losses and the length of the antenna are increased because of the additional element.

In this paper, an ultra-wideband (UWB) circularly polarized antenna based on the use of a single-phase feeding is described. Furthermore, the performance of the proposed antenna with respect to the reflection coefficient, radiation pattern, axial ratio and realized gain in the 26-37 GHz frequency band is presented.

The article is structured as follows: in Section 2 the antenna design is studied, including the simulation results that validate the proposed antenna and Section 3 concludes that paper and gives an outlook for future works.

#### **2 Antenna design and numerical results**

##### **2.1 Antenna design**

The geometry of the antenna used in this paper is shown in Figure 1 and the dimensions of the structure are described in Table 1. The length of the antenna is about  $1.6\lambda$  in order to operate in the 26-37 GHz frequency band.

The evolution steps of the proposed antenna are shown in Figure 1(a). At first, the feeding line is designed followed by the strip ( $D \times H$ ). The length of the strip has been carefully optimized in order to obtain the best possible results in the frequency of interest.

The antenna is essentially made of a small line and a single-phase feeding. It has the dimensions of 15.625 mm length, 7.5 mm width and is printed on a Rogers TMM 10 lossy substrate with the permittivity of  $\epsilon_r=9.2$ , tangent delta  $\tan\delta=0.0022$  and thickness of 0.51 mm. The antenna can be translated to operate at other frequencies by changing its size. Simulations using CST Microwave Studio were carried out by including the MM-wave connector.

The antenna covers the impedance bandwidth ( $S11 < -10\text{dB}$ ) from 26 to 37 GHz with an achieved maximum gain of 10 dBi at 33.2 GHz and an axial ratio less than 3 dB from 33.5 to 37.5 GHz.

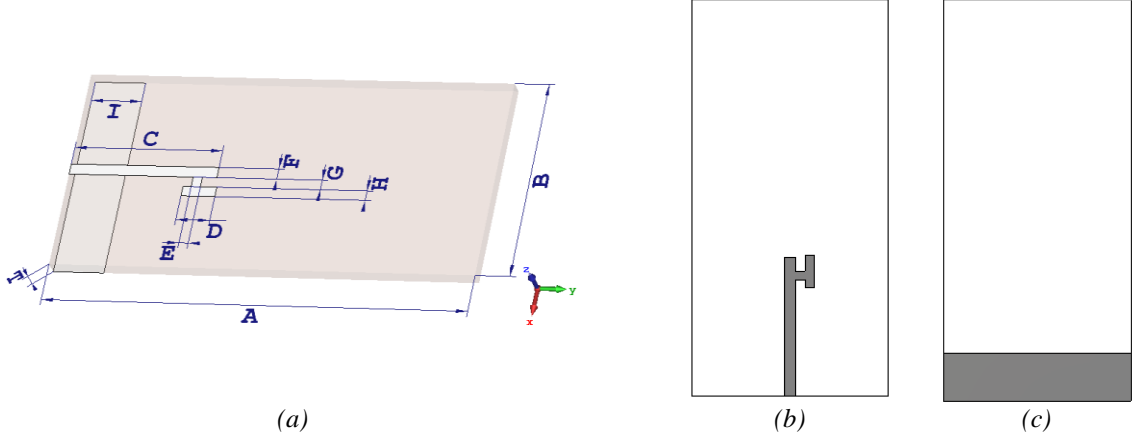


Figure 1 : Geometry of the proposed antenna: (a) 3D view, (b) Top view and (c) Bottom view

A	B	C	D	E	F	G	H	I	T
mm									
15.625	7.5	5.475	1.25	0.34	0.4	0.375	0.37	1.875	0.51

Table 1 : Dimensions of the antenna

## 2.2 Numerical results

In order to determine the performance of the antenna, a full-wave analysis using CST Microwave Studio is realized. The antenna is excited using a 2.92 mm (K) connector, also designed in CST Microwave Studio, that ensures that the antenna operates as expected. Figure 2(a) presents the simulated reflection coefficient of the antenna which provides a matching bandwidth in the 26–37 GHz band with a fractional bandwidth of 34.92%.

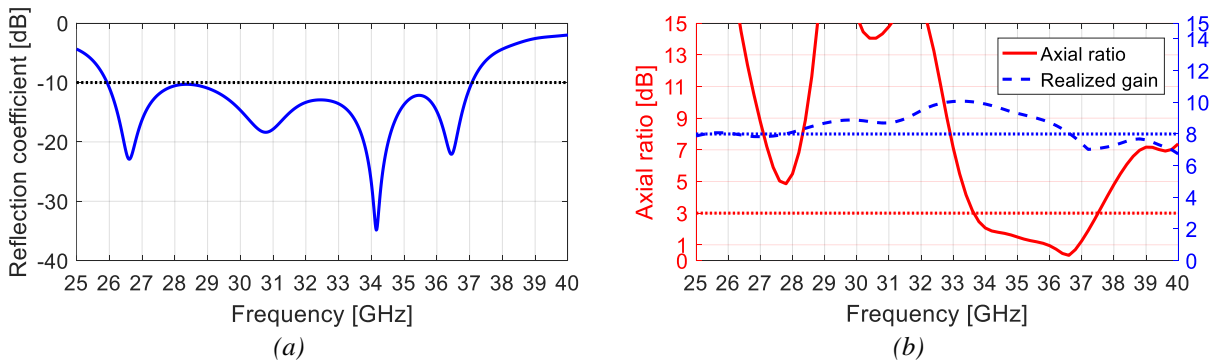


Figure 2 : Results : (a) Simulated reflection coefficient of the CP UWB antenna, (b) Realized gain and axial ratio of the CP UWB antenna

In Figure 2(b) the axial ratio and realized gain of the proposed antenna in the 25 – 40 GHz frequency band is shown. The antenna exhibits a 3-dB axial ratio bandwidth from 33.5 GHz to 37.5 GHz resulting in a fractional

bandwidth of 11.26%. The calculated realized gain of the antenna (Figure 2(b)) experiences a 2 dB gain increase from 26 GHz to 37 GHz. The realized peak gain of 10 dBi is obtained at 33.2 GHz.

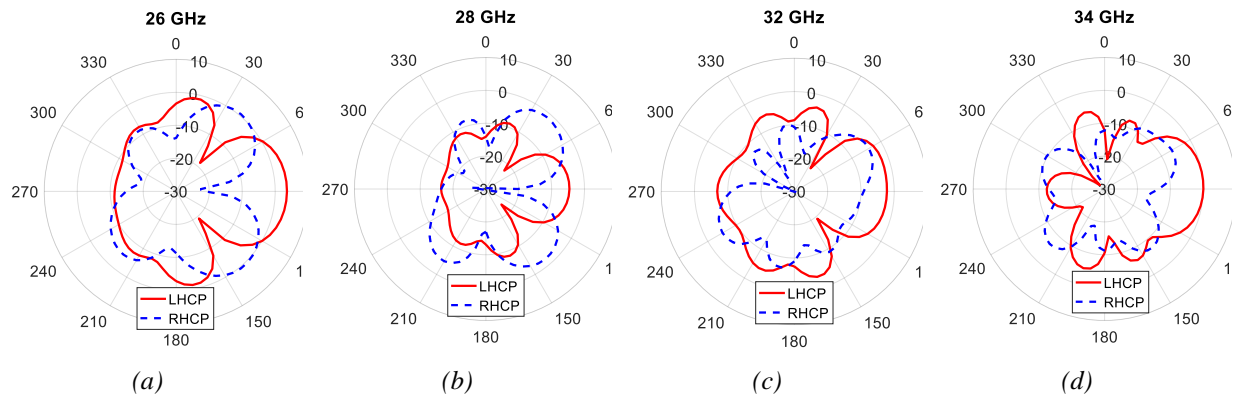


Figure 3 : Radiation pattern of the CP antenna in the YoZ-plane at: (a) 26 GHz, (b) 28 GHz, (c) 32 GHz and (d) 34 GHz

The circular polarization radiation patterns (LHCP: left-hand circular polarization and RHCP: right-hand circular polarization) at 26 GHz, 28 GHz, 32 GHz and 34 GHz in the YoZ-plane are shown in Figure 3. As it can be observed, the proposed antenna possesses LHCP (left-hand circular polarization) characteristics as the line and the single feeding are designed in the clockwise direction.

### 3 Conclusion

In this paper, an ultra-wideband circular polarization MM-wave antenna has been presented. The proposed antenna has been designed to operate in the 26 – 37 GHz frequency band by combining a small line with a single-phase feeding system. The antenna provides a very high matching bandwidth of 11 GHz (34.92%), a 3-dB axial ratio bandwidth of 4 GHz (11.26%) and a maximum realized gain of 10 dBi at 33.2 GHz. The proposed antenna van be a good candidate for ultra-wideband circular polarization millimeter-wave applications.

### Références bibliographiques

- [1] J. Wu, Y. J. Cheng, and Y. Fan, “Millimeter-wave wideband high-efficiency circularly polarized planar array antenna,” IEEE Trans. Antennas Propag., vol. 64, no. 2, pp. 535–542, Feb. 2016.
- [2] Aliakbari, Hanieh et al. “A single feed dual-band circularly polarized millimeter-wave antenna for 5G communication”, EuCAP, pp. 1-5, 2016.
- [3] M. Mantash, J Zaid, A. Kesavan, T. A. Denidni, “Wideband Circularly-Polarized 3D Antenna Array for Millimeter-Wave Applications”, APS2018, Boston, Massachusetts, 8-13 July 2018.
- [4] M. Mantash, T. A. Denidni, “CP Antenna Array with Switching-Beam Capability Using Electromagnetic Periodic Structures for 5G Applications”, IEEE Access, vol. 7, pp. 26192-26199, 25 Feb. 2019.
- [5] M. Mantash and T. A. Denidni, “Finger-worn end-fire antenna for MM-wave applications,” Microw. Opt. Technol. Lett., vol. 59, pp. 2591–2593, 2017.
- [6] M. Mantash, A. Kesavan, T. A. Denidni, “Millimeter-Wave Antenna with Tilted Beam for Future Base Station applications”, IET Microwaves, Antennas & Propagation, vol. 13, issue 2, pp. 223-230, 06 Feb. 2019.
- [7] M Mantash, A. Kesavan, T. A Denidni, “Beam-Tilting End-Fire Antenna Using a Single-Layer FSS for 5G Communication Networks”, IEEE Antennas and Wireless Propagation Letters, vol. 17, issue 1, pp. 29-33, January 2018.
- [8] M. Mantash, T. A. Denidni, “Simple beam control of end-fire antenna using FSS for MM-wave applications”, IEEE International Symposium on Antennas and Propagation & USNC/URSI National Radio Science Meeting, pp. 1075-1076, San Diego, CA, USA, 9-14 July 2017

## Observatoire des Ondes, une réponse au débat sociétal *EMF observatory, an answer to the societal debate*

---

**Philippe Pinel<sup>1</sup>, Pascal Tajan<sup>2</sup>, Yannick Poiré<sup>3</sup>, Lamine Ourak<sup>4</sup>**

<sup>1,2,3,4</sup> Exem SAS, <sup>1</sup>[pinel@exem.fr](mailto:pinel@exem.fr), <sup>2</sup>[tajan@exem.fr](mailto:tajan@exem.fr), <sup>3</sup>[poire@exem.fr](mailto:poire@exem.fr), <sup>4</sup>[ourak@exem.fr](mailto:ourak@exem.fr)

---

*Mots clés (key words) : sonde large bande, suivi de l'exposition, champ électrique, capteurs communicants (broadband probe, exposure monitoring, E-field, communicating sensors)*

---

### Résumé

Cet article a pour but de présenter le projet « Observatoire des Ondes » et sa solution technique. Le projet « OdO » vise la transparence de l'information du grand public. C'est un accompagnement du débat sociétal sur l'exposition aux champs électromagnétiques (radio, TV, téléphonie mobile 4G/5G...). Pour ce faire, la solution technique consiste à déployer sur le territoire des capteurs de champs électriques large bande (80 MHz – 6 GHz) afin de relever les niveaux d'exposition aux champs électromagnétiques.

### Abstract

The purpose of this article is to present the « Observatoire des Ondes » project (EMF observatory project) and its technical solution. The « OdO » project aims at transparency and the access right to information of the general public. It is a support of the societal debate on exposure to electromagnetic fields (radio, TV, mobile broadcast...). To achieve this, the technical solution consists in deploying on overall territory broadband E-field probes (80 MHz – 6 GHz) in order to monitor levels of electromagnetic fields exposure.

## 1 Contexte du projet & Objectifs

Dans le contexte de transformation digitale très rapide de notre société, l'Observatoire des Ondes offre un outil impartial et fiable pour éclairer le débat sociétal qui oppose les enjeux de développement économique aux préoccupations environnementales et de santé publique. Il a pour vocation d'accompagner les collectivités pour leur permettre d'apporter des réponses aux questions du grand public sur leur exposition aux ondes électromagnétiques.

L'Observatoire des Ondes est un projet de R&D conçu et développé par Exem. Il est basé sur le déploiement d'un réseau de capteurs communicants qui rendent les données accessibles en temps réel. Ce projet s'intègre dans l'écosystème Smart City en proposant une solution innovante de consultation des niveaux de champs électromagnétiques dans les villes.

## 2 Vue d'ensemble du système

### 2.1 Méthodologie de déploiement :

Le déploiement de réseau est précédé par une étude de l'environnement électromagnétique afin de définir les sites et les adresses retenues pour l'implantation des capteurs. Un repérage préalable est réalisé grâce aux « street views » sur internet puis une validation sur place permet de confirmer la pertinence en termes d'accessibilité, de niveaux mesurés, de non-masquage par l'environnement.

Pour cette étude, plusieurs facteurs sont pris en compte : l'intérêt technique pour lequel nous étudions les spécificités du réseau radioélectrique (point d'exposition maximal, azimut de l'antenne...), l'intérêt démographique qui consiste à évaluer avec vous les lieux publics fréquentés par des populations sensibles (écoles, crèches, hôpitaux...) ou à fortes affluences et enfin l'intérêt symbolique que peuvent représenter les lieux représentatifs d'une ville.



Les capteurs sont placés entre 3.5m et 4.5m de hauteur et préférentiellement sur les candélabres. Cette hauteur correspond à un compromis entre : une limitation à leur accessibilité par le public, un éloignement des sources de perturbations proches (comme l'éclairage lui-même), une facilité d'installation et une hauteur toutefois limitée pour permettre une bonne représentativité de l'exposition au niveau du sol.

L'expertise préalable au déploiement dans un quartier est notamment nécessaire afin de vérifier la disponibilité et l'accès au mobilier urbain. Les mâts d'éclairage public représentent des postes idéaux car formant un maillage urbain propice. Cependant, certaines zones (notamment dans les centres villes ou dans des quartiers historiques) peuvent manquer de mobilier pour installer nos capteurs. Dans ce cas de figure, l'utilisation d'autres mobiliers comme les mâts de caméra ou les feux signalétiques peut être envisagée.

Le temps d'installation d'un capteur (première installation) varie en moyenne entre 10 et 30 minutes selon l'accessibilité du site. L'installation est faite par des techniciens spécialisés et selon le plan de déploiement convenu avec les autorités locales.

## 2.2 Infrastructure Sigfox globale :

La connectivité des capteurs est assurée par le réseau IoT de Sigfox. Les deux raisons principales de ce choix sont : la faible consommation énergétique et l'excellente couverture qu'offre le réseau notamment en zone urbaine). La consultation des niveaux est faite sur une plateforme internet dédiée ([www.observatoiredesondes.com](http://www.observatoiredesondes.com)).

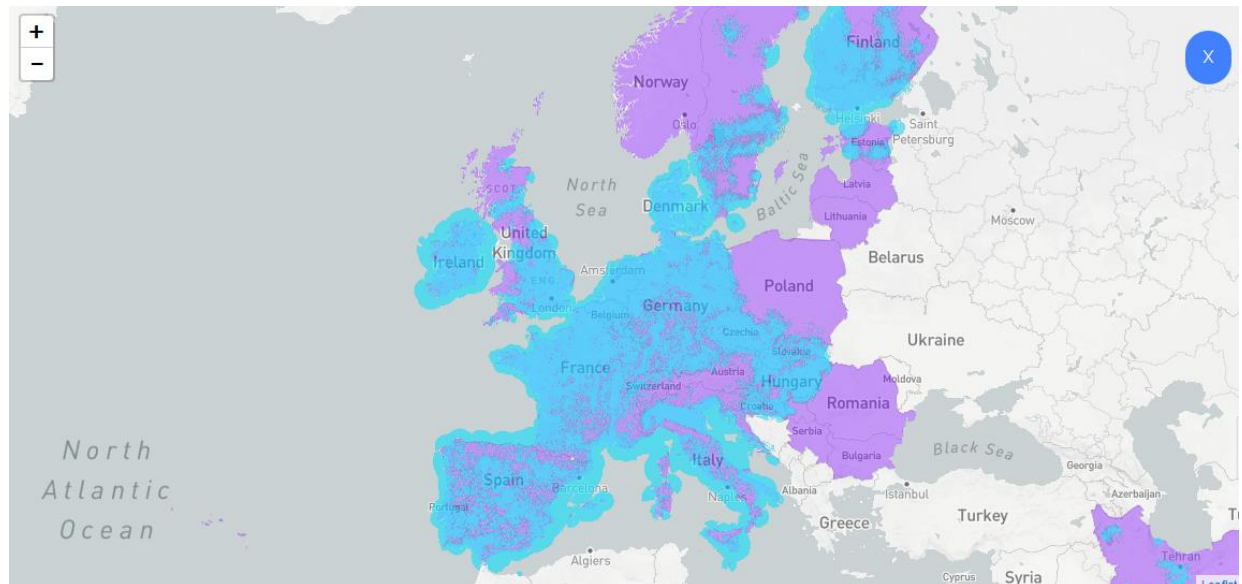


Figure 1 : Couverture Sigfox – Europe de l'ouest (source : <https://www.sigfox.com/en/coverage>)

Sur cette figure, nous pouvons constater la couverture en France en utilisant l'infrastructure Sigfox. Les zones urbanisées sont couvertes (couleur bleue). À l'usage, nous n'avons jamais eu de problématique de couverture même en plaçant nos capteurs en *indoor* et dans des situations très défavorables (sous-sol par exemple). Cependant, pour les usages à l'intérieur des bâtiments et en cas de mauvaise couverture, des solutions de routeurs spécifiques Sigfox permettent d'utiliser le réseau WiFi ou Ethernet pour assurer la connectivité des capteurs.

## 2.3 Présentation de résultats :

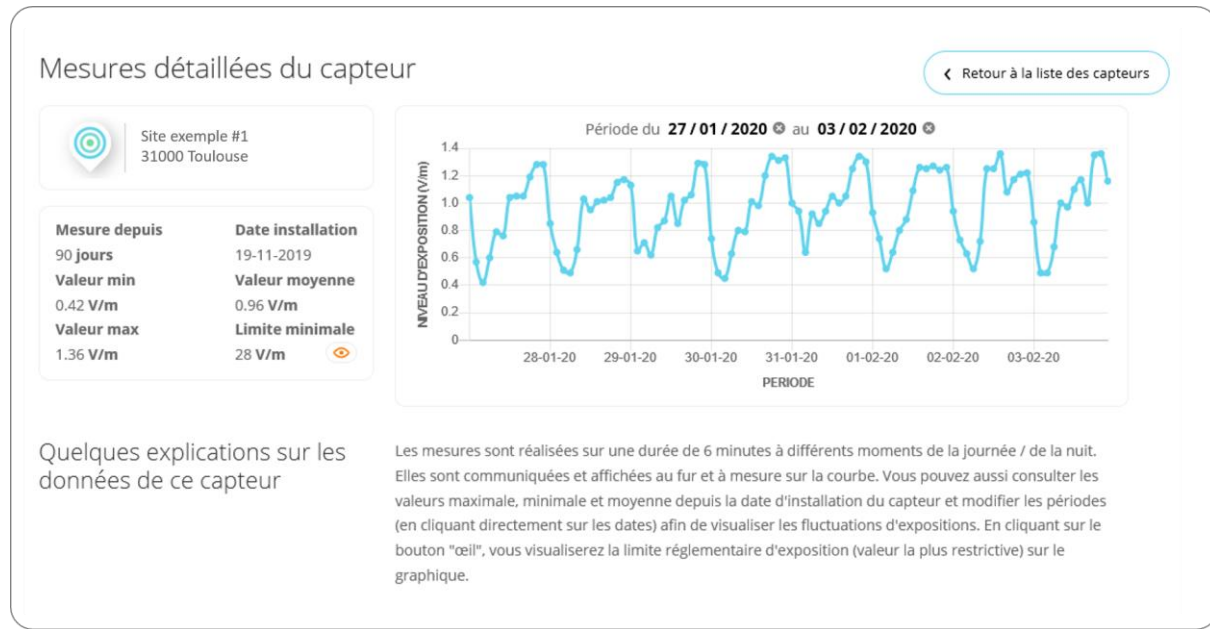


Figure 2 : Capture d'écran site internet de consultation des mesures ([www.observatoiredesondes.com](http://www.observatoiredesondes.com))

Sur la Figure 2, un exemple de mesures vous est présenté. Il s'agit d'un capteur placé à une hauteur de 3,7 m du sol sur une candélabre. Nous pouvons constater la répétabilité des cycles jour et nuit. Le niveau de champ électrique suit les activités humaines : les creux sont très généralement constatés entre 2h et 6h du matin, ce qui correspond à la plus faible période d'activité humaine.

## 3 Description du capteur

### 3.1 Caractéristiques

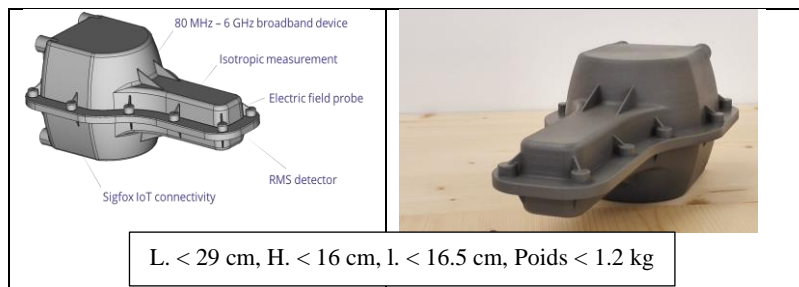


Figure 3 : Présentation des capteurs (CAO 3D à gauche, photo à droite)

Le capteur d'EXEM est composé de trois sondes basées sur une technologie de diode [1]. Chaque sonde mesure une composante spatiale du champ électrique (X, Y, Z). Les trois sondes sont reliées au système d'acquisition via des lignes hautes résistivités [2][3] (cf. Figure 7 : Chaîne analogique) permettant d'assurer une haute performance du système de mesures, une bonne immunité aux rayonnements électromagnétiques indésirables et de garantir une bonne platitude en fréquence sur toute la bande de fréquences (< 1.5 dB entre 900 MHz et 3 GHz ; < 3 dB en dessous de 900 MHz et au-dessus de 3 GHz) [4].

Une optimisation de la distance entre la carte d’acquisition et le trièdre de sonde permet au dispositif à la fois de ne pas mesurer l’activité propre de notre électronique et de garder une distance suffisante par rapport au mobilier urbain (pour être en environnement « libre »).

Les chaines d’alimentations des sondes sont optimisées pour atteindre une autonomie minimale de 3 ans à l’aide de piles Lithium (pour 10 à 15 mesures par jour de 6 min chacune).

Avec l’aide de la société SAFT Batteries, selon leurs données [5] et leurs modèles de calculs, une étude spécifique a été réalisée afin de sélectionner les piles en prenant en compte un profil thermique spécifique « pire cas ». En effet, notre boîtier (IP66) pouvant être considéré comme « adiabatique », la température peut augmenter significativement en cas d’exposition au soleil.

### 3.2 Architecture et fonctionnement du capteur

Le système d’acquisition du capteur est équipé d’un module IoT assurant la communication des données de mesure via le réseau Sigfox. Le tout piloté par un microcontrôleur sur lequel s’articule les différentes fonctionnalités du capteur. Le microcontrôleur embarqué est chargé du pilotage du système de mesure tri-axe, du système de gestion de l’énergie, du module de mise en veille et de réveil du capteur, d’un capteur de température et d’humidité et finalement du module IoT Sigfox. L’architecture globale du capteur ainsi que celle de la chaîne analogique sont illustrées par les figures 6 et 7.

Le design et les dimensions du capteur sont présentées sur la Figure 3. La conception du dipôle et le choix de la diode permettent de mesurer le champ électrique entre 0,3 V/m et 61 V/m [6]. La sonde mesure le champ électrique dans la bande de fréquence comprise entre 80 MHz et 6 GHz.

L’algorithme de fonctionnement est le suivant (*cf. Figure 4*) :

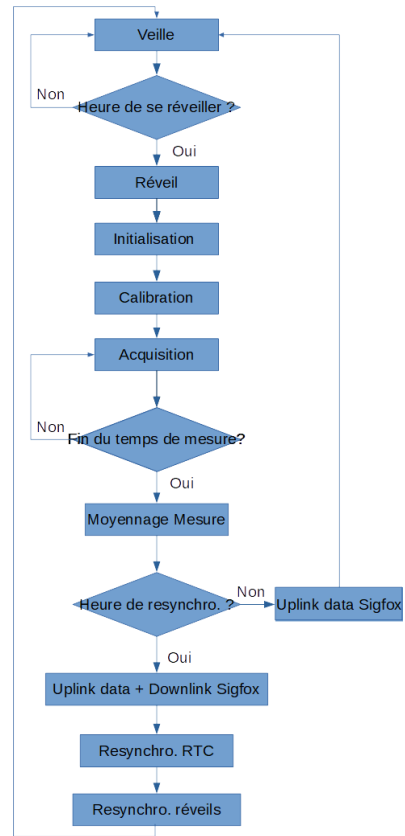


*Figure 4 : Algorithme de fonctionnement*

La mesure isotropique est réalisée par commutation du système d’acquisition sur les trois axes de la sonde. Le changement d’axe se fait en 100 ns via un multiplexeur après une acquisition de 120 ms. Ainsi, l’acquisition tri-axe est opérée en 360 ms (*cf. Figure 5 : chronogramme de l’acquisition par axe*).

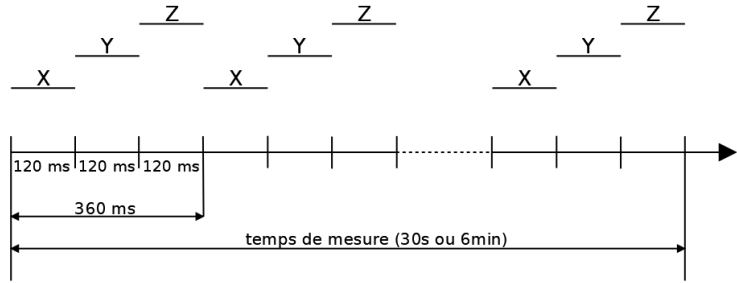


Figure 5 : chronogramme de l'acquisition par axe

Des algorithmes bas-niveau ont été développés afin d'assurer des phases de réveil de l'électronique pour l'instrumentation de la sonde et pour l'envoi des données collectées. Les heures de réveils peuvent être choisies ainsi que la durée de la mesure (30s ou 6 min).

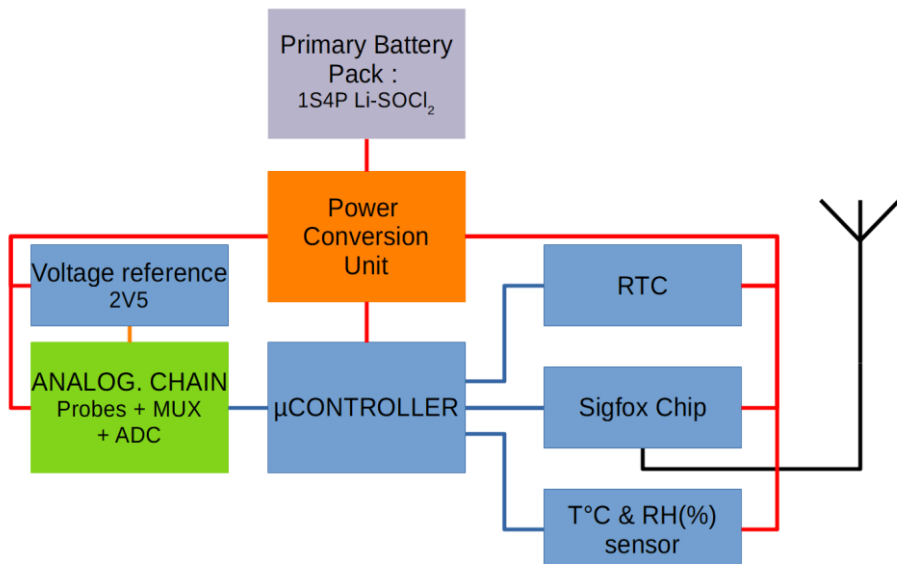


Figure 6 : Architecture du système

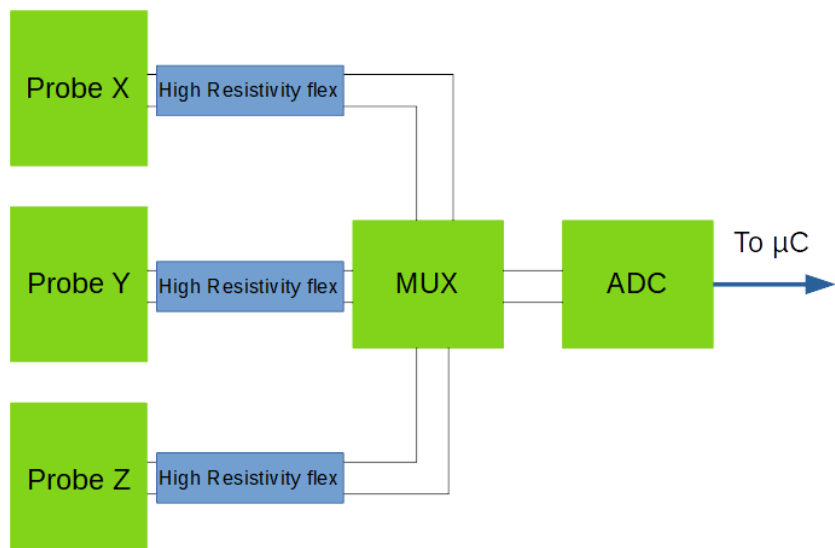


Figure 7 : Chaîne analogique

### 3.3 Méthodologie de calibrage du capteur

- Réponse en tension selon le niveau de champ :

Le calibrage de notre capteur est effectué en chambre anéchoïde, le setup est donné sur la Figure 8 [7]. L'antenne est de type cornet, alimentée par un amplificateur de puissance, lui-même relié à un synthétiseur de fréquence. Le capteur est positionné en zone de « champ lointain ». Une sonde de référence étalonnée par un laboratoire COFRAC est utilisée pour le réglage des puissances d'émission.

*NB : Une antenne semi-log est utilisée pour les fréquences <500 MHZ.*

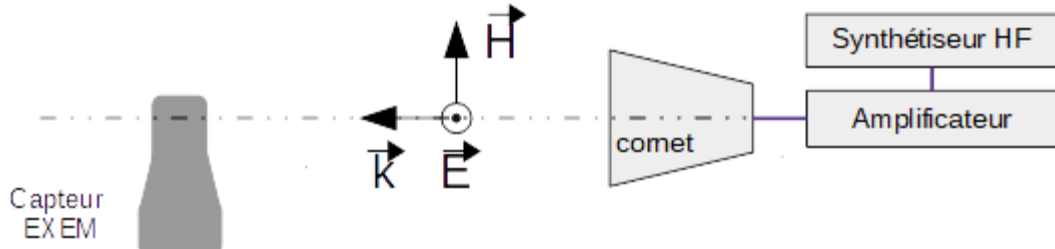


Figure 8 : Setup de calibrage

Nous injectons à différentes fréquences représentatives de la bande mesurée (500 MHz, 1GHz et 3GHz) et en déduisons la réponse du capteur ; qui est la somme linéaire des tensions DC issues de chaque sonde ( $\sum(\mu\text{V}) = X(\mu\text{V}) + Y(\mu\text{V}) + Z(\mu\text{V})$ ) en fonction du champ.

Nous observons 2 zones, une première à faible champ, de type parabolique, et une seconde, à champ plus élevé, de type linéaire. Nous obtenons donc 2 coefficients,  $\alpha_1$  et  $\alpha_2$ . Le choix de ce dernier à appliquer pour le calcul de E se fait logiciellement, selon la somme en tension mesurée.

Afin d'obtenir des coefficients  $\alpha_1$  et  $\alpha_2$  applicables sur la totalité de la bande de fréquence, nous prenons une valeur moyenne des différents coefficients obtenus aux différentes fréquences.

La sensibilité du capteur est définie comme le niveau de champ E pour lequel la somme des tensions issues des sondes n'est plus distincte du bruit de la chaîne analogique du capteur. Nos mesures nous permettent d'avancer une sensibilité **s = 0.3V/m**.

Une réponse en fréquences des capteurs est réalisée à l'issue de ce calibrage afin de s'assurer de leur bon fonctionnement et du respect des spécifications relatives à la platitude en fréquence.

- Linéarité :

La linéarité du capteur est mesurée en traçant sa réponse en champ par rapport au champ E de référence (cf. Figure 9). L'écart maximum toléré est de  $\pm 1.5\text{dB}$  par rapport à la courbe de régression linéaire [4].

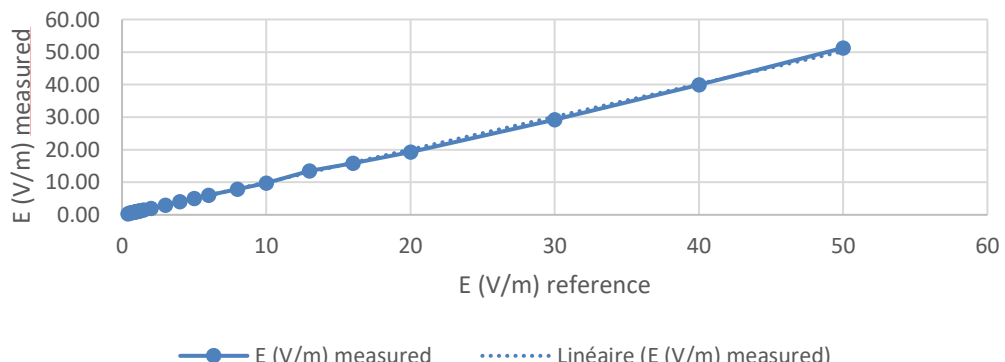


Figure 9 : Linéarité du capteur @1GHz

## 4 Conclusion et perspectives

L'Observatoire des Ondes est une solution complète pour la supervision de l'exposition électromagnétique. La plateforme de supervision permet de collecter en temps réel les données issues des capteurs de champ électrique déployés dans les villes.

L'Observatoire a pour vocation d'accompagner les collectivités pour leur permettre d'apporter des réponses aux questions du grand public sur leur exposition aux ondes électromagnétiques.

Nous avons présenté dans cette communication les capteurs que nous avons conçus et optimisés pour permettre un déploiement facile dans les villes (conception mécanique) tout en assurant une bonne qualité des mesures du champ électrique (conception de l'électronique). Le capteur permet de mesurer le champ électrique dans la bande 80 MHz – 6 GHz avec une platitude en fréquences comprise entre +/- 3 dB et une étendue dynamique de plus de 46 dB entre 0,3 V/m et 61 V/m.

L'optimisation de la consommation énergétique du capteur nous impose une quantité limitée des mesures sur 24h. Cependant, avec dizaine de mesures journalière, les variations des niveaux d'exposition sont bien représentées.

Des travaux de recherche sont menés actuellement par une équipe de Télécom Paris qui exploite les résultats des capteurs pour alimenter un algorithme d'intelligence artificiel basé sur les réseaux de neurones et qui a pour but la prédiction du champ électromagnétique dans les rues (pour une exposition représentative au niveau du sol) avec la prise en compte de la variation temporelle du champ électrique. Les premiers résultats de ce travail sont très encourageants et nous permettent d'envisager à l'avenir un système hybride pour la supervision de l'exposition aux champs électromagnétiques basés à la fois sur de la mesure et de la simulation.

## Références bibliographiques

- [1] Howard I. Bassen, “*Electric field probes for cellular phone dosimetry*” in IEEE Proceedings 19<sup>th</sup> international conference, Oct. 30 – Nov. 2, 1997, Chicago USA.
- [2] Howard I. Bassen, Senior Member, IEEE, and Glenn S. Smith, Senior Member, IEEE, “*Electric field probes – A Review*”, IEEE Transactions on antennas and propagation, VOL.AP-31, No.5, September 1983.
- [3] T. E. Batchman and P. H. Howerton, “*Development of a three-axis microwave E-field probe having submillimeter dimensions*” presented at the Conf. on Precision Electromagnetic Meas., Gaithersburg, MD, June 23 - 27, 1986.
- [4] Norme NF EN 50492, Janvier 2009.
- [5] SAFT Lithium Batteries, “*Selector guide*”, Document N°54083-2-0219, Edition: February 2019
- [6] Décret n°2002-775 du 3 mai 2002 pris en application du 12<sup>e</sup> de l'article L. 32 du code des postes et télécommunications et relatif aux valeurs limites d'exposition du public aux champs électromagnétiques émis par les équipements utilisés dans les réseaux de télécommunication ou par les installations radioélectriques.
- [7] Zlatko Živković, Damir Senić, Antonio Šarolić, Ante Vučić, “*Design and Testing of a Diode-Based Electric Field Probe Prototype*”, January 2011

## Métasurfaces à faible densité d'éléments : Application aux antennes *Sparse metasurfaces: Application to antennas*

Vladislav Popov<sup>1</sup>, Fabrice Boust<sup>2</sup>, B. Ratni<sup>3</sup>, Shah Nawaz Burokur<sup>3</sup>

<sup>1</sup>SONDRA, CentraleSupélec, Université Paris-Saclay, F-91190, Gif-sur-Yvette, France,  
uladzislau.popou@centralesupelec.fr

<sup>2</sup>DEMR, ONERA, Université Paris-Saclay, F-91123, Palaiseau, France, fabrice.boust@onera.fr

<sup>3</sup>LEME, UPL, Univ Paris Nanterre, F92410 Ville d'Avray, France, sburokur@parisnanterre.fr

*Mots clés : métasurface éparsée, antenne.*

*Keywords: sparse metasurface, antenna.*

### Résumé/Abstract

Dans ce travail, nous présentons une approche de métasurface à faible densité d'éléments pour des applications aux antennes reconfigurables électroniquement. Contrairement aux métasurfaces classiques très denses en éléments, les métasurfaces éparses présentent moins de pertes. De plus, elles ont un comportement ‘non-local’, qui les rend plus intéressantes pour des antennes en termes d’efficacité de rayonnement et de niveau de lobes secondaires. Une métasurface éparsée reconfigurable est proposée et mesurée pour valider l’approche théorique.

### 1 Introduction

Les avancées dans les études des interactions onde-matière nous permettent aujourd’hui d’envisager la conception de nouveaux types de dispositifs antennaires basés sur les métasurfaces. Les métasurfaces sont considérées comme une version 2D des métamatériaux. Leurs propriétés ont été décrites via des impédances de surface qui sont des fonctions continues des coordonnées spatiales [1]. Dans ce contexte, le nombre d’éléments constituant la métasurface est assez élevé (typiquement 64 par  $\lambda^2$ ), ce qui les rend assez dense. Cette approche a permis des réalisations telles que la réflexion anormale [2], la conversion de polarisation [3], la conversion d’une onde plane en onde de surface [4] pour n’en citer que quelques unes. Ces métasurfaces peuvent être rendues reconfigurables en introduisant des éléments accordables comme des diodes PIN ou varactor [5]. Toutefois, les performances des métasurfaces reconfigurables restent le plus souvent très modestes notamment au niveau de l’efficacité. Pour pallier ces inconvénients, nous proposons une nouvelle approche pour développer des métasurfaces à faible densité d’éléments (typiquement 10 par  $\lambda^2$ ) et une conception autorisant de fortes dispersions spatiales.

### 2 Conception de métasurfaces éparses

Nous considérons une géométrie 2D ; le cas d’une polarisation TE et la configuration de la Fig. 1(a). Il s’agit d’un ensemble de N fils chargés (à une échelle très sub-longueur d’onde) placés sur un substrat métallisé sur la face arrière et éclairé par une onde incidente quelconque ( $E_x^{(ref)}(\mathbf{r})$ ). Le champ diffracté par l’échantillon peut s’écrire :

$$E_x^{(sc)}(\mathbf{r}) = E_x^{(ref)}(\mathbf{r}) + \sum_{q=1}^N G(\mathbf{r}, \mathbf{r}_q) I_q \quad (1)$$

où  $I_q$  est le courant induit par l’onde incidente dans le fil  $q$  et  $G(\mathbf{r}, \mathbf{r}_q)$  est la fonction de Green associée à ce fil. Le courant  $I_q$  est relié à l’onde incidente via la loi d’Ohm qui s’écrit :

$$Z_q I_q = E_x^{(ref)}(\mathbf{r}_q) - Z_q^{(in)} I_q - \sum_{p \neq q}^N Z_{qp}^{(m)} I_p \quad (2)$$

Les impédances  $Z_{qp}^{(m)} = -G(\mathbf{r}, \mathbf{r}_q)$  traduisent les couplages entre fils et ne sont fonction que des caractéristiques géométriques de la configuration. En revanche,  $Z_q$  est fonction des impédances qui sont réparties le long du fil ( $Z_q^{(in)}$  est simplement l’impédance d’entrée du fil qui ne dépend que de son rayon). Un choix judicieux de ces impédances permet via l’équation (2) de contrôler les courants  $I_q$  et *in fine* le champ diffracté. En pratique, les

fonctions de Green sont calculées numériquement par éléments finis et les impédances réparties sur les fils qui contribuent à  $Z_q$  sont choisies pour satisfaire une contrainte sur  $E_x^{(sc)}$  à l'aide d'une méthode d'optimisation. Cette procédure permet de déterminer le jeu d'impédances nécessaire pour, par exemple, réfléchir l'énergie incidente dans une direction donnée. On peut également créer plusieurs faisceaux ou chercher à focaliser l'énergie réfléchie.

### 3 Application aux antennes reconfigurables

Pour illustrer la méthode, nous avons conçu une métasurface composée de 21 lignes espacées de 15 mm, placées sur un substrat d'épaisseur totale 2.5 mm et de permittivité 2.2 dont la face arrière est métallisée. Les lignes sont chargées par des diodes varactors (Fig. 1(b)). La simulation électromagnétique 3D de la cellule élémentaire est assortie de conditions de périodicité. Ensuite, l'utilisation des expressions présentées dans [6] permet de calculer l'impédance linéique. Les résultats présentés à 10 GHz sur la Fig. 1(c) illustrent la capacité de diriger le faisceau réfléchi dans différentes directions dans le cas où l'angle d'incidence est de 45°.

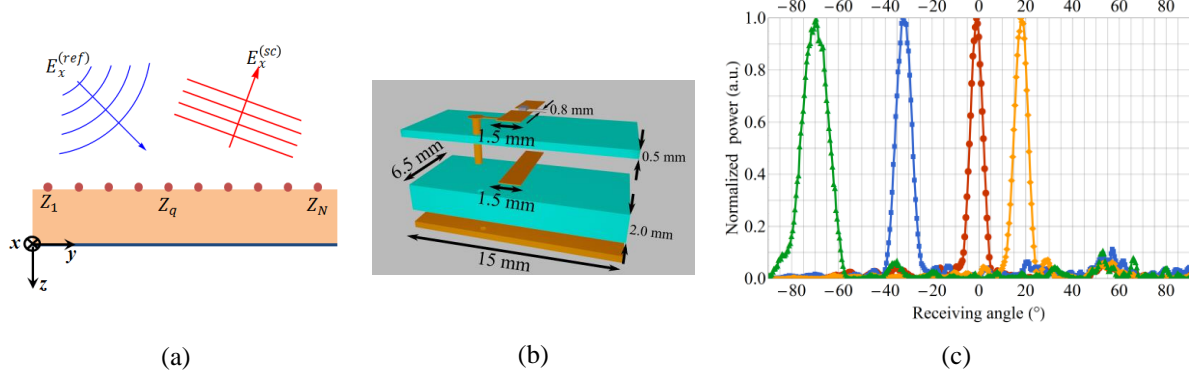


Figure 1 : (a) Schéma de la configuration, (b) Motif élémentaire de la métasurface et (c) Démonstration expérimentale montrant la capacité à réfléchir le faisceau incident dans différentes directions.

### 4 Conclusion

Les métasurfaces denses à gradient de phase sont très limitées en termes de performance, due à la désadaptation d'impédance entre l'onde incidente et l'onde réfléchie ou réfractée. La démarche proposée permet de concevoir des métasurfaces à faible densité avec un comportement fortement non-local. Cette possibilité permet par exemple de diminuer le niveau des lobes secondaires dans des configurations type 'reflect-array'. En outre, une diminution du nombre d'éléments permet, dans le cas de systèmes reconfigurables, de réduire les pertes associées aux éléments accordables. La démarche proposée est très générale et peut s'appliquer aux futurs systèmes de communication, que ce soit des structures planes ou conformes, voire aussi pour des fonctionnalités en champ proche.

### Références bibliographiques

- [1] S. A. Tretyakov, "Metasurfaces for general transformations of electromagnetic fields," *Phil. Trans. R. Soc. A-Math. Phys. Eng. Sci.*, vol. 373, no. 2049, p. 20140362, 2015.
- [2] N. Yu et al., "Light propagation with phase discontinuities: Generalized laws of reflection and refraction," *Science*, vol. 334, no. 6054, pg. 333-337, 2011.
- [3] B. Ratni, A. de Lustrac, G.-P. Piau, and S. N. Burokur, "Electronic control of linear-to-circular polarization conversion using a reconfigurable metasurface," *Appl. Phys. Lett.*, vol. 111, no. 21, p. 214101, 2017.
- [4] V. Popov et al., "Omega-bianisotropic metasurface for converting a propagating wave into a surface wave," *Phys. Rev. B*, vol. 100, no. 12, p. 125103, 2019.
- [5] B. Ratni, A. de Lustrac, G.-P. Piau, S. N. Burokur, "Reconfigurable meta-mirror for wavefronts control: applications to microwave antennas," *Opt. Express*, vol. 26, no. 3, pp. 2613-2624, 2018.
- [6] V. Popov et al., "Designing metagratings via local periodic approximation: From microwaves to infrared," *Phys. Rev. Appl.*, vol. 11, no. 4, p. 044054, 2019.

# Multi-beam Modulated Metasurface Antenna for Backhaul Applications at K-band

**Jorge Ruiz-García<sup>1</sup>, Marco Faenzi<sup>1</sup>, Adham Mahmoud<sup>1</sup>, Mauro Ettorre<sup>1</sup>, Patrick Potier<sup>2</sup>, Philippe Pouliquen<sup>3</sup>, Ronan Sauleau<sup>1</sup>, and David González-Ovejero<sup>1</sup>**

<sup>1</sup> Univ. Rennes, CNRS, IETR - UMR 6164, F-35000, Rennes, France, jorge.ruiz@univ-rennes1.fr

<sup>2</sup> Direction Générale de l'Armement, 35174 Bruz, France

<sup>3</sup> Direction Générale de l'Armement, Agence de l'innovation de défense, 75509 Paris, France

---

**Keywords:** Metasurface antennas, low profile, high gain, 5G

---

**Abstract:**

We explore the use of a new modulated metasurface (MTS) antenna topology as solution for wireless backhaul at K band. The proposed structure is composed of a quasi-optical beamformer, which feeds the modulated MTS radiating aperture. These two elements are vertically stacked in a two-layer pillbox architecture to produce a very compact antenna. Furthermore, our design is able to provide several beams at different pointing angles and, hence, it offers the possibility of discrete beam steering by beam switching. The employment of a modulated MTS and the compactness given by the pillbox approach lead to a high-gain and low-profile antenna that could be an appealing solution for mobile backhaul networks.

## 1 Introduction

Microwaves and millimeter waves frequencies are among the frequency bands allocated for small-cell backhaul in 5G networks [1]. The use of metasurfaces (MTSs) for 5G systems has been studied and proved to be extremely useful in the aforementioned frequency ranges. Indeed, some antenna prototypes based on MTSs have already been developed with the aim of satisfying the needs of the new generation of mobile networks [2, 3]. Modulated MTS antennas, which were initially developed for satellite communications, are a special category of MTS antennas [4]. The low profile, low cost and reduced power consumption of this kind of structures, along with the adaptability of the design process to different frequencies, make them a very attractive solution.

A MTS is generally formed by sub-wavelength elements arranged on a periodic lattice and either printed on a grounded dielectric slab or grown on a metallic base-plate. By changing the geometry of these constitutive elements in the lattice unit-cell, one can exert a high degree of control on the aperture fields [5, 6, 7]. The MTS layer can be modeled as a continuous impedance boundary condition (IBC) due to the small size of the elements compared to the wavelength. In modulated MTS antennas, a surface wave (SW) is excited on the aperture and gradually transformed into a leaky-wave owing to its interaction with the periodically modulated IBC, which results in a radiated beam [8]. By tuning the properties of the modulation one can control the attributes of the beam, such as the pointing angle, shape, and polarization.

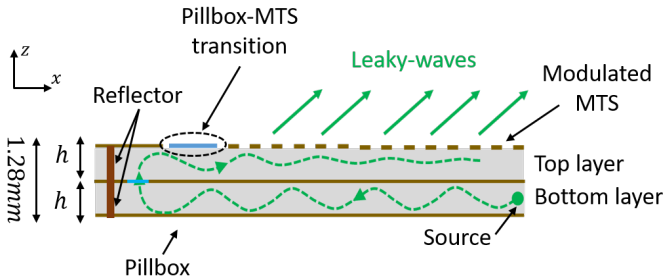
This paper presents a modulated MTS antenna operating at K-band with multibeam performance. The system is based on a pillbox quasi-optical beamformer [9], which essentially transforms the cylindrical wave propagating on the pillbox's lower layer into a plane wave in the upper layer. By adding a modulated MTS on the top layer (Figure 1a), one obtains a compact antenna. A pillbox-fed modulated MTS antenna at X-band was described in [10]. As mentioned before, the entire design process can be adapted for other frequency bands by properly modifying the material, the beamformer, and the MTS elements dimensions. Thus, in this work, we use a strategy similar to that described in [10] to design an antenna operating at  $f_o = 20.7$  GHz.

## 2 Design of a Multi-beam Modulated Metasurface Antenna

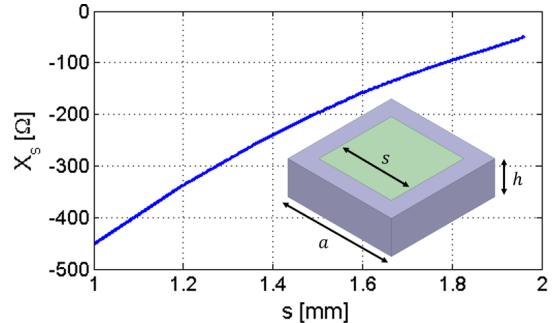
In the following, we will refer to the Cartesian reference system  $(x,y,z)$  shown in Figure 1a. The IBC used to model our MTS consists in a sheet transition [11, 12], penetrable [13] or transparent impedance [14, 15]  $Z_s = jX_s$  which lies on top of a grounded dielectric slab. This structure supports the propagation of a TM surface wave. In order to get the desired radiation effect, the sheet transition impedance is modulated along  $x$ -direction as

$$X_s(x) = X_{av}(1 + M(x) \cos(2\pi x/p)), \quad (1)$$

where  $X_{av}$  is the average reactance,  $M(x)$  is the modulation index ( $0 \leq M(x) \leq 1$ ) and  $p$  is the period. The chosen material is Rogers RO3006 ( $\varepsilon_r = 6.15$ ,  $\tan \delta = 0.002$ ) with thickness  $h = 0.64$ mm. In order to implement



(a) Side view of total structure

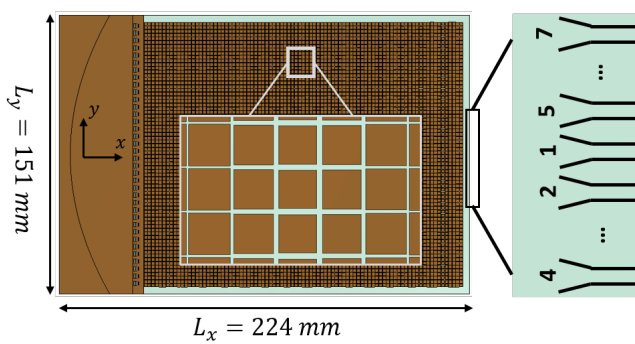


(b) Unit-cell and reactance 1D map

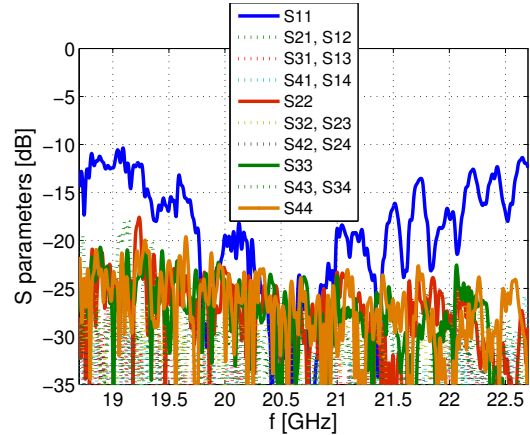
Figure 1 – (a) Side view of the pillbox fed MTS antenna. (b) Unit-cell with square metallic patch and curve representing  $X_s(s)$  for different patch sizes.

(1), we use square metallic patches whose size changes according to the spatial variation of  $X_s(x)$ . To that end, we first build a database that relates the patch dimensions to the sheet transition IBC values. Taking a unit-cell (a single MTS element) of side  $a$  on a substrate of thickness  $h$ , and assuming it inside a regular lattice to preserve the local periodicity principle, one can vary progressively the metallic patch size  $s$  and extract the equivalent sheet impedance  $Z_s$ . Figure 1b shows the curve that relates both parameters as well as an inset with the geometry of the unit-cell. The MTS element has a constant size  $a = \lambda_0/7$ , which makes it small compared to the SW wavelength, as indicated in Section 1. Once we have characterized the unit-cell, the next design step consists in retrieving the square patch dimensions that better match the ideal values in (1) to obtain our modulated MTS. The latter is placed then on the beamformer top layer to get the final structure depicted in Figure 2a.

In addition, it is important to note that the use of a pillbox allows one to place several sources (here, H-plane horns) in the bottom layer. These horns are arranged at the focal plane of the pillbox's reflector (Figure 2a) and each one provides a beam pointing at a different direction. Indeed, when the source position is shifted in the focal plane (along  $y$ -direction), the direction of propagation of the resulting plane-wave changes. As a result, the placement of  $N$  ports originates up to  $N$  beams at different pointing angles. This feature will be illustrated in the next section. Obviously, the number of sources is limited by the pillbox dimension, the horn size, and the HPBW of the radiated beams. The antenna dimensions are sketched in Figure 1a and Figure 2a, from where we emphasize a very low profile, with a total thickness of 1.28 mm.



(a) Top view of MTS antenna



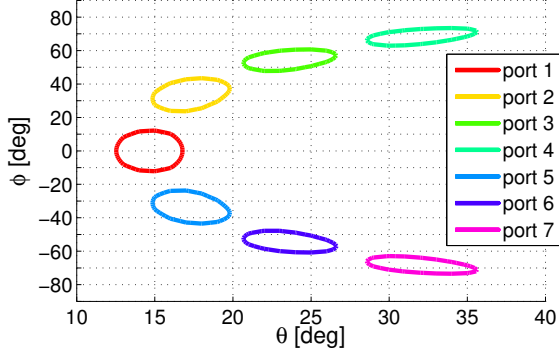
(b) S parameters

Figure 2 – (a) Disposition of patches and ports in the pillbox beamformer. (b) S-parameters for central and side ports, remaining ports behave as their symmetric ones.

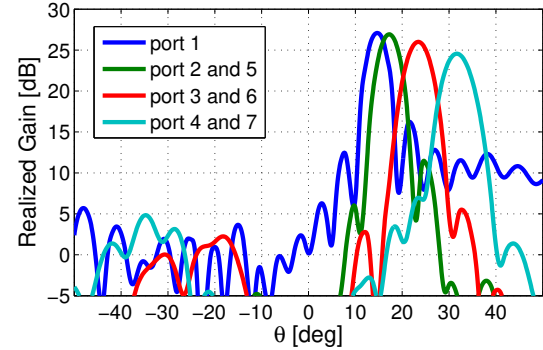
### 3 Simulation Results

For the design at hand, we implement (1) to obtain a beam at  $\theta_0 = 15^\circ$  for normal incidence ( $\phi_0 = 0^\circ$ ). The employed modulation parameters are  $p = 11.3$  mm,  $X_{av} = -0.24\eta_0$  (where  $\eta_0$  is the free-space impedance), and  $M$  varying with  $x$  to optimize the attenuation of the aperture fields and, therefore, enhance the aperture

efficiency of the antenna [16]. Switching between the  $N = 7$  ports implies the modification of both  $\theta_0$  and  $\phi_0$ . The simulated S-parameters of the horns are shown in Figure 2b, showing a bandwidth of 20% and a very good isolation between ports. Figure 3 presents the radiated beams for each source at  $f_o$ . The obtained angular coverage is displayed in Figure 3a, where the direction of the beam is given in  $(\theta, \phi)$  coordinates. Next, we represent in Figure 3b the radiation pattern in elevation at the E-plane for every port. The patterns are plotted by cutting every 3D beam at the angle  $\phi = \phi_0$ , where  $\phi_0$  is the azimuth angle of maximum gain for each source. The maximum realized gain at  $f_o$  is  $G = 27.1$  dB for port 1 and the beam-switching losses are up to 2.5dB (realized gain difference between port 1 and ports 4, 7). We note that the generated beams own the property of frequency scanning in  $\theta$ . Thus, it would be possible to operate at other frequencies around  $f_o$  within the bandwidth shown in Figure 2b, modifying then the individual beam directions and the angular coverage.



(a) -3dB contours of radiated beams



(b) E-plane radiation patterns at fixed  $\phi = \phi_0$  of each port

Figure 3 – (a) Radiation performance in  $(\theta, \phi)$  plane, and (b) realized gain at the E-plane cut for each horn.

## 4 Conclusion

We presented the design and numerical results of a compact modulated MTS antenna at 20.7 GHz. The radiating aperture consists of metallic patches whose size is modified to produce an equivalent modulated impedance. The MTS antenna is fed by a plane SW, which is obtained by means of a quasi-optical beamformer in a pillbox architecture. Moreover, one can change the propagation direction of this SW by exciting different ports in the pillbox focal plane. The proposed antenna topology is able to generate high-gain beams at different pointing angles, while providing a good scanning range in  $\theta$  and a wide angular coverage in  $\phi$ . The extremely thin profile of the structure ( $h_{total} = 1.28mm$ ), the high-gain behavior, and the multi-beam capability make this antenna a suitable candidate for backhaul applications. Last but not least, this flat aperture antenna can be easily integrated with a low visual impact on smart urban furniture, buildings, homes, and offices.

## 5 Acknowledgments

This publication has been supported by the European Union through the European Regional Development Fund (ERDF), and by the French Region of Brittany, Ministry of Higher Education and Research, Rennes Métropole and Conseil Départemental 35, through the CPER Project STIC & Ondes. It has also been supported by the Direction Générale de l'Armement (DGA) and by Brittany Region under ARED program.

## 6 References

- [1] M. M. Ahamed and S. Faruque, “5G backhaul: Requirements, challenges, and emerging technologies,” in *Broadband Communications Networks* (A. Haidine and A. Aqqal, eds.), ch. 4, Rijeka: IntechOpen, 2018.
- [2] S. Gupta, Z. Briqech, A. R. Sebak, and T. Ahmed Denidni, “Mutual-coupling reduction using metasurface corrugations for 28 GHz MIMO applications,” *IEEE Antennas Wireless Propag. Lett.*, vol. 16, pp. 2763–2766, 2017.
- [3] T. Li and Z. N. Chen, “Metasurface-based shared-aperture 5G S-/K-band antenna using characteristic mode analysis,” *IEEE Trans. Antennas Propag.*, vol. 66, pp. 6742–6750, Dec 2018.
- [4] M. Faenzi *et al.*, “Metasurface antennas: New models, applications and realizations,” *Sci. Rep.*, vol. 9, p. 10178, July 2019.

- [5] S. Maci, G. Minatti, M. Casaletti, and M. Bosiljevac, "Metasurfing: Addressing waves on impenetrable metasurfaces," *IEEE Antennas Wireless Propag. Lett.*, vol. 10, pp. 1499–1502, 2011.
- [6] D. González-Ovejero, G. Minatti, G. Chattopadhyay, and S. Maci, "Multibeam by metasurface antennas," *IEEE Trans. Antennas Propag.*, vol. 65, pp. 2923–2930, Jun. 2017.
- [7] D. González-Ovejero, N. Chahat, R. Sauleau, G. Chattopadhyay, S. Maci, and M. Ettorre, "Additive manufactured metal-only modulated metasurface antennas," *IEEE Trans. Antennas Propag.*, vol. 66, pp. 6106–6114, Nov 2018.
- [8] A. Oliner and A. Hessel, "Guided waves on sinusoidally-modulated reactance surfaces," *IRE Trans. Antennas Propag.*, vol. 7, pp. 201–208, Dec. 1959.
- [9] M. Ettorre, R. Sauleau, and L. Le Coq, "Multi-beam multi-layer leaky-wave SIW pillbox antenna for millimeter-wave applications," *IEEE Trans. Antennas Propag.*, vol. 59, pp. 1093–1100, April 2011.
- [10] J. Ruiz-García, D. González-Ovejero, M. Faenzi, A. Mahmoud, M. Ettorre, P. Potier, P. Pouliquen, and R. Sauleau, "Quasi-optical excitation of modulated metasurface antennas," in *13th Int. Congress on Artificial Materials for Novel Wave Phenomena (Metamaterials)*, pp. X–348–X–350, Sep. 2019.
- [11] E. F. Kuester, M. Mohamed, M. Piket-May, and C. Holloway, "Averaged transition conditions for electromagnetic fields at a metafilm," *IEEE Trans. Antennas Propag.*, vol. 51, pp. 2641–2651, Oct. 2003.
- [12] A. M. Patel and A. Grbic, "Effective surface impedance of a printed-circuit tensor impedance surface (PCTIS)," *IEEE Trans. Microw. Theory Tech.*, vol. 61, pp. 1403–1413, April 2013.
- [13] E. Bleszynski, M. Bleszynski, and T. Jaroszewicz, "Surface-integral equations for electromagnetic scattering from impenetrable and penetrable sheets," *IEEE Antennas Propag. Mag.*, vol. 35, pp. 14–25, Dec. 1993.
- [14] D. González-Ovejero and S. Maci, "Gaussian ring basis functions for the analysis of modulated metasurface antennas," *IEEE Trans. Antennas Propag.*, vol. 63, pp. 3982–3993, Sep. 2015.
- [15] G. Minatti, F. Caminita, E. Martini, M. Sabbadini, and S. Maci, "Synthesis of modulated-metasurface antennas with amplitude, phase, and polarization control," *IEEE Trans. Antennas Propag.*, vol. 64, pp. 3907–3919, Sept 2016.
- [16] D. R. Jackson and A. A. Oliner, "Leaky-wave antennas," in *Modern antenna handbook* (C. A. Balanis, ed.), ch. 7, pp. 325–367, Wiley, 2007.

# Passive reconstruction of the impulse response between two antennas in a reverberation chamber

## *Reconstruction passive de la réponse impulsionale entre deux antennes en chambre réverbérante*

---

**M. Tamart<sup>1</sup>, F. Sarrazin<sup>1</sup>, E. Richalot<sup>1</sup>, M. Davy<sup>2</sup>, and J. de Rosny<sup>3</sup>**

<sup>1</sup>Université Paris-Est, ESYCOM (FRE2028), UPEMLV, ESIEE-Paris, CNAM, meriem.tamart@u-pem.fr

<sup>2</sup>Univ Rennes, CNRS, IETR, matthieu.davy@univ-rennes1.fr

<sup>3</sup>ESPCI ParisTech, PSL Research University, CNRS, Institut Langevin, julien.derosny@espci.fr

---

**Keywords:** cross-correlation techniques, reverberation chamber, passive antennas

**Mots clés:** techniques d'inter-corrélation, chambre réverbérante, antennes passives

---

### **Abstract:**

The impulse response between two receiving antennas can be retrieved via cross-correlation techniques leveraging field uniformity within a reverberation chamber (RC). Exploiting the diffuse wave field generated by rotation of a mechanical mode stirrer inside an RC excited by a single transmitting antenna, we demonstrate the convergence of the cross-correlation toward the impulse response between the two receiving antennas. The obtained experimental results show that it is possible to characterize passively the coupling between two antennas in an RC.

### **Resumé:**

La réponse impulsionale entre deux antennes en réception peut être récupérée via des techniques d'inter-corrélation dans une chambre réverbérante (CR). En exploitant le champ diffus généré par la rotation d'un brasseur de modes mécanique à l'intérieur d'une CR excitée par une seule antenne émettrice, nous démontrons la convergence de la fonction d'inter-corrélation vers la réponse impulsionale entre les deux antennes réceptrices. Les résultats expérimentaux obtenus montrent qu'il est possible de caractériser passivement le couplage entre deux antennes dans une CR.

## 1 Introduction

The field of wireless communications is constantly evolving. This considerable growth has spawned huge needs in terms of developing new characterization techniques to measure the performance of antennas. For many applications, the coupling between receiving antennas should be estimated. When, the antenna are embedded in a complex system, it can be difficult, if not impossible to measure the direct responses between the antenna ports. Here we propose to validate the principle of a passive method based on the field cross-correlation in a Reverberation Chamber (RC). We exploit the properties of the RC to generate a diffuse field using a single source and a mechanical mode stirrer. Averaging over different realizations, the reconstructed signal is expected to converge towards the impulse response between two receiving antennas. This technique allows to passively characterize the two receivers and can be extended later to characterize an antenna network as in the MIMO case.

## 2 Cross-correlation function and impulse response

The relation between the transfer function and the correlation function is reflected by the fact that under the assumption of a diffuse field, the correlation of the signals recorded by two passive sensors contains essentially the same information on the medium as the signal that one would have acquired, if one of these sensors was active (transmitter) and the other was passive (receiver). In the case of a diffuse field, the correlation function converges to a function proportional to the sum of the causal and anticausal transfer functions between two sensors. This method was developed in different areas of theoretical and experimental physics and it has been applied to all types of waves (seismic [1], acoustic [2], elastic [3] and electromagnetic [4]).

The cross-correlation function  $C_{ab}$  between two points a and b can be obtained in the frequency domain from the measured impedance parameters Z using (1). The correlation function obtained has a part with positive times (or causal part) and a part with negative times (anti-causal part).

$$C_{ab}(f) = \sum_k Z_{ak} Z_{bk}^* \quad (1)$$

with

$k$ =source index

In the following, a single source is used and the different excitation configurations are generated by rotating the mode stirrer, so the sum applies on the different stirrer positions.

### 3 Experimental Setup

The experiment was made in an RC (2.751m x 2.951m x 2.354m, LUF around 400 MHz) as depicted in Fig. 1. The antennas under test (AUT) are two horn antennas (a and b) facing each other used in receiving mode and separated with a distance of 44 cm. The source antenna (c) is directed to a mechanical mode stirrer in order to generate a diffuse field. The measurements are carried out at 100001 frequency points uniformly spaced on the frequency band of [1-4] GHz for 60 regularly space stirrer positions over a whole rotation.

In order to study the convergence of the correlation function towards the estimated impulse response between the two receiving antennas, we examine the influence of the spacing between AUT. The antenna a is fixed, we move the antenna b so that the distance between both antenna apertures varies from 44 cm to 64 cm with a step of 10 cm.

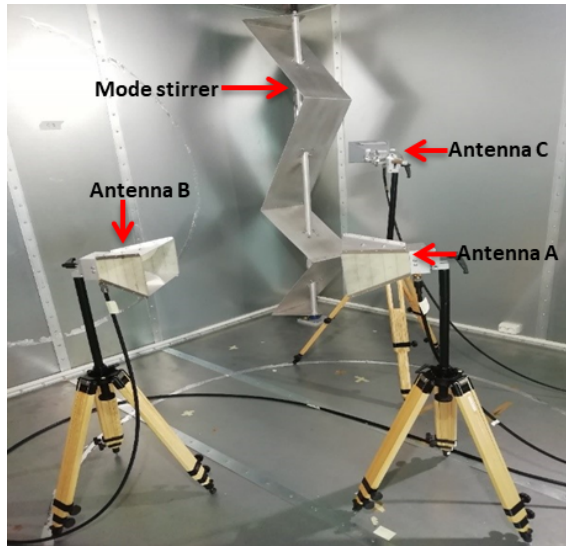


Figure 1 – Experimental setup in ESYCOM laboratory RC.

### 4 Results

Once the measurement data have been recovered, they are processed in the frequency domain because the calculation of the frequency correlation function is faster. First, we eliminate the amplitude information from the  $Z_{ij}$  parameters by working only with the information contained in the phase  $\Phi_{ij}$  of the signals. This allows for equivalent contributions from all frequencies in the working band. The effectiveness of phase information has already been demonstrated in [5].

Let  $Z'$  in (2) be the new parameters taking into account only the phase information, the indices a and b for the receiving antennas, and c for the source antenna. The  $C_{ab}$  cross-correlation is then calculated as in (3). The cross-correlation function is then converted in the time domain using an inverse Fourier transformation and it is averaged over the different stirring positions and excitation antenna orientations.

$$Z'_{ij}(f) = \exp(j\Phi_{ij}) \quad (2)$$

and :

$$C_{ab}(f) = Z'_{ac} Z'_{bc}^* \quad (3)$$

Fig. 2 shows the real part of results obtained by calculating the correlation function (blue curve) and by direct measurement of the impulse responses between the antennas a and b (red curve for causal part and green curve for anticausal part). As expected, the results obtained are roughly superimposed and the cross-correlation

function converges towards the mean impulse response between the antennas so that we can recover the ballistic wave and the first echoes in the RC.

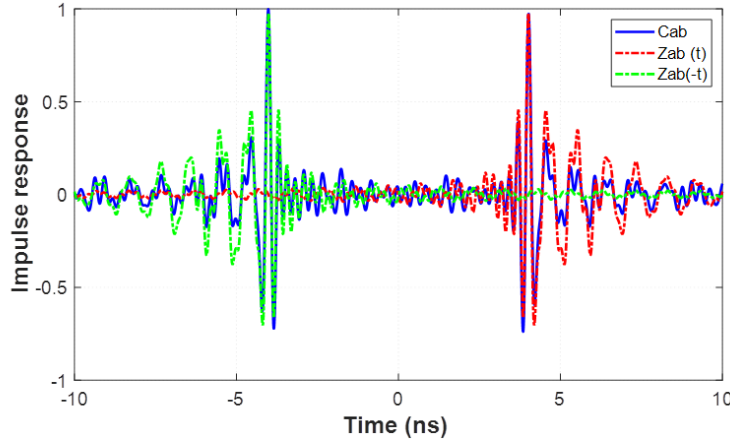


Figure 2 – Calculated cross-correlation function (blue) and measured impulse responses (red and green) in the time domain.

In order to see the measurement dynamics and after having applied an adequate time window between 3.49 ns and 10 ns to eliminate the first echoes while keeping the useful signal corresponding to the transfer function between antennas a and b, the results obtained for the correlation function and the direct measurement are normalized and plotted in dB (Fig. 3). The order of magnitude of the Zab frequency variation is recovered by the cross-correlation function.

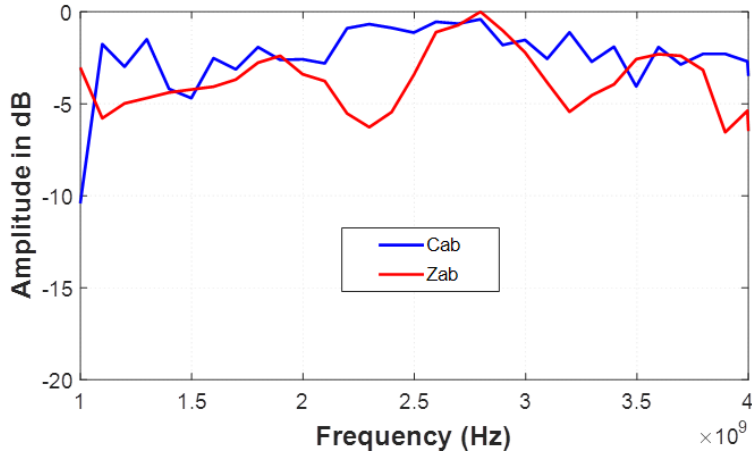


Figure 3 – Calculated cross-correlation function (blue) and measured response (red) in the frequency domain.

The result obtained for three different spacings between the AUT is shown in Fig. 4. Two peaks clearly appear and correspond to causal (the part with positive times) and anticausal (part with negative times) impulse responses. The position of the two symmetric peaks is translated towards larger times (in absolute value) when increasing the distance between both antennas. We can verify that, as expected, the peak position displacement between two consecutive measurements corresponds to a distance variation of 10 cm.

The symmetry obtained is a good indicator of the cross-correlation convergence. Note that when the distance between the AUT increases, the measurement becomes more sensitive to external interferences due to the decrease of the direct path amplitude. As the presented results in Fig. 4 are normalized to keep the maximal amplitude equal to one, this effect is noticeable on the symmetry of the time response. The further the receiving antennas are, the more slowly the cross-correlation converges to the theoretical response.

## 5 Conclusion

In this communication, we have demonstrated the ability to reconstruct the impulse response between two receiving antennas by computing the cross-correlation of the diffuse field in RC using a single source. We have

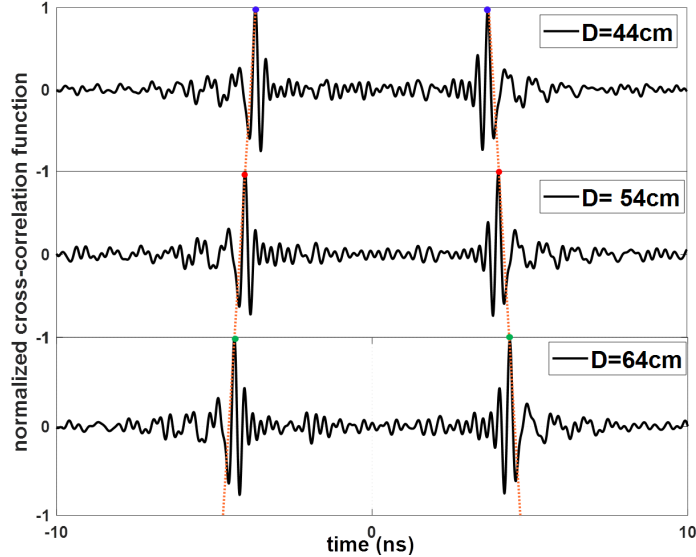


Figure 4 – Cross-correlation function for three different spacings between the two AUT.

presented the measurement results obtained allowing to validate the principle of reconstruction of the impulse response by studying the influence of the spacing between the receiving antennas on the convergence of the field cross-correlation towards the impulse response between the antennas. This approach provides a new framework for applications such as characterizing antennas that can only be used in their receiving mode. As in the case of MIMO network for 5G, in order to characterize the network set, it suffices to exploit the field received on the set of receivers and by post processing to be able to characterize all the network instead of making measurements for each pair of antennas one after the other.

## 6 References

- [1] M. Campillo and A. Paul, “Long-range correlations in the diffuse seismic coda,” in *Science 299, 547*, 2003.
- [2] P. Roux and W. Kuperman, “Extracting coherent wave fronts from acoustic ambient noise in the ocean,” in *J. Acoust. Soc. Am. 116*, 1995, 2004.
- [3] L. Chehami, J. D. Rosny, C. Prada, E. Moulin, and J. Assaad, “Extraction des fonctions de green par correlation de bruit : application pour la détection et l'imagerie de dé dans des plaques minces réverbérantes,” in *Lebanese Science Journal, Vol. 16, Special Issue*, 2015.
- [4] M. Davy, J. D. Rosny, and P. Besnier, “Green’s function retrieval with absorbing probes in reverberating cavities,” in *Phys. Rev. Lett., p.5*, 2016.
- [5] A. Derode, A. Tourin, and M. Fink, “Ultrasonic pulse compression with one-bit time reversal through multiple scattering,” in *J. Appl. Phys., vol. 85, p. 6434*, 2014.

## Antenne 3D filaire miniature pour les systèmes 5G

### *Miniature 3D wire antenna for 5G systems*

**Fateh Benmahmoud, Pierre Lemaître-Auger, Smail Tedjini.**

*Univ. Grenoble Alpes, Grenoble INP, LCIS, 26000 Valence, France, {firstname.name}@lcis.grenoble-inp.fr*

**Mots clés :** *antenne filaire, 5G, algorithme génétique, optimisation ; wire antenna, genetic algorithm, optimization*

#### Résumé/Abstract

Le développement d'antennes monopoles miniatures multi-segments en trois dimensions est présenté. Chaque segment est orienté arbitrairement dans l'espace afin de réduire le volume occupé par l'antenne tout en conservant de bonnes caractéristiques : compactité, efficacité, adaptation d'impédance et bande passante. Ces antennes sont destinées aux systèmes 5G par leur grande miniaturisation et leur bande-passante. Étant donné l'absence de pertes liées au diélectrique, les antennes filaires multi-segments sont une bonne alternative aux antennes planaires dans certains cas. Un algorithme génétique multi-objectif a été implémenté pour la conception. Une antenne formée de sept segments occupant un volume de  $\lambda_0/4.81 \times \lambda_0/6.10 \times \lambda_0/7.03$ , où  $\lambda_0$  représente la longueur d'onde à la fréquence 3.28 GHz a été obtenue. L'impédance est adaptée à  $50\Omega$  dans la bande (3.28-3.61) GHz, le coefficient de réflexion est inférieur ou égal à -10.41 dB. L'efficacité interne simulée est supérieure à 98% pour toute la bande C (3500-3600 MHz). La polarisation de l'antenne est quasiment linéaire et le gain mesuré est de 4.03 dBi.

The development of miniature segmented monopole antennas in three dimensions is presented. Each segment is oriented randomly in space to reduce the volume occupied by the antenna while obtaining good characteristics: compactness, efficiency, impedance matching and bandwidth. Because of its small size and large bandwidth, the designed antenna is intended for 5G systems. Because of the absence of any dielectric losses, segmented wire antennas are a good alternative to planar antennas in some cases. A multi-objective genetic algorithm has been implemented for the conception. A 7-segment antenna that occupies a volume of  $\lambda_0/4.81 \times \lambda_0/6.10 \times \lambda_0/7.03$ , where  $\lambda_0$  is the wavelength at the frequency 3.28 GHz was obtained. Its impedance is fairly close to  $50\Omega$  on all bandwidth (3.28-3.61) GHz, and the reflection coefficient is lower or equal to -10.41 dB. The simulated total efficiency is higher than 98% for the entire C-band (3500-3600 MHz). The polarization of the antenna is almost linear and the measured gain is 4.03 dBi.

#### 1 Introduction

Avec le développement rapide des systèmes et modules de communication 5G, la réduction de la taille des antennes devient un enjeu de plus en plus important. Cependant, selon la loi de Chu, plus une antenne est de petite taille, plus sa bande passante sera réduite [1]. Il est également difficile de concilier antenne miniature et adaptation d'impédance. Gérer ces aspects avec les techniques traditionnelles de conception d'antennes peut rapidement devenir une tâche très délicate et complexe. Beaucoup d'antennes planaires sont réalisées sur un substrat. Ceci réduit grandement leur volume, le problème revenant à minimiser leur surface. Cependant, la présence d'un substrat réduit leur efficacité intrinsèque de rayonnement. Dans ce travail, nous proposons une antenne en trois dimensions (3D) compacte, purement métallique qui couvre toute la bande C (3500-3600 MHz). Il s'agit d'un monopole multi-segments. Introduit par E. Altshuler dans [2], cette topologie d'antenne a déjà montré son efficacité dans plusieurs travaux [3]-[6]. Une telle structure offre un grand nombre de degrés de liberté qui permet d'augmenter la résistance de rayonnement de l'antenne tout en conservant un volume compact. La conception d'une telle antenne est réalisée avec des algorithmes génétiques.

#### 2 Conception d'antenne

La structure d'antenne est un monopole 3D composé d'un fil plié qui forme un ensemble de segments différemment orientés dans l'espace au-dessus d'un plan de masse. Cela rend la conception de ce type d'antenne très flexible et polyvalente afin d'obtenir les caractéristiques voulues pour un volume et une taille d'antenne donnés. Plus précisément chaque segment est défini dans l'espace par trois paramètres : une longueur  $l$ , un angle d'élévation  $\theta$ , un angle d'azimut  $\phi$  comme le montre la figure 1.

Dans cette étude, les angles d'élévation et d'azimut sont limités à l'intervalle  $[0-90^\circ]$  et  $[0-360^\circ]$ , respectivement avec un pas de  $2^\circ$ . Pour faciliter le prototypage, la longueur des segments est aussi limitée à des

valeurs supérieures à trois millimètres, longueur minimale nécessaire à la fabrication. Ceci minimise les erreurs liées à la précision de fabrication et la complexité de l'antenne. La structure simulée est un monopôle au-dessus d'un plan de masse infini. Le rayon de chaque segment a été fixé à une valeur de 0.6 mm. La figure 1 montre une représentation schématique d'une topologie tridimensionnelle de cinq segments sur un plan de masse.

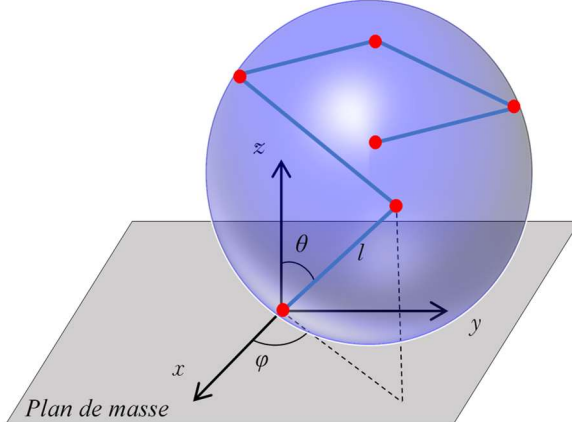


Figure 1. Représentation schématique d'une antenne filaire 3D de 5 segments.

L'algorithme génétique (AG) implémenté est de type multi-objectif [7]. On commence par créer la génération initiale de  $N$  individus (c.-à-d.  $N$  antennes). Un individu est constitué de  $M$  gènes ( $M = 3 \times N_b$ ,  $N_b$  est le nombre de brins). On évalue ensuite les performances de chaque individu par une simulation électromagnétique. Les meilleurs individus (50% de chaque génération) sont sélectionnés pour engendrer la prochaine génération. L'opération de sélection consiste à choisir les individus les plus adéquats vis-à-vis des critères et contraintes imposées. Les individus sélectionnés entament ensuite une phase de reproduction à travers les deux opérateurs génétiques principaux de croisement et mutation [8]. Cela donne naissance à une nouvelle génération. L'opération de croisement permet le brassage génétique de la population. Grâce à celui-ci, les gènes des meilleurs individus, et donc ses performances et caractéristiques, sont transmis de génération en génération. L'opérateur génétique de mutation consiste à altérer un ou plusieurs gènes dans un chromosome de manière aléatoire.

Pour garantir que l'algorithme implémenté engendre toujours des solutions fiables qui répondent aux besoins, nous avons implémenté un filtre géométrique qui permet d'exclure les topologies inacceptables. Le filtrage concerne les topologies avec des segments qui se croisent ou qui pénètrent dans le plan de masse. Les topologies qui présentent des tailles très élevées sont aussi éliminées pour accélérer la convergence du processus d'optimisation. Le remplacement des topologies incorrectes par d'autres solutions géométriquement correctes et générées aléatoirement maintient la diversité des générations et évite la convergence vers des minimums locaux [9].

L'outil d'optimisation est implémenté sous Matlab en conjonction avec l'environnement de simulation électromagnétique «Computer Simulation Technology» (CST) [10]. Le nombre de segments et le rayon des fils ont été fixés à 7 et à 0,6 mm respectivement. Le nombre d'individus d'une génération est de 120. Les fonctions de coût visent à réduire le volume occupé par l'antenne, maximiser la bande passante et obtenir l'adaptation d'impédance dans la bande ciblée. Le tableau 1 résume les fonctions objectifs de l'AG implémenté.

	Formule
$f_1$	<i>Volume occupé par l'antenne</i>
$f_2$	fonction de la bande passante

Tableau 1. Les fonctions objectifs implémentées.

La valeur de la fonction de la bande passante  $F_{BP}$  est calculée de la manière suivante :

$$F_{BP} = \begin{cases} 0 & \text{si } |S_{11}| \leq -10 \text{ dB } \forall f \in \Delta f \\ 1 & \text{si } |S_{11}| > -10 \text{ dB } \forall f \in \Delta f \\ 1 - BP/200 & \text{si } \exists f \in \Delta f \text{ où } |S_{11}(f)| \leq -10 \text{ dB} \end{cases} \quad (1)$$

où  $\Delta f$  est la bande de fréquences [3400-3600] MHz et  $BP$  représente la bande-passante en MHz.

### 3 Optimisation et caractérisation de l'antenne

Il a fallu 135 générations pour que l'optimisation arrive à une solution qui satisfait les objectifs ciblés. Avec un ordinateur à deux processeurs 2.20 GHz et une mémoire d'accès aléatoire (RAM) de 32GB, cela représente 157.5 heures de calcul. Nous avons aussi constaté que plus le volume dans lequel l'antenne est confinée est compact, plus le coefficient de réflexion est élevé [11]. Cela s'explique par l'apparition d'une partie réactive de l'impédance conduisant à une désadaptation. Notons que dans la littérature, en plus de l'apparition d'une partie réactive, une diminution de la partie active de l'impédance a été constatée [12].

La sélection de la solution parmi les individus de la dernière génération a été effectuée sur la base de bon compromis entre les différents objectifs fixés. La structure sélectionnée, illustrée à la figure 2, occupe un volume de  $19\text{mm} \times 15\text{mm} \times 13\text{mm}$  ce qui correspond à  $\lambda_0/4.81 \times \lambda_0/6.10 \times \lambda_0/7.03$ , où  $\lambda_0$  est la longueur d'onde pour la fréquence 3.28 GHz.

La fabrication d'un prototype a été effectuée en exploitant les techniques d'impression 3D. L'antenne est composée de cuivre et de quelques alliages pour assurer les conditions thermiques et moléculaires, indispensables pour le processus de fabrication.

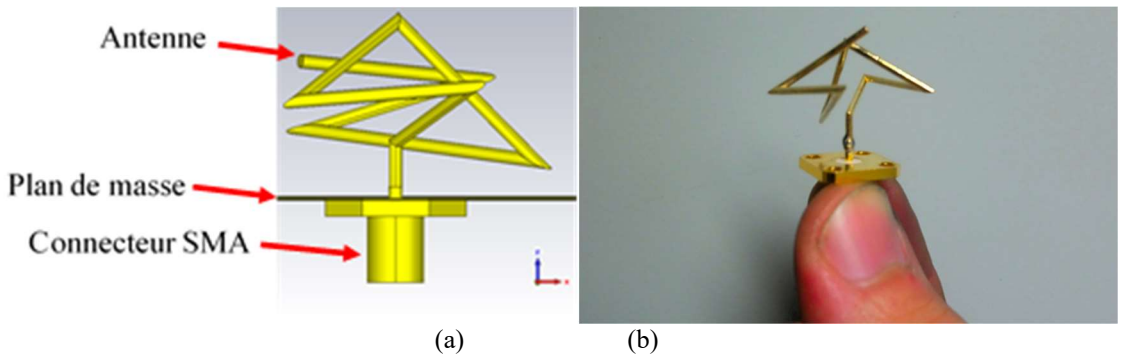


Figure 2. Antenne obtenue. (a) Schéma de l'antenne. (b) Prototype fabriqué.

L'antenne réalisée couvre une bande-passante de 330 MHz, de 3.28 à 3.61 GHz à -10 dB qui couvre l'intégralité de la bande C (3400-3600) MHz. Le coefficient de réflexion varie de -10.4 à -21.66 dB pour sur la bande C. Comme l'antenne est purement métallique, elle offre ainsi une efficacité interne très élevée qui dépend seulement de la conductivité du métal qui la compose. Les figures 3.a et 3.b montrent respectivement l'impédance d'entrée et l'amplitude du coefficient de réflexion. Un décalage de 67 MHz entre les valeurs simulées et mesurées est constaté, ce décalage n'impacte pas son fonctionnement, l'antenne est bien opérationnelle dans la bande ciblée. L'impédance proche de 50 ohms est assurée dans la bande cible malgré le degré de miniaturisation imposé.

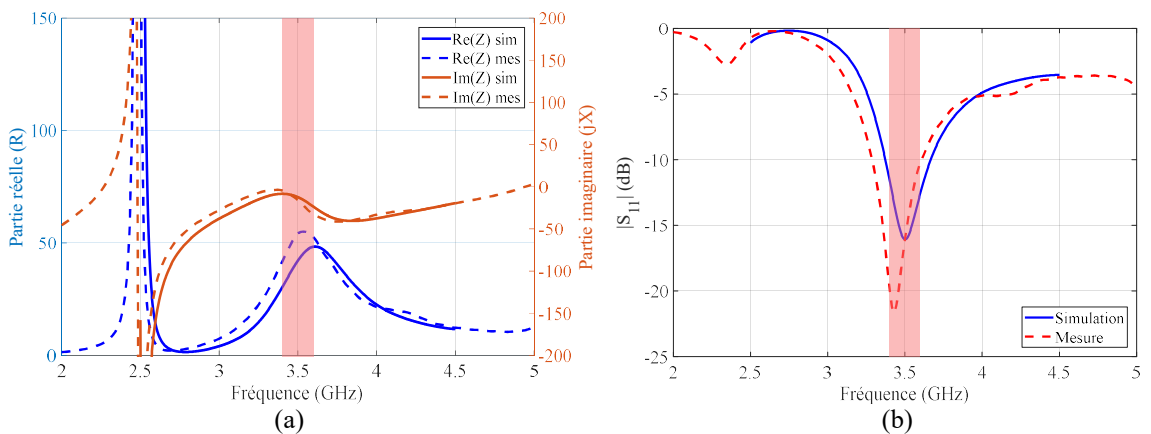
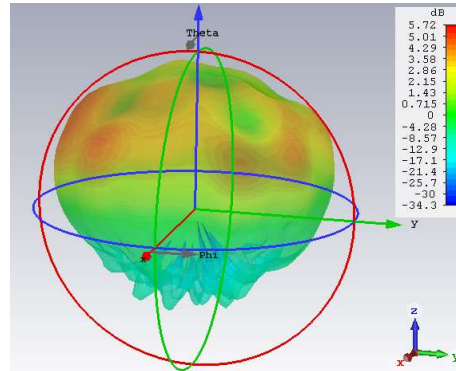
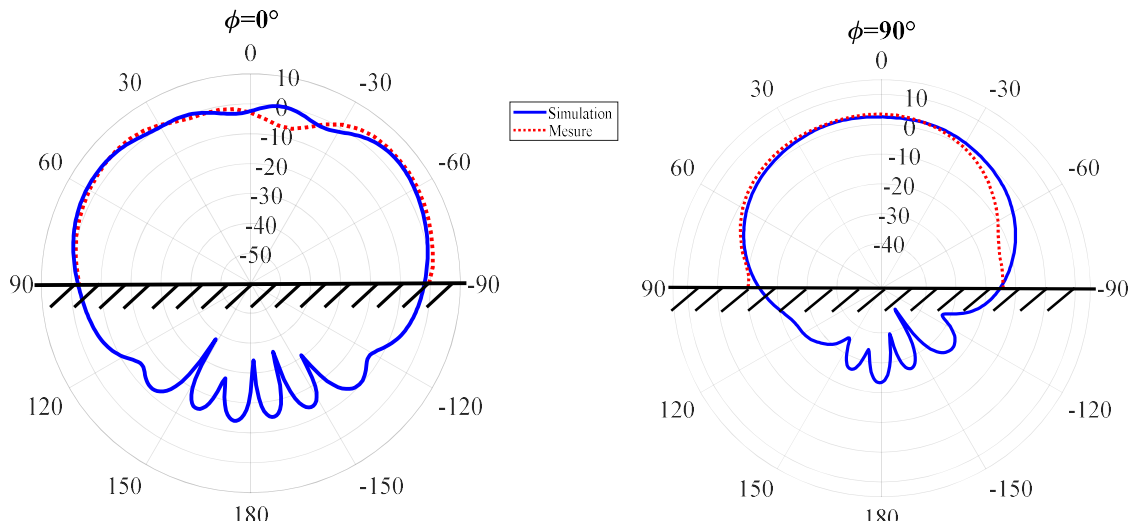


Figure 3. Caractéristiques de l'antenne : (a) Impédance. (b) Coefficient de réflexion.

Pour bien caractériser le prototype fabriqué, nous avons effectué des mesures en champ lointain au sein d'une chambre anéchoïque. Comme cela est illustré à la figure 4, la totalité du champ électromagnétique est rayonné dans la moitié supérieure de l'espace (de  $-90^\circ$  à  $90^\circ$ ), comme cela était attendu étant donné la présence du plan de masse. L'accord entre les mesures et les simulations est bon dans les deux plans : azimuthal et d'élévation. Les mesures ont montré que l'antenne a un gain 4.03 dBi, ce chiffre peut atteindre les 5.72 dBi pour certaines directions. L'efficacité interne simulée de l'antenne est supérieure à 98.7% en incluant les faibles pertes dans la connexion avec le connecteur SMA.



(a)



(b)

(c)

Figure 4. Le diagramme de rayonnement normalisé simulé et mesure de l'antenne : (a) Représentation 3D simulée. (b) Mesure et simulation dans le plan xoz. (c) Mesure et simulation dans le plan yoz.

La polarisation est de type linéaire. Cela est normal étant donné la taille relativement petite de l'antenne comparée à la longueur d'onde dans la bande de fréquence ciblée. L'obtention d'une polarisation circulaire (ou elliptique) nécessiterait le relâchement des contraintes liées au volume occupé.

Le tableau 2 montre une étude comparative entre l'antenne conçue et quelques conceptions qui existent dans la littérature. Pour les travaux de réseaux d'antennes, les propriétés des antennes élémentaires sont considérées. On peut constater que l'antenne filaire 3D est légèrement moins compacte que les solutions basée sur des structures planaires hybride et open-slot [11], [12], par contre elle démontre des propriétés de rayonnement supérieures en termes d'efficacité et de gain. Cette antenne est un très bon candidat lorsque les performances de rayonnement sont critiques.

Référence	Type d'antenne	Dim. Maximale (mm)	BP à -10 dB (MHz)	Gain (dBi)	Efficacité
[11]	Open-slot	17	420	3.6	56% à 70%
[13]	Patch	31.9	200	5.3	30%
[14]	Yagi planaire	60	440	7	(*)
[15]	Open-slot	21	280	<5	62% to 76%
[12]	Hybride	17.8	100	-4.8	<50%
[16]	Patch	40	240	~3	~50%
Ce travail	Filaire 3D	19	330	5.72	>98%

\* Dans [3], le substrat FR4 avec une tangente de perte de 0.02 est utilisé.

Tableau 2. Comparatif avec d'autres travaux.

## 4 Conclusion

La conception d'antennes miniatures avec une bande-passante importante et bien adaptée a été démontrée dans ce travail. Les mesures faites à partir d'un prototype corroborent les simulations. Ce type d'antenne constitue une solution intéressante dans des systèmes 5G. L'antenne offre une résistance de rayonnement bien adaptée à 50 ohms sur toute la bande C et une valeur d'efficacité de rayonnement très élevée grâce à sa structure purement métallique. Cette topologie d'antenne a été adaptée pour une impédance de 50 ohms, mais il est possible de concevoir des antennes avec d'autres valeurs d'impédance en suivant les mêmes démarches. Les travaux futurs se concentreront sur l'amélioration des caractéristiques de l'antenne vis-à-vis de l'adaptation d'impédance et l'exploitation de ce type d'antenne pour les systèmes de réseau d'antennes.

## References bibliographiques

- [1] H. A. Wheelert, "Fundamental Limitations of Small Antennas," *Proc. IRE*, vol. 35, no. 12, pp. 1479–1484, 1947.
- [2] E. E. Altshuler and D. S. Linden, "Wire-antenna designs using genetic algorithms," *IEEE Antennas Propag. Mag.*, vol. 39, no. 2, pp. 33–43, 1997.
- [3] J. D. Lohn, G. S. Hornby, and D. S. Linden, "Rapid Re-Evolution of an X-Band Antenna for Nasa's Space Technology 5 Mission BT - Genetic Programming Theory and Practice III," T. Yu, R. Riolo, and B. Worzel, Eds. Boston, MA: Springer US, 2006, pp. 65–78.
- [4] E. E. Altshuler, "Electrically small self-resonant wire antennas optimized using a genetic algorithm," *IEEE Trans. Antennas Propag.*, vol. 50, no. 3, pp. 297–300, 2002.
- [5] J. D. Lohn, D. S. Linden, B. Blevins, T. Greenling, and M. R. Allard, "Automated synthesis of a lunar satellite antenna system," *IEEE Trans. Antennas Propag.*, vol. 63, no. 4, pp. 1436–1444, 2015.
- [6] F. Benmahmoud, P. Lemaître-Augier, and S. Tedjini, "Design of electrically small 3D wire antennas for UHF RFID applications using genetic algorithm," in *32nd General Assembly and Scientific Symposium of the International Union of Radio Science, URSI GASS 2017*, 2017, pp. 1–4.
- [7] E. E. Altshuler and D. S. Linden, "Wire-antenna designs using genetic algorithms," *IEEE Antennas Propag. Mag.*, 1997.
- [8] H. Iba and C. C. Aranha, "Introduction to genetic algorithms," *Adaptation, Learning, and Optimization*, 2012.
- [9] P. Diaz-Gomez and D. Hougen, "Initial Population for Genetic Algorithms: A Metric Approach," *Proc. 2007 Int. Conf. Genet. Evol. Methods*, 2007.
- [10] C. M. Studio, "Antenna Design and Simulation," *CST Microwave Studio*, 2016. .
- [11] Y. Ban, C. Li, C. Sim, G. Wu, and K. Wong, "4G/5G Multiple Antennas for Future Multi-Mode Smartphone Applications," *IEEE Access*, vol. 4, pp. 2981–2988, 2016.
- [12] M. Li *et al.*, "Eight-Port Orthogonally Dual-Polarized Antenna Array for 5G Smartphone Applications," *IEEE Trans. Antennas Propag.*, vol. 64, no. 9, pp. 3820–3830, 2016.

- [13] W. Chen and Y. Lin, “Design of \$2\times 2\$ Microstrip Patch Array Antenna for 5G C-Band Access Point Applications,” in *2018 IEEE International Workshop on Electromagnetics: Applications and Student Innovation Competition (iWEM)*, 2018, pp. 1–2.
- [14] H. Wang and G. Yang, “Design of  $4 \times 4$  microstrip Quasi-Yagi beam-steering antenna array operation at 3.5GHz for future 5G vehicle applications,” in *2017 International Workshop on Antenna Technology: Small Antennas, Innovative Structures, and Applications (iWAT)*, 2017, pp. 331–334.
- [15] Y. Li, C. Sim, Y. Luo, and G. Yang, “High-Isolation 3.5 GHz Eight-Antenna MIMO Array Using Balanced Open-Slot Antenna Element for 5G Smartphones,” *IEEE Trans. Antennas Propag.*, vol. 67, no. 6, pp. 3820–3830, 2019.
- [16] A. Yadav, M. K. Saraswat, V. Palukuru, and R. Gautam, “Antenna array for 5G C-band for mobile terminals,” in *2019 TEQIP III Sponsored International Conference on Microwave Integrated Circuits, Photonics and Wireless Networks (IMICPW)*, 2019, pp. 293–297.

# **Propagation and physical layer**

# Sécurité à la Couche Physique pour une Communication SISO MROF dans le Domaine Fréquentiel avec Renversement Temporel

## *Physical Layer Security in Frequency-Domain Time-Reversal SISO OFDM Communication*

**Sidney Golstein<sup>1,2</sup>, Trung-Hien Nguyen<sup>2</sup>, François Horlin<sup>2</sup>, Philippe De Doncker<sup>2</sup>, Julien Sarrazin<sup>1</sup>**

<sup>1</sup> Sorbonne Université, CNRS, Laboratoire de Génie Electrique et Electronique de Paris, 75252, Paris, France  
Université Paris-Saclay, CentraleSupélec, CNRS, Laboratoire de Génie Electrique et Electronique de Paris,  
91192, Gif-sur-Yvette, France, Sidney Golstein, Julien Sarrazin, {julien.sarrazin}@sorbonne-universite.fr

<sup>2</sup>Wireless Communication Group, Université Libre de Bruxelles, 1050 Bruxelles, Belgique, Sidney Golstein,  
Trung-Hien Nguyen, François Horlin, Philippe De Doncker, {sigolste,trung-hien,fhorlin,philippe.dedoncker}@ulb.ac.be

*Mots clés - Keywords : sécurité à la couche physique, renversement temporel, bruit artificiel, taux de sécurité – physical layer security, time reversal, eavesdropper, secrecy rate.*

### Résumé/Abstract

Ce papier présente une technique permettant de sécuriser une communication à la couche physique. Un précodage en renversement temporel implanté dans le domaine fréquentiel utilisant un multiplexage par répartition orthogonale de la fréquence est considéré. Pour maximiser le taux de sécurité, le design d'un ajout de bruit artificiel est proposé. Ce nouveau schéma de communication assure une sécurité de communication vers un récepteur légitime tout en dégradant les performances de réception de la donnée vers un nœud espion. Le nœud espion est supposé passif à l'émetteur. L'effet du canal de propagation est également investigué.

## 1 Introduction

Les communications sans fil sont non sécurisées de nature. Avec le développement des réseaux 5G, la sécurité à la couche physique (SCP) suscite un grand intérêt pour ces communications. La SCP tire profit des caractéristiques du canal de propagation pour augmenter la sécurité de la communication vis à vis d'un nœud espion potentiel. Le schéma proposé dans ce papier implémente un précodage de la donnée en renversement temporel (RT). Dans domaine temporel (DT), le RT revient à suréchantillonner le signal ce qui permet d'offrir un gain de puissance reçue au récepteur légitime (Bob). Dans ce papier, le RT a été implanté dans le domaine fréquentiel (DF) en utilisant le multiplexage par répartition orthogonale de fréquences (MROF). L'équivalent du RT dans le DF est d'envoyer un même symbole sur un certain nombre (appelé BOR) de sous-porteuses. Cela permet ainsi de jouir de la sélectivité fréquentielle du canal de propagation [1]. Le scénario est décrit dans [2]. Du bruit artificiel (BA) est ajouté orthogonalement à Bob. Ce bruit a pour but de détériorer la communication avec le nœud espion passif (Ève) sans influencer la communication avec le récepteur légitime. Une analyse de l'effet du canal de propagation sur le taux de sécurité (SR) est proposée.

## 2 Modèle du système

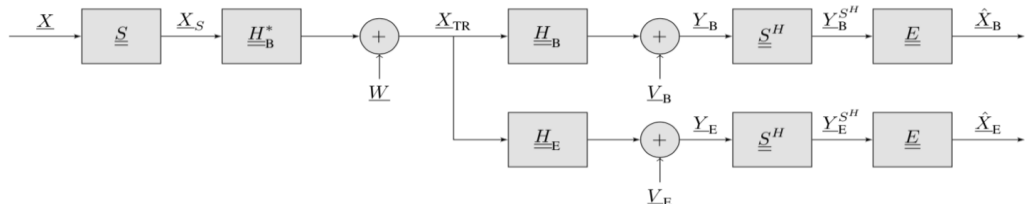


Figure 1. RT SISO MROF DF système avec ajout de BA

Un bloc de données  $\underline{X}$  composé de  $N$  symboles normalisés est envoyé. Chaque symbole est transmis via BOR sous-porteuses ( $Q=UN$  sous-porteuses seront utilisées à la transmission) via la matrice de spreading  $\underline{S}$ . Les canaux de Bob ( $\underline{H}_B$ ) et d'Ève ( $\underline{H}_E$ ) suivent une distribution normale de moyenne nulle et de variance unitaire. La communication a pour but d'atteindre Bob si bien que le produit entre la matrice de précodage  $\underline{H}_B^*$  et le canal de Bob  $\underline{H}_B$  donne un gain réel à chaque symbole, dépendant du BOR. Pour Ève, le gain entre  $\underline{H}_B^*$  et  $\underline{H}_E$  est complexe et ne dépend pas du BOR. Du BA ( $\underline{W}$ ) est ajouté et une optimisation analytique de l'énergie à transmettre est dérivée dans [2] pour maximiser le SR. Le signal transmis est donné par :

$$\underline{X}_{\text{TR}} = \sqrt{\alpha} \underline{H}_B^* \underline{S} \underline{X} + \sqrt{1-\alpha} \underline{W} \quad (\text{eq.1})$$

où le coefficient  $\alpha$  détermine le pourcentage d'énergie envoyée dédié à la donnée utile. Le SR est défini comme la différence des capacités entre les canaux de Bob et Ève :

$$C_S = \mathbb{E} [\log_2 (1 + \gamma_B) - \log_2 (1 + \gamma_E)] \quad , \quad \gamma_B > \gamma_E \quad (\text{eq. 2})$$

où  $\gamma_B$  et  $\gamma_E$  sont les RSIB à Bob et Ève respectivement.

### 3 Résultats

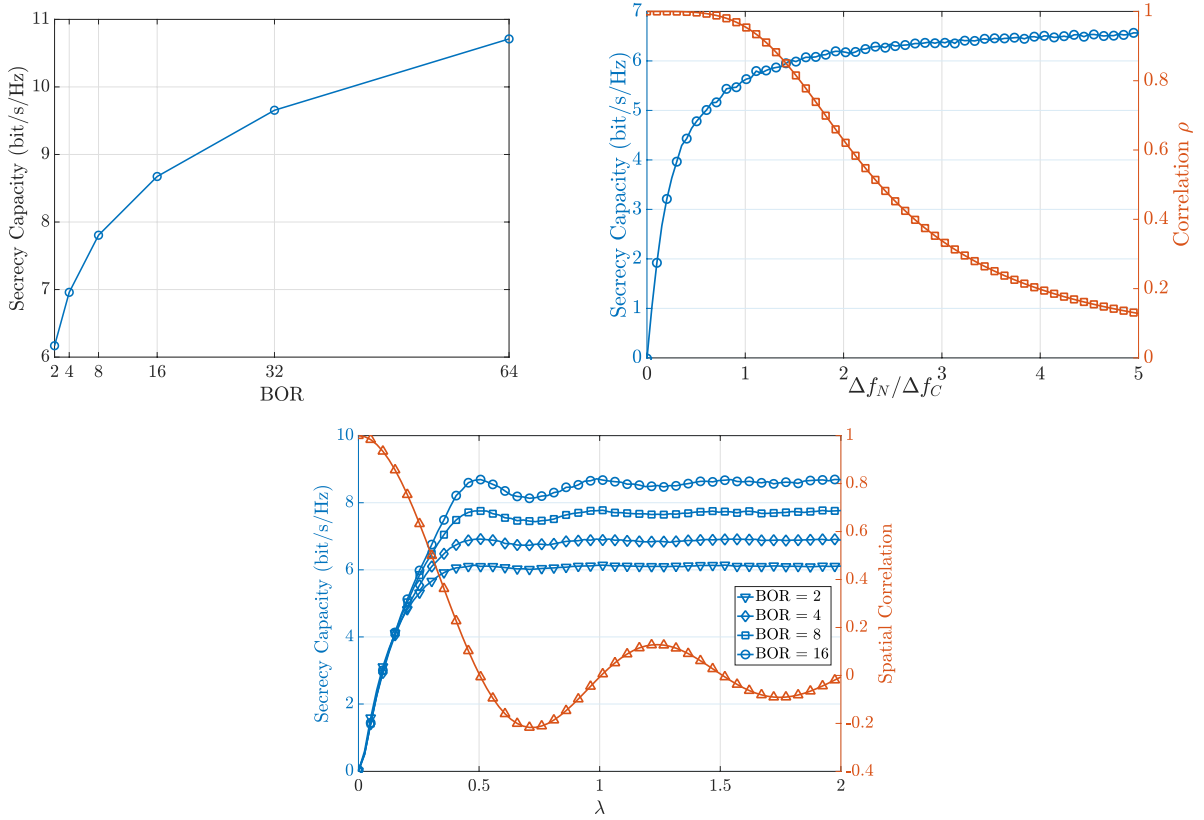


Figure 2. SR en fonction du BOR (gauche), de la corrélation fréquentielle (droite) et spatiale (bas),  $E_b/N_0=20$  dB

La figure de gauche montre les valeurs maximales de SR atteintes en fonction du BOR, lorsqu'aucune corrélation (spatiale et entre sous-porteuses) n'est considérée. On s'aperçoit que, lorsque le BOR augmente, le SR augmente. Ceci provient du fait que l'on jouit de plus de diversité fréquentielle pour des larges valeurs de BOR, augmentant ainsi le gain TR à Bob, et donc le SR de la communication. La figure du centre montre l'effet de la corrélation entre sous-porteuses

(dans les canaux  $\underline{H_B}$  et  $\underline{H_E}$ ) sur les valeurs de SR.  $\Delta f_N$  est défini comme la bande fréquentielle entre les BOR composantes d'un même symbole, et  $\Delta f_C$  est la bande de cohérence du canal. Lorsque  $\Delta f_N < \Delta f_C$ , la corrélation entre les BOR composantes d'un même symbole est grande, la diversité fréquentielle du canal est moindre, i.e. forte corrélation fréquentielle, ce qui diminue le SR (ici pour un BOR de 4). La figure de droite montre l'effet de la corrélation spatiale dans un environnement isotrope entre Bob et Ève, en fonction de la longueur d'onde  $\lambda$ , sur le SR. Lorsqu'ils sont suffisamment proches, i.e.,  $d < \lambda/3$ , la corrélation est élevée et l'effet du précodage RT diminue, réduisant le SR atteint.

## 4 Conclusion

Ce papier présente un schéma de SCP pour une communication SISO MROF dans le DF avec RT. Le SR atteint augmente dès lors que l'on jouit au maximum de la diversité fréquentielle du canal de propagation. Les performances du schéma étudié dépendent donc fortement de l'effet du canal de propagation.

## 5 Remerciements

Ce travail a été soutenu par le projet ANR GEOHYPE, bourse ANR-16-CE25-0003 de l'Agence Nationale de la Recherche Française, et par l'Action du COST CA15104 IRACON.

## 6 Références bibliographiques

- [1] S. Golstein, J. Sarrazin, T-H. Nguyen, P. De Doncker, F. Horlin, Physical Layer Security in Frequency-Domain Time-Reversal SISO OFDM Communication, DOI: 1910.01905, 2019
- [2] T-H. Nguyen, J-F. Determe, M. Van Eeckhaute, J. Louveaux, P. De Doncker, F. Horlin, Frequency-Domain Time-Reversal Precoding in Wideband MISO OFDM Communication Systems, DOI: 1904.10727, 2019

# Investigating Sub-THz PHY Layer for Future High-data-rate Wireless Backhaul

**Grégory Gougeon<sup>1</sup>, Yoann Corre<sup>1</sup>, Mohammed Zahid Aslam<sup>1</sup>, Simon Bicaës<sup>2</sup>, Jean-Baptiste Dore<sup>2</sup>**

<sup>1</sup>SIRADEL, Saint-Grégoire, France, [ycorre@siradel.com](mailto:ycorre@siradel.com)

<sup>2</sup>CEA-Leti, Grenoble, France, [jean-baptiste.dore@cea.fr](mailto:jean-baptiste.dore@cea.fr)

Keywords: *Sub TeraHertz ; Backhaul; Propagation model ; Modulation.*

## Abstract

Spectrum above 90 GHz is a promising investigation domain to offer future wireless networks with performance beyond IMT 2020 such as 100+ Gbit/s data rate or sub-ms latency. In particular, the huge available bandwidth can serve the backhaul transport network in the perspective of future ultra-dense deployments, and massive front-haul data streams. This paper investigates the feasibility and characteristics of the sub-THz mesh backhauling either installed in the streets or inside a large venue. The study relies on the highly realistic simulation of the physical layer performance, based on detailed geographical representation, ray-based propagation modelling, RF phase noise impairment, and a new modulation scheme robust to phase noise. It is shown that each link of a dense mesh backhaul network can reliably deliver several Gbit/s per 1-GHz carrier bandwidth.

## 1 Introduction

The long-term limitations of 5G standards are stressed already by the telecommunication industry and community research, for e.g. the delivery of ultra-low-latency broadband services, or the emergence of ubiquitous intelligence [1]. Next-generation wireless networks are imagined to be faster (1 Tbps for instance), more reactive (sub-ms latency), ultra-reliable and denser, thus allowing for very accurate positioning, highly-immersive experiences, smarter autonomous objects, etc. The exploitation of new and wider bandwidths at higher frequencies is an obvious and promising solution towards significantly increased data rates and capacity in beyond-5G or 6G communication systems. The “sub-THz” spectrum from 90 to 300 GHz is definitively identified as a key enabler. An aggregated bandwidth of 58.6 GHz was identified in [2] as possibly available for terrestrial radio-communications between 90 and 200 GHz. Elaboration of future sub-THz systems is facing many challenges in particular at the PHY layer such as the strong propagation losses, or the increased phase noise (PN) w.r.t mmWave band, which are both considered in this paper. Due to the strong propagation constraints, the short-range connectivity is a relevant sub-THz target application. However, the huge available bandwidth can also serve the backhaul transport network, and offer the future capacity required by cloud-RAN, ubiquitous AI (artificial intelligence), etc. That is why the authors explore the feasibility, reliability and achievable data rates of such a backhaul solution, with specific focus on the propagation impact.

First, the paper addresses the design of robust communication from both receiver and transmitter perspectives. The optimum symbol detection criterion and the corresponding probabilistic demapper is derived for PN channel upon the maximum likelihood (ML) decision rule. We also propose a PN robust modulation scheme defined upon an efficient and structured constellation, adaptable to any signal-to-noise ratio (SNR) and PN variance. Second, the propagation channel properties are characterized and modelled to achieve a realistic evaluation of the proposed modulation. Only few sub-THz channel sounding campaigns have been published yet, as the equipments are new, complex and costly. Those recently realized inside a commercial hall [3], various indoor environments [4], a data center [5] or for outdoor-indoor penetration [6] are bringing valuable data that confirms the clear line-of-sight predominance, the channel sparsity and strong attenuations. Numerical simulation is a convenient solution to produce on-demand channel samples for any kind of scenario. The Volcano ray-based model [7], which has been updated up to the sub-THz frequencies, is employed in the present study to predict the propagation in two backhaul use cases: in-street outdoor, and inside a large venue. The performance of the proposed modulation scheme has been assessed considering this propagation data combined with highly-directive antennas and different phase-noise conditions.

The PN characterization and proposed modulation scheme are presented in section 2. The ray-based propagation model is described in section 3. Then both techniques are combined in section 4 to evaluate the performance of wireless outdoor and indoor backhaul scenarios. A conclusion is given in section 5.

## 2 Phase Noise and Proposed modulation

Oscillator PN in communications systems arises from the integration and amplification of noise sources within the circuitry by the phase-locked loop (PLL). Due to integration, PN presents a cumulative nature. Under the assumption that the oscillator is only subject to thermal noise, the oscillator PN is described with the superposition of a cumulative Wiener process (a Gaussian random-walk) and an uncorrelated Gaussian one. These stochastic processes respectively express the integration and amplification within the PLL of thermal noise. The spectrum of oscillator PN is in this case described by a colored characteristic (Wiener PN) and a white noise floor  $K_0$  (Gaussian PN). However, it has been shown in [8] and confirmed in [9] that the impact on communication performance of the Wiener PN is negligible in comparison to the Gaussian in case of large bandwidth systems. Subsequently, for sub-THz systems, the impact of oscillator PN on received symbols may be efficiently modeled with a Gaussian distribution. That is

$$r = s \cdot e^{j\phi} + n, \quad \phi \sim N(0, \sigma_p^2),$$

where  $r$  is the received symbol,  $s$  is the modulated one,  $\phi$  is the oscillator PN, and  $n$  is the thermal noise with spectral density  $N_0$ . In the rest of the paper, a medium PN level has been considered with  $\sigma_p^2 = 10^{-2}$ . This corresponds to a floor noise spectral density of -110 dBc/Hz for a channel bandwidth of 1 GHz.

The design of the optimum modulation scheme for the PN channels has been largely investigated in the literature [10]. However many works derive complex optimization problems to determine the shape of a constellation, we have consider a pragmatic approach supported by a theoretical framework. Under a high-SNR assumption, it can be demonstrated that the PN channel in the polar domain (amplitude/phase) is highly similar to an additive white Gaussian noise channel in the complex plan [11]. It follows that the optimum modulation, *i.e.* minimizing the symbol error probability, is the constellation that maximizes the minimum distance. Then for a fixed modulation order and average power, characterizing the optimal constellation may be interpreted as finding the densest sphere packing in the polar domain. Therefore, the optimal constellation is defined upon an hexagonal lattice in the polar domain. Nevertheless, for implementation considerations, it is relevant to exploit a rectangular lattice since the corresponding demodulation and binary labelling are greatly simplified with minor loss in performance. As a result, we propose the polar quadrature amplitude modulation (P-QAM) that will be considered as the modulation scheme throughout the performance assessment.

## 3 Ray-based sub-THz modelling

The Volcano ray-based propagation channel model has recently been extended to support the sub-THz spectrum between 90 and 300 GHz [7], and serves in the assessment of new technologies and scenarios. Comparison to measurements has not been possible yet. However, the predicted mechanisms rely on a physical calculation approach -Fresnel reflection, Uniform Theory of Diffraction (UTD) and knife-edge diffraction-, which are already exploited and validated in the 5G millimeter-wave (mmW) spectrum. Major mmW trends are supposed to persist: diffractions become negligible; critical blockage may come from environment details, in particular furnitures and trees; reflections are still strong except when impacted by local surface roughness.

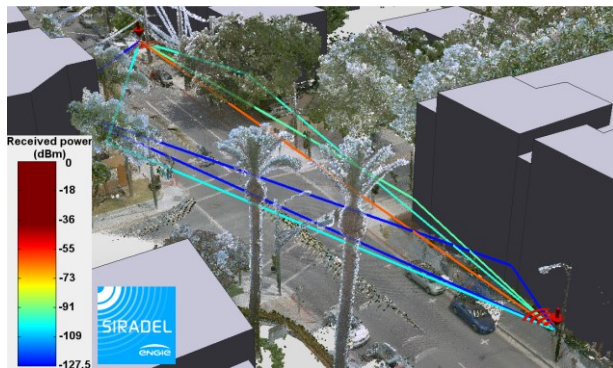


Figure 1: Propagation path withing LiDAR data

Parameter	Outdoor node-to-node	Indoor node-to-node	Indoor node-to-relay (DL)
Frequency band	150 GHz		
Signal BW	1 GHz		
Tx power/ch.	1 W	0.1 W	0.1 W
Tx antenna		25.0 dBi	
Rx antenna	25.0 dBi	25.0 dBi	8.0 dBi
Th. noise floor		-84.0 dBm	
Noise figure		10.0 dB	
Rx sensibility	-98.2 dBm	-98.2 dBm	-81.2 dBm
Implement. loss		3.0 dB	
Rain	12.5 mm/h	N/A	N/A
Adj. factor		[−5;+5] dB	

Table 1: System parameters

The validity range of the ITU attenuation models for rain and atmospheric gas [12], which are implemented in Volcano, includes the target sub-THz frequencies. Besides, the update of the dielectric materials properties (permittivity and conductivity) has been done by following a non-rigorous approach. In absence of reliable and generic sub-THz figures, we have decided to extend the application range of the ITU dielectric values [13 – Table 3] beyond the recommended upper limit, typically 100 GHz.

Volcano predicts 3D ray-paths from the combination of multiple reflections, transmission and diffractions, based on a fast ray-launching technique, the UTD and knife-edge diffraction coefficients. It applies to outdoor, indoor and mixed environments. As illustrated in Fig. 1, for the outdoor scenario presented in this paper, Volcano is taking benefit of a LiDAR point cloud representation. This data allow the model to evaluate the blockage and transmission losses due to the trees and street furniture in a more realistic way compared to conventional geographical database.

## 4 Backhaul evaluation result

### 4.1 System parameters

Mapping between SNR levels and spectral efficiency is derived from the previously described P-QAM modulation scheme and following assumptions. A perfectly synchronized single-carrier modulation is considered. The channel phase shift is perfectly estimated and corrected. A Forward Error Correction (FEC) scheme based on the 5G-NR LDPC with an input packet size of 1500 bytes is considered with a coding rate ranging from 0.3 to 0.9. The performance of the physical layer were first assessed to determine the best set of parameters: coding rate, modulation order and modulation shape given the SNR, the PN level and the targeted packet error rate of 10-2. Resulting spectral efficiency goes from 0.6 bps/Hz at -0.8 dB SNR, to 7.2 bps/Hz at 29.7 dB SNR.

The system is operating in the 150 GHz band, with a bandwidth of possibly several tenths of GHz, divided in 1-GHz channels. The effective bandwidth of the signal is 800MHz with a 20% overhead due to the control plane. The maximum reachable throughput is then 4.6 Gbps/channel. Parameters regarding the transmit power, antenna, and link budget are given in Table I for each simulated scenario. The adjustment factor in the last row of the table is used as a varying parameter to evaluate the sensibility of the simulated system to any change or uncertainty in the link budget. As an exemple, a positive adjustment can be used to assess the impact of a larger transmit power or reduced noise figure.

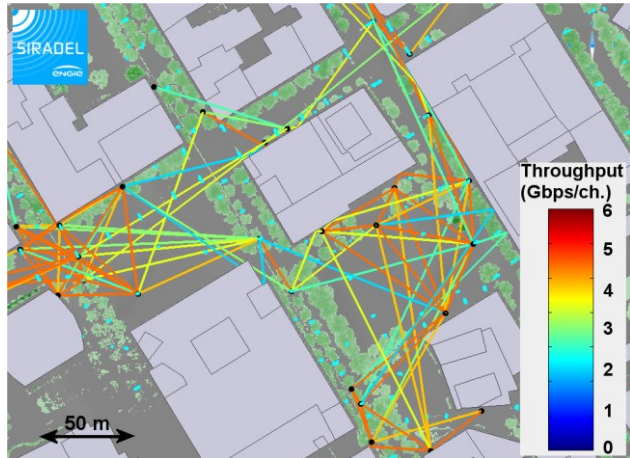


Figure 2 : Mesh links in the outdoor backhaul network

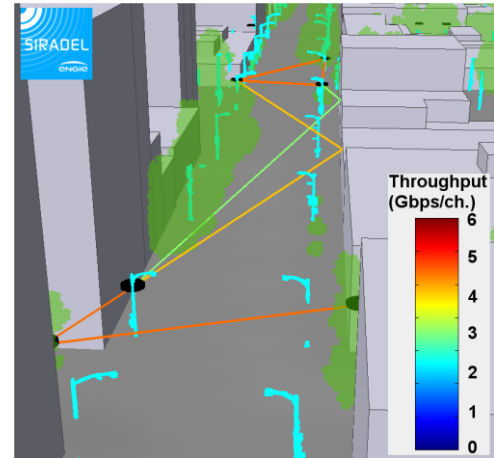


Figure 3 : Direct and indirect connections

### 4.2 In-street scenario

The in-street backhaul scenario is run in a dense-urban densely-vegetated environment, actually in San José downtown, California. The digital geographical data is composed of 3D vector buildings and a point cloud LiDAR data that includes trees and furnitures such as lampposts.

A subset of 134 lampposts in this area is used as virtual sub-THz device positions. Antennas are localized at 8 meters above the ground. All possible lamppost-to-lamppost links with range lower than 200 meters are computed at frequency 150 GHz, leading to a total of 1873 predicted links. First, the link visibility is determined: 136 line-of-sight (LoS) links; 553 vegetation obstructions; and 1204 building obstructions. A total of 585 links have sufficient SNR to establish a connection if antennas at both ends are perfectly aligned on the strongest propagation path. Fig. 2 shows the simulated connections with their achievable throughput in part of the study area; maximum throughput can be reached in clear LoS, while the vegetation significantly degrades the performance. We note that a few connections are allowed in building shadowed area due to indirect paths. Fig. 3 zooms on some particular links and displays the main propagation paths, either line-of-sight or reflected along a trajectory out of any tree's obstruction.

Fig. 4 gives statistics on the achievable throughput versus the distance between antennas, and for two different situations: 1) in case of LoS or tree's obstruction; 2) in case of a building obstruction (NLoS). In first case, 98% links with range below 25 meters reach a peak throughput greater than 4 Gbps/channel; the percentage drops to 81% and 52% for respectively the ranges ]25;50] and ]50;75] meters, due to more likely and longer obstructions. It further decreases below 35% when the range is longer than 75 meters. This result demonstrates that sub-THz hops longer than 75 meters can provide more than 4 Gbps/channel, but need to be carefully chosen, based on an accurate knowledge of the environment. Fig. 4 also gives the statistics for the Non-LoS links, and shows that indirect propagation paths can sometimes lead to high-throughput links, in particular for ranges below 75 meters, which may be very useful for creating a link between orthogonal streets or as a backup connection. Finally, in the last 175-200 meters range, the performance is strongly degraded for most of the predicted links; high-throughput connection is hardly possible.

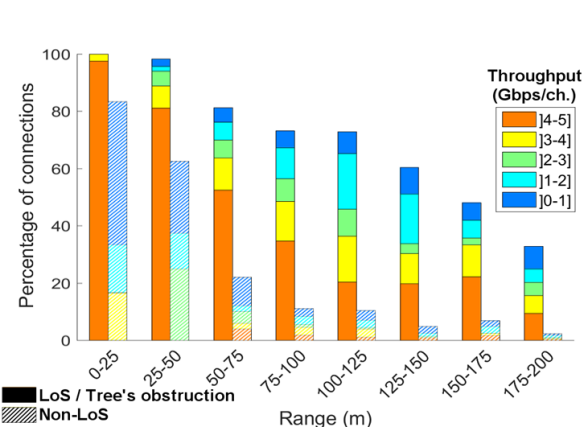


Figure 4: Percentage of links reaching a given throughput vs. distance.

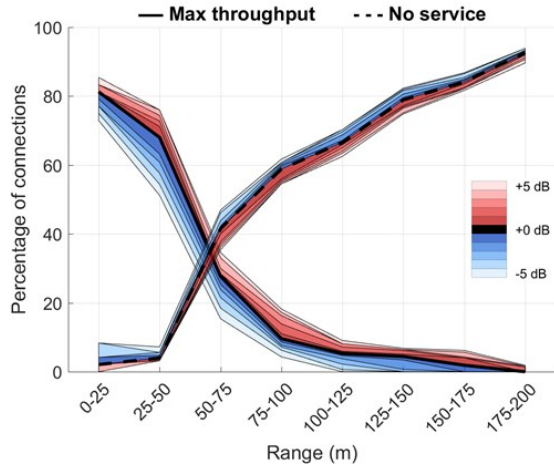


Figure 5: Percentage of links reaching a given throughput vs. link budget gain.

The sensitivity of those results to the considered link budget parameters is illustrated in Fig. 5, where the percentage of connections is plotted as a function of the distance and an additional gain in range [-5;+5] dB. A 4 dB adjustment in the link budget leads to 100% connection in the ]0-25] meters range, while 8% links in same range are losing connection with -5 dB adjustment. Besides, the [-5;+5] dB gain converts into maximum 25% variation in the high-throughput connection rate, as observed in the ]25-50] meters range.

Link diversity is a critical factor for reliability of such a network in order to optimize routing, to minimize interference, but also to combat temporary blockage on the best propagation path. In this study, the link diversity has been characterized by counting the average number of available connections per node. Fig. 7 gives the average number of connections as a function of a target peak throughput, and for both kinds of alignment approaches. As an example, the average number of connections above 1 Gbps/channel at any node of the backhaul network is 5.1, when the system aligns on the strongest path. Some improvement is observed when comparing the strongest-path alignment to the direct-path alignment; however, the clear direct propagation path is often the dominant component.

#### 4.3 Large venue scenario

The sub-THz transport network could also be deployed as a complement to the optical fiber inside large venues, e.g. airports, railway stations, stadium, campus, or commercial halls. While the optical fiber is distributing strong capacity in the different blocks of the venue, the wireless mesh backhaul may be the final link to some fixed, portable or even mobile (e.g.. flying) access points. If combined with efficient auto-alignment and dynamic routing algorithms, the sub-THz transport layer can adapt to changes e.g. related to densification, maintenance, event, or construction works.

The strong obstruction losses oblige the sub-THz hops to be deployed in a clear space, typically in large rooms or open areas, above most furniture and bodies. Fiber relays can be used to extend the network coverage to another room.

The evaluation study is carried out in a model of commercial hall. Fig. 6 shows the two-floor 120m×80m building, which is composed of a large entrance area, large alleys with few obstacles (booths, vegetation, and pillars), and a succession of shops. Each floor is five meters high. A mesh sub-THz network has been designed to feed the wireless access points located at the first floor and entrance area. Two different kinds of access points

are considered: those inside the shops, which require a sub-THz relay to be positioned on the outer surface of the shop window; and those connected to a portable/mobile sub-THz relay installed outside the shops.

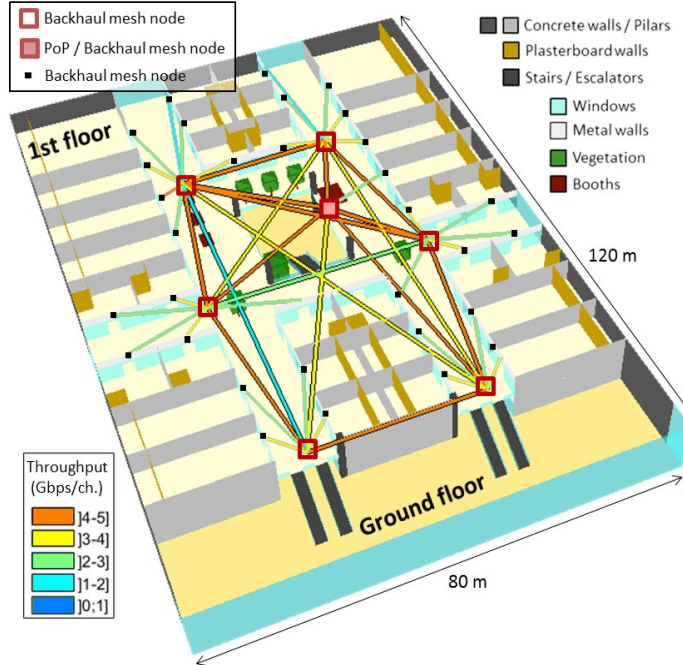


Figure 6: Main connections between mesh nodes, and to the shop-relays

The sub-THz backhaul network is composed of 6 mesh nodes at height 4 meters, i.e. below the cables, pipes or lights installed below the roof, but above most ground obstacles; one of those nodes is directly connected to a fiber Point of Presence (PoP). The following kinds of radio link are evaluated: 1) node to node; 2) node to the fixed shop relays at height 4 meters; 3) node to any portable/mobile relays at height 2 meters. The sub-THz system parameters are given in Table I. The propagation model is enabling a maximum of two reflections and one diffraction along each ray path. Reflections on the ceiling or floor surfaces are not allowed as they are likely to be obstructed. Shop windows are assumed as opaque surfaces for the considered frequency.

The peak throughput on each radio link is predicted in two different ways: either the antennas are aligned on the direct-path, or aligned on the strongest propagation path. Fig. 7 depicts the latest calculated throughput for all mesh connections and the best shop-relay connections. Every mesh node is linked to the PoP with maximum two hops having a peak throughput greater than 4 Gbps/channel. All shop-relays are attached to the mesh network with more than 2 Gbps/channel peak throughput.

The right plot in Fig. 8 indicates how many different propagation paths can be used by the system (with automatic antenna alignment) to connect a node and reach a given peak throughput level. When aggregating all paths from all neighbor mesh nodes, the average number of potential paths that offer more than 1 Gbps/channel at a mesh node is 123, which might guarantee very good service availability.

Finally, the sensitivity of those results to the considered link budget is illustrated in Fig. 8, where the average number of connections is plotted as a function of an adjustment factor in range [-5;+5] dB. The shop-relays reliability is significantly affected by this adjustment factor. The average diversity at 2 Gbps/channel is 1.8 with initial settings; it goes to 3.6 when adding 5dB, and degrades to 1.2 when removing 5 dB. Besides, thanks to many LoS links and strong reflections, the considered mesh network remains viable with 5dB degradation but still 3.4 connections per node.

## 5 Conclusion

The presented simulation studies demonstrate the feasibility of sub-THz mesh backhaul networks, using a PN-robust modulation scheme, and considering real propagation constraints. This study shows the potential of the sub-THz technology to reach multi Gbps link in indoor and outdoor in-street typical scenarios. This work must be continued for other applications such as kiosks or hotspots, considering other antenna configurations and propagation constraints.

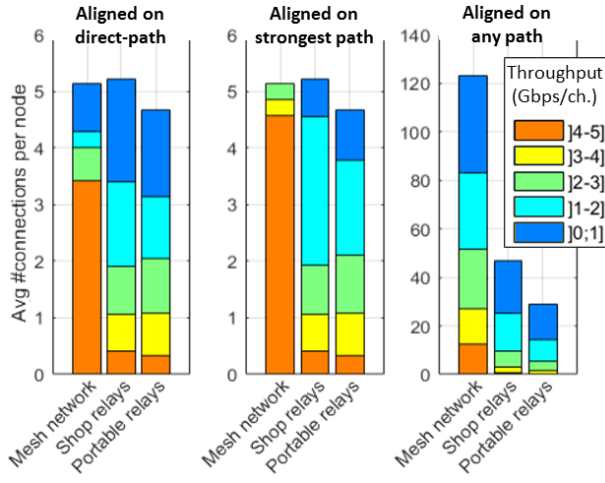


Figure 7: Number of connections per throughput range

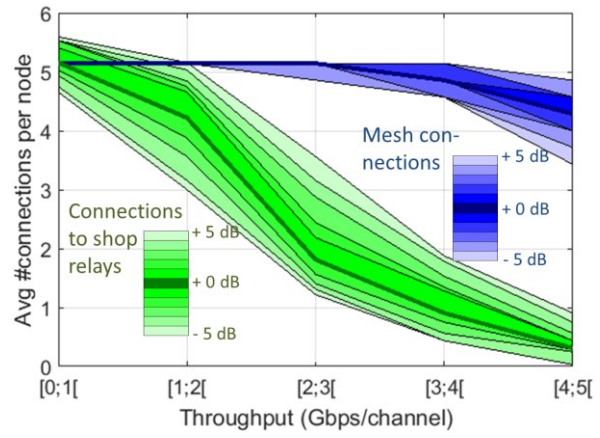


Figure 8: Number of connections per throughput range vs. link budget adjustment

## Acknowledgment

The research leading to these results received funding from the French National Research Agency (ANR-17-CE25-0013) within the frame of the project BRAVE.

## References

- [1] M. Latva-aho, and K. Leppänen, *Key drivers and research challenges for 6G ubiquitous wireless intelligence*, White paper, Sept. 2019.
- [2] Y. Corre, G. Gougeon, J-B. Doré, S. Bicaïs, B. Miscopein, M. Saad, J. Palicot, F. Bader, E. Faussurier, “Sub-THz Spectrum as Enabler for 6G Wireless Communications up to 1 Tbit/s”, 1st 6G wireless summit, Levi, Finland, March 2019.
- [3] S. Nguyen, J. Jarvelainen, A. Karttunen, K. Haneda and J. Putkonen, “Comparing Radio Propagation Channels Between 28 and 140 GHz Bands in a Shopping Mall”, EuCAP 2018, London, UK, Apr. 2018.
- [4] L. Pometcu and R. D’Errico, “Channel Model Characteristics in D-Band for NLOS Indoor Scenarios”, EuCAP 2019, Krackow, Poland, March 2019.
- [5] J. M. Eckhardt, T. Doeker, S. Rey, and T. Kürner, “Measurements in a Real Data Center at 300 GHz and Recent Results”, EuCAP 2019, Krackow, Poland, March 2019.
- [6] T. Xing, and T. S. Rappaport, “Propagation Measurement System and Approach at 140 GHz—Moving to 6G and Above 100 GHz”, GLOBECOM 2018, Abu Dhabi, UAE, Dec. 2018.
- [7] G. Gougeon, Y. Corre and M. Z. Aslam, “Ray-based Deterministic Channel Modelling for sub-THz Band”, Int. workshop on Enabling Technologies for THz Comm., Istanbul, Turkey, Sept. 2019.
- [8] M. R. Khanzadi, D. Kyulenstierna, A. Panahi, T. Eriksson, and H. Zirath, “Calculation of the performance of communication systems from measured oscillator phase noise,” *IEEE Transactions on Circuits and Systems I: Regular Papers*, May 2014.
- [9] S. Bicaïs, and J.-B. Doré, “Phase Noise Model Selection for Sub-TeraHertz Communications,” GLOBECOM 2019, Waikoloa, USA, Dec. 2019.
- [10] R. Krishnan, A. G. i Amat, T. Eriksson, and G. Colavolpe, “Constellation Optimization in the Presence of Strong Phase Noise,” *IEEE Transactions on Communications*, Dec. 2013.
- [11] S. Bicaïs, J.-B. Doré, and J.-L. Gonzalez Jimenez, “On the Optimum Demodulation in the Presence of Gaussian Phase Noise,” ICT 2018, St Malo, France, June 2018.
- [12] ITU-R P.1238-9, *Propagation data and prediction methods for the planning of indoor radiocommunication systems and radio local area networks in the frequency range 300 MHz to 100 GHz*, June 2017.
- [13] ITU-R P2040-1, *Effects of building materials and structures on radiowave propagation above about 100 MHz*, July 2015.

## **Performances en puissance et délai pour des communications optiques sans fil dans un cockpit**

### ***Power and Delay performance of Optical Wireless Communication inside Aircraft Cockpit***

**Steve Joumelli-Demeffo<sup>1</sup>, Stephanie Sahuguede<sup>1</sup>, Anne Julien-Vergonjanne<sup>1</sup>, Pierre Combeau<sup>2</sup>, Lilian Aveneau<sup>2</sup>, Hervé Boeglen<sup>2</sup>, Damien Sauveron<sup>1</sup>**

<sup>1</sup> University of Limoges, CNRS, XLIM UMR 7252, F-87000 Limoges, France, {steve.joumelli-demeffo ; stephanie.sahuguede ; anne.julien-vergonjanne ; damien.sauveron}@unilim.fr

<sup>2</sup> University of Poitiers, CNRS, XLIM UMR 7252, F-86000 Poitiers, France {pierre.combeau ; lilian.aveneau herve.boeglen}@univ-poitiers.fr

**Keywords/Mots clés :** *Li-Fi, optical wireless communication, channel modeling, channel access control*  
*Li-Fi, communications optiques sans fil, modélisation du canal, méthodes d'accès*

#### **Abstract/Résumé**

This work investigates optical wireless links between four pilot headsets and access point inside aircraft cockpit for audio and physiological data transmission. We determine the impact of optical wireless channel on DCF (Distributed Coordination Function) control mechanism performance. The results show the trade-offs between emitted optical power and communication delay.

Ce travail présente l'étude de liaisons optiques sans fil entre les casques des pilotes et le point d'accès à l'intérieur d'un cockpit d'avion pour la transmission de données audio et physiologiques. Nous déterminons l'impact du canal optique sans fil sur les performances du mécanisme d'accès au canal DCF (Distributed Coordination Function). Les résultats montrent les compromis entre la puissance optique émise et le délai de communication.

#### **1 Introduction**

The aeronautical industry is constantly seeking to introduce new technologies to improve aircraft performance and their ecological impact, but also to increase the safety and comfort of crews and passengers. Thus, the use of wireless communication technologies to replace aircraft cables can help reduce weight and therefore fuel consumption and CO<sub>2</sub> emissions but can also improve crew efficiency [1]. Indeed, the majority of pilots are now looking for high-performance wireless headsets because they contribute to comfort, especially for long-haul flights, which require the pilot constantly wearing his headset for long hours. Wired headsets are well known to cause pain and reduce mobility. This contributes to increase pilot stress, which can be critical, especially for operations where the safety margin is already low (for example, take-off or landing). Wireless connectivity in the cockpit therefore makes perfect sense to support pilot operations and decision-making aimed at improving the performance and efficiency of the crew on duty, reducing the workload and the risk of human error. The wireless communications currently available in the cockpit are Wi-Fi and Bluetooth. Although effective, these solutions suffer from some drawbacks. Due to radio waves propagation, one problem is that the signal can be scrambled or listened to [2]. In addition, radiofrequencies (RF) are sensitive to electromagnetic interference. These issues render RF technologies unsuitable for such a sensible environment as the cockpit where safety and security are paramount.

Optical wireless communication (OWC) is today the most promising candidate capable of overcoming these disadvantages because it provides a secure mode of communication [3-6]. Indeed, optical waves cannot pass through walls or opaque objects. Thus, unlike RF communications, it is very difficult to hack the link and take control. In addition, the use of optical wavelengths guarantees the absence of electromagnetic interference with other electronic devices. However, these advantages can also constitute limitations because the range is limited and the performances are very sensitive to blockages. Thus, one of the main challenges in airplanes context relies on ensuring coverage, requiring a thorough analysis of the communication channel. Several projects have studied the use of OWC technology in aircraft, generally for applications and services relating to passengers in the cabin [7-11]. For example, the scenarios studied concern entertainment [7], video broadcasting [8], communications between passengers [9], and even medical surveillance of travelers [10]. In [11] the infrared optical wireless path loss inside an aircraft cabin is estimated. However, the optical channel in the cockpit has not yet been much studied, this environment having a particular geometric complexity and expected connection blockages due to the pilot's movements. In [12], we have studied for the first time the OWC channel between optical transceivers included on two pilot headsets and an access point located at the cockpit ceiling. This work was based on a Monte Carlo ray-

tracing methodology, from the 3D representation of an aircraft cockpit including pilot and copilot body models and head movements. Based on the channel analysis we have determined the channel path losses corresponding to 100% link reliability. Here, we have first extended our study presented in [12] by considering four pilots inside the cockpit whose heads and bodies can move. Based on channel analysis, our aim is to investigate network performance for audio transmissions between pilot headsets and one access point located in the cockpit. As the brightness in the cockpit must be greatly reduced during critical flight phases, the visible band is not appropriate. Therefore, optical wavelengths in the infrared (IR) range are used. Moreover, one main specification for audio headset is to guarantee sufficient autonomy to ensure long-haul flights. In order to satisfy this constraint, typical single carrier modulation schemes for OWC systems which are easy to implement and power efficient are considered [13, 14]. In addition, these modulation schemes are known to be suitable for low-medium data rate applications such as audio transmissions. Furthermore, considering that pilots can use the headset in other environments than the cockpit, we are interested in the IEEE 802.11 channel access standard such as carrier-sense multiple access with collision avoidance (CSMA/CA). Indeed, currently there are standardization efforts on the commercial development of OWC technology, in particular Li-Fi [15], which aim at interoperability with Wi-Fi standards. In this work, we will consider the DCF (Distributed Coordination Function) algorithm with RTS/CTS (Request To Send /Clear to Send) method [16]. One main impact of channel access method is on delay between the acoustic signal and the audio management unit of the aircraft, which can decrease as data rate increases, considering a given data packet size. On the other hand, we have also to consider limitations on data rate to achieve a given performance in terms of Bit Error Rate (BER) linked to autonomy and IR eye safety constraints.

Consequently, the main contribution of this paper is to highlight the trade-offs between minimal optical emitted power needed to attempt a given BER for typical OWC modulation schemes [13] and successful communication delay, considering a network based on IEEE802.11 channel access mechanism with four optical wireless pilot headsets and one access point inside the cockpit. The remainder of the paper is organized as follows. Section 2 presents the description of cockpit environment including crew presence and the extended channel analysis. We then introduce in section 3 the used modulation performance related to optical emitted power and the definition of communication delay regarding DCF method. Section 4 shows the results and discussions on trade-offs before conclusion.

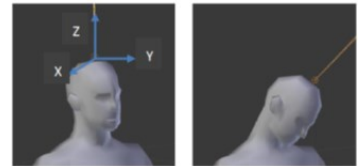
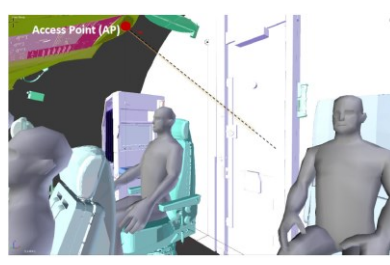
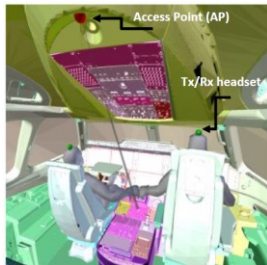


Figure 1: AIRBUS A350 cockpit, AP and pilot/co-pilots position

Figure 2 : Tx/Rx headset orientation on the head top

## 2 Cockpit environment and channel model

### 2.1 Environment description

The studied environment is the cockpit of an AIRBUS A350 aircraft. In this environment, we are focusing on a scenario using optical wireless links to ensure the connectivity of the headsets worn by the crew (pilot, co-pilot, third and four occupants). We consider the IR bidirectional link between the transceivers (Tx/Rx) integrated on the headset and those located on the cockpit ceiling at the access point (AP). There are two pairs of transceivers on AP. The first one is situated at about 1m from the top of the pilot and co-pilot heads (see Fig. 1, with orientation in grey line). The second pair is at the same location but with orientation towards the cockpit door between the two third and four occupant at the cockpit rear (Fig. 1 with orientation in dotted line). In addition, note in Fig.1, that pilot and co-pilot seats have different settings corresponding to the two extreme possible positions. The pilot is the farthest from the control panel (the face is at 60 cm) at the lowest height (the top of the head is 40 cm under the ceiling and 1.17 m above the floor). The co-pilot is the closest to the control panel (the face is at 45 cm) at the highest height (the top of the head is 15 cm under the ceiling, 1.30 m above the floor). For the headset, we have considered one location of Tx/Rx on the top of pilot head. They are oriented parallel to user spine (see Fig. 2), but it can randomly change according pilot movements, inducing link attenuation or blockages.

### 2.2 Channel model

To determine the channel impulse response for uplink between the headset and the AP, the reverse in downlink,

we adopted a modeling approach based on a stochastic Monte Carlo method, associated with the ray-tracing algorithm [12, 17]. This methodology allows determining the received power for Line-Of-Sight (LOS) and non-LOS (NLOS) paths, i.e. reflected paths over all the elements inside the cockpit. Actually, because of random movements of pilot, the LOS link condition cannot always be fulfilled. Thus, we have developed a detailed 3D geometric model of the cockpit (illustrated in Fig.1) generated from a CAO file provided by AIRBUS, and then imported into our software [12]. In addition, we have included the pilots' bodies, fully articulated and animated using the Blender software [18]. The mobility scenario we have studied considers that a pilot first looks ahead and then turns his/her head to the left, then tilts it forward, and then turns it to the right before returning it to its initial position. This is illustrated in Fig.3 (a). In addition, we have also simulated the case where a pilot has to lean to the ground to pick up a fallen object (see Fig.3 (b)).



Figure 3: (a) Head movement (b) Body movement

Each of these discretized movements induces different IR links according to the orientation changes of the headset transceivers. So this corresponds to a set of impulse responses  $h(t)$ . One of the main parameters characterizing the optical channel is the DC gain  $H_0$ , which is related to  $h(t)$  by [13] :

$$H(0) = \int_{-\infty}^{+\infty} h(t)dt = H_0 \quad (1)$$

Other features are time dispersion parameters related to  $h(t)$  length and mean delay spreading. Here, all the surfaces in the scene and the bodies are considered as perfectly diffuse and are consequently modeled using a Lambertian Bidirectionnal Reflectance Distribution Function (BRDF) [17]. The reflection coefficients are set to 0.5, which is the mean value between absorbent and perfectly reflective material [12]. The receivers on headset and AP are generic IR photodiodes with Field-Of-View of 60° and surface detection of 7mm<sup>2</sup>. Moreover, the optimal half-power angles of emitters on headset, respectively on AP, are of 60°, respectively 40°, as established in [12]. With these parameters, we have verified that the temporal dispersion induced by the reflected paths can be ignored for data rate lower than 20 Mbps. In the following, we only focus on the DC gain and neglect inter-symbol interference.

	uplink Head movement	uplink Body movement	downlink Head movement	downlink Body movement
Pilot	-70.3	-69.4	-69.7	-67.2
Co-pilot	-72.1	-71.9	-71.2	-70.1
Pilot rear	-66.5	-67.9	-65.5	-68
Copilot rear	-61.1	<b>-72.2</b>	-52.7	<b>-74</b>

Table 1: Minimum DC gain (dB)

To investigate the performance of the network constituted of the 4 headsets and the access point, we consider the case where the gain value is the most reliable among all the possible values linked to the movements of the pilots. This corresponds to the lowest gain values obtained in each case. Table 1 reports the minimum  $H_0$  values in dB. We first observe that the head movements are the most penalizing for the headsets worn by the pilot and co-pilot while for the occupants in the rear it is the body movements. In addition, for pilot and co-pilot headsets the lowest DC gains are obtained in uplink whereas this is for the downlink for rear pilot and rear co-pilot. Finally, considering all the cases, the worst corresponds to the bidirectional link with the rear co-pilot headset (in bold in Table 1).

### 3 Emitted power and communication delay

In this part, we first consider the emitted power required to attempt a given BER for classical optical modulation schemes. Then, to determine the delay, we describe the multi-user medium access control mechanism that is DCF algorithm with RTS/CTS method. As the delay diminishes with the data rate, while the required power increases, our objective is to analyze the compromise for OWC-based audio transmission inside aircraft cockpit.

### 3.1 Emitted power

The channel analysis has been performed in previous section in term of optical DC gain  $H_0$ . For a fixed average emitted power  $P_t$ , the SNR is expressed as [13]:

$$SNR = \frac{H_0^2 P_t^2 R^2}{2qI_B \cdot B} \quad (2)$$

Where  $R$  is the photodiode responsivity set to 1 A/W in the following,  $q$  is the electron quantum charge and  $B$  the bandwidth of the modulated signal equal to the data rate  $R_b$ . For indoor environments, a classical assumption is to consider the noise as Additive White Gaussian Noise (AWGN) with power linked to induced ambient current  $I_B$  whose typical values is 200  $\mu$ A for  $I_B$  [19].

Moreover, BER performance of typical modulation schemes depends of SNR. OOK (On-Off Keying) modulation is the basic modulation for OWC communication systems due to its simple implementation. The  $BER_{OOK}$  is expressed as follows:

$$BER_{OOK} = \frac{1}{2} erfc\left(\sqrt{\frac{SNR}{2}}\right) \quad (3)$$

As the use-case of audio headset needs power autonomy, we also study a power-efficient modulation scheme, standardized for OWC, which is L-level PPM (Pulse Position Modulation). L-PPM maps M bits of binary data into a single pulse placed at one of the  $L=2^M$  possible positions or slots. It has been shown [6], that the  $BER_{L-PPM}$  is obtained from:

$$\begin{cases} BER_{L-PPM} = \frac{\frac{L}{2}}{L-1} P_{sye-PPM} \\ P_{sye-PPM} = 1 - (1 - P_{sle-PPM})^L \\ P_{sle-PPM} = \frac{1}{2} erfc\left(\sqrt{\frac{LM SNR}{4}}\right) \end{cases} \quad (4)$$

Where  $P_{sye-PPM}$  is the symbol error rate and  $P_{sle-PPM}$ , the slot error probability.

By exploiting the expressions (3) and (4) for OOK and L-PPM, we can determine the targeted values of SNR for a given BER performance. Then, using the values of Table 1 for DC-gain and equation (2) it is possible to obtain the requested  $P_t$  value for the studied system according the data rate  $R_b$ .

### 3.2 Communication delay

To ensure multi-user communication, we propose an approach based on 802.11 medium access control mechanism. We are interested in the DCF basic method, which is used for 802.11 devices [16], and investigated for Li-Fi [20]. The DCF method is known as Carrier Sense Multiple Access with Collision Avoidance (CSMA/CA) mechanism. With the basic DCF, if the channel is free for the transmitters, each one randomly chooses a waiting time called backoff contention windows (CW), which is in the interval [CWmin, CWmax]. The waiting time is thus expressed in number of slot time ( $N_s$ ) defined by the standard (see Table 2). As long as the channel is detected idle for a slot time, the backoff is decreased by one. The communication begins when it is to zero if the channel is free. When the channel is busy, the timer counter is blocked and resumes when the channel is inactive again for at least one slot time. One strong limitation of DCF arises from the obligation to send a request to the physical layer to know if the channel is free. Indeed, the node has to be able to listen the channel. This is the well-known issue of hidden nodes, which can be relaxed by the use of RTS/CTS mechanism which is optional in WLANs but mandatory in Li-Fi networks [20]. The compromise is additional exchanges introducing transmission overhead. The scenario of the RTS/CTS process is illustrated in Fig.4. The sending node uses an RTS frame for the receiver node after a distributed inter-frame space (DIFS) waiting time. The other nodes present in its coverage area receive this frame and initialize their NAV (Vector Allocator Network) counter. During NAV time, they know that they cannot transmit frames at the risk of causing collisions. The receiving node responds after a short inter-frame space (SIFS) with a CTS frame. Other nodes present in its CTS coverage area initialize their NAV. If the listening of the channel goes well, the sending node waits for the SIFS duration and sends a data frame. An ACK acknowledgment is received after a short SIFS period if the transmission is correct. Table 2 contains the specifications for the DCF method with RTS/CTS that we consider, where  $R_b$  is the PHY data rate. The values of RTS , CTS ,ACK and data take into account the PHY overhead. The metrics usually used to analyse the network performance are throughput

and delay. We use an analytical approach to evaluate these criteria, based on the Bianchi's [21] model and its extension proposed in [22]. In these models, the slot time duration indicates the time during which a node needs to detect the transmission of other nodes [22].

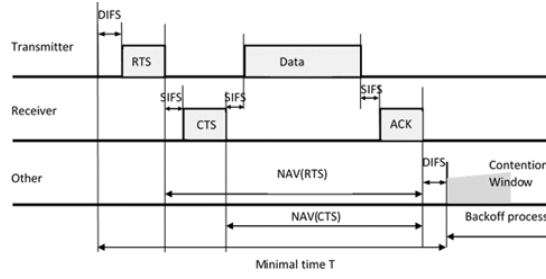


Figure 4: Principle of DCF mechanism with RTS/CTS

Attribute	Values
RTS (s)	288(bits)/ $R_b$
CTS (s)	240(bits)/ $R_b$
ACK (s)	240(bits)/ $R_b$
Data (s)	(MPDU+128) (bytes)/ $R_b$
Media access control Protocol Data UnitMPDU (bytes)	[0;2500]
DIFS ( $\mu$ s)	26
SIFS ( $\mu$ s)	10
SlotTime ( $N_s$ ) ( $\mu$ s)	8
CWmin (integer)	63
CWmax (integer)	1023

Table 2: DCF specification

It is assumed that a node transmits in a slot time randomly chosen with a probability  $\tau$ . The packet been transmitted experiences a collision with a probability  $p$ . These two parameters are the main features of Binary Exponential-Backoff (BEB) algorithm in DCF [21]. Considering  $m$  attempts, the probabilities  $\tau$  and  $p$  are given by:

$$\begin{cases} \tau = \frac{2}{1 + CW + pCW \sum_{i=0}^{m-1} (2p)^i} \\ p = 1 - (1 - \tau)^{n-1} \end{cases} \quad (5)$$

Where  $n$  is the number of nodes. This assumes that at least one of the  $(n - 1)$  remaining nodes transmits in a given slot time. The probability  $P_{tr}$  that there is at least one transmission in the considered slot time is:

$$P_{tr} = 1 - (1 - \tau)^n \quad (6)$$

The probability  $P_s$  that a transmission occurring on the channel is successful is given by:

$$P_s = \frac{n\tau(1 - \tau)^{n-1}}{P_{tr}} \quad (7)$$

During the mean time  $T_{succ}$ , the channel is detected busy due to a successful transmission. In addition, during the average time  $T_{col}$ , the channel is detected as busy because a collision occurred during the transmission attempt [21]:

$$\begin{cases} T_{succ} = RTS + CTS + Data + ACK + 3SIFS + DIFS \\ T_{col} = RTS + DIFS + SIFS + CTS \end{cases} \quad (8)$$

For reasons of simplification, we have supposed that there is no collision, so  $p = 0\%$  and therefore a successful transmission from the first attempt ( $m = 1$ ). This is a reasonable approximation because we are studying a network with a very low number of nodes.

In this case, the delay  $D_{succ}$  of a successfully transmitted packet can be obtained from [21]:

$$D_{succ} = L_{slot} N_{slot} \quad (9)$$

$L_{slot}$  is the average length of a slot time which and  $N_{slot}$ , the average number of time slots for a successful packet transmission.

$L_{slot}$  is expressed as follows:

$$L_{slot} = P_{idle} N_s + P_{succ} T_{succ} + P_{col} T_{col} \quad (10)$$

$P_{succ}$  and  $P_{col}$  are respectively expressed as :

$$\begin{cases} P_{succ} = P_{tr} P_s \\ P_{col} = P_{tr} - P_s \end{cases} \quad (11)$$

The probability of having a randomly chosen idle slot  $P_{idle}$  is obtained from:

$$P_{idle} = 1 - P_{tr} \quad (12)$$

$N_{slot}$  is expressed as follows:

$$N_{slot} = \frac{(1 + CW)(1 - 2p) + CWp(1 - (2p)^m)}{2(1 - 2p)(1 - p)} \quad (13)$$

In the following, we determine the successful delay  $D_{succ}$  defined in (9), using the DCF parameters of table 2.

## 4 Performance analysis

In order to evaluate performance considering both PHY and MAC layer metrics, we determine the trade-offs between the emitted power and the delay corresponding to a successful packet transmission. For this aim, we first consider the packet error rate (PER) defined by:

$$PER = 1 - (1 - BER)^N \quad (14)$$

The BER is a PHY layer metric, linked to the optical emitted power. The number of bits N is the packet size, a MAC layer parameter. Thus, PER metric is considered as a cross-layer PHY/MAC metric from which we will be able to discuss on the trade-offs between emitted power and delay of successful transmission.

### 4.1 Emitted power $P_t$ for a target quality of service

From (3)-(4), we can compute the BER as a function of the SNR according OOK and L-PPM modulations. Using (1), we then determine the value of  $P_t$  required to reach a given SNR so BER, according data rate  $R_b$ . In this section, we consider the worst DC gain values reported in Table 1 (values in bold) for uplink and downlink. Considering the maximal MPDU size from specifications reported on Table 2 (2500 bytes, so N=2500\*8 bits) and a targeted  $PER$  of  $10^{-3}$ , this corresponds to a BER of around  $5 \times 10^{-8}$ . For this BER value, the minimal average emitted power  $P_t$  is determined as a function of the data rate and reported in Fig.5 for OOK and 4-PPM modulations.

As expected, for a given performance, increasing the data rate  $R_b$  requires increasing the emitted power  $P_t$ . In addition, we can note that the required power with OOK modulation is more important than with a 4-PPM for both uplink and downlink configurations. This permits verifying power efficiency of 4-PPM modulation over OOK. For example, for  $R_b=1\text{Mbps}$ , the required power is 365mW with 4-PPM and 710mW with OOK for the uplink. Another way to interpret this curve is to analyze the data rate for a given transmitted power, which is much more important with 4-PPM than with OOK. For example, for an emitted power of 300mW, the data rate in uplink for OOK is around 180 kbps whereas it is of 670 kbps for 4-PPM, so almost multiplied by a factor 4. In addition, it can be noted that the power required is higher for the downlink than for the uplink. Indeed, the DC gain  $H_0$  considered is lower in downlink than in uplink. This observation has to be taken into account as we use infrared waves. Indeed, emitted power is limited by the eye safety criterion defined in the available standards. For laser equipment, the basic standard is the IEC 60825-1[23], for lamps and LEDs, it is the IEC 62471 [24]. Another important performance indicator depending on the data rate is the transmission delay, as presented in the next section.

### 4.2 Successful transmission delay for a target quality of service

As described from part 3, the transmission delay depends on data rate and on network parameters. The network is constituted of the four pilots and the AP. Results are reported in Fig.6, as a function of the data rate  $R_b$  for network parameter values summarized in Table 3 and for the two extreme contention window values CW equals to 63 and 1023. We first observe that as expected, the delay  $D_{succ}$  decreases when  $R_b$  increases. For a data rate of 2Mbps, it reaches values around 45ms, respectively. 55ms, for  $CW_{min}$ , respectively.  $CW_{max}$ . In this case, the contention window variation has an impact of around 18% on the delay. For lower data rates, the delay increases, but the relative variation is lower. For example, for  $R_b = 0.6\text{Mbps}$ , the delay varies from 155ms to 178ms according CW. This corresponds to 13% of increase between the minimal CW value and the maximal one. To reduce the delay, the data rate can be increased, but the value of the CW window has a slightly larger effect. In addition, the increase in data rate is limited by the power value as indicated in part 4.1. Therefore, we have compromises between power and delay. To illustrate the trade-offs between emitted power and successful transmission delay, we consider in this analysis 4-PPM modulation with an emitted power of  $P_t=300\text{mW}$ . From Fig.5, the maximal achievable data rates for a targeted PER of  $10^{-3}$  in downlink, respectively uplink, are 290 kbps, respectively 670 kbps. Considering these two data rates, we have reported in Table 4 the delay obtained with maximal MPDU size of 2500 bytes, for the two extreme values of CW. We can observe that the minimal reachable delay in this case is 138ms. We analyse in the following the impact of PER value and higher order L of PPM modulation on the emitted power, thus on the delay.

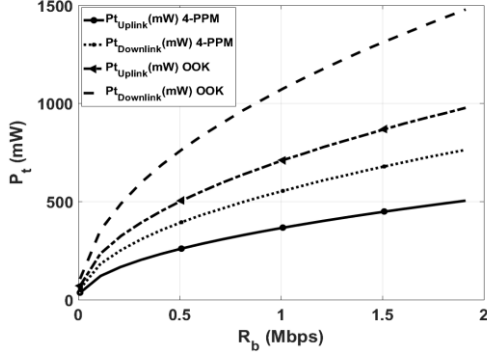


Figure 5:  $P_t$  according  $R_b$  PER=  $10^{-3}$ , MPDU = 2500 bytes

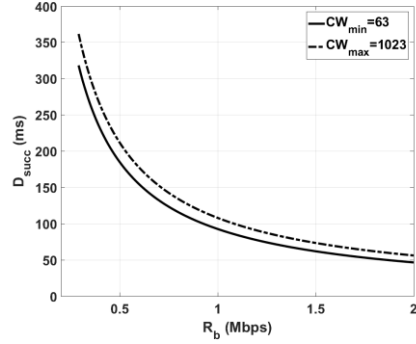


Fig.6  $D_{succ}$  according  $R_b$ . MPDU=2500 bytes,  $CW_{min}=63$  and  $CW_{max}=1023$

Attribut	Values
$n$	5
$m$	1
$p$	0%

Table 3: Network parameters

	Date rate	$CW_{min}=63$	$CW_{max}=1023$
	MPDU 2500 bytes	290 kbps 670 kbps	318 ms 138 ms

Table 4: Delay  $D_{succ}$ , 4-PPM modulation,  $P_t=300mW$

#### 4.3 Impact of targeted PER and higher order modulation

As an example, we focus here on the uplink. We have reported in Fig.7 the minimal emitted power required to reach different targeted PER with 4-PPM modulation and with 16-PPM for targeted PER of  $10^{-3}$ . As expected, we can observe that the power required with a given data rate is decreased when the targeted PER is higher, and even more when using a 16-PPM instead of the 4-PPM. For example, for the data rate of 670 kbps (corresponding to a PER of  $10^{-3}$  with  $P_t=300mW$ ) we can note that emitted power is equal to 320mW for PER= $10^{-4}$ , reduced to 250mW for PER= $10^{-2}$  and even to 110mW for a 16-PPM modulation with PER= $10^{-3}$ . In addition, we can determine from Fig. 7 for each configuration the corresponding maximal reachable data rate and then by using Fig.6, the corresponding delay for a given emitted power. Values are reported in Table 5 for  $P_t=300mW$ . For the 16-PPM configuration, it is not possible to extract results from Fig. 7 due to the range of the axis, but the analysis was done following the same process. We can observe from values in Table 5 that reducing the constraint on targeted PER by one decade (PER= $10^{-2}$ ) permits lowering the delay by approximately 30%. Furthermore, changing the order of the modulation to 16-PPM has a much more significant impact (delay reducing by 85%), but at the cost of an implementation complexity increase and potential Inter Symbol Interference (ISI) due to a greater required bandwidth.

## 5 Conclusions

In this article, we have studied a network composed of four audio headsets connected in optical wireless and an access point to the cockpit ceiling of an Airbus A350. The main objective was to study the trade-offs as a function of the data rate and linked to the physical channel parameters, in particular the transmission power, and those resulting from the channel access method based on DCF with RTS / CTS. We first studied the modelling of the channels for the uplink and downlink between the headsets and the access point. This contribution was based on the advanced cockpit simulation from a 3D geometric model of the cockpit. In addition, the presence of the pilots and their movements was taken into account. Simulation of the channel by ray tracing associated with a Monte-Carlo method allowed determining the gain values of the channel in a worse case but with 100% reliability in uplink and downlink. The results show that the worst case corresponds to the position of the rear co-pilot. Based on these results, we then performed a combined analysis of the transmitted power and the delay for successful communication. The minimum optical power necessary for a given performance has been evaluated for conventional OWC modulation schemes (OOK and PPM) as a function of the data rate. Likewise, we have studied the delay values for successful communication in the network for the studied protocol. The approach has highlighted the trade-offs between power and delay linked to maximal achievable data rate for a given performance. Finally, we have shown that increasing the order of the modulation is the most effective way to reduce the delay but at the cost of an implementation complexity and potential ISI. When a very low delay is required, adding diversity on the headset can be investigated as an alternative.

	Targeted PER	Date rate	$CW_{min} = 63$	$CW_{max} = 1023$
4-PPM	PER=10 <sup>-4</sup>	590 kbps	<b>157 ms</b>	<b>180 ms</b>
	PER=10 <sup>-3</sup>	670 kbps	<b>138 ms</b>	<b>159 ms</b>
	PER=10 <sup>-2</sup>	970 kbps	<b>96 ms</b>	<b>111 ms</b>
16-PPM	PER=10 <sup>-3</sup>	5 Mbps	<b>19 ms</b>	<b>25.2 ms</b>

Table 5: Delay  $D_{succ}$ ,  $P_t=300\text{mW}$  for different target PER and MDPU = 2500 bytes

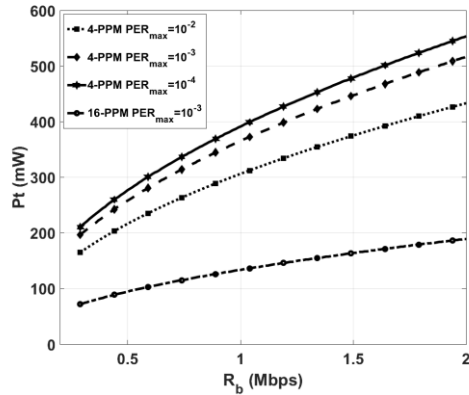


Figure 7: Emitted power  $P_t$  as a function of  $R_b$  for different PER with 4-PPM and for  $\text{PER}=10^{-3}$  with 16-PPM.

## References

- [1] Dinh-Khanh Dang, A. Mifdaoui and T. Gayraud, "Fly-By-Wireless for next generation aircraft: Challenges and potential solutions," 2012 IFIP Wireless Days, Dublin, 2012, pp. 1-8. doi: 10.1109/WD.2012.6402820
- [2] Y. Zou, J. Zhu, X. Wang, and L. Hanzo, "A survey on wireless security: Technical challenges, recent advances, and future trends" Proc. IEEE, vol. 104, no. 9, pp. 1727–1765, Sep. 2016
- [3] S. Arnon, J. Barry, G. Karagiannidis, R. Schober, and M. Uysal, editors. *Advanced Optical Wireless Communication Systems*. Cambridge University Press, 2012.
- [4] [S. Arnon, editor. *Visible Light Communication*. Cambridge University Press, 1st edition, 2015.
- [5] [S. Dimitrov and H. Haas, editors. *Principles of LED Light Communications Towards Networked Li-Fi*. Cambridge University Press, 1<sup>st</sup> edition, 2015.
- [6] Z. Ghassemlooy, L.N. Alves, S. Zvanovec, and M-A Khalighi, editors. *Visible Light Communications: Theory and Applications*. CRC Press, 1st edition, 2017.
- [7] N. Schmitt. "Wireless optical NLOS Communication in Aircraft Cabin for In-flight Entertainment" In Proceedings of ESA 1st Optical Wireless Onboard Communications Workshop, September 2004.
- [8] S. Dimitrov, H. Haas, M. Cappitelli, and M. Olbert."On the throughput of an OFDM-based cellular optical wireless system for an aircraft cabin". In Proceedings of the 5th European Conference on Antennas and Propagation (EUCAP), pages 3089–3093, Roma, May 2011.
- [9] C. Vassilopoulos, D. Marinos, A. C. Boucouvalas, N. P. Schmitt, Th.Pistner, and C. Aidinis. "Diffuse wireless optical link for aircraft intra-cabin passenger communication". In Proceedings of the fifth International Symposium on Communication Systems Networks and Digital Signal Processing C.3: Optical Wireless Systems, pages 625–628, July 2006.
- [10] D. Marinos, F. Leonidas, N. Vlissidis, C. Giovanis, G. Pagiatakis,C. Aidinis, C. Vassilopoulos, T. Pistner, N. Schmitt, and J. Klaue. "Medical and safety monitoring system over an in-cabin optical wireless network". International Journal of Electronics, 98(2):223–233, feb 2011
- [11] S. Dimitrov, R. Mesleh, H. Haas, M. Cappitelli, M. Olbert and E. Bassow, "Path Loss Simulation of an Infrared Optical Wireless System for Aircrafts", GLOBECOM 2009 - 2009 IEEE Global Telecommunications Conference, Honolulu, HI, 2009, pp. 1-6
- [12] S.Jpumessi-Demeffo, S.Sahuguende, D.Sauveron, A.Julien-Vergonjanne et al "A Link Reliability Study of Optical Wireless Headset inside Aircraft Cockpit" 2019 Global LiFi Congress (GLC), Paris, France, 2019, pp. 1-6.doi: 10.1109/GLC.2019.8864135
- [13] Z. Ghassemlooy, W. Popoola, and S. Rajbhandari, *Optical wireless communications: system and channel modelling with Matlab®*. CRC Press, 2012
- [14] A. Mahdiraji and E. Zahedi, "Comparison of Selected Digital Modulation Schemes (OOK, PPM and DPIM) for Wireless Optical Communications," in In the Proceeding of the 4th Student Conference on Research and Development (SCoReD 06), Jun. 27–28, 2006, pp. 5–10.
- [15] H. Haas, L. Yin, Y. Wang, and C. Chen, "What is LiFi?" J. Lightw. Technol., vol. 34, no. 6, pp. 1533–1544, Mar. 2016.
- [16] IEEE, «Part 11: Wireless LAN medium access control (MAC) and physical layer (PHY) specifications,» pp. 1489-1503, 2012.
- [17] A. Behloui, P. Combeau, and L. Aveneau. "MCMC Methods for Realistic Indoor Wireless Optical Channels Simulation." IEEE/OSA Journal of Lightwave Technology, 35(9):1575–1587, May 2017
- [18] Blender. <https://www.blender.org>.
- [19] A.J.C. Moreira, R.T. Valadas, and A.M. de Oliveira Duarte. "Characterization and modelling of artificial light interference in optical wireless communication systems". In Proceedings of 6th International Symposium on Personal, Indoor and Mobile Radio Communications, pages 326–331. IEEE, September 1995
- [20] M. Dehghani Soltani, X. Wu, M. Safari and H. Haas, "Bidirectional User Throughput Maximization Based on Feedback Reduction in LiFi Networks," in IEEE Transactions on Communications, vol. 66, no. 7, pp. 3172-3186, July 2018.doi: 10.1109/TCOMM.2018.2809435
- [21] G. Bianchi, "Performance analysis of the IEEE 802.11 distributed coordination function," in IEEE Journal on Selected Areas in Communications, vol. 18, no. 3, pp. 535-547, March 2000.doi: 10.1109/49.840210
- [22] Alabady, S.A., Salleh, M.F.M. & Hasib, A. Throughput and Delay Analysis of IEEE 802.11 DCF in the Presence of Hidden Nodes for Multi-hop Wireless Networks. Wireless Pers Commun 79, 907–927 (2014). <https://doi.org/10.1007/s11277-014-1894-9>
- [23] 'IEC 60825-1:2007, Safety of laser products — Part1 Equipment classification and requirement'.
- [24] 'IEC 62471 (2006) Photobiological safety of lamps and lamp systems (identical with CIE S009)'.

## IQ Based Direct Sequence Spread Spectrum Spatial Data Focusing implemented over a 6 Ray Urban Canyon Channel Model

---

*Odhiambo Michael<sup>1,2</sup>, Molineaux Guylian<sup>2,1</sup>, De Doncker Philippe<sup>2</sup>, and Sarrazin Julien<sup>1</sup>*

<sup>1</sup>*Sorbonne Université, CNRS, Laboratoire de Génie Electrique et Electronique de Paris, 75252, Paris, France,  
Université Paris-Saclay, CentraleSupélec, CNRS, Laboratoire de GEEPs, 91192, Gif-sur-Yvette, France., Email:  
michael.odhiambo@sorbonne-universite.fr*

<sup>2</sup>*Université Libre de Bruxelles (ULB), OPERA - Wireless Communications Group, CP 165/81 Avenue F.  
Roosevelt 50 1050 Brussels, Belgium*

---

**Keywords:** Spatial Data Focusing, Geocasting, Spread Spectrum Modulation, Beamforming, Antenna Arrays, Multipath Channel models

### **Abstract:**

Spatial Data Focusing is implemented using Direct Sequence Spread Spectrum technique with orthogonal Gold code sequences forming the orthogonal transmit signal basis. IQ resources are used to facilitate additional degree of freedom. With a four element antenna array, it is demonstrated that this scheme attains a beam-width of less than 4°. The robustness of this schemes' performance is assessed using a 6-ray urban canyon multipath micro-cell channel model simulation. (In SDF, the beamwidth is defined as the region within which transmitted signals can be decoded)

### **Résumé:**

La Focalisation Spatiale de Données (FSD) est mise en œuvre en utilisant la technique d'étalement de spectre basée sur des codes orthogonaux dit Gold. Les ressources de I,Q sont utilisées pour faciliter un degré de liberté supplémentaire. En particulier, il est montré que pour des réseaux d'antennes à quatre éléments, ce schéma atteint une largeur de faisceau inférieure à 4°. La robustesse de cette schéma est évaluée l'aide d'un modèle de canal micro cellulaires à 6 multitrajets (6-Ray Urban Canyon) (En FSD, la faisceau est définie comme la région dans laquelle les signaux transmis peuvent être décodés)

## 1 Introduction

SDF was proposed as a candidate alternative to classical beamforming in geocasting applications [1–3]. Geocasting being the ability to broadcast data to predefined geographical locations. In this work we seek to demonstrate the robustness of the Complex Code based Direct Sequence Spread Spectrum Spatial Data Focusing over classical Urban micro channels. In this case the 6-Ray Urban Canyon channel. Urban micro (UMi) was chosen due to the fact it is a classic 5G deployment scenario with outdoor to outdoor (O2O) propagation [4]. The subject of geocasting has been extensively researched in the recent past due to its potential implication on futuristic communication applications including the internet of Things (IoT), design of smart cities, specifically in Vehicular Ad-hoc networks (VANets) design, tourist guide applications and wearable gadgets that may require some sort of knowledge about their present environment. One key area that SDF is envisaged to be of great potential is with applications that may aid the physically challenged, say the blind, to easily navigate through their day to day activity, like walking around the city and being kept constantly aware of the state of their location/position. A typical scenario would be at a traffic crossing, here they can get information broadcast about the state of the traffic directly to their connected devices. The unifying specification for all geocasting applications will be accurate **location selectivity** in addition to the need for increased data capacity and speed, in essence, the key promises of the 5G technology. 5G technologies will largely rely on MIMO, beamforming, and other candidate alternatives to beamforming like the proposed Spatial Data Focusing.

In classical scenarios, geocasting is implemented using beam-forming which is an energy focusing technique as opposed to the proposed SDF which seeks to focus the transmitted data. The advent of 5G has reinvigorated work on beamforming in the recent past, albeit, research on beamforming (BF) and phased arrays has been ongoing over decades now [5–10]. The design of beamformers classically involve the use of phase shifters at RF frequencies [7]. This design approach faces several challenges including hardware design complexity and the fact that implementation cost increases with an increase in array aperture which is a requirement to achieve narrower beams. In addition, the fact that phase shifters are inherently low bandwidth equipment will limit this approach on grounds of attainable bandwidth. However this latter challenge can be counteracted by employing Local

Oscillator (LO) phase shifting that make use of tunable oscillators that sweep over the bandwidth , significantly improving phase shifter bandwidth performance [11]. This improvement notwithstanding, a prerequisite for reliable phase scanning is a fine phase resolution that increases hardware complexity. The challenges described above maybe remedied by the use of digital beamformers [11], however, they too require a large number of ADCs that consume a great amount of power. [12] looked at reduction of the number of used ADCs by taking advantage of inter channel correlation, this could only be implemented on analogue beamformers, which as we already mentioned, are limited by phase shifter performance. [13] on the other hand sought to minimize filtering requirements at RF by employing some mixed domain approach for phase shifting and beam-forming in both analogue and digital domains, this approach equally experienced hardware complexity challenge.

In the context of directional selectivity, another approach that has been gaining research track is the Directional Modulation (DM) technique [14] which is specifically concerned with data security at the physical layer. DM attains directionality by intentionally transmitting distorted signals towards all spatial locations apart from the predefined secure spatial communication direction(s). It does well in limiting ability to decode data at the side-lobes but the main lobe selectivity remains the same as for the case for classical beamforming.

Recently, we proposed a novel technique envisaged as an alternative to classical beamforming, Spatial Data Focusing [1–3]. Specifically in [3], SDF employing spread spectrum modulation using orthogonal gold codes was proposed. SDF promises to tackle the twin challenge of minimizing the required hardware and simultaneously increasing locational selectivity. It employs techniques that maps the symbols to be transmitted onto an N-dimensional signal space which are then spread using the orthogonal gold codes that also act as the signal's orthogonal basis, the spread signals are subsequently transmitted over separate paths as uncorrelated signals. Despread at the receiver is performed using the same time synchronized codes as those used at the transmitter. DS-SS-SDF significantly reduces the number of antenna elements required to broadcast data over narrow beamwidth, in comparison to classical beamforming scheme. Indeed in this case the beamwidth is defied as the region within which data can be decoded and not the classical half power beamwidth.

In this paper, an overview of classical digital beamforming technique is presented in section 2. Section 3 outlines the proposed DS-SS-SDF architecture, demonstrating its capability to realise reduced hardware and increased selectivity. Section 4 will review the channel models and metrics used. Section 5 will cover the simulation and results and finally the conclusion and perspectives will be developed in section 6.

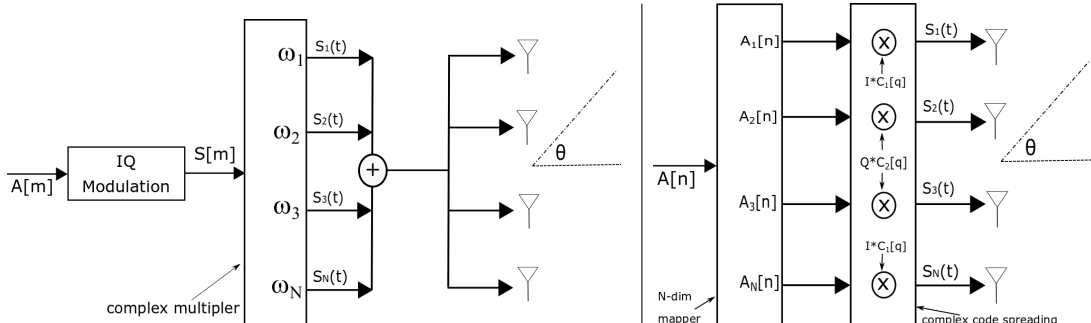


Figure 1 – Transmit architecture of classical beamforming (left) and proposed Orthogonal code based Spatial Data Focusing (right)

## 2 Digital beamforming

With the coming to age of FPGAs and software defined radio (SDR) in general, communications engineers have prioritised digital beamforming over analogue given the design flexibility that it presents [15]. Specifically, in digital beamforming the RF front end only does the signal reception. The phase shifting and amplitude scaling and combining are all passed to the digital back end as shown in left diagram of figure 1. It is shown that to carry out beamforming the baseband signals  $s[m]$  is multiplied by complex weights  $\omega_i$  at each of the paths. The complex weight at the  $i$ th path is given as  $\omega_i = a_i \exp^{j\phi_i}$ , where  $a_i$  and  $\phi_i$  are the amplitude and phase weights respectively. Due to beamforming, the signals from the various paths are combined as  $S_{out} = \sum_N s[m]\omega_i$ .  $S_{out}$  is attained by two specific approaches, side lobe control or beam scanning [16].

### 2.0.1 Side Lobe Control

Side lobes are undesired and lead to reception or transmission of energy in unwanted directions. With beamforming they can be controlled using amplitude tapering also referred as amplitude weighting. This process varies the excitation amplitude of individual elements in the array. For the case of non-uniformly excited array,

the amplitude taper runs from the array centre to its end to control the minor lobes. Smooth tapers attains larger small side lobe levels but at half-power beam-width. In short, using amplitude tapering on the linear array, it is possible to control the side lobes and achieve a better main beam in the desired direction.

### 2.0.2 Beam Scanning

Beam scanning is the movement of a radiation pattern in space. It is achieved by controlling the progressive phase difference between the elements to direct the beam in any desired direction [16]. The phase shift changes the phase of the excitation currents of each element in an array. As earlier outlined, apart from digital beamforming, phase shift can be carried out by the use of phase shifter devices, a time delay, frequency scanning or digital beamforming.

## 3 Principle of Complex Code Direct Sequence Spread Spectrum Spatial Data Focusing

In section 2 we saw that beam formation in power focusing approached is achieved by either manipulating the phase shift or amplitudes, this section introduces Direct Sequence Spread Spectrum approach to SDF, specifically we will demonstrate that SDF attains beam resolution by exploiting time delay of the signals arriving at the receiver from various paths. It will be demonstrated that unlike in beamforming where separate process carry out beamforming and demodulation, in orthogonal code based SDF, the same process responsible for data despreading determines beam resolution. This approach enables this scheme to attain finer beam resolutions at the symbol level and simultaneously minimizing the required hardware. Figure 2 shows plotted results comparing *BER* and  $\theta$  results for beamforming and SDF as was seen in [3]. It was shown that to attain similar beam-width of  $4^\circ$ , IQ-DSSS-SDF and beamforming employed 4 and 12 antennas respectively.

### 3.1 Transmitter

The transmitter architecture for the IQ-DSSS-SDF is shown on the right hand side of figure 1.  $A[n]$ , the symbols streams to be transmitted, are mapped into an N-dimensional signal space,  $A_i[n]$ ,  $i : 1, 2, \dots, N$ . A set of  $N/2$  complex orthogonal Gold codes  $C_{ic}[q] = C_i[q] + jC_i[q]$ ,  $i : 1, \dots, N/2$  with  $C_i[q] \in [-1, 1]$  are subsequently generated. The mapped data streams are uniquely spread using separate quadrature components of the generated IQ codes, the spread data is subsequently used to separately excite the various elements of the antenna array. Code orthogonality enables efficient separation of the codes at the receiver and significantly reduces inter channel interference (ICI). To minimize the bandwidth requirement, the spread signals are shaped using a root raised cosine filter  $g(t)$ . The antenna array elements output can be expressed as,

$$s_{i=a}^R(t) = \sum_{n=0}^{\infty} A_i[n] \sum_{q=1}^{L_c} C_i^R[q] g(t - nT - qT_c) \quad (1a)$$

$$s_{i=u}^Q(t) = \sum_{n=0}^{\infty} A_i[n] \sum_{q=1}^{L_c} C_{N+1-i}^I[q] g(t - nT - qT_c) \quad (1b)$$

where  $T_c$ ,  $T$ , and  $q$  represent the chip duration, symbol duration and chip index respectively,  $L_c$  is the length of the applied orthogonal sequences and  $\mathbf{a}$  and  $\mathbf{u}$  are  $1 : N/2$  and  $(N/2 + 1) : N$  respectively. For the spreading and despreading orthogonal Gold codes are preferred as opposed to Walsh codes, due to the fact that they consistently exhibit narrow auto correlation peak with very low side lobes guarding against false registration of the main peak of the autocorrelation function throughout the whole set of codes that form an orthogonal code family. The diagram to the left part of figure 2 depicts typical orthogonal code autocorrelation function performance. In IQ-DSSS-SDF the beam resolution is made finer with an increase in code length. Similarly orthogonal Gold codes exhibit very good cross correlation functions. This two qualities are at the core of the delay based beam resolution employed by SDF. Indeed the same qualities are employed in the capability to accurately control the phase of the channel coding making it possible to achieve a zero cross correlation with respect to the phase between the channels.

### 3.2 Propagation Channel Considerations

The simulations were carried over a 6-Ray Urban Canyon Multipath channel model with an impulse response  $h_i(t)$  due to each dimension given as;  $h_i(t) = \sum_l^L \alpha_{il} \delta(t - \tau_{il}) e^{-j\omega\tau_{il}}$ , where  $\alpha_{il}$  is the wave attenuation constant between  $TX_i$  and  $RX$ .  $\tau_{il}$  is the propagation delay due to antenna array elements spatial location with respect to  $RX$ .  $L$  is the number of multipath components.  $l = 1$  will be considered as the *LOS* path for the individual

$N$  paths, the general equation will be given as,

$$h(t, \tau) = \sum_i^N \sum_l^L \alpha_{il} \delta(t - \tau_{il}) e^{-j\omega\tau_{il}} \quad (2)$$

### 3.3 Receiver

The received signal  $r(t) = \sum_i^N s_i(t) * h_i(t)$ , a convolution of the transmitted signal with the channel response that reduces to,

$$r(t) = \sum_{i=1}^N \sum_l^{L^{MP}} e^{-j\omega\tau_{il}} s_i(t - \tau_{il}) + z(t) \quad (3)$$

$z(t)$  is AWGN. The channel output feeds into a matched filter matched to the incoming signals. This approach

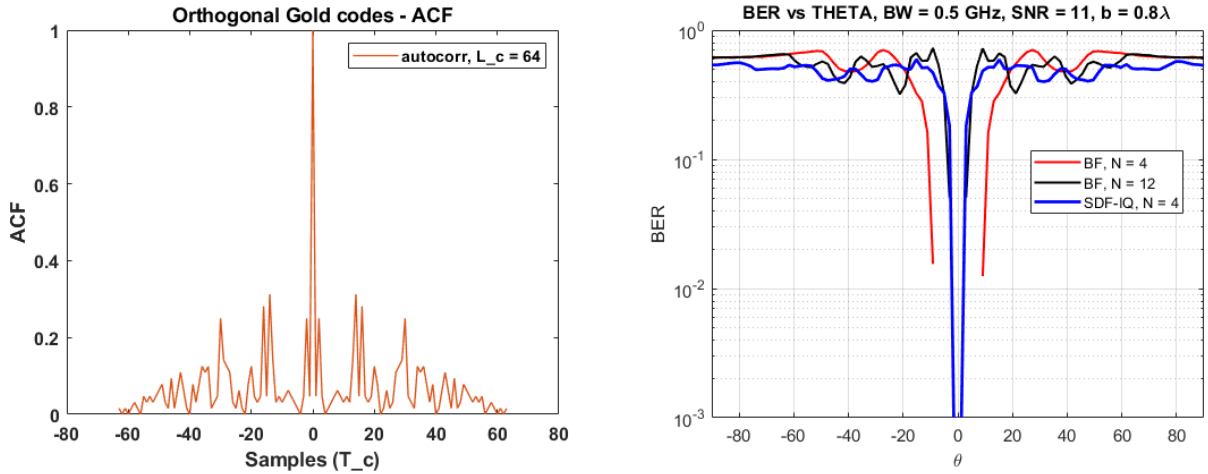


Figure 2 – Typical autocorrelation function for orthogonal Gold codes (left), BER vs  $\theta$  comparison for BF and SDF applied in LOS scenario(right)

has the advantage of not requiring the use of pilot symbols for synchronization, instead it uses the known code sequences as the reference signal. The output of the matched filter  $y(t) = r(t) * g^*(T_c - t)$  is given as:

$$y(t) = \sum_{i=1}^N \sum_l^{L^{MP}} e^{-j\omega\tau_{il}} s_i(T_c - \tau_{il}) + z(t) \quad (4)$$

The matched filter output  $y(t)$  is passed through an I/Q modulator then sampled periodically every  $l_c T_c$ .  $l_c$  and  $T_c$  are the code length and chip duration respectively. The real component of the sampled output is shown in (5).

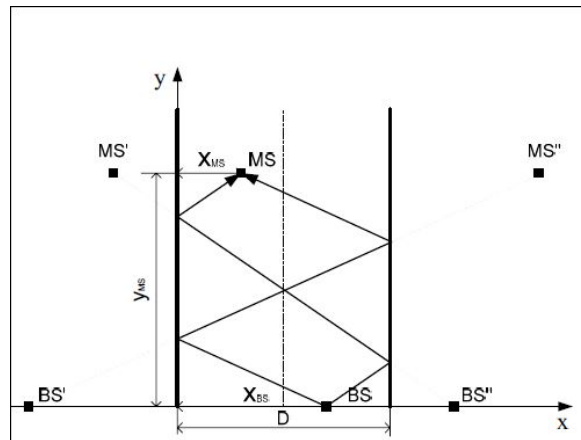


Figure 3 – Geometry of street canyon 6 ray model

$$\hat{y}(l_c T_c) = \sum_{i=0}^{N-1} \sum_{n=0}^{\infty} A_i[n] \left\{ \alpha_i^{LOS} \sum_{j=0}^{L_c-1} C^c[j] f(\psi_L) e^{-j\omega \tau_i^{LOS}} + \sum_{l=0}^{L^{MP}-1} R_{il}^{MP} \alpha_{il}^{MP} \sum_{j=0}^{L_c-1} C^c[j] f(\psi_{MP}) e^{-j\omega \tau_{il}^{MP}} + z(l_c T_c) \right\} \quad (5)$$

where  $\psi_L = ((l_c - j)T_c - nT - \tau_i^{LOS})$  and  $\psi_{MP} = ((l_c - j)T_c - nT - \tau_{il}^{MP})$ .  $\tau_i^{LOS}$ ,  $\tau_{il}^{MP}$  and  $L^{MP}$  are the propagation delay due to the LOS, NLOS paths and the number of multipath components (MPC) respectively.  $N$  is the number of applied dimensions and  $R_{il}^{MP}$  is the reflection coefficient due to each MPC [17]. The  $\tau_i^{LOS}$ ,  $\tau_{il}^{MP}$  are obtained from the various path distances on division by speed of  $c$  (speed of light). The distance can be calculated as [17],

$$d(BS, MS)_{LOS} = \sqrt{(X_{MS} - X_{BS})^2 + (Y_{MS} + Y_{BS})^2 + (Z_{MS} - Z_{BS})^2} \quad (6a)$$

$$d(BS, MS)_{GR} = \sqrt{(X_{MS} - X_{BS})^2 + (Y_{MS} + Y_{BS})^2 + (Z'_{MS} - Z_{BS})^2} \quad (6b)$$

$$d(BS, MS)_{LR} = \sqrt{(X'_{MS} - X_{BS})^2 + (Y_{MS} + Y_{BS})^2 + (Z_{MS} - Z_{BS})^2} \quad (6c)$$

$$d(BS, MS)_{RR} = \sqrt{(X''_{MS} - X_{BS})^2 + (Y_{MS} + Y_{BS})^2 + (Z_{MS} - Z_{BS})^2} \quad (6d)$$

$$d(BS, MS)_{RLD} = \sqrt{(X'_{MS} - X''_{BS})^2 + (Y_{MS} + Y_{BS})^2 + (Z_{MS} - Z_{BS})^2} \quad (6e)$$

$$d(BS, MS)_{LRD} = \sqrt{(X''_{MS} - X'_{BS})^2 + (Y_{MS} + Y_{BS})^2 + (Z_{MS} - Z_{BS})^2} \quad (6f)$$

The real and imaginary components coming out of the IQ demodulator are used to acquire the initial synchronisation values. This is done with respect to a reference path with the aid of the known despreading codes generated at the receiver. The results of synchronisation due to the preferred reference path forms the basis for aligning all the members of the despread code sequence as to synchronize them with the incoming signals prior to despreading. The  $m$ th estimated symbol coefficients derived by cross correlating  $\hat{y}_i(l_c T_c)$  with the receiver generated and synchronized codes are given as:

$$\hat{s}_i[m] = \hat{y}(l_c T_c) \sum_{z=mLc+1}^{m+1} \left\{ C_{is}^c[z - mLc] + \sum_{i \neq i}^N C_{is}^c[z - mLc] + C_{is}^c[z - mLc] z(l_c T_c) \right\} \quad (7)$$

### 3.4 Beam resolution

As was mentioned earlier, beamwidth in SDF is defined as the area within which data can be decoded. Thus, (7) is responsible for this process. It has three distinct components viz: the desired signal due to autocorrelation function; the cross correlation function; and the noise component. Assuming an ideal scenario, i.e., perfect synchronisation and receiver located at broadside, phase shift with respect to the reference dimension and position is zero. Based on Orthogonal Gold code properties, the cross correlation components will all go to zero, the noise component will be spread out giving low noise energy and the autocorrelation will attain very high peaks thus we can decode the transmitted signal. On the other hand as the receiver moves away from the designated position, the autocorrelation function is no longer at peak, in addition the cross correlation function now introduces interference to the overall signal akin to inter channel interference. Indeed time delay (phase) mismatch with respect to the reference dimension as a function of receiver position will lead to mismatch of the incoming signals with the synchronised copies thus reducing receiver SINR. The likeness of the signal time spaced copies rapidly diminishes with the delay mismatch, this is attributed to the receiver moving away from the targeted geographical location. In summary unlike in classical beamforming where sidelobe control is carried out by amplitude tapering, in IQ-DSSS-SDF, side lobe control is a by product of the correlation process.

### 3.5 Multipath mitigation

Recall from (5) that  $\psi_L = ((l_c - j)T_c - nT - \tau_i^{LOS})$  and  $\psi_{MP} = ((l_c - j)T_c - nT - \tau_{il}^{MP})$ . With the assumption of perfect synchronisation and receiver at broadside,  $\tau_i^{LOS} = 0$  with respect to LOS path and the synchronised despreading code, this subsequently implies that all delay due to  $\tau_{il}^{MP}$  will be attenuated by the autocorrelation of the spreading code at time  $\tau_{il}^{MP}$ .

## 4 Channel Model Evaluation Metrics

Figure 3 depicts the modelled channel, a classical 5G deployment scenario of the urban micro (UMi) with outdoor to outdoor (O2O) propagation [4]. The power, delay, time, spatial or angular characteristics of the

channel were characterized as shown in figure 4, this outlook at the dispersion of the received signal gave us an understanding of the impact of multipath propagation on IQ-DSSS-SDF.

#### 4.0.1 Power Delay Profile(PDP)

PDP defines the variation of individual path powers with respect to the delay due to the position of the receiver from the transmitter. Ray tracing being a typical deterministic channel model, power and delays are the direct outputs of this channel model.

#### 4.0.2 RMS Delay Spread

The multiple rays introduced by multipath propagation have varying gains and delays. The knowledge of delay spread get us to understand the impact of ISI on the channel. RMS delay spread is required to characterize wide band channels [18]. [19] outlines the approach towards calculation of the standard deviation and mean of the delay spread. The delay spread is given as,

$$DS = \sqrt{\frac{\sum_1^N P_l \tau_l^2}{\sum_1^N P_l} - \tau_0^2}; \quad \tau_0 = \frac{\sum_1^N P_l \tau_l^2}{\sum_1^N P_l} \quad (8)$$

where  $P_l$  and  $\tau_l$  refer the power and the delay of the  $l$ th path

#### 4.0.3 RMS angle spread

The dispersion of the received signal in the angular domain is demonstrated using angular spread such that channels exhibiting wide angular spread depict large capacity and those with narrow angular spread on the other depict efficient beamformer design [20]. Angular spread can be derived from two approaches; the first one takes the LOS path as reference and calculates the spreads while the other employs circular wrapping [21]

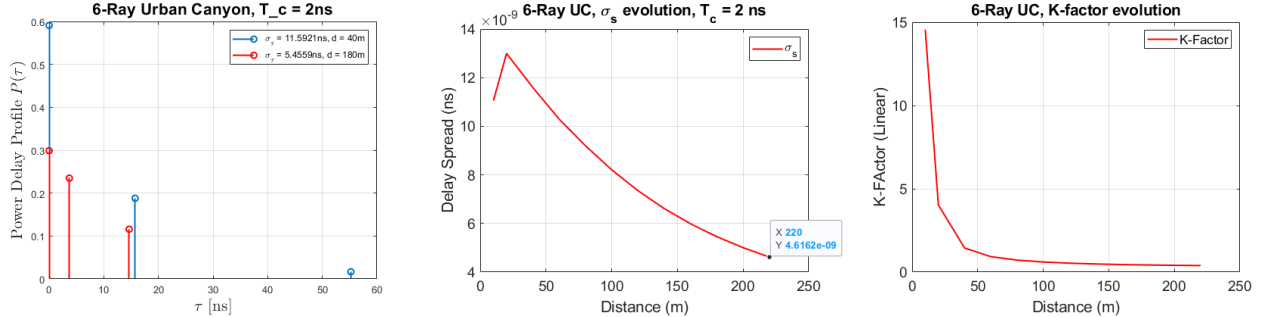


Figure 4 – Channel characterization plots; Power Delay Profile(PDP) (left); Evolution of Delay Spread with distance (centre) and Evolution of K-Factor with distance (right)

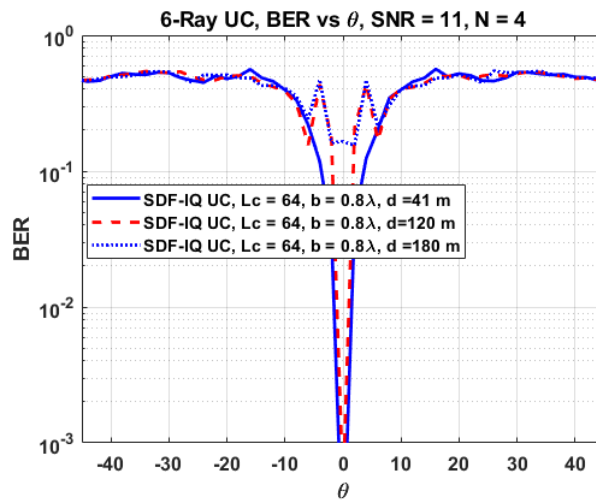


Figure 5 – 6-Ray Urban Canyon, BER vs  $\theta$  plots

#### 4.0.4 K-factor

The K-factor measures of ratio of the power between the LOS ray and the NLOS ray. In [22] it was shown that an increase in the use of higher bands and access point density leads to an increase in LOS condition thus the K-factor influences the fading statistics of BER, spectral efficiency and mean fading duration. K-factor can be calculated as,

$$KF = \frac{P_{LOS}}{\sum_{l \neq LOS} P'_l} \quad (9)$$

where  $P_{LOS}$  is the power from the LOS ray and  $l$  is the number of rays.

## 5 Simulation and Results

This sections outlines the simulation process and the discusses the acquired results. The simulations were carried on Matlab Software. For this specific work orthogonal Gold codes of code length 64 were used. The SNR was set to  $11dB$  and occupied bandwidth set at  $500MHz$ . For channel characterization various distances in metres between the receiver and antenna array were considered (10 - 220 m). The number of elements in the array was set to  $N = 4$ . Distance between the array elements set to  $0.8\lambda$  and indeed the chosen channel model is a 6-Ray urban canyon micro-cell.

The first plot of figure 4 depicts power delay profile taken from two ends of the distance. We see that at around 40 metres, i.e, closer to the antenna array, the LOS signal is clearly dominant and the time delay between and the first NLOS is significant a typical Rician channel scenario. On the other hand further away the LOS channel is no more dominant ant the system moves towards a typical Rayleigh scenario. The plot in the centre 4 represents the evolution of the delay spread. Despite the fact that it diminishes with increasing distance, it does not get to non resolvable levels ( $T_c > \sigma_s/2$ ), thus in this case the evolution of delay spread does not impact the system. The third plot to the right depicts the evolution of K-Factor with distance. We see that initially it is high and with distance it reduces to very low level. The lower K-Factor are an indicator that the NLOS signals have power almost equal to or even equal to the LOS signal. In such a scenario K-factor is said to influence the fading statistics of BER, spectral efficiency, and average fading duration.

The above cases come out clearly in the  $BER vs \theta$  plot of figure 5, where we see that at 41 metres and 120 metres respectively, IQ-DSSS-SDF attained beamwidths of less than  $2.3^\circ$  at a set BER threshold of  $10^{-3}$ , on the other hand at around 180m the BER was quite high which can be attributed fading as earlier demonstrated reducing K-factor.

## 6 Conclusion

In this work we have outlined the difference between classical beamforming and DSSS-SDF, as regards the process of beam formation and explained that in beamforming, beam formation is due to amplitude tapering whereas in DSSS-SDF it is a function of time delay that is inherent in the process of correlation. We showed that from earlier work done [3], for a similar size beamwidth, DSSS-SDF and beamforming employed 4 and 12 antennas respectively. We also carried out the characterization of a 6-Ray urban canyon channel and showed how it impacts the signals transmitted vis the DSSS-SDF application

## 7 References

- [1] J. Sarrazin, M. Odhiambo, S. Golstein, P. De Doncker, and F. Horlin, "Spatial data focusing: An alternative to beamforming for geocasting scenarios," in *2018 USNC-URSI Radio Science Meeting (Joint with AP-S Symposium)*, pp. 139–140, July 2018.
- [2] Molineaux, G., Golstein, S., Odhiambo, M., Horlin, F., De Doncker, P., & Sarrazin, J. S. J., "Spatial data focusing using time and iq resources for wireless geocasting," in *Proc. of the IEEE Global Communications Conference, GLOBECOM (09-13 December, 2019: Waikoloa, HI, USA)*, Dec 2019.
- [3] Odhiambo, M., Golstein, S., Sarrazin, J. S. J., De Doncker, P., & Horlin, F., "Spatial data focusing, implementation using spread spectrum modulation techniques," in *Actes des 21èmes Journées Nationales Micro-ondes, JNM (15-17 May, 2019: Caen, France)*, May 2019.
- [4] 38.901 (2018), *Study on channel model for frequencies from 0.5 to 100 GHz. Technical Specification (TS) Release 15, 3rd Generation Partnership Project (3GPP)*. IEEE personal communications, vol. 5, no. 1, pp. 10–22, 2018.

- [5] R. Ertel, P. Caroieri, K. Sowerby, T. Rappaport, and J. Reed, *Overview of spatial channel models for antenna array communication systems*, pp. 20–32. United States: John Wiley and Sons Inc., 1 2009.
- [6] L. C. Godara, “Application of antenna arrays to mobile communications. ii. beam-forming and direction-of-arrival considerations,” *Proceedings of the IEEE*, vol. 85, pp. 1195–1245, Aug 1997.
- [7] H. Steyskal, “Digital beamforming antennas - An introduction,” *Microwave Journal*, vol. 30, p. 107, Jan 1987.
- [8] Volakis J. L, *Antenna engineering handbook. 4th ed. Chapter 3,20,21*. NewYork (NY):McGraw Hill, 2007.
- [9] D. Parker and D. C. Zimmerman, “Phased arrays - part 1: theory and architectures,” *IEEE Transactions on Microwave Theory and Techniques*, vol. 50, pp. 678–687, March 2002.
- [10] J. Blass, “Multidirectional antenna—a new approach to stacked beams,” *IRE International Convention Record. New York (NY)*, vol. 8, pp. 48–50, Mar 1960.
- [11] H. Hashemi, X. Guan, A. Komijani, and A. Hajimiri, “A 24-ghz sige phased-array receiver-lo phase-shifting approach,” *Microwave Theory and Techniques, IEEE Transactions on*, vol. 53, pp. 614 – 626, 03 2005.
- [12] J. H. C. van den Heuvel, J. M. G. Linnartz, P. G. M. Baltus, and D. Cabric, “Full mimo spatial filtering approach for dynamic range reduction in wideband cognitive radios,” *IEEE Transactions on Circuits and Systems I: Regular Papers*, vol. 59, pp. 2761–2773, Nov 2012.
- [13] C. Wijenayake, Y. Xu, A. Madanayake, L. Belostotski, and L. T. Bruton, “Rf analog beamforming fan filters using cmos all-pass time delay approximations,” *IEEE Transactions on Circuits and Systems I: Regular Papers*, vol. 59, pp. 1061–1073, May 2012.
- [14] T. Hong, M. Song, and Y. Liu, “Dual-beam directional modulation technique for physical-layer secure communication,” *IEEE Antennas and Wireless Propagation Letters*, vol. 10, pp. 1417–1420, 2011.
- [15] J. Razavilar, F. Rashid-Farrokhi, and K. J. R. Liu, “Software radio architecture with smart antennas: a tutorial on algorithms and complexity,” *IEEE Journal on Selected Areas in Communications*, vol. 17, pp. 662–676, April 1999.
- [16] Stutzman, W.L. Thiele, *Antenna Theory and Design, 3rd Edition*. New York: Wiley, 2013.
- [17] D. Bojanjac, R. Nad, and G. Šišul, “Ray tracing model of pedestrian urban zone,” in *Proceedings ELMAR-2010*, pp. 289–292, Sep. 2010.
- [18] M. P. Fitton, A. R. Nix, and M. A. Beach, “A comparison of rms delay spread and coherence bandwidth for characterisation of wideband channels,” in *IEE Colloquium on Propagation Aspects of Future Mobile Systems (Digest No: 1996/220)*, pp. 9/1–9/6, Oct 1996.
- [19] Saunders S. and Aragón-Zavala A, *Antennas and propagation for wireless communication systems*. John Wiley and Sons, 2007.
- [20] Meinilä J., Kyösti P. et al., *Winner+ final channel models v1. 0*. IEEE personal communications, vol. 5, no. 1, pp. 10–22, Jun 2010.
- [21] 3GPP, *Circular angle spread. Teleconference, 3rd Generation Partnership Project (3GPP)*. 3GPP Project, 2003.
- [22] S. Mukherjee, S. S. Das, A. Chatterjee, and S. Chatterjee, “Analytical calculation of rician k-factor for indoor wireless channel models,” *IEEE Access*, vol. 5, pp. 19194–19212, 2017.

# An adaptive Uplink SCMA Scheme Based on Channel State Information

*Manel Rebhi<sup>1</sup>, Kais Hassan<sup>1</sup>, Kosai Raoof<sup>1</sup>, and Pascal Charge<sup>2</sup>*

<sup>1</sup>*LAUM, Le Mans University, e-mail: manel.rabhi.tn@ieee.org, kais.hassan@univ-lemans.fr, kosai.raoof@univ-lemans.fr*

<sup>2</sup>*IETR, University of Nantes, Pascal.Charge@univ-nantes.fr*

**Keywords:** SCMA, adaptive codebook design, CSI, sparsity degree

## Abstract:

The sparse code multiple access (SCMA) is one of the promoting candidate of code-domain non-orthogonal multiple access (CD-NOMA) for the upcoming generations of wireless communications systems, and it has been actively investigated in recent years. The key distinguishing feature of SCMA comes from the gain of its multi-dimensional sparse codebooks. Nevertheless, all users have not the same business requirements, and their physical layer needs depend on many factors such as the maximum allowed delay, the required rate and the targeted quality of service. In this paper, an adaptive SCMA scheme is proposed to tackle this problem. The idea is to divide users into different groups such as an adaptive designed codebook is allocated to each group. Unlike the traditional SCMA, the sparsity degree, the constellation size, and the allocated power per user, can be adapted to each group requirements in order to increase the overall performance of an uplink SCMA system. Simulation results show that the proposed scheme outperforms the traditional regular SCMA.

## 1 Introduction

Soon, the number of devices and connected users will be exceeding more than 50 billion of active hosts. As a result, a massive automatic data will be exchanged among huge number of connected devices. Among the fifth generation (5G) promises, when compared to fourth generation (4G), is to increase the user data rate by 10 to 100 (up to 10 Gbit/s), to reduce the latency by 10, to increase the connectivity density by 10. In order to meet the massive connectivity requirement of the upcoming future generations of wireless networks, innovative non-orthogonal multiple-access (NOMA) techniques were proposed and they are mainly divided into two categories: power-domain NOMA (PD-NOMA) and code-domain NOMA (CD-NOMA) [1]. PD-NOMA (which is traditionally called NOMA) exploits the power dimension to allow different users to access the same resources element (RE). Sparse code multiple access (SCMA) [2] is a multiple-carrier CD-NOMA technique which enjoys a good spectrum-efficiency thanks to the shaping gain of its multi-dimensional codebook [3]. The new radio (NR) study in 3GPP considered the SCMA among the multiple access techniques for 5G [4, 5].

SCMA can serve several users simultaneously by using a specific sparse codebook for each user such as bits are directly mapped to the multi-dimensional codewords, the inter-user interference is eliminated by employing the low-complexity message passing algorithm (MPA) or one of its variations [6]. Well designed multi-dimensional codebook plays a major factor in improving SCMA performance since it increases its shaping gain. Constellation with low projections [2], spherical codebooks [7], and star-QAM based multi-dimensional constellation [8] are among existing codebook designs. A comprehensive review of multi-dimensional constellations for SCMA systems is introduced in [3].

Most existing SCMA systems are based on regular structure where users are treated equally that is why they can not be adapted to users' business needs or conditions in the same scenario which is not realistic. So new irregular SCMA systems are needed to manage different requirements such as capacity, connectivity, and data rate, and to also exploit the knowledge of channel state information (CSI). Some existing work tried to solve this problem, for instance an irregular SCMA codebook design [9] was proposed to assign different codebooks with various dimensions according to different users' requirements. Simulations show that using an irregular codebook design does improve the system performance in terms of bit error rate (BER), however the authors did not take into consideration the impact of the correlation among users. Another irregular SCMA design was proposed in [10], the idea was to employ different rotated angles to design different codebooks for several user's needs, nevertheless the proposed codebooks are still far from optimization. The authors in [11] studied the resource allocation for different users in the same system by proposing a flexible resource scheduling scheme.

Other contribution in [12] proposed an energy-saving algorithm for a joint codebook design and assignment, and power allocation for both uplink and downlink SCMA scenarios.

Here, we propose two optimized adaptive codebooks for irregular SCMA structure by adapting either the constellation size or the sparsity degree of each codebook such as we can respectively adjust either the data rate or the quality of service of each user. The served users are divided into several groups such as each group has its specific characteristics of the designed codebook. The proposed codebook design extends the work in [8] to propose a joint optimization of the mother constellations and the rotation operators which are employed to generate the different codebooks. The log-domain MPA (Log-MPA) detector is employed at the receiver. Simulation results demonstrate that the BER performance of the optimized adaptive codebooks is better than that of existing regular codebooks.

The rest of the paper is organized as follows. The SCMA system model is presented in section 2, the optimized codebooks are introduced in section 3. Simulation results are then provided in section 4. Finally, the conclusions of this research work are summarized in section 5.

## 2 System model

We consider a synchronous uplink SCMA system with a base station and  $J$  separate users so-called layers and  $K$  orthogonal frequency-division multiplexing (OFDM) sub-carriers, so-called resource elements (REs). An SCMA transmitter encodes the data bits of user  $j$  and maps them into a  $K$  dimensional codeword,  $\mathbf{x}_j$ . The constellation function, associated for each user  $j$ ,  $g_j$ , generates a constellation set with  $M_j$  alphabets of length  $N_j$ . Then, the mapping matrix  $V_j$  maps the  $N_j$  dimensional constellation points to SCMA codewords to form a distinct codebook  $\mathbf{C}_j$ . Each codebook presents the signature of the corresponding user. The codebooks are built based on multi-dimensional constellations whose shaping gain enables to outperform the traditional spread code based schemes [13]. As to the codewords of SCMA, they are sparse, i.e. only  $N_j \ll K$  of their entries are non-zero, which is called *codebook sparsity degree*, and the rest are zeros. The sparsity key of SCMA that all codewords corresponding to the  $j^{\text{th}}$  SCMA layer have a unique location of non-zero entries at the same  $(K - N_j)$  positions.

Figure 1 illustrates the SCMA system under three scenarios. A regular SCMA is presented in Fig.1(a) where all users are spread over two REs ( $N = 2$ ) and employs a codebook of size  $M = 4$ . The system is described with the factor graph matrix  $\mathbf{F}_{\text{ss}} = (\mathbf{f}_{\text{ss},1}, \dots, \mathbf{f}_{\text{ss},J})$ , it is obvious that all users have the same codebook sparsity degree. The same factor graph matrix is valid when each user employs his specific constellation size  $M_j$  as shown in Fig.1(b). This scenario allows to serve users at different data rates. On the other hand, different sparsity degrees can be used such as each user sends  $\log_2(M)$  bits over a specific number of sub-carriers as depicted in Fig.1(c). An example of a factor graph with different sparsity degrees,  $\mathbf{F}_{\text{ds}}$ , is given in the following.

$$\mathbf{F}_{\text{ss}} = \begin{bmatrix} 1 & 0 & 0 & 1 & 1 & 0 \\ 0 & 1 & 0 & 1 & 0 & 1 \\ 1 & 0 & 1 & 0 & 0 & 1 \\ 0 & 1 & 1 & 0 & 1 & 0 \end{bmatrix}, \quad \mathbf{F}_{\text{ds}} = \begin{bmatrix} 0 & 1 & 1 & 1 & 0 & 0 \\ 1 & 0 & 1 & 0 & 0 & 1 \\ 1 & 1 & 0 & 1 & 0 & 0 \\ 1 & 1 & 0 & 0 & 1 & 0 \end{bmatrix} \quad (1)$$

The codewords of all layers are then superimposed and exchanged over the  $K$  REs. The  $K$ -dimensional received vector is given by,

$$\mathbf{y} = \sum_{j=1}^J \text{diag}(\mathbf{h}_j) \mathbf{x}_j + \mathbf{n}, \quad (2)$$

where  $\mathbf{h}_j$  is the  $K \times 1$  channel gain vector and  $\text{diag}(\mathbf{h}_j)$  is a diagonal matrix whose diagonal elements are the entries of  $\mathbf{h}_j$ . The  $K \times 1$  vector  $\mathbf{n}$  corresponds to the additive zero-mean white circularly complex Gaussian noise with variance  $N_0$ ; i.e.  $\mathbf{n} \sim \mathcal{CN}(0, N_0 \mathbf{I}_K)$ , where  $\mathbf{I}_K$  is the identity matrix of size  $K$ .

## 3 Adaptive SCMA Codebook Design

The SCMA codebook design problem involves finding the optimum user-to-RE spreading matrix  $\mathcal{S}^*$ , along with the optimum multi-dimensional constellation  $\mathcal{X}^*$ , and can be defined as:

$$\mathcal{S}^*, \mathcal{X}^* = \arg \max_{\mathcal{S}, \mathcal{X}} D(\phi(\mathcal{S}, \mathcal{X}; J, \{M_j\}, \{N_j\}, K)) \quad (3)$$

where  $D$  is a design criterion and  $\phi$  is the SCMA system as it was described in section 2. Also,  $\mathcal{S} = \{\mathbf{S}_j, 1 \leq j \leq J\}$  where  $\mathbf{S}_j$  is the spreading matrix of user  $j$ , it is worth noting that  $\mathbf{f}_{\text{ss},j} = \mathbf{S}_j \mathbf{S}_j^T$ . Existing SCMA codebooks

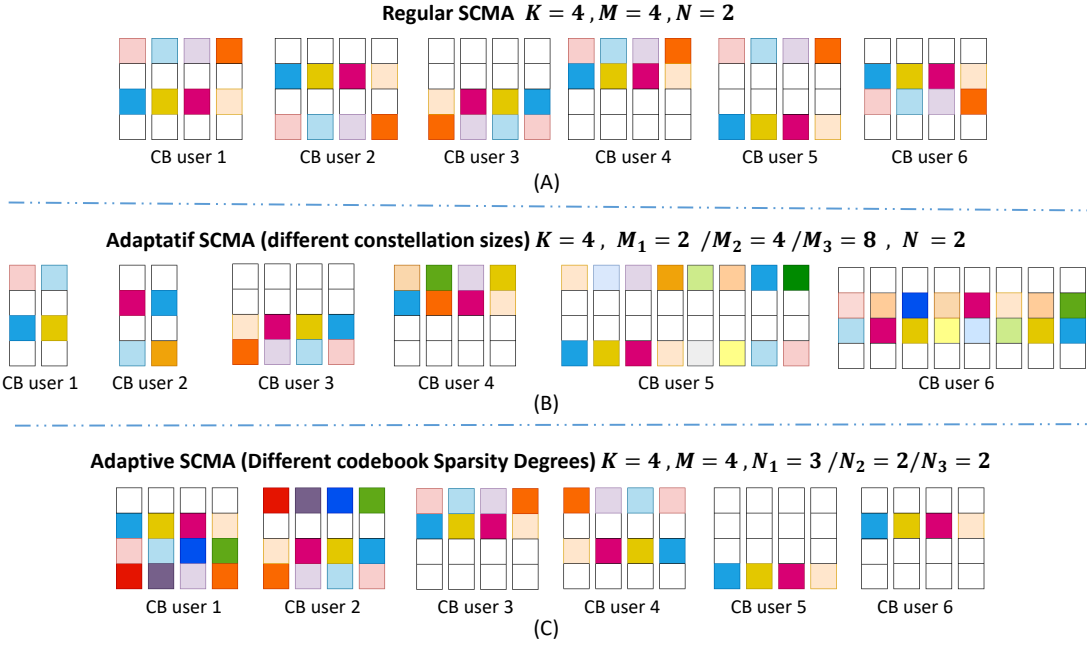


Figure 1 – Presentation of the SCMA encoder for (a) regular system (b) adaptive system with different codebook sparsity degrees (b) adaptive system with different constellation sizes.

designs simplified this optimization problem into a sub-optimal multi-stage approach [3], such as the design of SCMA codebook is performed in three main steps : Firstly a mother constellation,  $\mathbf{X}_m$ , is designed, then a user-specific rotation matrices,  $\Delta_j$ , are used to generate user-specific multi-dimensional constellations which are finally spread to generate the  $J$  codebooks. Hence, the optimization problem in (3) is reformulated as follows,

$$\{\Delta_j\}, \mathbf{X}_m^* = \arg \max_{\{\Delta_j\}, \mathbf{X}_m} D(\phi(\mathcal{S}^*, \{\Delta_j \mathbf{X}_m\}; J, \{M_j\}, \{N_j\}, K)) \quad (4)$$

such as the  $j^{\text{th}}$  codebook is calculated by,

$$\mathbf{C}_j = \mathbf{S}_j^* \Delta_j^* \mathbf{X}_m^*. \quad (5)$$

In the following subsections, the design of mother constellations and rotation matrices will be introduced.

### 3.1 Mother constellation design

The  $N \times M$  mother constellation consists of  $N$  vector or dimension of size  $M$ , that is the  $N$  rows of  $\mathbf{X}_m$ . The proposed design is inspired by the work in [8] and extends it to the case of adaptive SCMA. We have two distinct cases, namely systems with different codebook sparsity degrees and those with different constellation sizes.

For the former case, we need to design a constellation matrix  $\mathbf{X}_m$  of size  $N = \max(N_1, \dots, N_J)$  such as only  $N_j$  dimension are used to generate the codebook  $\mathbf{C}_j$ . Each dimension is generated from the previous one by adding an interleaving and power scaling effect such as inter-layer interference can be eliminated more easily. Here, we will study an SCMA system with three distinct groups of users that is  $N_1 = 3, N_2 = 2, N_3 = 1, M = 4$  where the factor graph matrix  $\mathbf{F}_{\text{ds}}$  as defined in (1) is adopted. The employed mother constellation is expressed as,

$$\mathbf{X}_m = \begin{bmatrix} \alpha R_1 & R_1 & -R_1 & -\alpha R_1 \\ -R_2 & \alpha R_2 & -\alpha R_2 & R_2 \\ \alpha R_3 & R_3 & -R_3 & -\alpha R_3 \end{bmatrix} \quad (6)$$

where  $R_2 = \beta R_1$  and  $R_3 = \beta R_2$ . The optimization approach in this paper is more powerful since we consider  $\alpha, \beta \in \mathbb{C}$  in contrast to [8] which allows to have some inter- and intra-dimensional rotations in addition to the power variation. The optimization consists of finding the values of  $\alpha$  and  $\beta$  which maximizes the codebook design criterion.

For SCMA systems with different constellation sizes, the same approach is used but it must be adapted such as we have a distinct mother constellation for each value of  $M$ , that is  $\mathbf{X}_{m,1} \in \mathbb{C}^{N \times M_1}, \mathbf{X}_{m,2} \in \mathbb{C}^{N \times M_2}, \mathbf{X}_{m,3} \in \mathbb{C}^{N \times M_3}$

$\mathbb{C}^{N \times M_3}$ . These matrices are given by,

$$\begin{aligned}\mathbf{X}_{m,1} &= \begin{bmatrix} R_1 & -R_1 \\ -R_3 & R_3 \end{bmatrix} \\ \mathbf{X}_{m,2} &= \begin{bmatrix} \alpha R_1 & R_1 & -R_1 & -\alpha R_1 \\ -R_2 & \alpha R_2 & -\alpha R_2 & R_2 \end{bmatrix} \\ \mathbf{X}_{m,3} &= \begin{bmatrix} \alpha R_3 & \alpha R_1 & R_3 & R_1 & -R_1 & -R_3 & -\alpha R_1 & -\alpha R_3 \\ -R_4 & -R_2 & \alpha R_4 & \alpha R_2 & -\alpha R_2 & -\alpha R_4 & R_2 & R_4 \end{bmatrix}\end{aligned}\tag{7}$$

Based on that the codebooks are designed for  $J = 6$  users belonging to three distinct groups such as  $N = 2, M_1 = 1, M_2 = 2, M_3 = 3$ , and the factor graph matrix  $\mathbf{F}_{ss}$  as defined in (1) is used.

One essential key to optimize the codebooks is to chose the best design criterion. Existing design criteria including Euclidean distance, Euclidean kissing number, product distance, modulation diversity order and others are reviewed in [3]. The authors in [8] showed that the pairwise error probability between two transmitted vectors  $\mathbf{x}_a, \mathbf{x}_b \in \mathcal{M}$  is given by,

$$\mathbb{P}(\mathbf{x}_a, \mathbf{x}_b | \mathbf{H}) = Q\left(\sqrt{\frac{\|\mathbf{H}(\mathbf{x}_a - \mathbf{x}_b)\|^2}{2N_0}}\right)\tag{8}$$

where  $\mathcal{M}$  is the combination constellation. Hence, the optimization objective is to find  $\alpha, \beta$  values that maximize the minimum square Euclidean distance of the combination constellation  $\mathcal{M}$ . A numerical search algorithm is employed for this objective. Obviously, codebooks for all users must be calculated to find  $\mathcal{M}$ .

### 3.2 Rotation matrix design

The last step of the codebook design is to find the optimal rotation angles. All existing works employ the typical rotation angles in [2, 10]. In this paper, we propose an optimized set of user-specific rotation matrices. The  $n^{\text{th}}$  entry of the  $N_j \times N_j$  diagonal rotation matrix for user  $j$  is defined as,

$$[\Delta_j]_{n,n} = e^{j\theta_{j,n}},\tag{9}$$

where  $\theta_{j,n} \in [0, \pi[$  since the different dimensions of each mother constellation are symmetric. In order to simplify the optimization, quantized angles can be employed to represent the semi-circle, i.e.  $\theta_{j,n}$  can be obtained from a uniform grid as following,

$$\theta = \left\{ \frac{i\pi}{N_\theta}; 0 \leq i \leq N_\theta - 1 \right\}\tag{10}$$

when  $N_\theta$  is a design parameter. It is worth mentioning that for the system proposed in Fig.1(c), a total number of distinct rotation angles of  $N_1 + N_2 + N_3$  is needed. However, for the system with different constellation sizes, we assign two rotation angles for each dimension with eight constellation points which is considered as a combination of two vectors with four constellation points. This makes the total number of distinct rotation angles of  $M_1 + M_2 + 2M_3$ .

A numerical search algorithm is employed to assign the optimal rotation angle for each dimension of each user. This requires to find the optimal values of  $\alpha$  and  $\beta$  first which itself requires to know the rotation matrices. To solve this problem the rotation angles are assigned successively in the first step,  $\alpha$  and  $\beta$  are optimized before optimizing the rotation angles in the second step.

## 4 Simulation Results

In this section, we will present the simulation results to highlight the performance of the proposed adaptive SCMA when compared with the SCMA proposed in [2] which will be denoted as regular SCMA. The simulation parameters are listed in Table 1. All results are based on Monte Carlo trials, for each realization the channel is assumed to follow a Rayleigh distribution and a random AWGN is added. SCMA system performance is evaluated through the BER for different values of  $E_b/N_0$ .

### 4.1 The impact of different channel conditions on the performance of regular SCMA

All existing SCMA research works assume that all the users have the same channel conditions which is not exact. Here, we will study the SCMA performance when users have different channel states. We suppose that

Table 1 – Simulation Parameters for adaptive SCMA

Parameter	Value
SCMA Constellation Type	Optimized
Number of Monte Carlo trials	10000
Maximum number of symbol	1e7
Maximum number of bit errors	100
Number of MPA iterations	5
Number of sub-carrier	4
Number of users	6
Overload factor	1.5
Channel type	Rayleigh fading

the  $J = 6$  users can be classified into three groups such as the average signal-to-noise ratio (SNR) varies from one group to another. The SNR level fluctuation (in dB) among the groups is denoted by  $\delta$  such as when the average SNR for all users is  $\gamma$  then the average SNR per groups is either  $\gamma - \delta, \gamma$  or  $\gamma + \delta$ . A performance evaluation of regular SCMA for different values of SNR level fluctuation is shown in Fig.2. Obviously, the BER increases when  $\delta$  increases, for instance the BER is 5 and 50 times higher for  $E_b/N_0 = 15$ dB when  $\delta = 2$  and  $\delta = 4$ . Hence, it is recommended to design adaptive SCMA codebooks which take into consideration the variable nature of the channel state of each user. For the rest of simulation results, we will consider  $\delta = 2$ .

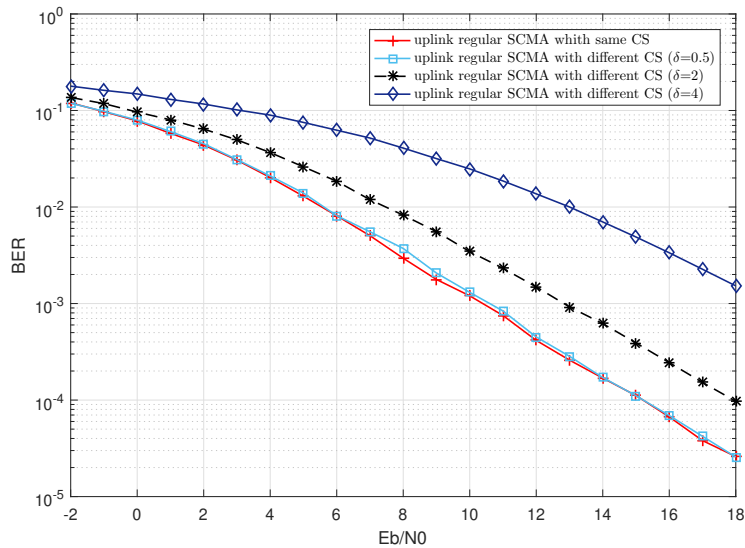


Figure 2 – Performance evaluation of uplink SCMA in [2] when users have different channel states for different values of SNR level fluctuation  $\delta = 0.5, \delta = 2, \delta = 4$

#### 4.2 Performance of adaptive SCMA with $N_1 = 3, N_2 = 2, N_3 = 1$ and $M = 4$

Fig.3 compares the performance of regular SCMA with SCMA based on the optimized codebook as proposed in this paper. Despite the fact that regular uplink SCMA outperforms the proposed adaptive SCMA when all users have the same channel state, it is the opposite when different channel states are taken into consideration, that is the performance of regular SCMA degrades and that of the adaptive SCMA becomes better. Clearly, the BER performance of the optimized adaptive SCMA codebook is better than that of regular uplink SCMA through Rayleigh fading channels, e.g. for a BER of  $10^{-4}$ , a gain of almost 3 dB is achieved. This can be explained by the fact that we allocate more RE ( $N_1 = 3$ ) for the users with the worst channel conditions.

#### 4.3 Performance of adaptive SCMA codebooks with $M_1 = 2, M_2 = 4, M_3 = 8$ and $N = 2$

The idea of codebooks with different constellation sizes was inspired from the adaptive digital modulation where the size of the constellation increases when the channel is better and vice versa. Here, we have three groups of users with three different channel states, hence the two codebooks with 8 codewords are assigned to the group

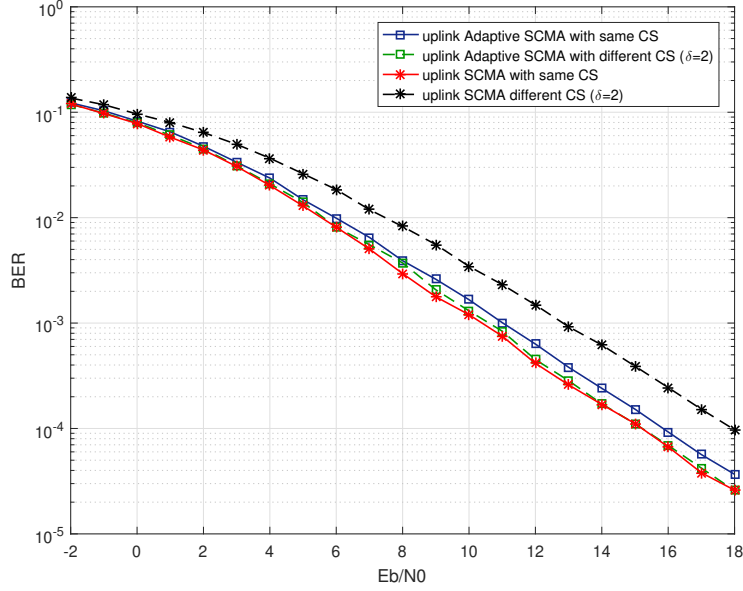


Figure 3 – Performance comparison between regular uplink SCMA and adaptive uplink SCMA with different sparsity degrees ( $N_1 = 3, N_2 = 2, N_3 = 1$ ) when the different channel states are taken into consideration.

with the better channel conditions, and the two codebooks with 2 codewords are assigned to the group with the worst ones. BER performance of the proposed adaptive SCMA with different constellation sizes is compared to the regular SCMA is Fig.4. Our proposal provides better performance, for instance a gain of 2 dB is achieved when BER is of  $10^{-4}$ .

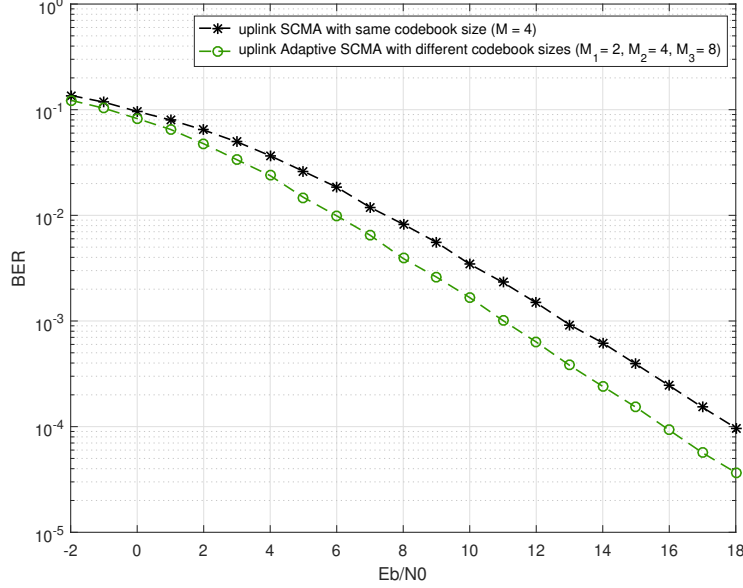


Figure 4 – Performance comparison between regular uplink SCMA and adaptive uplink SCMA with different constellation sizes ( $M_1 = 2, M_2 = 4, M_3 = 8$ ) when the different channel states are taken into consideration.

## 5 Conclusions

In this paper, we discussed how to adapt the SCMA system according to user business requirements or his environment conditions such as his channel state for example. The proposed adaptive SCMA scheme divides users into groups and assigns to them either different codebook sparsity degrees or different constellation sizes. We introduced an enhanced method to optimize the mother constellations and the rotation matrices in the two

cases. The total performance of the system is adjusted according to users' channel conditions by either allocating more REs to the users with the worst channel conditions, or by assigning largest codebook size to users with the best channel conditions. The performance of our proposed adaptive SCMA was evaluated through link-level simulations and it was compared to that of the conventional regular SCMA. Simulation results show that the optimized adaptive SCMA system provides better performance in terms of BER in the two cases.

## 6 References

- [1] L. Dai, B. Wang, Z. Ding, Z. Wang, S. Chen, and L. Hanzo, "A survey of non-orthogonal multiple access for 5g," *IEEE Communications Surveys Tutorials*, vol. 20, pp. 2294–2323, thirdquarter 2018.
- [2] M. Taherzadeh, H. Nikopour, A. Bayesteh, and H. Baligh, "SCMA Codebook Design," in *2014 IEEE 80th Vehicular Technology Conference (VTC2014-Fall)*, pp. 1–5, Sept. 2014. ISSN: 1090-3038.
- [3] M. Vameghestahbanati, I. D. Marsland, R. H. Gohary, and H. Yanikomeroglu, "Multidimensional constellations for uplink scma systems—a comparative study," *IEEE Communications Surveys Tutorials*, vol. 21, pp. 2169–2194, thirdquarter 2019.
- [4] Y. Wu, C. Wang, Y. Chen, and A. Bayesteh, "Sparse code multiple access for 5g radio transmission," in *2017 IEEE 86th Vehicular Technology Conference (VTC-Fall)*, pp. 1–6, Sep. 2017.
- [5] A. Ghaffari, M. Léonardon, A. Cassagne, C. Leroux, and Y. Savaria, "Toward High-Performance Implementation of 5g SCMA Algorithms," *IEEE Access*, vol. 7, pp. 10402–10414, 2019.
- [6] W. B. Ameur, P. Mary, M. Dumay, J. Hélard, and J. Schwoerer, "Performance study of mpa, log-mpa and max-log-mpa for an uplink scma scenario," in *2019 26th International Conference on Telecommunications (ICT)*, pp. 411–416, April 2019.
- [7] J. Bao, Z. Ma, M. A. Mahamadu, Z. Zhu, and D. Chen, "Spherical codes for scma codebook," in *2016 IEEE 83rd Vehicular Technology Conference (VTC Spring)*, pp. 1–5, May 2016.
- [8] L. Yu, P. Fan, D. Cai, and Z. Ma, "Design and analysis of scma codebook based on star-qam signaling constellations," *IEEE Transactions on Vehicular Technology*, vol. 67, pp. 10543–10553, Nov 2018.
- [9] S. Zhang, B. Xiao, K. Xiao, Z. Chen, and B. Xia, "Design and analysis of irregular sparse code multiple access," in *2015 International Conference on Wireless Communications Signal Processing (WCSP)*, pp. 1–5, Oct 2015.
- [10] L. Yu, P. Fan, Z. Ma, X. Lei, and D. Chen, "An optimized design of irregular scma codebook based on rotated angles and exit chart," in *2016 IEEE 84th Vehicular Technology Conference (VTC-Fall)*, pp. 1–5, Sep. 2016.
- [11] D. Zhai, "Adaptive codebook design and assignment for energy saving in scma networks," *IEEE Access*, vol. 5, pp. 23550–23562, 2017.
- [12] S. Han, C. Guo, W. Meng, and C. Li, "A flexible resource scheduling scheme for an adaptive scma system," *Computer Networks*, vol. 129, pp. 384 – 391, 2017. Special Issue on 5G Wireless Networks for IoT and Body Sensors.
- [13] R. Laroia, N. Farvardin, and S. Tretter, "On optimal shaping of multidimensional constellations," *IEEE Transactions on Information Theory*, vol. 40, pp. 1044–1056, July 1994.

## Capteur communicant par rétro-modulation dans la bande 5G Backscattered communication in the 5G band for ultra-low power sensors

**Neel Samat<sup>1</sup>, Arnaud Vena<sup>2</sup>, Brice Sorli<sup>3</sup>, Jean Podlecki<sup>4</sup>**

<sup>1</sup>*IES, University of Montpellier/CNRS, samatneel@gmail.com*

<sup>2</sup>*IES, University of Montpellier/CNRS, arnaud.vena@umontpellier.fr*

<sup>3</sup>*IES, University of Montpellier/CNRS, brice.sorli@umontpellier.fr*

<sup>4</sup>*IES, University of Montpellier/CNRS, jean.podlecki@umontpellier.fr*

*Mots clés (en français et en anglais) : Rétro-modulation, 5G, capteurs sans fils, radio-logicielle, Backscattering, 5G, wireless, sensor, software defined radio.*

### Résumé/Abstract

Dans cet article nous présentons une nouvelle architecture de capteurs sans fil alimenté par une cellule photovoltaïque de taille réduite. Le dispositif communique en sans-fil via le principe de rétro-modulation sur une bande de fréquence relativement large incluant la bande 5G (3.4GHz – 3.8GHz). Le dispositif réalisé est capable de transmettre une information de température et d'humidité à plusieurs mètres dans un environnement indoor en consommant très peu d'énergie pouvant être fournie par une petite cellule solaire positionnée proche d'une fenêtre pour capter le rayonnement solaire. Le capteur sans fil a été réalisé et testé à l'aide d'un équipement de radio logicielle (USRP).

We report the study of a novel ultra-low power wireless sensor node with self-energy harvesting based on a limited size photovoltaic cell. This device communicates wirelessly based on backscattering principle over a wide frequency band compatible with 5G (3.4GHz – 3.8GHz). The realized device is able to communicate both temperature and humidity over a range of several meters in indoor environment while consuming few energy that can be supplied by a small photovoltaic cell located close to a window to catch the sun light. The wireless sensor was realized and tested with a help of a software defined radio based equipment (USRP).

### 1 Introduction

The principle of wireless communication by means of reflected power is studied and utilized since the second world war. It has been theorized first by Stockman [1] and later applied for the well known RFID technology [2][3] specially in the UHF band (840 MHz – 960 MHz). Since few years, backscattering communication principle is subject to a growing interest for the IoT (internet of things) [4] because it allows communicating between a base station and remote devices with few energy to compare with others conventional wireless communication systems [4][5][6][7][8]. It is particularly interesting to focus this study in the 3.4GHz-3.8GHz band because in the novel paradigm proposed with the 5G, base stations are supposed to be ubiquitous so that radio devices will likely find a 5G signal surrounding them. For the remote node, the communication section requires only a switching component to connect the antenna to two different loads (see Fig. 1).

This paper presents a novel ultra-low power wireless sensor node operating in 5G with self-energy harvesting based on a limited size photovoltaic cell. The structure of this paper is as follows. Section 2 provides the theory and design of the proposed novel backscattered based transponder. Section 3 explains the detection system based on a software defined radio operating in 5G. Section 4 presents measurements results before concluding.

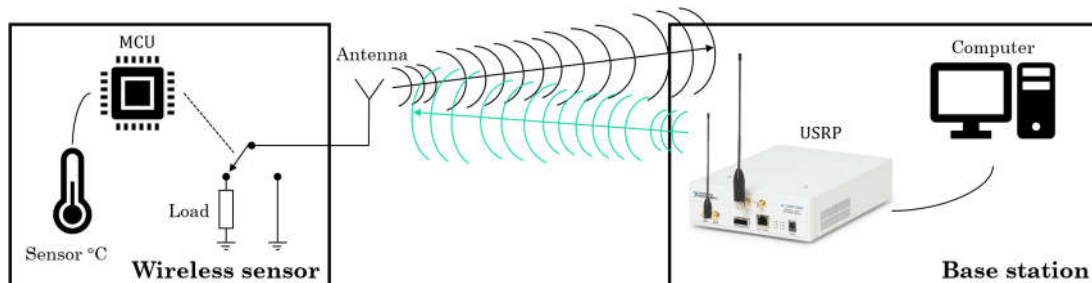


Figure 1 – Backscattering communication principle

## 2 Theory and design of an ultra-low power backscatter communication based transponder

The studied remote node is based on a bistatic backscatter communication system (BBCS). In the BBCS architecture, there is an RF source (carrier emitter), a backscatter receiver and a backscatter transmitter. The RF source generates continuous carrier signal that will serve as a support for the backscatter based communication from the remote transponder to the base station. Unlike UHF passive RFID, the remote transponder is not remotely powered by the EM field of the base station, but it uses an external power supply; hence, the distance of communication can be increased. Besides, the coding and modulation scheme is open and not ruled by the EPC Gen2 standard.

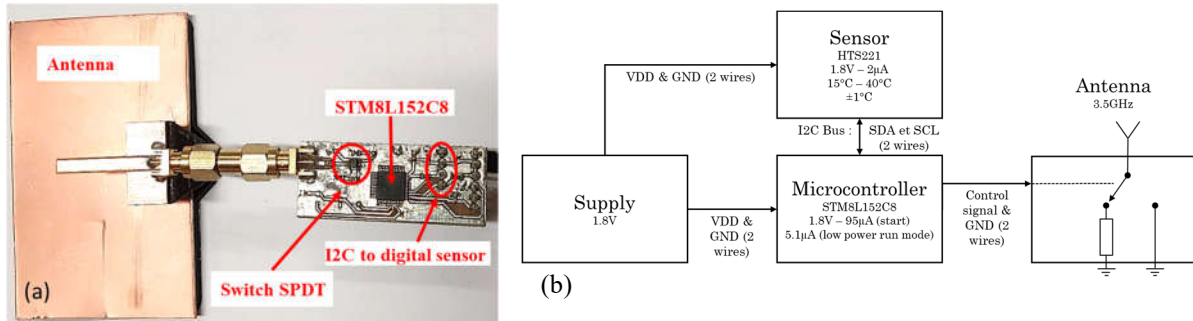


Figure 2: (a) Realized remote low power node (b) Circuit diagram of the remote low power node

The transponder is based on an 8-bit ultra-low power microcontroller (STM8L152C8) connected to a SPDT switch for antenna load modulation as shown in Fig. 2 (a) and (b). For the sake of demonstration, we connected the microcontroller to a low power digital sensor (HTS221) through an I2C connection. The microcontroller (STM8L152C8) is the key of the power consumption. Indeed, as shown in the Fig. 3 (a), the “main” function uses several functions such the “Low Power Run Mode” which allows to set low frequency clock and to copy the program in the RAM. The data acquisition from the sensor (HTS221) and the data transmission is executed from the RAM, that helps in saving power. Indeed, current consumed is equal to 1mA with all peripherals switched on and with the program executed from the Flash memory, whereas it is below 10µA under 1.8V when executed in RAM in “low power run” mode with all peripherals switched off.

In this study we decided to modulate the incoming CW of the base station by switching a load between off state and  $50\Omega$ . This switching is driven by a low frequency subcarrier according to a frequency shift-keying (FSK) modulation illustrated in Fig. 3 (b), (c), (d) that show the serialized 8-bits binary data, the FSK modulated subcarrier that command the SPDT switch, and the reflected EM signal modulated by the subcarrier signal, respectively. As shown in Fig. 3 (b) and (c), a binary ‘0’ generates a subcarrier at  $f_{sc1}=5\text{kHz}$ , whereas a ‘1’ is coded by a subcarrier at  $f_{sc2}=10\text{kHz}$ . As a result, we can observe in the spectrum (see Fig. 6) the apparition of two sidebands around the carrier frequency for which the frequency is modulated between two values  $f_{sc1}=5\text{kHz}$  and  $f_{sc2}=10\text{kHz}$  to encode a binary value ‘0’ and ‘1’, respectively.

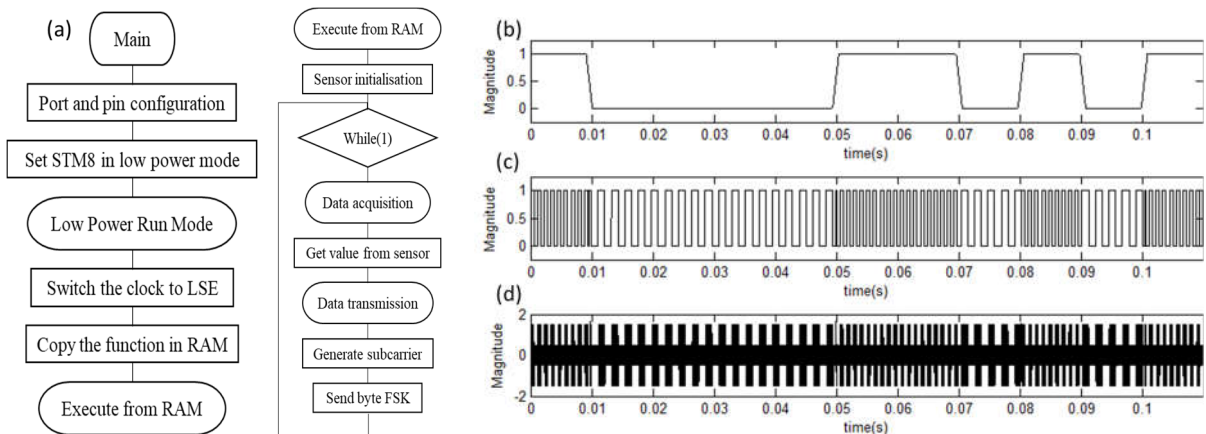


Figure 3 – (a) Flowchart of the main function and the function run in RAM (b) Serialized 8-bits binary data (b) FSK modulated subcarrier according to the 8-bits binary data (c) Reflected EM signal modulated by the subcarrier

The antenna shown in Fig. 2 (a) was design on FR-4 substrate ( $\epsilon_r=4.5$ ) to operate within the range 3.4GHz to 3.8GHz. It is based on a monopole antenna fed by a coaxial termination via a  $50\Omega$  CPW line. In order to increase the gain to an acceptable value, a reflector is inserted back of the monopole antenna at distance of 15mm. The overall dimensions of the reflector are 50mmx80mm and the monopole antenna has a length of 18.35mm. As shown in Fig. 4 (a) and (b) the simulated results of the antenna show a -10dB operating bandwidth between 3.41GHz and 3.88GHz and a gain of 6.22dBi at 3.6GHz. This antenna is directly connected to the SPDT switch of the transponder board via an SMA connector (see Fig 2 (a)).

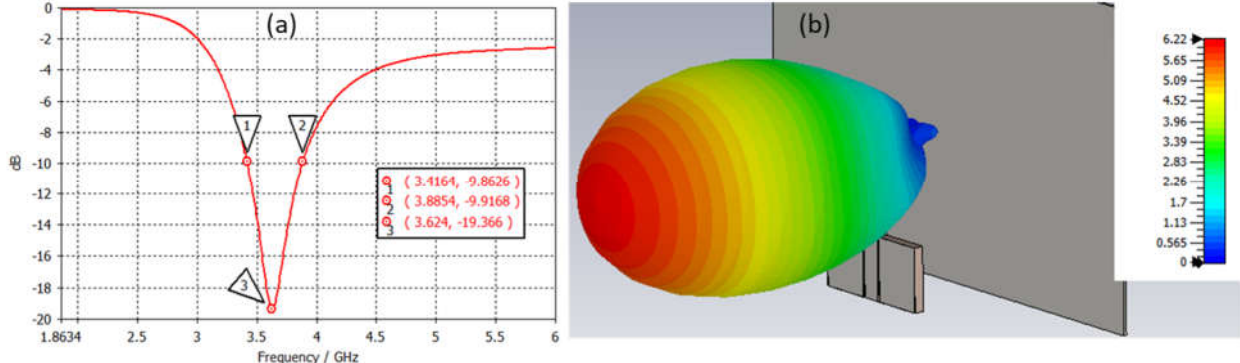


Figure 4 –(a) Simulated return loss of the designed 5G antenna (b) Radiation pattern (IEEE Gain) in dBi

## 2.1 Design of the 5G backscattering communication based base station

At the receiver side we used an USRP NI-2901 from National Instrument that is a software defined radio operating within the frequency range 70MHz to 6GHz with a maximum sampling rate of 61.44Ms/s. We developed a control software based on GnuRadio libraries to manage one TX channel and one RX channel. As shown in the architecture diagram of the software in Fig. 5, the TX channel is used to generate an unmodulated single tone carrier signal in the frequency range 3.4GHz to 3.8GHz.

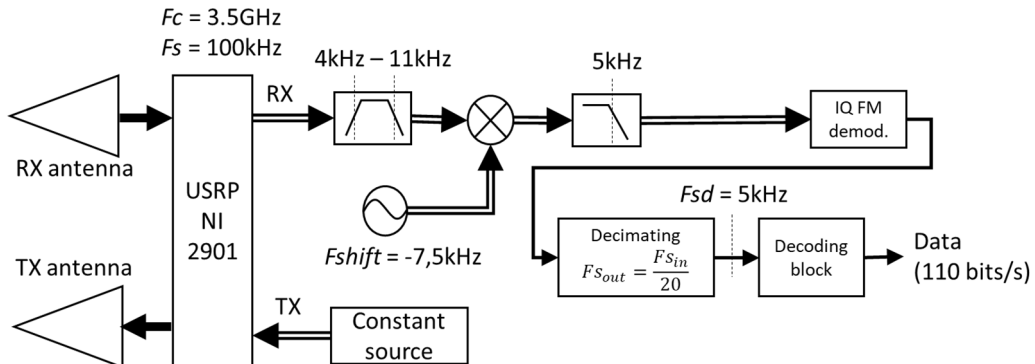


Figure 5 – Architecture of the software driving the USRP NI-2901

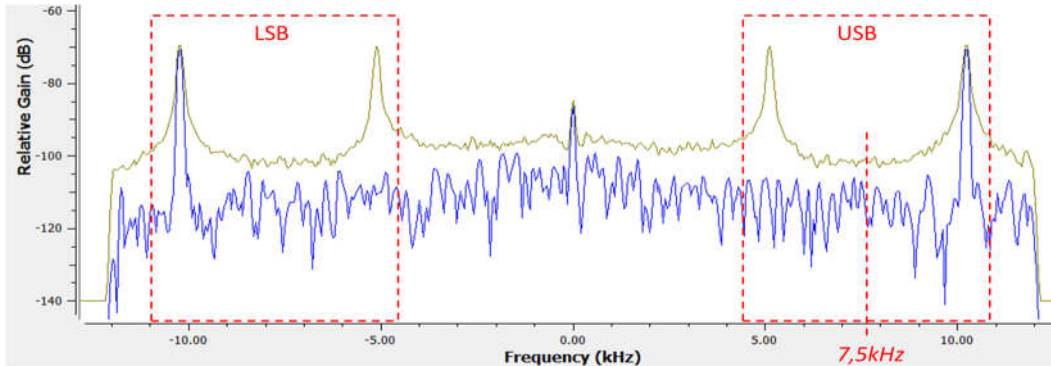


Figure 6 – Frequency spectrum of the RX signal sampled by the USRP NI-2901 in presence of the backscattered EM response from the transponder. The Figure shows the instantaneous trace in blue and the max hold trace.

Rem: The centre frequency (0Hz) is normalized to the carrier frequency which is 3.5GHz in this case.

At the receiver side, the USRP first demodulate the incoming RX signal at the carrier frequency  $f_c$ . This step is done by the hardware frontend. Typical frequency spectrum recorded with the USRP in presence of the transponder are shown in Fig. 6. Then, the following processing is done by software. First, the IQ signals are filtered with a band-pass filter from 4kHz to 11kHz to isolate the upper side band (USB) and the lower side band (LSB) generated by the subcarrier of the backscattered signal ( $5\text{kHz} < f_{sc} < 10\text{kHz}$ ). This signal is then frequency shifted by mixing it with a sinusoid of frequency 7.5kHz to center the USB around 0Hz. A low pass filtering with a cutting frequency of 5kHz is then applied to remove the LSB component and keep only the USB. This remaining signal is then demodulated with an IQ FM demodulator. The output of this block is the baseband signal which is first decimated before being de-serialized by a decoding block. The useful data rate is close to 110 bits/s and we obtain two bytes for each transmission.

### 3 Validation

#### 3.1 Power consumption measurement

We first evaluated the power consumption of the transponder during initialization and in run stage. As shown in Fig. 7 (a), we connected a 3.3V DC voltage generator in series with a  $1\text{k}\Omega$  resistor and the transponder to perform a current measurement as a function of the time using a digital sampling oscilloscope. We can note that the initialization stage lasts 0.91s. During this stage we observe a current peak starting at  $200\mu\text{A}$  and decreasing by step until reaching  $13.9\mu\text{A}$  when entering in low power run mode. After the device passed the starting time it remains stable to a very small value of current, i.e.,  $13.9\mu\text{A}$  for 3.3V. An average value of  $8.7\mu\text{A}$  under 1.8V was measured with an ammeter (in absence of the  $1\text{k}\Omega$  series resistor). It is to be noted that during low power run stage, a frame is sent every 1.75s. Thus, the power to run the device with sensor reading and backscattering based communication in low power run is as low as  $15.66\mu\text{W}$ .

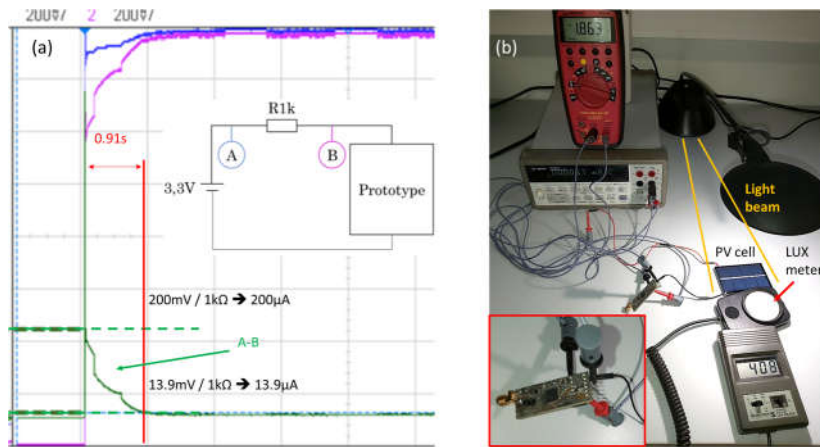


Figure 7 – (a) Current consumption measurement (b) Setup for power consumption measurement when the transponder is fed by a PV cell

#### 3.2 Empowering with a photovoltaic cell

As outlined above, the transponder requires a small amount of power to operate. Thus, it is particularly interesting to study a suitable external power supply, such a solar cell. For this study we chose a polycrystalline solar cell SOL4N of size 72mm x 46mm delivering 2V / 200mA under direct sun light (~120 000 lux) but much less under overcast weather conditions (typically 2000 lux) or at sunrise / sunset (typically 400 lux). We evaluated the performance of the PV cell when directly connected to the transponder board as shown in Fig. 7(b) exposed to variable illumination condition from 500 lux to 5000 lux with the help of a desk lamp. The illuminance was controlled with a lux meter LX-101 featuring a detection spectrum in accordance with the average human vision (C.I.E. photopic). Relationship between the measured voltage and current feeding the transponder as a function of the illuminance is shown in Fig. 8 (a) and (b), respectively. One can observe a hysteresis between the rising curve (see red curve in Fig. 8 (a) and (b)) of the illuminance from the minimum (500 lux) to the maximum (5000 lux) and the falling curve (see blue curve in Fig. 8 (a) and (b)) back to the minimum. This phenomenon is explained by the initialisation stage of the microcontroller that requires much more power to start than in low power run mode.

Indeed, the microcontroller needs a voltage above 1.8V with a maximum current of  $200\mu\text{A}$  that last 0.91s to be initialized as shown in Fig. 7 (a). In Fig. 8 (a), we observe a sharp step from  $1200\mu\text{A}$  down to  $5.6\mu\text{A}$  when illuminance is above 3400 lux while the voltage rises from 1.69V to 1.826V (see Fig. 8 (b)). Once the microcontroller operates in low power run, the falling curve shows that it can operate properly down to 1200 lux. These results prove that the device can be fed in outdoor environment without any storage capacity even under cloudy condition as well as in indoor environment when located close to windows in order to catch the sunlight.

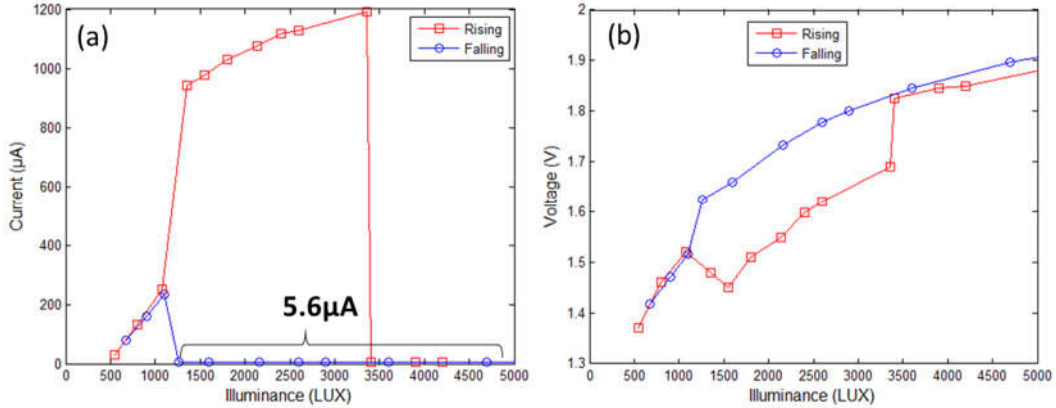


Figure 8 –Current (a) and voltage (b) fed to the transponder by a PV cell as a function of illuminance

### 3.3 Wireless communication measurements

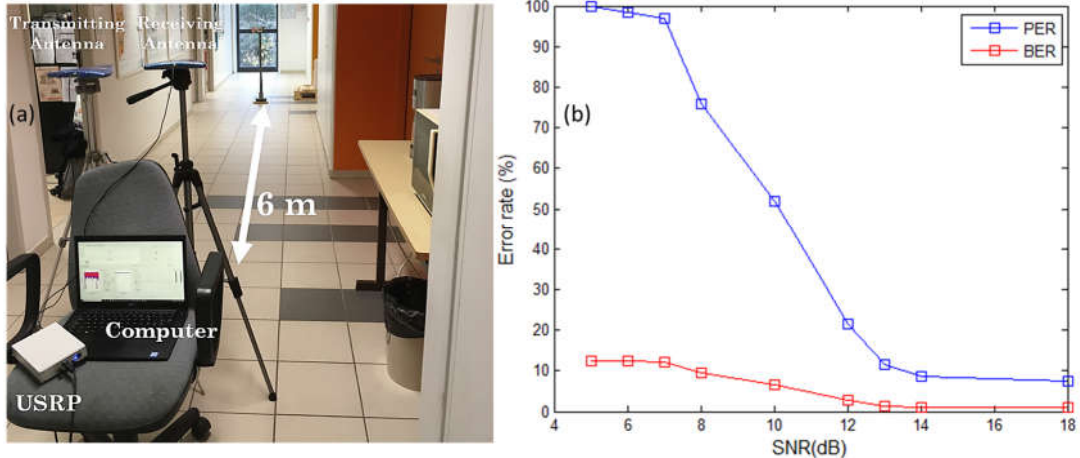


Figure 9 – (a) Measurement set-up for wireless communication testing in indoor environment (b) PER and BER as a function of SNR

The setup to test the wireless communication performance between the remote sensor and the USRP is shown in Fig. 9 (a). The testing environment is a lab corridor subjected to interferences by other radio systems and multipath, thus it is a real life scenario. The USRP NI-2901 is connected in a bistatic configuration to two wideband antennas (Aaronia Hyperlog 60100) featuring a gain close to 5dBi from 3.4GHz to 3.8GHz. As shown in the architecture diagram of Fig. 5, a continuous wave is transmitted to the TX antenna with a 20dBm of maximum output power (25dBm EIRP). It is to be noted that the receiving channel embeds an internal low noise amplifier with a gain that can be modified by software to adjust the level of demodulated IQ signals. The remote sensor is placed in front of the antenna, varying the distance to reach the maximum achievable distance measured at 6.5m for a packet error rate (PER) below 10%. This is an acceptable value because the two-bytes length data frame (temperature + humidity coded with 16 bits in this example) is permanently sent by the sensor at a refresh rate of one frame every 1.75s so that data is redundant. The measured received power with a spectrum analyzer at the location of the transponder (distance of 6.5m) is -33dBm giving a loss path of -53dB from the output port of the

USRP to the output of the receiving antenna of the remote transponder. The relationship between the measured PER and the signal to noise ratio (SNR) is given in Fig. 9 (b). A PER below 10%, giving a BER 1.4% by calculation, is achieved for a SNR above 12dB.

#### 4 Conclusion

We demonstrated the possibility to design a backscatter communication based wireless sensor operating in the 5G band from 3.4GHz to 3.8GHz. The measured average current consumption of the remote device composed of a microcontroller, a digital temperature / humidity sensor, and a SPDT switch is as low as  $8.7\mu\text{A}$  under 1.8V in low power run mode. This gives a power consumption of  $15.66\mu\text{W}$  to send a data frame permanently every 1.75s. A PV cell of size 72mm x 46mm allowed to feed the wireless sensor since an illuminance of 3400 lux when the microcontroller is first time empowered, and down to 1200 lux once initialisation stage is done. A dedicated reading system based on an USRP NI-2901 connected to two antennas in a bistatic configuration has been developed to communicate with the wireless sensor. We observe successful reading at a maximum distance of 6.5m with a PER of 10% for a radiating power of 25dBm EIRP. In a future work we will improve the decoding block of the reading system to decrease the PER for a given SNR, and we will integrate an interface block between the PV cell and the transponder to ensure operating the device under lower illuminance conditions.

#### Acknowledgments

The authors are grateful to the University of Montpellier for its support.

#### References

- [1] H. Stockman, "Communication by Means of Reflected Power," Proceedings of the I.R.E., vol. 36, pp. 1196-1204, Octobre 1948.
- [2] J. Landt, «The history of RFID,» in Proceedings of IEEE Potentials, vol. 24, pp. 8-11, 2005.
- [3] K. Finkenzeller, "RFID Handbook: Fundamentals and Applications in Contactless Smart Cards, Radio Frequency Identification and Near-field Communication," Wiley. 2010.
- [4] N. V. Huynh, D. T. Hoang, X. Lu, D. Niyato, P. Wang et D. I. Kim, «Ambient Backscatter Communications: A Contemporary Survey,» IEEE Communications Surveys & Tutorials, vol. 20, pp. 2889-2922, 2018.
- [5] S. Thomas et M. S. Reynolds, «QAM Backscatter for Passive UHF RFID Tags,» 2010 IEEE International Conference on RFID (IEEE RFID 2010), pp. 210-214, 2010.
- [6] S. N. Daskalakis, J. Kimionis, A. Collado, M. M. Tentzeris et A. Georgiadis, «Ambient FM Backscattering for Smart Agricultural Monitoring,» 2017 IEEE MTT-S International Microwave Symposium (IMS), pp. 1339-1341, Oct. 2017.
- [7] S. N. Daskalakis, J. Kimionis, A. Collado, G. Goussetis, M. M. Tentzeris et A. Georgiadis, «Ambient Backscatterers Using FM Broadcasting for Low Cost and Low Power Wireless Applications,» in IEEE Transactions on Microwave Theory and Techniques, vol. 65, pp. 5251-5262, Dec. 2017.
- [8] S. N. Daskalakis, G. Goussetis et A. Georgiadis, "Low Bitrate Ambient FM Backscattering for Low Cost and Low Power Sensing," 2018 2nd URSI Atlantic Radio Science Meeting (ATRASC), pp. 1-2, 27 September 2018.

# A light neural network for modulation detection under impairments

---

**Thomas Courtat<sup>\*†1</sup> and Hélion du Mas des Bourboux<sup>‡1</sup>**

<sup>1</sup> Thales SIX Theresis, 1 av. Augustin Fresnel, 91120 Palaiseau

---

**Keywords:** Machine learning, deep learning, modulation recognition, propagation channel, data augmentation

**Abstract:**

We present a neural network architecture able to efficiently detect modulation techniques in a portion of I/Q signals. This network is lighter by up to two orders of magnitude than other architectures working on the same or similar tasks. Moreover, the number of parameters does not depend on the signal duration, which allows processing stream of data, and results in a signal-length invariant network. In addition, we develop a custom simulator able to model the different impairments the propagation channel and the demodulator can bring to the recorded I/Q signal: random phase shifts, delays, roll-off, sampling rates, and frequency offsets. We benefit from this data set to train our neural network to be invariant to impairments and quantify its accuracy at disentangling between modulations under realistic real-life conditions.

## 1 Introduction

During the last few years, a lot of effort has been put into applying the performances of machine learning to the physical layer of radio transmission. Toward this goal, multiple directions are investigated; of interest in this study is modulation classification through supervised learning [1].

A large step in this direction was accomplished by [1] through the publication of a public data set for radio modulation classification, along with an artificial neural network architecture. Following this release multiple publications presented neural networks and analyses with respect to this data set, e.g. [2, 3, 4, 5, 6, 7, 8, 9]. [10] showed that machine learning (ML) based modulation classifiers already outperform traditional techniques based on higher order statistics. On the other hand [11] showed that even though ML based classifiers give better results, they can be less robust to data with impairments not present in the training set. This outlines the need to feed realistic and complete data sets to machine learning algorithms.

This study presents a novel neural network architecture that outperforms existing ones in the modulation recognition task. It is lighter than previously published networks [1, 10] and is built to be invariant under signal duration. We also develop a synthetic data set generator that allows to better control the sets of impairments and better understand their effects on the accuracy of our classifier.

This article is organized as follows. Section 2 presents all the data sets, either publicly available or developed here. Then, section 3 details the three state of the art architectures and the two developed for this study. They are compared in section 4 with respect to their accuracy at classifying modulations and we show that our network outperforms the others, while being two to ten times lighter. We study the performances of our architecture under variation of the signal length, and under frequency shifts in section 5. We present a conclusion in section 6.

## 2 Data sets

The industry standard data set, and its following updates, for modulation classification in radio is given by [12, 1, 13]. The first release, RadioML2016.04C (ML: Machine Learning), is composed of 11 modulations: 8PSK, AM-DSB, AM-SSB, BPSK, CPFSK, GFSK, PAM4, QAM16, QAM64, QPSK, and WBFM, with 20 evenly spaced bins in signal-to-noise ratio (SNR), ranging from -20 to 18 dB. The set is composed of 162,060 examples, consisting in 128 samples of I/Q (in-phase/quadrature) signals. The simulated synthetic data were produced using software defined radio programmed with GNU radio [14].

Three releases expanded and completed the set. RadioML2016.10A expanded to 220,000 the number of examples. RadioML2016.10B provides 1,200,000 examples on the same grid of SNR, but removes the AM-SSB modulation, leading to a total of 10 classes. RadioML2018.01A [10] provides a total of 2,555,904 examples, 1024 samples long, with a signal-to-noise ratio ranging from -20 up to 30 dB. Along with synthetic data, this set provides

---

<sup>\*</sup>These authors contributed equally to this work.

<sup>†</sup>thomas.courtat@thalesgroup.com

<sup>‡</sup>helion.dumasdesbourboux@thalesgroup.com

Impairment	Range
$T_{\text{sample}}/T_{\text{symbol}}$	[0.3, 0.5]
Phase	$[0, 2\pi]$
Delay	[0, 1]
Roll off	[0.1, 0.5]
SNR	{0, 10, 20, 30, 40}
Relative frequency offset, $\Delta f$	$\pm[10^{-6}, 5 \times 10^{-1}]$

Table 1 – Set of impairments simulated in the AugMod synthetic data set, developed in this study.

Number of signal samples	RML-ConvNet	RML-CNN/VGG	RML-ResNet	Mod-LCNN (ours)	Mod-LRCNN (ours)
128	2,829,399	199,111	179,303	37,487	97,663
1024	21,179,479	256,455	236,647	37,487	97,663

Table 2 – Number of parameters of the five different networks for signals with 128 or 1024 samples. For this table we choose 7 output classes, slightly different number of classes do not yield significant changes in the order of magnitude of the number of parameters.

radio signals propagated through real indoor environment, transmitted and received via two universal software radio peripherals (USRP). This former data set expands to 24 the number of different modulations classes: 32PSK, 16APSK, 32QAM, FM, GMSK, 32APSK, OQPSK, 8ASK, BPSK, 8PSK, AM-SSB-SC, 4ASK, 16PSK, 64APSK, 128QAM, 128APSK, AM-DSB-SC, AM-SSB-WC, 64QAM, QPSK, 256QAM, AM-DSB-WC, OOK, and 16QAM. For simplicity, in this study we limit the data sets to positive SNR, we verify nonetheless that similar results are obtained on the whole range. All of these data sets are publicly available<sup>1</sup>.

In order to independently study the performances of machine learning in modulation classification, we develop a synthetic custom data set. In addition, this module allows us to tune different parameters which are fixed or unknown in the previously defined data sets. As a consequence it allows us to study its robustness against parameters, while improving upon it. Seven linear modulations are simulated: BPSK, QPSK, PSK8, QAM8, QAM16, QAM32, and QAM64, with 5 evenly spaced bins of SNR from 0 to 40 dB. We generate 175,000 examples, i.e. 5000 per (SNR, modulation) pairs. The I/Q signal is produced for 1024 samples. A vast range of impairments brought by the propagation channel and the demodulator are added to the baseline data set: random phase shifts, delays, roll-off, sampling rates, and additive Gaussian noise. We also produce an additional data set enhanced with an extra impairment: relative frequency offsets. This allows us to better study its individual impact on modulation classification. Hereafter, we refer to this data set as AugMod, for “augmented modulation” data set. The range of the parameters are given in table 1.

As a result we benefit from five different data sets, with positive SNR, with both synthetic and indoor-propagated signals, to perform modulation classification under impairments. The first four data sets are public: RadioML2016.04C has 81,030 examples, RadioML2016.10A has 110,000 examples, RadioML2016.10B has 600,000 examples, and RadioML2018.01A has 1,572,864 examples. The fifth data set is private: AugMod with 175,000 examples. Each data set is split into two halves, one for training and the other for testing. Each individual signal is normalized by its root mean square, to have a power of 1.

### 3 Neural network architectures

Along with the available data set, [1] presents a convolutional neural network (ConvNet [15]) performing modulation classification, hereafter referred as “RML-ConvNet” (RML: Radio Machine Learning). This network treats the complex I/Q signal as a two-dimensional image, with a single “color” channel. As it is presented, this network has 2,829,399 parameters, when the I/Q signal has 128 samples and the data set has 7 different classes. The architecture is not invariant with the number of samples; this imposes to train a different network for every possible length of the input signal. Furthermore, a signal given with 1024 samples would multiply the number of parameters by approximately one order of magnitude, compared to the one for 128. This aspect produces a hardly scalable architecture for longer signals. Table 2 gives for two different length of signals, 128 and 1024, the number of parameters, or weights, of the neural networks studied here.

In a more recent release of their work, [10] presented an updated data set, RadioML2018.01A, with 1024 samples long signals. They also developed two extra neural networks: “RML-CNN/VGG” and “RML-ResNet”. The first network builds upon the already developed RML-ConvNet network, but limits the explosion of the

<sup>1</sup><https://www.deepsig.io/datasets>

number of parameters at 1024 samples through a VGG network (Visual Geometry Group [16]). It is modified to fit a 1-dimensional convolutional neural network (CNN). The second network has a residual architecture (ResNet [17]). ResNet has historically been invented to be easier to train for deep neural networks. Although both of these networks have less parameters than RML-ConvNet, as shown on table 2, they still suffer from the augmentation of the number of parameters with the signal length. For example, going from 128 to 1024 samples adds 30% more parameters. Because of this aspect, they lack the ability to adapt to signals of different sizes and, as for RML-ConvNet, must be re-trained for each signal length.

We propose a lighter convolutional neural network to perform modulation classification, invariant of the input signal length: Light Modulation Convolutional Neural Network, “Mod-LCNN”. The complex I/Q signal is treated as a one-dimensional signal with two channels. These channels are expanded to higher dimension space through consecutive 1-dimensional convolutional layers. Then through an average pooling layer, the time dimension is collapsed to produce a one-dimensional layer of dimension that of the last convolutional layer, which is fed into a fully connected layer, and a softmax [18] layer to perform classification. Each convolutional layer of kernel size 7, along with the first fully connected layer, are followed by the rectified linear unit (ReLU [19]) activation function. During training, we apply dropout [20] to the output weights of the first fully connected layer, thus preventing overfitting.

We develop two different networks: “Mod-LCNN” and “Mod-LRCNN”. Both are presented on figure 1. These two networks have the structure presented above, they differ in how each convolutional layer is applied. In the case of Mod-LCNN (top panel), we use a regular CNN, Mod-LRCNN (bottom panel) is a ResNet [17]. As a consequence each convolution step is split into three simple convolutions. The first one has a kernel size 1, allowing to expand the filter dimension [21], the two following convolutions have a kernel size of 7. The output of these last two consecutive convolutions is added to the output of the first one, through a skip connection (see figure 1).

For these two networks, the number of parameters does not depend on the signal duration. The consequence of this design is that the same trained network can be used for signals of different lengths. The resulting networks have 37,487 parameters for Mod-LCNN and 97,663 for Mod-LRCNN (table 2). As shown on figure 1, these two networks can be modeled as two blocks. The first one is a “latent space embedding”, i.e. it extracts latent features of the signal, invariant of its length. The second block is a fully connected network that performs the “classification”. The average pooling layer serves thus as a bottleneck between these two blocks.

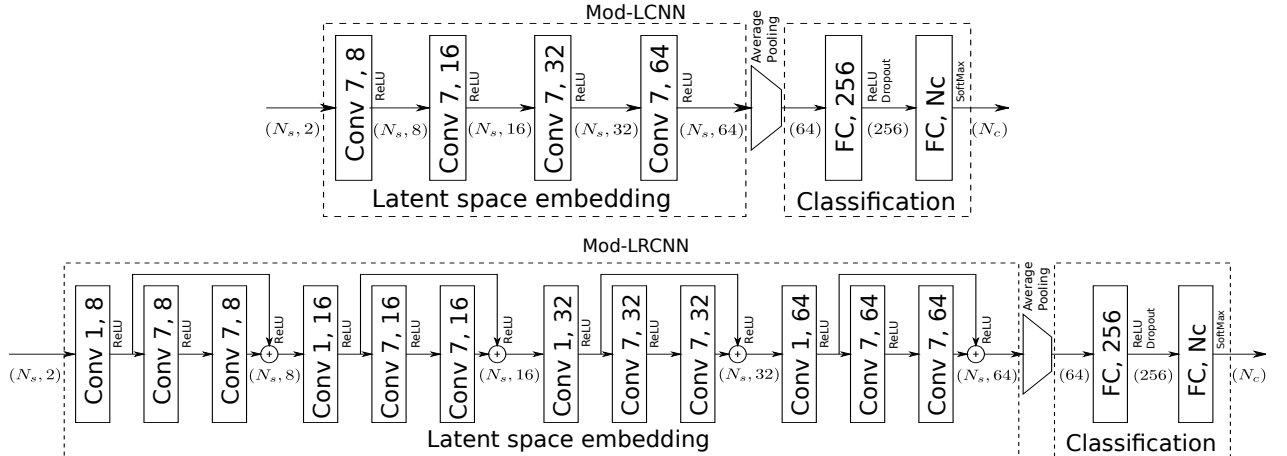


Figure 1 – Architecture of Mod-LCNN (top) and Mod-LRCNN (bottom), the neural networks developed in this study.  $N_s$  is the number of samples: 128 or 1024 in this study,  $N_c$  is the number of output classes: 7, 10, 11 or 24 in this study. The 1-dimensional convolutions have a kernel size of 7. During training the dropout rate is 0.5.

#### 4 Comparison of the different architectures

We benefit from the five different data sets presented in section 2 to train and compare the five artificial neural networks of section 3. RML-ConvNet implementation is publicly provided by the author<sup>2</sup>, in Keras [22], with TensorFlow backend [23], we thus use the same framework for all the other network architectures. Following the publicly available implementation of RML-ConvNet, we initialize all weights using the “Glorot” uniform initializer [24] for convolutional layers and through “He” normal initializer [25] for fully connected layers. The training is ran on a Nvidia 1080 Ti.

<sup>2</sup><https://github.com/radioML/examples>

Data set	RML-ConvNet	RML-CNN/VGG	RML-ResNet	Mod-LCNN (ours)	Mod-LRCNN (ours)
128 samples					
RadioML2016.04C	93	93	95	93	<b>95</b>
RadioML2016.10A	84	83	90	90	<b>91</b>
RadioML2016.10B	89	91	93	93	<b>93</b>
RadioML2018.01A	50	70	76	68	<b>78</b>
AugMod (ours)	64	60	71	75	<b>75</b>
1024 samples					
RadioML2018.01A	61	87	88	85	<b>89</b>
AugMod (ours)	74	76	83	89	<b>89</b>

Table 3 – Accuracy of the five different neural network architectures on the different data sets. The performances are given for a signal of size 128 for all data sets, and for 1024 samples when available. Boldface texts highlight the best results for each data sets.

The neural network weights are learned using the training set through the Adam optimizer [26], to minimize the categorical cross-entropy loss function. Among the five data sets, two have 1024 samples long signals: RadioML2018.01A and AugMod. We train the networks on these two data sets twice: once on the full signal duration, and another time keeping only the first 128 samples. The training is performed for 200 iterations, or epochs, through each data set with a batch size of 512 examples. Because of computation time, all networks are trained for only 50 iterations for RadioML2018.01A, when using the full 1024 samples long signals.

Table 3 presents the accuracy on the test sets for the five data sets, over the five different neural networks. The accuracy, in percent, is given by the proportion of correctly assigned modulations on the test set, after the end of training. Boldface texts highlight the best results for each data set. All networks perform relatively equally well on RadioML2016.04C and on RadioML2016.10B. RML-ConvNet and RML-CNN/VGG do not manage to reach as good performances as other networks on other data sets. This is explained by the too large number of parameters for the first network, resulting in overfitting the training set. For the second network this is explained by the depth of the network, preventing the gradient updates to efficiently propagate through the network.

We confirm the results noted by [10], RML-ResNet gives indeed the best performances over all the data sets, when compared to RML-ConvNet and RML-CNN/VGG. Mod-LCNN, developed in this study, outperforms RML-ResNet when testing on the AugMod data set, however it fails at giving good results on RadioML2018.01A. This can be interpreted by the too small number of parameters. Adding more layers would reduce the performances by producing a too deep architecture, harder to train. Mod-LRCNN manages to outperforms all the other networks, building on Mod-LCNN performances, but adding a residual network architecture. It increases the accuracy by up to 2% on RadioML2018.01A, with 128 samples, and by up to 6% on AugMod, with 1024 samples.

Figure 2 presents the learning curves, i.e. the error rate as a function of the number of epochs, for all the networks, on the AugMod data set, with 1024 samples. Unbroken curves give the results on the test sets, and dotted curves on the training sets. This figure outlines the advantages of the Mod-LRCNN architecture: it outperforms other architectures with the lowest error rate, converges faster and continuously, and is less prone to overfitting.

We compare the performances of each neural network at classifying modulations, on the AugMod data set, as a function of signal-to-noise ratio. The results are presented on the left panel of figure 3. The panel gives the error rate as a function of SNR. Mod-LRCNN, developed for this study, performs more than 40% better than the best architecture of previous studies, RML-ResNet, at  $SNR = 0$ . In the  $SNR \in [0, 30]$  range, Mod-LRCNN effectively improves the performances by  $\sim 5$  dB.

We assess the training time by looking at the time per epoch when running on the AugMod data set, with 1024 samples. Other data sets give similar results. Mod-LRCNN runs in 3.1 ms per example, resulting in 27 seconds per epoch, with 512 examples per batch, for a total training time of 1.5 hours with 200 epochs. Mod-LCNN and RML-CNN/VGG are twice as fast, however, RML-ResNet is 1.25 times longer. Finally RML-ConvNet runs in twice as long due to the large number of parameters (table 2). The fact that Mod-LRCNN runs each epoch in twice the time compared to Mod-LCNN is balanced by both its higher accuracy (table 3) and the fact that less epochs are needed to converge (figure 2).

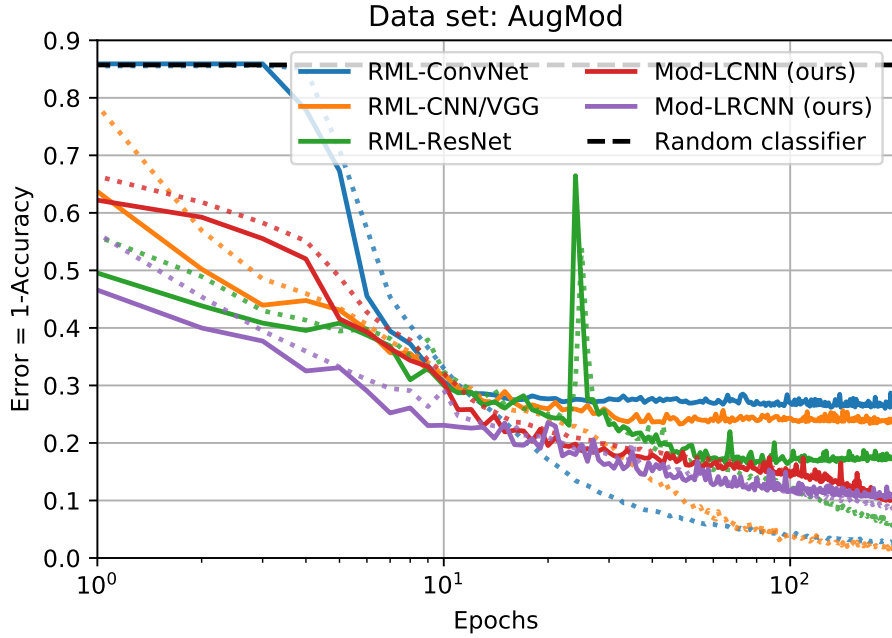


Figure 2 – Error rate as a function of the number of epochs for the five different neural network architectures, compared with the performances of a random classifier. Solid curves are for the test set and dotted curves for the training set. The comparison is performed with the AugMod data set on 1024 samples long signals.

## 5 Specific performances of Mod-LRCNN

As discussed previously in section 4, the Mod-LRCNN architecture outperforms all other architectures in accuracy. We investigate in this section its performances on different signal lengths, and under different sets of impairments.

### 5.1 Signal duration

Mod-LCNN and Mod-LRCNN’s strength are their invariance under the signal duration. This means that once the network has been trained, it can be used to infer the signal modulation, whatever its length. We test this property on three different training strategies for Mod-LRCNN. The following results are given through the implementation of Mod-LRCNN in PyTorch [2]. This choice gives us more flexibility during training.

The right panel of figure 3 presents the classification error rate as a function of the signal length. These results are given on the AugMod data set. The first strategy is to train Mod-LRCNN on 128 samples long signals. The second strategy is to train on 1024 samples long signals. On the test set, we limit each example to the first  $\{16, 32, 64, 128, 256, 512, 1024\}$  samples, infer the modulation class, and give the resulting error rate.

In the right panel of figure 3 the blue dashed curve presents the results for the first strategy, and the orange for the second. One could have expected Mod-LRCNN trained on 1024 to outperform the first strategy on the full range. It is the case for signals more than 256 samples long, however it is not the case below. This indicates a tendency of Mod-LRCNN, trained on 1024, to overfit long signals.

We develop a third strategy where we modify dynamically the length of the signal during training. At each batch iteration we randomly pick an integer  $N_s \in [16, 1024]$ , and limit the signal duration to the first  $N_s$  samples. The resulting accuracy on the test set is given in the green unbroken curve. We observe that indeed this new training scheme allows to get good performances for short and long signals.

### 5.2 Frequency shift

The AugMod synthetic data set is reproduced adding a relative frequency offset (table 1) on top of the other baseline impairments. We span a wide range of values, from positive and negative 50% of the carrier frequency, with a logarithmic scale:  $\Delta f \in \pm[10^{-6}, 5 \times 10^{-1}]$ . The effect of this latter impairment is to drift the constellations into circular patterns with a typical time scale  $\Delta f \cdot T_{sample}$ . The results are presented on the left panel of figure 4, for Mod-LRCNN trained on the AugMod data set, with 1024 samples long signals.

In this figure, the unbroken blue curve gives the result when Mod-LRCNN is trained on the AugMod data set without the frequency shift impairment, with variable length of signals (sec. 5.1). This curve thus displays the

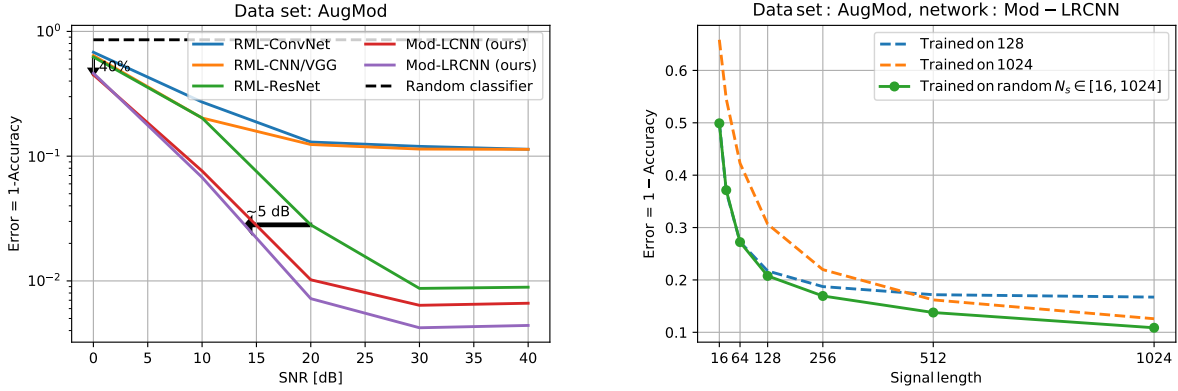


**Figure 3 – Left:** Error rate as a function of the signal-to-noise ratio for the five different networks. The performances are given for the **AugMod** data set, with 1024 samples long signals. **Right:** Error rate of the Mod-LRCNN architecture, developed for this study, on the **AugMod** data set as a function of the signal length. The blue dashed curve gives the performances for a model trained on 128 samples long signals, the orange dashed curve for a model trained on 1024, and the green unbroken curve for a training with signals of dynamically random sizes  $N_s \in [16, 1024]$ .

ability of the network to generalize to out of distribution example signals. The dotted blue curve presents the same results, but for a training with fixed 1024 samples long signals. We observe that the accuracy starts to drop at  $|\Delta f| = 10^{-4}$  and falls out at  $10^{-2}$ . This behavior is even more drastic when the network is trained on fix 1024 samples long signals. This later behavior confirms the tendency of networks trained on fixed size signals to overfit long signals and thus be less robust to time varying impairments.

The orange curves show the accuracy on the test set when Mod-LRCNN is trained on half of the **AugMod** data set, impaired with frequency shifts. We recover good performances at large frequency shifts. Following the methods of curriculum learning [27], only few epochs are needed to perform this re-training, if the weights are initialized to the best values found when trained on the simpler **Augmod** data set.

## 6 Conclusion

This study presented an artificial neural network architecture allowing to classify modulations: the light residual convolutional neural network for modulation classification, “Mod-LRCNN”. This architecture is lighter than previously published networks. Its architecture is invariant to the signal length, allowing it to adapt perfectly to signals recorded on more or less samples, without a need for re-training. The network is designed to search for the natural symmetries of the signals, extract latent features and use them to classify modulations. It simply builds statistical significance with the signal duration, and thus can process data stream.

It performs better than three public networks [1, 10] on all four publicly available data sets, e.g. RadioML2018.01A, and on a custom made data set, **AugMod**. It is defined by up to two orders of magnitude less parameters. In the  $\text{SNR} \in [0, 30]$  range, Mod-LRCNN effectively improves the threshold by  $\sim 5$  dB (up to 10 dB) compared to previously published networks.

We characterize some of the performances of the network. When trained on dynamically changing examples lengths, between 16 to 1024 samples, the network is able to give very good accuracy whatever the inferred signal lengths. This training technique prevents overfitting long signals, and thus gives good performances on evolving impairments, e.g. frequency shift. We show the ability of the network to efficiently classify signals under frequency shift impairment, even when they are out of the distribution given in the training set. Even better performances can be obtained through curriculum learning, by training the network in few epochs, if the weights are initialized at their values for the simpler data set.

The data set introduced in this study has allowed us to train our network to create signal representation invariant to real life impairments. We aim at adding more complexity to this set, e.g. non-linear modulations, multi-path propagation, and test the network under more real indoor and outdoor propagated signals.

## 7 References

- [1] T. J. O’Shea, J. Corgan, and T. C. Clancy, “Convolutional radio modulation recognition networks,” in *Engineering Applications of Neural Networks* (C. Jayne and L. Iliadis, eds.), (Cham), pp. 213–226, Springer International Publishing, 2016.

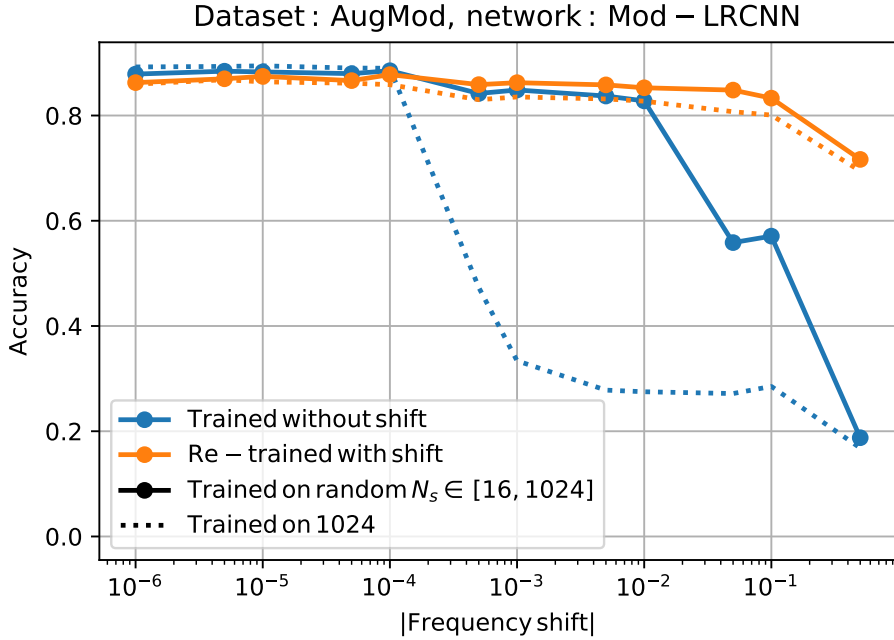


Figure 4 – Accuracy of the Mod-LRCNN architecture, developed for this study, on the AugMod data set, with 1024 samples long signals, enhanced with frequency shift impairments: in blue the results for the network trained on a data set without carrier shift, and in orange for a re-training on the data set including it. Unbroken curves are for a training with variable random signal lengths,  $N_s \in [16, 1024]$ , and dotted curves for training on fixed 1024 samples long signals.

- [2] A. Paszke, S. Gross, F. Massa, A. Lerer, J. Bradbury, G. Chanan, T. Killeen, Z. Lin, N. Gimelshein, L. Antiga, et al., “Pytorch: An imperative style, high-performance deep learning library,” in *Advances in Neural Information Processing Systems*, pp. 8024–8035, 2019.
- [3] K. Sankhe, M. Belgiovine, F. Zhou, S. Riyaz, S. Ioannidis, and K. Chowdhury, “Oracle: Optimized radio classification through convolutional neural networks,” in *IEEE INFOCOM 2019 - IEEE Conference on Computer Communications*, pp. 370–378, April 2019.
- [4] M. Sadeghi and E. G. Larsson, “Adversarial attacks on deep-learning based radio signal classification,” *IEEE Wireless Communications Letters*, vol. 8, pp. 213–216, Feb 2019.
- [5] S. Ramjee, S. Ju, D. Yang, X. Liu, A. El Gamal, and Y. C. Eldar, “Fast Deep Learning for Automatic Modulation Classification,” *arXiv e-prints*, p. arXiv:1901.05850, Jan 2019.
- [6] L. Huang, W. Pan, Y. Zhang, L. Qian, N. Gao, and Y. Wu, “Data augmentation for deep learning-based radio modulation classification,” *IEEE Access*, vol. 8, pp. 1498–1506, 2020.
- [7] Y. Shi, K. Davaslioglu, Y. E. Sagduyu, W. C. Headley, M. Fowler, and G. Green, “Deep learning for rf signal classification in unknown and dynamic spectrum environments,” in *2019 IEEE International Symposium on Dynamic Spectrum Access Networks (DySPAN)*, pp. 1–10, IEEE, 2019.
- [8] K. Tekbiyik, A. Riza Ekti, A. Görçin, G. Karabulut Kurt, and C. Keçeci, “Robust and Fast Automatic Modulation Classification with CNN under Multipath Fading Channels,” *arXiv e-prints*, p. arXiv:1911.04970, Nov 2019.
- [9] C.-F. Teng, C.-Y. Chou, C.-H. Chen, and A.-Y. Wu, “Accumulated Polar Feature based Deep Learning with Channel Compensation Mechanism for Efficient Automatic Modulation Classification under Time varying Channels,” *arXiv e-prints*, p. arXiv:2001.01395, Jan 2020.
- [10] T. J. O’Shea, T. Roy, and T. C. Clancy, “Over-the-Air Deep Learning Based Radio Signal Classification,” *IEEE Journal of Selected Topics in Signal Processing*, vol. 12, pp. 168–179, Feb 2018.
- [11] B. Luo, Q. Peng, P. C. Cosman, and L. B. Milstein, “Robustness of deep modulation recognition under awgn and rician fading,” in *2018 52nd Asilomar Conference on Signals, Systems, and Computers*, pp. 447–450, Oct 2018.

- [12] T. O’Shea and N. West, “Radio machine learning dataset generation with gnu radio,” *Proceedings of the GNU Radio Conference*, vol. 1, no. 1, 2016.
- [13] T. J. O’Shea, J. Corgan, and T. C. Clancy, “Unsupervised representation learning of structured radio communication signals,” in *2016 First International Workshop on Sensing, Processing and Learning for Intelligent Machines (SPLINE)*, pp. 1–5, IEEE, 2016.
- [14] E. Blossom, “Gnu radio: Tools for exploring the radio frequency spectrum,” *Linux J.*, vol. 2004, pp. 4–, June 2004.
- [15] Y. Le Cun, B. Boser, J. S. Denker, D. Henderson, R. E. Howard, W. Hubbard, and L. D. Jackel, “Handwritten digit recognition with a back-propagation network,” in *Proceedings of the 2Nd International Conference on Neural Information Processing Systems*, NIPS’89, (Cambridge, MA, USA), pp. 396–404, MIT Press, 1989.
- [16] K. Simonyan and A. Zisserman, “Very deep convolutional networks for large-scale image recognition,” in *International Conference on Learning Representations*, 2015.
- [17] K. He, X. Zhang, S. Ren, and J. Sun, “Deep residual learning for image recognition,” in *2016 IEEE Conference on Computer Vision and Pattern Recognition (CVPR)*, pp. 770–778, June 2016.
- [18] J. S. Bridle, “Training stochastic model recognition algorithms as networks can lead to maximum mutual information estimation of parameters,” in *Advances in Neural Information Processing Systems 2* (D. S. Touretzky, ed.), pp. 211–217, Morgan-Kaufmann, 1990.
- [19] X. Glorot, A. Bordes, and Y. Bengio, “Deep sparse rectifier neural networks,” in *Proceedings of the Fourteenth International Conference on Artificial Intelligence and Statistics* (G. Gordon, D. Dunson, and M. Dudík, eds.), vol. 15 of *Proceedings of Machine Learning Research*, (Fort Lauderdale, FL, USA), pp. 315–323, PMLR, 11–13 Apr 2011.
- [20] N. Srivastava, G. Hinton, A. Krizhevsky, I. Sutskever, and R. Salakhutdinov, “Dropout: A simple way to prevent neural networks from overfitting,” *Journal of Machine Learning Research*, vol. 15, pp. 1929–1958, 2014.
- [21] M. Lin, Q. Chen, and S. Yan, “Network In Network,” *arXiv e-prints*, p. arXiv:1312.4400, Dec 2013.
- [22] F. Chollet *et al.*, “Keras.” <https://keras.io>, 2015.
- [23] M. Abadi, A. Agarwal, P. Barham, E. Brevdo, Z. Chen, C. Citro, G. S. Corrado, A. Davis, J. Dean, M. Devin, *et al.*, “Tensorflow: Large-scale machine learning on heterogeneous distributed systems,” *arXiv preprint arXiv:1603.04467*, 2016.
- [24] X. Glorot and Y. Bengio, “Understanding the difficulty of training deep feedforward neural networks,” in *Proceedings of the Thirteenth International Conference on Artificial Intelligence and Statistics* (Y. W. Teh and M. Titterington, eds.), vol. 9 of *Proceedings of Machine Learning Research*, (Chia Laguna Resort, Sardinia, Italy), pp. 249–256, PMLR, 13–15 May 2010.
- [25] K. He, X. Zhang, S. Ren, and J. Sun, “Delving deep into rectifiers: Surpassing human-level performance on imagenet classification,” in *Proceedings of the 2015 IEEE International Conference on Computer Vision (ICCV)*, ICCV 15, (USA), p. 10261034, IEEE Computer Society, 2015.
- [26] D. P. Kingma and J. Ba, “Adam: A Method for Stochastic Optimization,” *arXiv e-prints*, p. arXiv:1412.6980, Dec 2014.
- [27] Y. Bengio, J. Louradour, R. Collobert, and J. Weston, “Curriculum learning,” in *Proceedings of the 26th Annual International Conference on Machine Learning*, ICML 09, (New York, NY, USA), p. 4148, Association for Computing Machinery, 2009.

# **Dimensioning and Optimization of 5G systems**

# Wireless communication in presence of digitally controllable scatterers: channel decomposition and capacity analysis

---

**Juan Carlos Bucheli Garcia<sup>1</sup>, Mohamed Kamoun<sup>2</sup>, and Alain Sibille<sup>3</sup>**

<sup>1</sup> Huawei Paris Research Center, 18 Quai du point du jour, Boulogne Billancourt, juan.bucheli@huawei.com

<sup>2</sup> Huawei Paris Research Center, 18 Quai du point du jour, Boulogne Billancourt, mohamed.kamoun@huawei.com

<sup>3</sup> Telecom Paris, Palaiseau, alain.sibille@telecom-paris.fr

---

**Keywords:** channel model, digitally controllable scatterer, near field

## Abstract:

Digitally controllable scatterers initiated a new paradigm in the design of wireless communication systems. With these new devices, the wireless channel can be altered by the network to enhance the propagation conditions between communicating devices. This opened the door to new schemes where the wireless channel is not only counterbalanced, but can also be influenced to create more favorable communication conditions. Recently, loaded passive antenna arrays employed in controllable scatterer setting attracted significant attention. This trend is motivated by the use of off-the-shelf components, namely antennas and controllable loads, to achieve controllable scattering function. Such variant offers the advantage of being low cost and immediately available compared to other options relying on meta-materials [1].

The investigation of physical layer schemes leveraging controllable scattering requires representative channel models that capture the main underlying physical effects. Most of the models presented so far rely on a simple approach where the scattering array is represented by a set of phase shifters that are illuminated by incident plane waves [2]. This representation, even valid in far field conditions, neglects significant effects, in particular in near field regions where its function as a scatterer is beneficial the most.

This contribution aims to fill this gap by proposing a channel model which is valid in both the so-called array near field and far field regions. To be clear, the array near field is referring to the intersection of the element's far field and the DCS (as the composition of all elements) near field [3]. The proposed model shows different power decay laws that depend on the distances separating the transmitter, the receiver and the scattering array as well as the size of the latter device. The new power decay law shows new conditions where controllable scattering is beneficial. A capacity analysis taking into account the new model is provided. It shows the regions where the DCS enhances the diversity and the rank of the channel in multi-path environments.

## 1 Scenario and notations

The scenario of interest is represented in figure 1. The transmitter and receiver are both using a multi-antenna array of size  $N_t$  and  $N_r$  respectively. The base-band channel is represented by a matrix of size  $N_r \times N_r$  denoted  $\mathbf{H}$ . The distance between the TX and RX is denoted  $d_0$  and the distances between the scattering array and the transmitter and the receiver are denoted  $d_t$  and  $d_r$  respectively.

## 2 Far field models for digitally controllable scatterers

In this section we remind decomposition tools that have been proposed to represent the spatial dependence between the channel matrix and the geometry of the scenario in far field setting. These tools are extended to include a digitally controllable scatterer.

### 2.1 Power decay law in line-of-sight setting

The first channel model that have been proposed to study digitally controllable scatterers employed a diagonal matrix with unitary elements representing phase the shift that is applied on incident plane waves [2, 4].

$$\mathbf{H} = \sqrt{\rho_d} \mathbf{H}_d + \sqrt{\rho_{rs}\rho_{st}} \mathbf{H}_{rs} \boldsymbol{\Theta} \mathbf{H}_{st} \quad (1)$$

The coefficients  $\rho_d$ ,  $\rho_{rs}$  and  $\rho_{st}$  account respectively for the path-loss of the direct link, the path-loss of link between the receiver and the scattering array, and the path-loss of the link between the scattering array and the transmitter.

When all links are line-of-sight, the coefficients  $\rho_d$ ,  $\rho_{rs}$  and  $\rho_{st}$  follow a  $d^{-2}$  where  $d$  is the distance traveled by the signal for each link. This results in  $d^{-4}$  decay for the scattered link (namely, from the  $\rho_{rs}\rho_{st}$  product). These observations have been confirmed for the array far field with a radar cross-section analysis in [5], where it is shown that the signal level observed on the scattered link follows a  $d^{-4}$  decay law, and that it is more beneficial to place the scattering array close either to the transmitter or to the receiver.

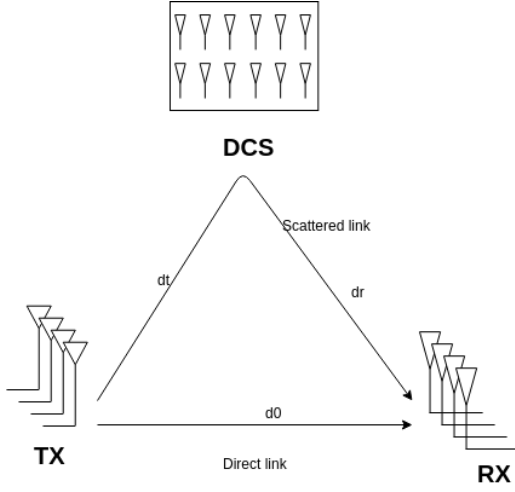


Figure 1 – Scenario of interest

## 2.2 Channel decomposition

In a multi-path Tx-Rx environment, while assuming far-field propagation for all links, the channel of equation (1) can be decomposed as a set of plane wave components [6]:

$$\mathbf{H} = \sum_{i \in \mathcal{S}} \alpha_i \mathbf{a}_R(\phi_{R,i}^{\text{LOS}}) \mathbf{a}_T^H(\phi_{T,i}^{\text{LOS}}) + \underbrace{\sum_{j \in \mathcal{D}} \gamma_j \mathbf{a}_R(\phi_{R,j}^{\text{DCS}}) \mathbf{a}_T^H(\phi_{T,j}^{\text{DCS}})}_{\mathbf{H}_{\text{DCS}}} \quad (2)$$

where azimuth propagation has been assumed for simplicity. Additionally,  $\mathcal{S}$  is the set of scatterers as seen in the link by TX and RX, excluding those related to the DCS.  $\mathcal{D}$  is the set of antennas that compose the DCS.  $\phi_{R,i}^{\text{LOS}}$  is the angle of arrival of the direct (line-of-sight) link from DCS to RX and  $\phi_{T,i}^{\text{LOS}}$  is the angle of departure of the direct link from TX to DCS. Moreover, here we assume that the contribution of the DCS is dominated by the line-of-sight components TX to DCS and DCS to RX. The vectors  $\mathbf{a}_R(\phi)$  and  $\mathbf{a}_T(\phi)$  are the steering vectors of the RX and the TX respectively for an incident plane wave illuminating from angle  $\phi$ . For each scatterer  $i \in \mathcal{S}$ ,  $\phi_{T,i}^{\text{LOS}}$  and  $\phi_{R,i}^{\text{LOS}}$  are the  $i^{\text{th}}$  angles of departure and arrival from and towards the TX and RX, respectively.  $\alpha_i$  is the complex channel seen on the link TX to  $i^{\text{th}}$  scatterer to RX (including power decay and phase shift related to propagation) and  $\gamma_j$  is the complex channel seen on the TX to  $j^{\text{th}}$  antenna of the DCS to the RX, accounting for the power decay, the phase shift related to propagation and the phase shift applied by the DCS element on the incident waves.

## 3 Near field model with digitally controllable scatterers

One of the main motivations of using DCS is to counterbalance strong blockage in non-of-sight TX-RX links. Thus, in what follows, we assume that the direct TX-RX link is entirely blocked. Nonetheless, the links corresponding to TX-DCS and DCS-RX are line-of-sight. In particular, when the transmitter and receiver are not necessarily in the far-field of the DCS, their contribution to the link is instead given by:

$$\mathbf{H}_{\text{DCS}} = \sum_{j \in \mathcal{D}} \gamma_j \tilde{\mathbf{a}}_R(\mathbf{r}_j^{\text{DCS}}) \tilde{\mathbf{a}}_T(\mathbf{r}_j^{\text{DCS}})^T \quad (3)$$

where each coefficient in the RX array manifold  $\tilde{\mathbf{a}}_R(\mathbf{r})$  and in the TX array manifold  $\tilde{\mathbf{a}}_T(\mathbf{r})$  is given by [3]:

$$\tilde{\mathbf{a}}_{R,T}(\mathbf{r})|_n(\mathbf{r}) = G(\mathbf{r} - \mathbf{r}_n) F\left(\frac{\mathbf{r} - \mathbf{r}_n}{|\mathbf{r} - \mathbf{r}_n|}\right), \quad G(\mathbf{r}) = \frac{\exp(-2\pi ik|\mathbf{r}|)}{4\pi|\mathbf{r}|}, \quad (4)$$

where  $\mathbf{r}_n$  is the 3D vector corresponding to the location of the  $n^{\text{th}}$  element at the receiver or transmitter array. Additionally,  $G(\mathbf{r})$  is the Green function of the Helmholtz equation in free space characterizing the field strength of a spherical wave departing from the origin with a wavelength  $2\pi/k$  and observed at the location represented by the 3D vector  $\mathbf{r}$ . Furthermore,  $F(\hat{\mathbf{r}})$  characterizes the directional properties of the antenna element. Using this model, and assuming isotropic elements and single-antenna transmitter and receiver sides, it has been shown that the path-loss experienced through the TX-DCS-RX link follows two slope model as displayed in figure 2 [3].

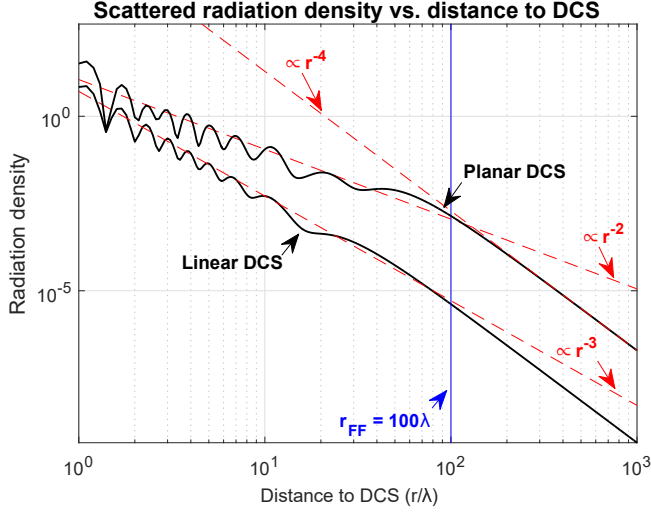


Figure 2 – Path-loss regimes for the TX-DCS-RX link. Extracted from [3].

More specifically, figure 2 shows that in the so-called array near field (i.e. for distances smaller than  $r_{FF}$ ), the radiation density at the receiver's location oscillates around a path-loss related to  $d^{-2}$  even-though the direct TX-RX link is entirely obstructed. On the other hand, in the array far-field (i.e. for distances greater than  $r_{FF}$ ), the path-loss is related to  $d^{-4}$  as it could be expected from an analysis based on the radar equation [5]. For more information on the so-mentioned near/far-field differentiation the reader is referred to [3].

#### 4 Spatial multiplexing analysis in non line-of-sight scenarios with DCS

In the following, we reformulate the results shown in [3] to study the impact of the DCS on the MIMO channel. In particular we study the impact of the DCS on the ability of the TX-DCS-RX link to construct spatial streams that can be relied upon to spatially multiplex information. As such, the metric known as effective rank [7] is used as means of computing the effective number of contributing modes.

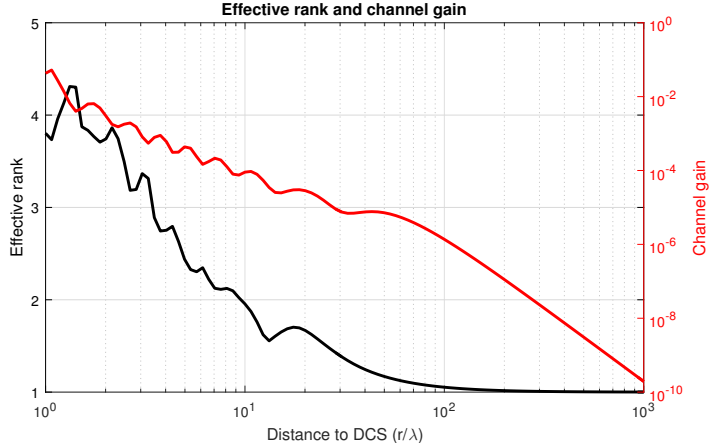


Figure 3 – Effective rank of the TX-DCS-RX link

More specifically, figure 3 shows the effective rank of a 5x5 MIMO system composed of  $\lambda/2$ -spaced ULA transmitter and receiver sides under a completely obstructed TX-RX link (i.e. only the DCS contribution is exposed). The planar configuration and setup of [3] was given use: 21x21 for a total of 441 short-circuited DCS elements with symmetrically disposed TX and RX arrays.

As it can be observed, the DCS mediated link exhibits an effective rank up to four when the TX and RX are sufficiently close to the surface. The latter can be explained by the richness that is created near the surface when the propagation environment to every DCS element vary significantly from one another. On the other hand, as expected, when these are located farther away than the far-field distance (i.e.  $r_{FF}$ ), the effective rank falls to one. The latter can be seen as the dual of a key-hole channel where a single ray is present for the Tx-DCS-Rx link.

Finally, as it was corroborated, in the case of a MIMO system, the channel gain (computed as the sum of

the square of the channel singular values) follows the same behavior as for the single-antenna TX-RX case of figure 2.

## 5 Conclusions

This paper extends channel decomposition tools to derive the channel model of the wireless links relying on a DCS. By using array manifold vectors derived from free space Green function, the proposed model inherently accounts for both far field and near field regimes. This allowed to measure the impact of the DCS in a MIMO communication link. The simulation results show that DCS improves the rank of the channel in near field regime and provides only a small enhancement in the link budget for far field regime.

## 6 Acknowledgements

The authors would like to thank Melissa Duarte for the fruitful discussions around the implications of DCS on spatial multiplexing when in presence of multi-antenna transmitter and receiver sites.

## 7 References

- [1] S. Dash, C. Liaskos, I. F. Akyildiz, and A. Pitsillides, “Wideband perfect absorption polarization insensitive reconfigurable graphene metasurface for thz wireless environment,” in *2019 IEEE Microwave Theory and Techniques in Wireless Communications (MTTW)*, vol. 1, pp. 93–96, Oct 2019.
- [2] Q. Wu and R. Zhang, “Intelligent reflecting surface enhanced wireless network: Joint active and passive beamforming design,” in *2018 IEEE Global Communications Conference (GLOBECOM)*, pp. 1–6, Dec 2018.
- [3] J. Bucheli Garcia, A. Sibille, and M. Kamoun, “Reconfigurable Intelligent Surfaces: Bridging the gap between scattering and reflection,” *arXiv e-prints*, p. arXiv:1912.05344, Dec 2019.
- [4] Y. Han, W. Tang, S. Jin, C. Wen, and X. Ma, “Large intelligent surface-assisted wireless communication exploiting statistical csi,” *IEEE Transactions on Vehicular Technology*, vol. 68, pp. 8238–8242, Aug 2019.
- [5] J. C. Bucheli Garcia, M. Kamoun, and A. Sibille, “Reconfigurable passive relaying array for coverage enhancement,” in *2019 IEEE Wireless Communications and Networking Conference (WCNC)*, pp. 1–6, April 2019.
- [6] A. M. Sayeed, “Deconstructing multiantenna fading channels,” *IEEE Transactions on Signal Processing*, vol. 50, pp. 2563–2579, Oct 2002.
- [7] P. del Hougne, M. Fink, and G. Lerosey, “Optimal Communication Channels in a Disordered World with Tamed Randomness,” *arXiv e-prints*, p. arXiv:1810.00430, Sep 2018.

## **Performances des techniques de diversité de polarisation dans les systèmes MIMO massifs**

*Polarization Diversity Performance in massive MIMO systems*

---

**Frédéric Challita<sup>1</sup>, Pierre Laly<sup>1</sup>, Davy P. Gaillot<sup>1</sup>, Martine Liénard<sup>1</sup>, Pierre Degauque<sup>1</sup>, Marwan Yusuf<sup>2</sup>, Wout Joseph<sup>2</sup>, Emmeric Tanghe<sup>2</sup>**

<sup>1</sup>Université de Lille, IEMN/TELICE, {frédéric.challita}@univ-lille.fr

<sup>2</sup>Université de Gand, IMEC {wout.joseph}@ugent.be

---

*Mots clés : MIMO massifs, diversité de polarisation, corrélation spatiale.  
Massive MIMO, polarization diversity, spatial correlation, Industry 4.0, 5G*

---

### **Résumé/Abstract**

L'objectif de cette contribution est d'étudier les possibilités offertes par la diversité de polarisation dans les systèmes MIMO massifs, pouvant ainsi mener à une diminution de la taille géométrique du réseau, évitant entre autre, la non-stationnarité spatiale sur celui-ci. Les performances des différentes approches possibles sont comparées théoriquement entre elles et exprimées en termes de capacité totale théorique ("sum-rate capacity"). Pour cela, des mesures de matrices de transfert du canal ont été menées dans un hall industriel, les applications visées dans cet article concernant essentiellement l'industrie 4.0. Les valeurs des éléments de ces matrices servent de données d'entrée dans le calcul de la capacité permettant ainsi d'optimiser les techniques de diversité et de quantifier leur apport.

This paper describes a possible way of using polarization diversity in massive MIMO systems, thus leading to a decrease of the size of the array. The predicted gain in terms of sum-rate capacity is compared to that obtained without diversity, assuming well-known precoding techniques. To achieve this goal, measurements of channel transfer matrices have been carried out in an industrial hall, typical of an industry 4.0 environment. Their values are then used as an input for optimizing the diversity scheme and for quantifying its performances.

### **1 Introduction**

Afin d'assurer des communications haut débit entre une station de base, que nous noterons BS pour simplifier, et un grand nombre d'utilisateurs (UE), les techniques dites « MIMO massifs» (Multiple Input Multiple Output) ont été largement étudiées. Comme, typiquement, un réseau massif implanté à la BS comporte une centaine d'éléments, les avantages attendus de cette technique ont trait notamment à : la diminution des interférences entre utilisateurs, une efficacité spectrale élevée et des gains de réseaux importants. Il en résulte une grande fiabilité des liens montants et descendants, ainsi qu'une possibilité de focaliser l'énergie dans des petites régions de l'espace. De plus, l'augmentation du nombre d'antennes procure une meilleure orthogonalité entre canaux.

Cependant les performances des MIMO massifs dépendent des caractéristiques globales des canaux et notamment des corrélations entre les canaux des différents UEs. Par exemple, dans le cas d'une liaison en vue directe (LOS, Line of Sight), une corrélation importante mènera à une forte diminution de la capacité totale du canal (« sum-rate capacity »). Pour pallier ce problème, tout au moins en partie, nous avons proposé une nouvelle stratégie d'allocation des antennes de la BS, basée sur la diversité de polarisation [1]. Les exemples que nous présenterons se rapportent à des liaisons à l'intérieur de bâtiments et notamment en environnement industriel, dans le cadre de l'industrie 4.0 [2].

Nous présentons tout d'abord la configuration géométrique de l'environnement dans lequel les mesures ont été effectuées ainsi que les caractéristiques du système de mesure. Nous exploiterons ensuite les résultats de ces mesures afin d'en déduire les propriétés statistiques des canaux de propagation et notamment les facteurs de dépolarisatoin et de corrélation entre ces canaux. La méthode proposée basée sur une diversité de polarisation et utilisant, pour le réseau massif, des antennes à double polarisation, est ensuite décrite, les canaux mesurés servant de données d'entrée pour évaluer ses performances.

## 2 Description de l'environnement et du principe de mesure

Les mesures ont été effectuées dans un grand hall industriel de dimensions 21.3x77.2x12.2 m<sup>3</sup>. Les diverses parois de ce hall sont en béton, une large porte métallique située à l'extrémité du hall est restée fermée durant toute la période de mesures. De nombreuses structures métalliques sont présentes au sein du hall et correspondent soit à des machines outils, soit à des systèmes de mesure et de test que l'on peut trouver dans des ensembles automatisés associés à l'industrie 4.0. La Figure 1a permet de se rendre compte de la configuration de l'environnement vue du réseau d'émission (Tx). Le récepteur (Rx) est déplacé au niveau du rez de chaussée du bâtiment en K=15 positions successives et se trouve donc dans des situations LOS ou NLOS (Non-LOS). A titre d'exemple, La Figure 1b montre une position de Rx en configuration NLOS.



Figure 1 : a) Configuration du hall vue de l'antenne d'émission; b) Antenne de réception en situation NLOS

Les 15 positions successives de Rx sont indiquées sur la Figure 2 [1].

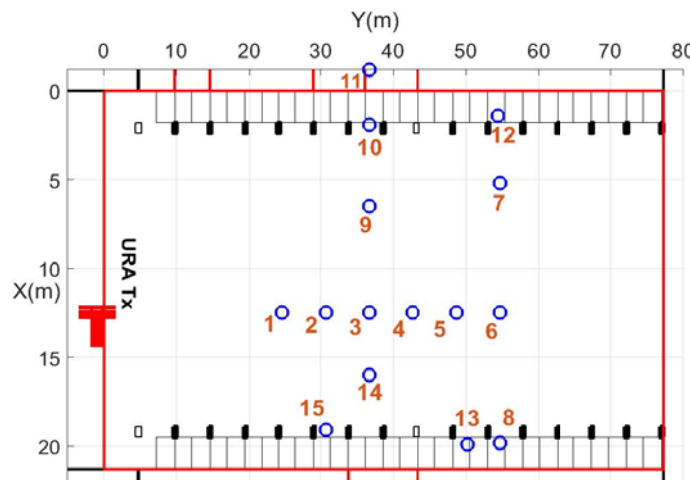


Figure 2 : Positions successives de l'antenne de réception

Lors des mesures, 3 fréquences ont été envisagées : 1.35, 3.5 et 6 GHz et pour ces 3 cas, des antennes planaires (patchs) à simple polarisation ont été utilisées. La direction de polarisation du patch en réception est verticale, celle du patch d'émission étant soit verticale, soit horizontale, le changement de polarisation s'effectuant par simple rotation du patch. Le réseau massif a été simulé par un réseau virtuel, le patch étant déplacé dans le plan vertical grâce à un moteur pas à pas piloté par le dispositif de mesure. Des mesures préliminaires en chambre anéchoïque ont montré que la réjection entre des mesures en polarisation et verticale est de 25 dB.

Pour la fréquence la plus basse de 1.35 GHz, ce réseau virtuel est rectangulaire et de dimensions 5x10 (50 éléments). Pour les 2 autres fréquences, le réseau est carré et comporte 100 éléments. L'espacement entre les éléments de ce réseau virtuel est d'environ  $\lambda/2$ ,  $\lambda$  étant la longueur d'onde de la fréquence centrale. Les mesures des fonctions de transfert entre Rx et les divers éléments de Tx sont effectuées à l'aide d'un analyseur de réseau dans 80 MHz de bande. Cet analyseur étant placé à proximité de Tx, un de ses ports est relié à Rx par l'intermédiaire d'une fibre optique et d'un convertisseur électro-optique, la distance Tx-Rx pouvant atteindre 60 m.

### 3 Caractéristiques statistiques des différents canaux

Dans une première étape, les configurations LOS et NLOS qui ont été choisies correspondent à la position du Rx notée respectivement 1 et 11 sur la Figure 2. Le facteur de discrimination en polarisation croisée (XPD) qui sera présenté, a été calculé pour une fréquence de 3.5 GHz.

Les différentes valeurs de XPD sont celles déduites de la valeur moyenne de la puissance reçue dans la bande des 80 MHz mais calculées pour chaque lien entre un UE et une des antennes du réseau virtuel. Pour cette fréquence de 3.5 GHz, le réseau étant de taille 10x10, on obtient ainsi 100 valeurs du XPD, dont l'étalement traduit la non stationnarité des caractéristiques des canaux sur la surface du réseau. La Figure 3 montre la fonction cumulative de distribution (cdf) du XPD ainsi obtenue. On remarque que la valeur médiane de XPD est de 7 dB en NLOS et de 17 dB en LOS.

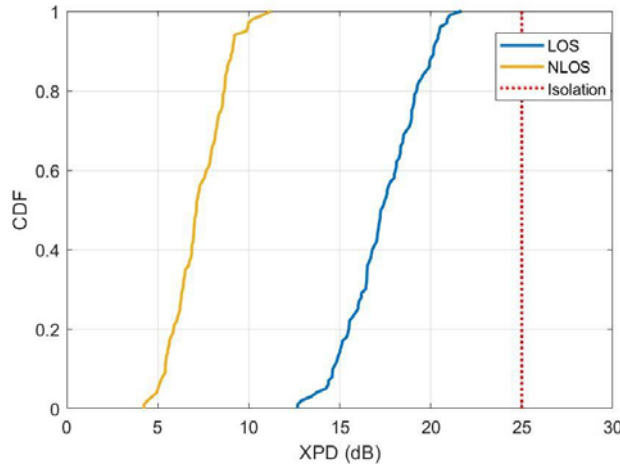


Figure 3. Fonction cumulative de distribution du facteur de discrimination en polarisation croisée

Signalons enfin que l'atténuation supplémentaire moyenne que présente l'ensemble des configurations NLOS par rapport aux configurations LOS est d'environ 15 dB.

Une autre caractéristique importante des canaux MIMO massifs est la matrice de corrélation spatiale en réception  $\mathbf{R}_{rx}$  qui traduit la corrélation entre les différents UEs. Pour simplifier la présentation des figures, choisissons un exemple correspondant à un réseau de 32 éléments à double polarisation. Les Figures 4a et 4b indiquent la valeur moyenne des éléments de  $\mathbf{R}_{rx}$  si les orientations des antennes de Tx et de l'UE correspondent respectivement à une liaison en situation de co-polarisation (co-polar), verticale dans notre cas, ou de cross polarisation (X-polar).

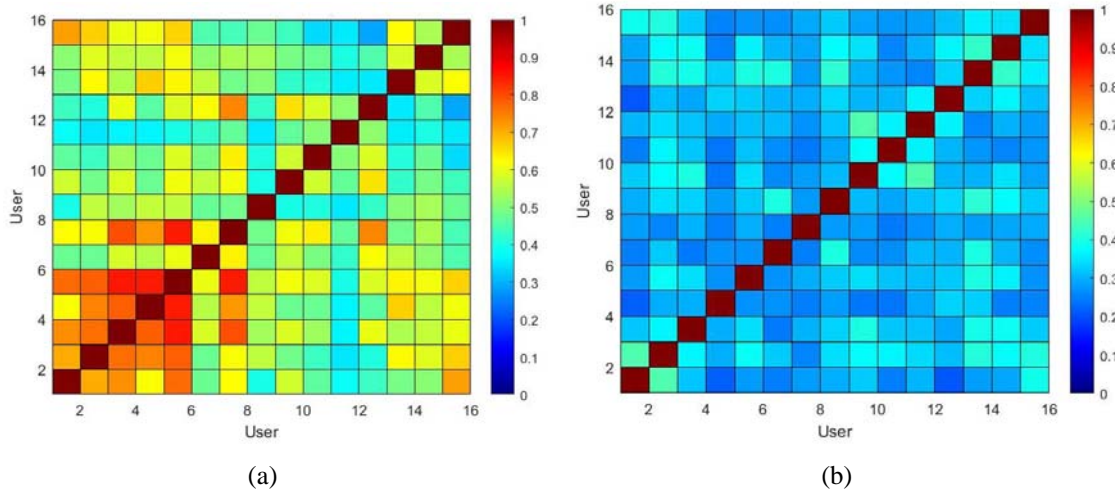


Figure 4. Valeurs des éléments de la matrice de corrélation spatiale  $\mathbf{R}_{rx}$  les antennes Tx et Rx étant toutes, soit co-polarisées (a) soit en polarisation croisée (b)

Tout d'abord, si toutes les antennes sont co-polar, la corrélation entre les UEs qui sont en condition LOS et numérotés de 1 à 7 sur la Figure 2, est beaucoup plus grande que celle pour les UEs en NLOS (8 à 15). De plus,

la comparaison entre les Figures 4a et 4b montre que la corrélation décroît rapidement en utilisant des antennes en X-polar plutôt qu'en co-polar, mais au prix d'une diminution de la puissance reçue, compte tenu des valeurs de XPD indiquées précédemment.

#### 4 Diversité de polarisation : principe et performances

Pour aboutir donc au meilleur compromis entre corrélation et perte de puissance, nous proposons d'utiliser, pour le réseau massif, des antennes à double polarisation. L'idée de base de la méthode consiste à choisir, pour chaque UE, une liaison co-polar ou X-polar en fonction de la corrélation que présente ce canal avec ses proches voisins. Les K UEs seront ainsi divisés en 2 groupes  $K_{co}$  et  $K_X$ , pour lesquels les liens s'effectueront respectivement en co- et X-polar. L'affection d'un UE à l'un ou l'autre groupe, est faite à partir des caractéristiques de la matrice de corrélation entre canaux, mesurée lors d'une phase d'initialisation [1].

Diverses stratégies d'allocation des polarisations ont été étudiées mais nous nous limiterons dans ce résumé à l'une d'entre elles. Celle-ci consiste à affecter des polarisations différentes à 2 liens, entre Tx et un premier UE repéré par son indice  $i$  et entre Tx et un autre UE d'indice  $j$ , si et seulement si le coefficient de corrélation  $\rho_{i,j}$  est supérieur à un seuil de valeur donnée,  $\rho_{th}$ . Des études paramétriques ont montré que la valeur optimum de  $\rho_{th}$  est de 0.75. Avec cette approche, ce seront donc surtout les liens en LOS qui utiliseront une transmission en X-polar car ils présentent une corrélation beaucoup plus élevée que pour les liens NLOS.

Pour quantifier la performance de cette méthode sur un exemple, la capacité totale des liaisons décrites dans les paragraphes 2 et 3 a été calculée en envisageant 2 précodages linéaires : MRT (Maximum Ratio Transmission) ou Zero-Forcing (ZF) et en supposant que le réseau massif est constitué de 50 antennes à double polarisation. La fréquence d'émission est de 3.5 GHz et le rapport signal sur bruit moyen lorsque les antennes sont co-polar est de 20 dB. La capacité ainsi obtenue peut être comparée dans le tableau 1 à celle calculée en supposant que tous les liens ont une polarisation soit co-polar, soit X-polar. Le nombre d'éléments du réseau est, dans ce dernier cas, égal à 100 pour que le nombre de ports d'entrée sur le réseau soit identique.

Precodage	Co-polar	X-polar	Diversité
MRT	9	21	12
ZF	100	67	96

Tableau 1 : Capacité totale (bps/Hz) pour 2 types de précodage linéaire et en supposant que tous les liens s'effectuent dans des conditions co-polar, X-polar ou avec diversité de polarisation

Ce tableau montre tout d'abord que la polarisation croisée permet d'atteindre, avec le MRT, des performances supérieures à celle d'une co-polarisation, malgré la diminution de la puissance reçue. Cependant, les résultats avec le MRT restent notablement inférieurs à ceux du ZF. Comme le ZF tend à minimiser les interférences entre utilisateurs, les meilleurs résultats sont obtenus en co-polar, la puissance reçue étant plus importante dans ce cas. On remarque que la diversité de polarisation permet d'atteindre des performances comparables, en termes de capacité, à celles obtenues en utilisant des canaux soient tous co-polarisés soit tous en polarisation croisée.

Un des avantages de cette technique est qu'elle permet de diviser d'un facteur 2 la taille du réseau, minimisant ainsi sa non-stationnarité spatiale.

Pour conclure, rappelons que ce seront surtout les liaisons en LOS qui seront en polarisation croisée. Il en résultera que le rapport signal sur bruit moyen sera du même ordre de grandeur pour tous les liens. En effet l'atténuation supplémentaire pour les liens NLOS en co-polar à une valeur très voisine du XPD qui s'appliquera aux liaisons LOS.

#### Références bibliographiques

- [1] F. Challita, P. Laly, D. P. Gaillot, M. Liénard, P. Degauque, M. Yusuf, W. Joseph and E. Tanghe, "Massive MIMO communication strategy using polarization diversity for industrial scenarios," IEEE Antennas and Wireless Propag. Letters, à paraître, 2020
- [2] E. G. Larsson, O. Edfors, F. Tufvesson, and T. L. Marzetta, "Massive MIMO for next generation wireless systems," IEEE Commun. Mag., vol. 52, no2, pp. 186–195, February 2014

## Path-Loss Modeling of Reconfigurable Intelligent Surfaces – Mirror or Diffuser?

---

*Marco Di Renzo<sup>1</sup>*

<sup>1</sup> Université Paris-Saclay, CNRS, CentraleSupélec, Laboratoire des Signaux et Systèmes, Gif-sur-Yvette, France  
*{marco.direnzo@centralesupelec.fr}*

---

**Keywords:** Smart radio environments, reconfigurable intelligent surfaces.

---

### Abstract

In this paper, we will illustrate when a reconfigurable intelligent surfaces behaves as a mirror and as a diffuser

### 1 Introduction

Future wireless networks will be as pervasive as the air we breathe, not only connecting us but embracing us through a web of systems that support personal and societal well-being. That is, the ubiquity, speed and low latency of such networks will allow currently disparate devices and services to become a distributed intelligent communications, sensing, and computing platform.

Small cells, massive MIMO, millimeter-wave communications are three fundamental technologies that will spearhead the emergence of 5G wireless networks - Their advantages are undeniable. The question is, however, whether these technologies will be sufficient to meet the requirements of future wireless networks that integrate communications, sensing, and computing in a single platform.

Wireless networks, in addition, are rapidly evolving towards a software-defined design paradigm, where every part of the network can be configured and controlled via software. In this optimization process, however, the wireless environment itself - the medium or channel - is generally assumed uncontrollable and often an impediment to be reckoned with. For example, signal attenuation limits the network connectivity, multi-path propagation results in fading phenomena, reflections and refractions from objects are a source of uncontrollable interference.

Recently, a new concept called reconfigurable intelligent surfaces (RISs) has emerged wherein every environmental object is coated with man-made intelligent surfaces of configurable electromagnetic materials. These materials would contain integrated electronic circuits and software that enable control of the wireless medium. Thus, RISs enable telecommunication operators to sculpt the very medium that comprises the network. With the aid of RISs, wireless networks will not be designed anymore to adapt themselves to the environment, but the environment will become part of the optimization space. As such, RISs have the potential to fundamentally change how wireless networks are designed and usher in that hoped-for wireless future. But, RISs are not currently well-understood.

One of the main open and most debated issues in the emerging research field of RISs is the development of a practical, accurate, and tractable path-loss model. In this talk, by using electromagnetic theory, we show when RISs can be modeled as mirrors and diffusers, which directly impacts the path-loss model. Numerical results are illustrated to substantiate the analytical findings. In addition to theory, experimental results by using small-size and large-size RISs will be illustrated.

### References

- [1] arXiv:1911.05326.
- [2] arXiv:2001.10862.

# Optimization and Analysis of Deep Unfolding Based Double Loop Turbo Equalizers

**Serdar Sahin<sup>1</sup>, Antonio M. Cipriano<sup>1</sup>, and Charly Poulliat<sup>2</sup>**

<sup>1</sup> Thales, {serdar.sahin, antonio.cipriano}@thalesgroup.com

<sup>2</sup> Toulouse INP, IRIT-ENSEEIHT, charly.poulliat@enseeiht.fr

---

**Keywords:** inter-symbol interference, iterative equalization, expectation propagation, deep unfolding

---

**Abstract:**

This paper investigates the use of hybrid model-and-data-based deep learning on a recently proposed doubly-iterative turbo equalizer for handling inter-symbol interference (ISI) channel with single-carrier frequency domain equalization (SC-FDE). The receiver is obtained through a message-passing-based approximate Bayesian inference technique, known as expectation propagation (EP). Although this turbo-equalizer has been shown to behave asymptotically like maximum a posteriori (MAP) detection, finite-length numerical results suffer from drawbacks due to simplifying assumptions used during the modelling. Such limitations are partially mitigated by tuning heuristic hyper-parameters through robust learning algorithms. In this article, this strategy is further investigated with discussion on optimized parameters and with the use of an alternative loss function for training, or by adding further capabilities to adapt learned parameters to the channel state information.

## 1 Introduction

The potential impact of deep learning techniques for addressing interference mitigation problems at the physical layer is a hot topic. While data-driven artificial intelligence (AI) techniques with “black-box” neural networks have proven their worth in various signal processing fields with a modelling deficit, such as image or audio processing, their use for classical digital communications problems at the physical layer is questionable. The transmitter and channel models for most wireless systems are often accurate enough for the derivation of near-optimal signal processing algorithms, however resulting solutions may suffer from excessive computational complexity. In this context, hybrid AI techniques are of interest, by locally using learnable functions or parameters within a model-based algorithm, for handling modelling deficiency or for reducing algorithm complexity [1]. These techniques also have the advantage of requiring lower training complexity and their behaviour is more explainable than complex neural-network structures [2, 3, 4].

Here we study near-optimal detection and decoding of single-carrier transmissions with bit interleaved coded modulation (BICM). There is a long research track addressing this problem with iterative turbo detection and decoding techniques that provide reasonable performance and computational complexity trade-off [5, 6, 7]. More recently, doubly-iterative soft-input soft-output (SISO) detectors have gathered attention, and they are derived by exploiting Bayesian learning with expectation propagation (EP) [8].

Frequency domain equalizers (FDEs) obtained with such structures share similarities with approximate message passing (AMP) techniques [9], and, by using the deep unfolding approach [4], they can be seen as neural networks with some free hyper-parameters to be tuned.

## 2 System Model and EP-based Equalization

### 2.1 SC-FDE Transmission Model

This paper considers single-carrier block transmissions, circularized with cyclic prefix. Using a BICM scheme, a  $K_b$ -bits information block  $\mathbf{b}$  is encoded and then interleaved into a binary sequence  $\mathbf{d}$  of length  $K_d$ . A memoryless modulator  $\varphi$  maps this sequence to  $\mathbf{x} \in \mathcal{X}^K$ , with  $|\mathcal{X}| = M$ ,  $Q = \log_2 M$  and  $K = K_d/Q$ . This operation maps the  $Q$ -word  $\mathbf{d}_k \triangleq [d_{Q(k-1)+1}, \dots, d_{Qk}]$  to the symbol  $x_k$ , and  $\varphi_q^{-1}(x_k)$  or  $d_{k,q}$  are used to refer to  $d_{kQ+q}$ .  $\mathcal{X}$  is such that independently and identically distributed (IID) data symbols have a zero-mean and unit variance, i.e.  $\sigma_x^2 = 1$ .

Assuming perfect synchronization in both time and frequency with the transmitter, and ideal channel state information, the received baseband observations are  $\mathbf{y} = \mathbf{H}\mathbf{x} + \mathbf{w}$ , with,  $\mathbf{H}$  being the channel matrix and  $\mathbf{w} \sim \mathcal{CN}(\mathbf{0}_K, \sigma_w^2 \mathbf{I}_K)$  is the additive complex circularly symmetric white Gaussian noise (AWGN).  $\mathbf{H}$  is a circulant

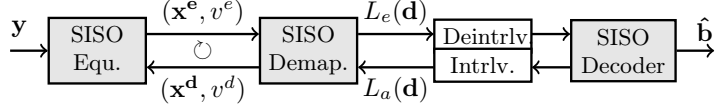


Figure 1 – Doubly-iterative EP-based receiver structure.

matrix, whose first column is  $\mathbf{h} = [h_0, \dots, h_{L-1}, \mathbf{0}_{1,K-L}]$ ,  $L < K$  being the channel spread. In the frequency domain, the observation are

$$\underline{\mathbf{y}} = \mathcal{F}_K \mathbf{y} = \underline{\mathbf{H}} \mathbf{x} + \underline{\mathbf{w}}, \quad (1)$$

where  $\underline{\mathbf{x}} = \mathcal{F}_K \mathbf{x}$ ,  $\underline{\mathbf{w}} = \mathcal{F}_K \mathbf{w}$  and  $\underline{\mathbf{H}} = \mathcal{F}_K \mathbf{H} \mathcal{F}_K^H$ .  $\mathcal{F}_K$  is the normalized  $K$ -point discrete Fourier transform (DFT) matrix whose elements are  $[\mathcal{F}_K]_{k,l} = \exp(-2j\pi kl/K)/\sqrt{K}$ , and such that  $\mathcal{F}_K \mathcal{F}_K^H = \mathbf{I}_K$ . Thanks to DFT properties, we have  $\underline{\mathbf{w}} \sim \mathcal{CN}(\mathbf{0}_K, \sigma_w^2 \mathbf{I}_K)$  and  $\underline{\mathbf{H}} = \text{Diag}(\underline{\mathbf{h}})$  with  $\underline{\mathbf{h}} = \sqrt{K} \mathcal{F}_K \mathbf{h}$ .

At the receiver, we consider the use of an iterative detection and decoding scheme, where a SISO decoder exchanges extrinsic information with a SISO detector, through log-likelihood ratios (LLRs) on coded bits, thanks to BICM. From the SISO detector's point of view, prior and extrinsic LLRs are respectively denoted as  $L_a(d_{k,q})$  and  $L_e(d_{k,q})$ , and the prior probability mass function (PMF) on a symbol  $x_k$  is denoted as  $\mathcal{P}_k(\alpha)$ ,  $\forall \alpha \in \mathcal{X}$ . Iterations between these two modules will be denoted with  $\tau = 0, \dots, \mathcal{T}$  in the superscript, with  $\mathcal{T}$  being the fixed total number of turbo-iterations.

## 2.2 EP-based Iterative Frequency Domain Equalizer

The optimal detection and decoding solution for the considered communication system is well-known to be given by the maximum a posteriori (MAP) criterion over the posterior probability density function (PDF)  $p(\mathbf{b}, \mathbf{d}, \mathbf{x}|\mathbf{y})$  marginalized on  $\mathbf{b}$ . The use of turbo detection through BICM facilitates this problem by decoupling the problem of detection and decoding thanks to SISO modules, which carry out MAP inference to estimate the coded block  $\mathbf{d}$ , under the assumption of using a sufficiently long interleaver along with memoryless mapping.

Nevertheless the computational and memory complexity of SISO MAP detection alone remains too high for the problem of equalization, due to exponentially growing number of states of the optimal BCJR algorithm. To alleviate this approximate Bayesian inference is performed with message passing algorithms such as Gaussian-approximated belief propagation (GaBP) or expectation propagation (EP), which yield filter-based turbo equalizers with lower complexity. In particular it is possible to derive low-complexity detectors (e.g. complexity scaling log-linearly in  $K$ ) in the FD through the use of fast Fourier transform (FFT) algorithm. In the remainder of this paper we will discuss a recently proposed EP-based double-loop frequency domain equalizer who has attractive properties compared to alternative AMP techniques in the same category [9].

The operating principle of this SISO detector is given in Figure 1, where the detector itself consists of a SISO equalizer, which is an minimum-mean square error-like (MMSE-like) filter, exchanges soft estimates on data symbols with a SISO demapper. This technique major advantage compared to alternative iterative FDE is that soft data estimates  $(\mathbf{x}^e, v^e)$  and  $(\mathbf{x}^d, v^d)$  correspond to extrinsic information in the conventional turbo principle, and their correlation and orthogonality properties ensure good and predictable convergence properties for the iterations between the equalizer and the demapper [10]. Soft estimates from the demapper enable the equalizer to more adequately remove interference from the observations, while limiting the possible bias to its own outputs, and thus improving the equalization performance. The detailed description of this detection algorithm, called double-loop scalar EP (DL-SEP), is provided in Algorithm 1.

## 3 Unfolded Doubly-Iterative Turbo Equalization

Deep unfolding is a machine learning technique which enables deriving a multi-layer neural structure based on an iterative algorithm. The parameters of the original algorithm can become learnable parameters, or additional learnable parameters can be added based on expert insight on the involved heuristics and loose approximations on the original algorithm. This approach has been successfully applied to belief propagation (BP) based decoding algorithms by applying smoothing weights on exchanged messages [12]. On the other hand, in [13], Vector AMP (VAMP) algorithm has been unfolded (without any additional smoothing), and all its linear filtering parameters and non-linear decision parameters has been left free for optimization through learning. As a result, the optimized parameters behave identically to the analytical MMSE-optimal solution of VAMP, thus showing that among iterative detection structures that consist of successive linear and non-linear estimators, EP-based algorithms such as VAMP/OAMP (without smoothing, i.e.  $\beta = 0$ ) are already optimal with respect to their structures, and exhaustive learning of all parameters is not necessary.

The unfolding concept has been applied to SISO detector design in [9], by optimizing some hyper-parameters of the DL-SEP algorithm. As this algorithm belongs to the category of EP-based MMSE-optimal VAMP/OAMP-like techniques, relearning the filters and the decision function is not expected to bring any significant gain.

---

**Algorithm 1** Double-Loop Scalar EP Equalizer (DL-SEP) [11]

---

**Input**  $\underline{\mathbf{y}}$ ,  $\underline{\mathbf{H}}$ ,  $\sigma_w^2$ 

- 1: Initialize the decoder with  $L_a^{(0)}(\mathbf{d}_k) = 0, \forall k$ .
  - 2: **for**  $\tau = 0$  to  $\mathcal{T}$  **do**
  - 3:   Update the prior PMF on  $x_k$ , with  $\forall k, \forall \alpha \in \mathcal{X}$ ,
  - 4:   
$$\mathcal{P}_k^{(\tau)}(\alpha) \propto \exp\left(-\sum_{q=1}^Q \varphi_q^{-1}(\alpha) L_a(d_{k,q})\right).$$
  - 5:   Compute the prior mean and variance of  $x_k$ ,  $\forall k$   

$$x_k^{p(\tau)} \triangleq \mathbb{E}_{\mathcal{P}}[x_k] = \sum_{\alpha \in \mathcal{X}} \alpha \mathcal{P}_k^{(\tau)}(\alpha), \quad v^{p(\tau)} \triangleq \frac{1}{K} \sum_k \text{Var}_{\mathcal{P}}[x_k] = \frac{1}{K} \sum_k \left( \sum_{\alpha \in \mathcal{X}} |\alpha|^2 \mathcal{P}_k^{(\tau)}(\alpha) - |x_k^{p(\tau)}|^2 \right).$$
  - 6:   Initialize the soft feedback on  $x_k$  with the priors,  $\forall k$ ,  $x_k^{d(\tau,0)} = x_k^{p(\tau)}$  and  $v^{d(\tau,0)} = v^{p(\tau)}$ .
  - 7:   **for**  $s = 0$  to  $\mathcal{S}$  **do**
  - 8:     Perform FFT on  $\mathbf{x}^{\mathbf{d}(\tau,s)}$  to get  $\underline{\mathbf{x}}^{\mathbf{d}(\tau,s)}$ .  
 MMSE filtering with interference cancellation is performed for  $k = 1, \dots, K$ ,  

$$\xi^{(\tau,s)} = K^{-1} \sum_k |\underline{h}_k|^2 / (\sigma_w^2 + v^{d(\tau,s)} |\underline{h}_k|^2),$$
  

$$\underline{f}_k^{(\tau,s)} = \underline{h}_k / [\xi^{(\tau,s)} (\sigma_w^2 + v^{d(\tau,s)} |\underline{h}_k|^2)],$$
  

$$\underline{x}_k^{e(\tau,s)} = \underline{x}_k^{d(\tau,s)} + \underline{f}_k^{(\tau,s)*} (\underline{y}_k - \underline{h}_k \underline{x}_k^{d(\tau,s)}),$$
  

$$v^{e(\tau,s)} = 1/\xi^{(\tau,s)} - v^{d(\tau,s)}.$$
  - 9:     Perform IFFT on  $\underline{\mathbf{x}}^{d(\tau,s)}$  to get  $\mathbf{x}^{d(\tau,s)}$ .
  - 10:    Update a posteriori PMF of  $x_k$ , with  $\forall k, \forall \alpha \in \mathcal{X}$ ,  

$$\mathcal{D}_k^{(\tau,s)}(\alpha) \propto \exp\left(-|x_k^{e(\tau,s)} - \alpha|^2 / v^{e(\tau,s)}\right) \mathcal{P}_k^{(\tau)}(\alpha).$$
  - 11:    **if**  $s < \mathcal{S}$  **then**
  - 12:     Compute the mean and the variance of APP PMF of  $x_k$ ,  $\forall k$   

$$\mu_k^{d(\tau,s)} \triangleq \mathbb{E}_{\mathcal{D}}[x_k] = \sum_{\alpha \in \mathcal{X}} \alpha \mathcal{D}_k^{(\tau,s)}(\alpha), \quad \gamma^{d(\tau,s)} \triangleq K^{-1} \sum_k \text{Var}_{\mathcal{D}}[x_k],$$
  - 13:     The soft data feedback towards the equalizer is computed through the division of the PDF  $\mathcal{CN}(\mu_{p,k}^{d(\tau,s)}, \gamma_p^d)$ , by the PDF  $\mathcal{CN}(x_{p,k}^{e(\tau,s)}, v_p^e)$   

$$v^{*(\tau,s)} \triangleq 1/(1/\gamma^{d(\tau,s)} - 1/v^{e(\tau,s)}),$$
  

$$x_k^{*(\tau,s)} \triangleq v^{*(\tau,s)} \left( \mu_k^{d(\tau,s)} / \gamma^{d(\tau,s)} - x_k^{e(\tau,s)} / v^{e(\tau,s)} \right).$$
  - 14:     Avoid undesirable fixed points of EP (local extrema) through smoothing ( $0 \leq \beta \leq 1$ ),  

$$x_k^{d(\tau,s+1)} \triangleq (1 - \beta)x_k^{*(\tau,s)} + \beta x_k^{d(\tau,s)},$$
  

$$v^{d(\tau,s+1)} \triangleq (1 - \beta)v^{*(\tau,s)} + \beta v^{d(\tau,s)}.$$
  - 15:    **end if**
  - 16:   **end for**
  - 17:   Compute extrinsic LLRs,  $\forall k, q$   

$$L_e^{(\tau)}(d_{k,q}) \triangleq \ln \sum_{\alpha \in \mathcal{X}_q^0} \mathcal{D}_k^{(\tau,s)}(\alpha) - \ln \sum_{\alpha \in \mathcal{X}_q^1} \mathcal{D}_k^{(\tau,s)}(\alpha) - L_a^{(\tau)}(d_{k,q}),$$
  
 with  $\mathcal{X}_q^b = \{\alpha \in \mathcal{X} : \varphi_q^{-1}(\alpha) = b\}$ ,  $b \in \mathbb{F}_2$ , then feed them to the decoder to get next priors  $L_a^{(\tau+1)}(\mathbf{d}_k), \forall k$ .
  - 18: **end for**
- 

However, smoothing parameters can be learned in order to alleviate the message passing algorithm's weaknesses to short cycles on the factor graph. By considering a different damping value at each self-iteration, the learnable parameters are  $\{\beta^{(0)}, \beta^{(1)}, \dots, \beta^{(\mathcal{S})}\}$ , and to render them independent of the selected channel code, a mutual-information based loss function has been used in [9].

### 3.1 Mutual Information based Loss Functions for Learning SISO Detectors

In order to optimize the SISO detector with no dependence on the channel code, we propose to use a loss function that is directly inspired from the extrinsic information transfer (EXIT) analysis of turbo iterative systems [14]. The behaviour of the loss function is characterized by a single scalar that corresponds to the average mutual information (AMI)  $I_A$  between  $L_a(\mathbf{d})$  and  $\mathbf{d}$ . This approach can be effectively applied by considering the prior LLRs to be consistently Gaussian-distributed, i.e.  $L_a(\mathbf{d}) \sim \mathcal{N}((1 - 2d_{k,q})\mu_a, 2\mu_a)$ , with  $\mu_a = J^{-1}(I_A)$  and  $J(\mu) \triangleq 1 - \mathbb{E}_{L \sim \mathcal{N}(\mu, 2\mu)}[\log_2(1 + e^{-L})]$ . Next, in order to optimize the iterative convergence capabilities of the detector, the loss function should be directly dependent on the extrinsic LLRs  $L_e(\mathbf{d})$ , such that the optimized receiver also maximizes the area under the EXIT chart of the detector and thus enhance the achievable rates.

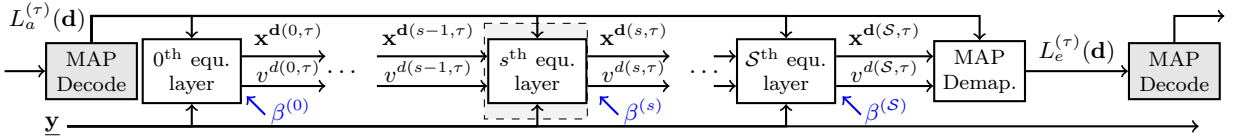


Figure 2 – “Learned-DL-SEP”: Unfolded deep EP network (with  $\mathcal{S}$  layers) at the  $\tau^{\text{th}}$  turbo iteration.

Hence the proposed training loss function  $\mathcal{L}$  is given as

$$\mathcal{L}(\mathbf{d}, \hat{\mathbf{d}}, I_A) \triangleq -\frac{1}{QNK} \sum_{k,q} \sum_n \ell(d_{k,q}, \hat{d}_{k,q}[n](I_A)), \quad (2)$$

$$\hat{d}_{k,q}[n](I_A) \triangleq \frac{1}{1 + \exp(L_e(d_{k,q}, I_A)[n])}, \quad (3)$$

where  $I_A$  is the AMI between artificially generated  $L_a(\mathbf{d})$  and  $\mathbf{d}$ ,  $L_e(\mathbf{d}, I_A)[n]$  is the extrinsic output of the unfolded network, when  $L_a(d_{k,q}, I_A)[n]$  is provided as priors, and  $n = 1, \dots, N$  denotes the index of prior LLR samples.  $\hat{d}_{k,q}[n](I_A)$  is a soft bit equivalent of the extrinsic messages, and  $\ell(d_{k,q}, \hat{d}_{k,q}[n](I_A))$  denotes a bit-wise loss metric, which will be specified in Section 3.2.

The training process is carried out with the ADAM optimizer [15], which is a stochastic gradient descent technique where the learning rate is automatically adjusted depending on the first and second order statistics’ estimates of the changes in the gradient of the loss function. By initializing the learning rate to 0.025, and by using mini-batches with 200 samples of

- noise variance realizations  $\sigma_w^2$ , with  $\text{SNR}_c = 20 \log_{10} \sigma_x / \sigma_w$  following uniform distribution over the interval of interest (e.g. 5 to 30 dB).
- a pseudo-codeword realization  $\mathbf{d}$ , uniformly selected among  $2^{K_d}$  possibilities,
- realizations of the noise vector  $\mathbf{w}$  and of the channel  $\mathbf{H}$ , according to  $\sigma_w^2$  and channel power-delay profile,
- a set of prior LLR realizations  $L_a(\mathbf{d}, I_a)[n]$ , for  $n = 1, \dots, N$ .

Learning process carries out an averaging over  $N$  prior codeword LLRs, for each sample of the mini-batch, in order to learn a value of the desired parameters  $\boldsymbol{\beta} = [\beta^{(0)}, \beta^{(1)}, \dots, \beta^{(\mathcal{S})}]$  as a function of  $I_A$ . Moreover, as there is a bijective between  $I_A$  and the prior variance of soft symbol estimates,  $v^{p(\tau)}$  (see line 4 of Algorithm 1),  $\boldsymbol{\beta}$  can be tabulated as a function of  $v^{p(\tau)}$ . Finally, during the practical deployment of the optimized receiver, instantaneous value of  $v^{p(\tau)}$  at the ongoing turbo-iteration  $\tau$  would enable the receiver to select its optimal weights  $\boldsymbol{\beta}$ .

This framework has enabled us to optimize DL-SEP by considering it as a deep neural network, and overcome somme error-floor issues at high SNR operating points in [9]. In the remainder of this paper we further investigate the capabilities and the extensions of this hybrid-AI based FDE structure.

### 3.2 The Impact of the Selected Loss Function

In our previous work, we have used the negative cross-entropy (CE) loss function, given by

$$\ell_{\text{CE}}(d_{k,q}, \hat{d}_{k,q}) = - \left[ d_{k,q} \log \left( \hat{d}_{k,q} \right) + (1 - d_{k,q}) \log \left( 1 - \hat{d}_{k,q} \right) \right], \quad (4)$$

which was selected due to its strong link to the mutual information of extrinsic LLRs, which enables the learning framework to optimize the extrinsic information of the SISO module.

In the context of channel decoding with unfolded BP, the use of an alternative metric, called the soft-bit-error-rate (SBER), given by

$$\ell_{\text{SBER}}(d_{k,q}, \hat{d}_{k,q}) = \hat{d}_{k,q}^{1-d_{k,q}} \left( 1 - \hat{d}_{k,q} \right)^{d_{k,q}}, \quad (5)$$

yields better results for optimizing the bit error rate (BER) and the packet error rate (PER) of the system [16]. Hence, we are interest to test its pertinence in the equalization application under investigation.

Finally, it is also possible to use a symbol-wise metric to optimize this receivers performance, by using the mean-squared error (MSE) between the equalized estimate  $x_k^e$  and the transmitted symbols  $x_k$  in order to focus the training on optimizing the filtering and interference cancellation stage.

First, in order to illustrate the capacity of each one of these loss functions to capture the behaviour of BER, or PER, we consider a simplified neural equalizer with up to two layers, where the same fixed parameter  $\beta$  is

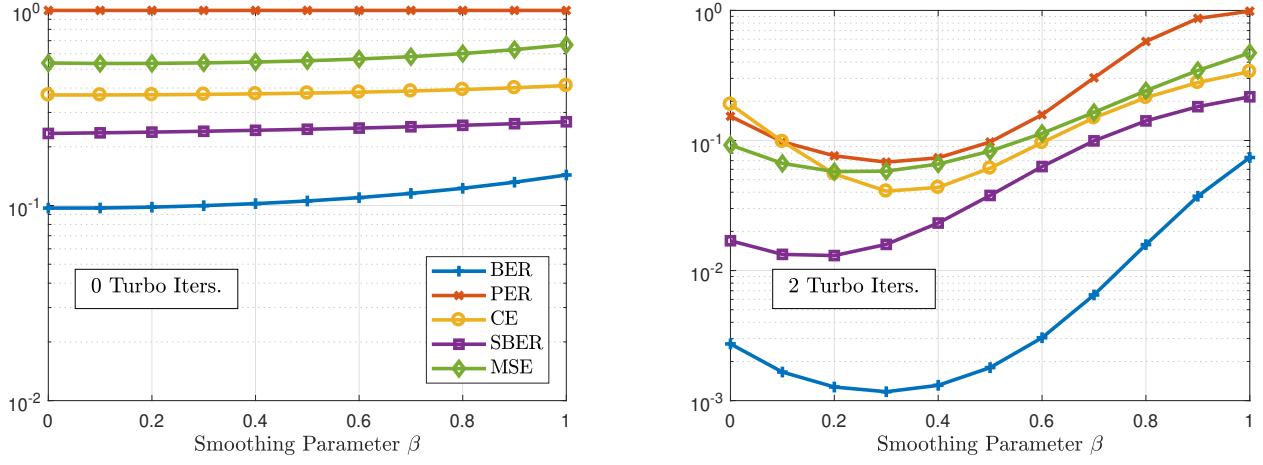


Figure 3 – Comparison of alternative loss metrics with BER and PER as a function of  $\beta$  for a 2-layer equalizer.

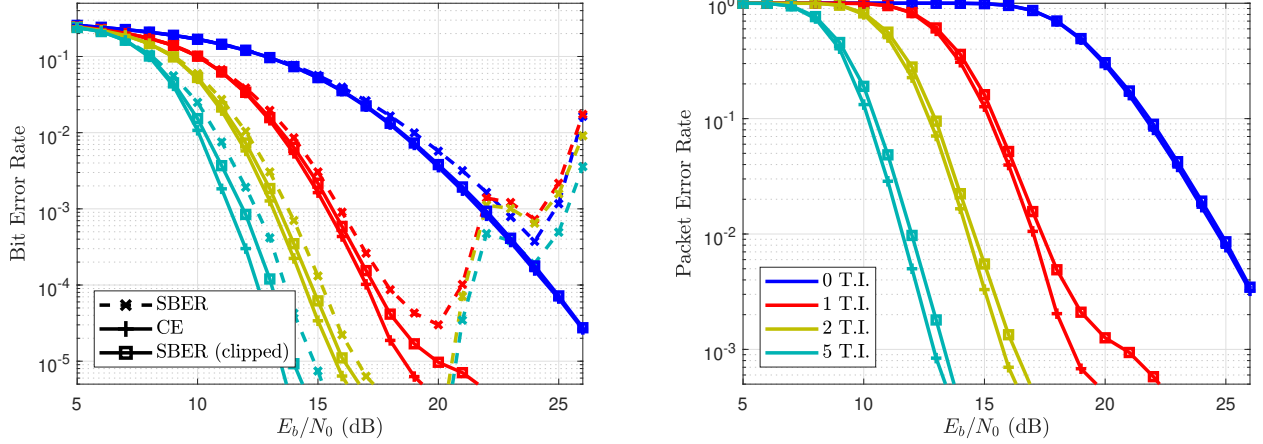


Figure 4 – Comparison of a 2-layer DL-SEP with trained parameters from different loss metrics.

used for smoothing. In this setting, for  $\beta$  varying from 0 to 1, BER, PER and the three loss functions above are measured.

In Figure 3, these loss functions are compared in the Proakis C channel for  $E_b/N_0 = 13$  dB, when a 2-layer (2 self-iterations) DL-SEP receiver is used with a recursive systematic convolutional (RSC) channel code of polynomials [7, 5]8 and rate 1/2 with 8-PSK modulation. It is seen that the minimum of SBER manages to accurately follow the optimum BER when the system is not turbo-iterated (i.e.  $I_A = 0$ , left plot), but not necessarily when there is feedback from the decoder (right plot). On the other hand, the minimum of CE provides overall a closer estimate to the optimum PER, whether the system is iterated or not. MSE does not provide a sufficiently accurate representation of optimal error rates.

Hence, we have carried out the training framework for both CE and SBER loss functions, in order to evaluate their impact on the actual receiver performance. The training of SBER appeared to be numerically more challenging than CE; the ADAM optimizer tends to seek values of  $\beta$  outside the interval  $[0, 1]$ , and trained values for low  $I_A$  can be negative. This results in severe degradation of BER performance at high SNR, and to overcome this limitation, we have manually clipped learned parameters to  $[0, 1]$ . The impact of this approach is illustrated in Figure 4-(a), where the raw use of trained parameters from SBER causes unacceptable BER degradations above 20 dB, and interestingly the use of clipping slightly improves the receiver decoding threshold. In Figure 4-(b), we compare the PER behaviour of a 2-layer DL-SEP when parameters are trained with CE and SBER (clipped), and CE is shown to outperform SBER overall, except in the absence of prior information, i.e. 0 T.I. (turbo iterations) where they nearly yield the same PER.

### 3.3 Interpretation of the Learned Parameters

Next, the values of the learned parameters (in our case the damping coefficients which control the receiver convergence behaviour) are discussed to illustrate that such hybrid learning techniques provide explainable results. In order to correctly interpret results, we recall that damping factors close to one means that the feedback from the previous self-iteration (equivalently, layer) is privileged. If damping factors of all self-iterations

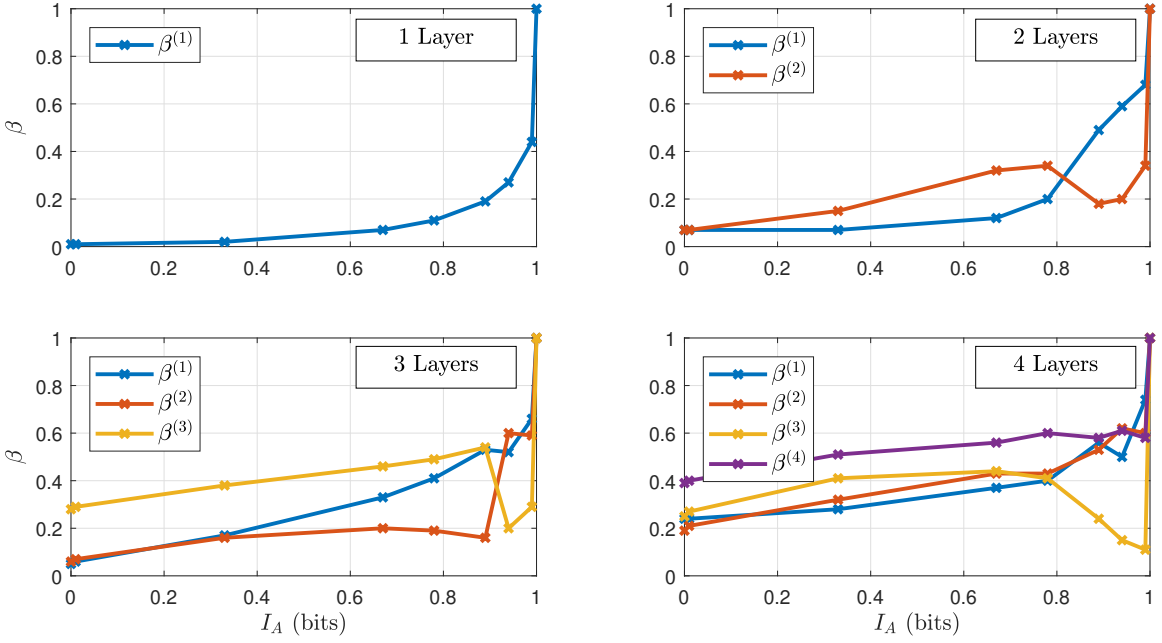


Figure 5 – Learned values of the damping parameters as a function of the mutual information  $I_A$  of prior LLRs provided by the decoder, for 1 to 4 inner “self-iteration” layers.

are high, the feedback from the decoder is weighted more. If damping factors are close to zero, the current feedback from the demapper takes more importance.

Figure 5 shows the values of the learned damping parameter as a function of the prior information  $I_A \in \{0, 0.33, 0.67, 0.78, 0.89, 0.94, 0.99, 1\}$  for different number of layers, by using the CE. The plotted values of  $\beta$  correspond to those used for simulations with CE in Figure 4. When there is no or very weak prior information  $I_A \approx 0$ , confidence is given to the demapper feedback ( $\beta \approx 0$ ), but in case of multiple layers, the damping factors of the deeper ones are higher (i.e. their feedback has weaker impact), thus controlling residual error propagation. When the prior information from the decoder is perfect, there is no need to equalize, hence  $\beta \rightarrow 1$ , otherwise a compromise is made across the layers. In particular, oppositely to the cases with low  $I_A$ , when  $I_A$  gets closer to 1 increased damping is used at the first layers in order thus privileging decoder feedback.

### 3.4 The Impact of SNR-adaptative Learned Parameters

In our previous works, as described in Subsection 3.1, the training is performed over a vast range of signal-to-noise ratio (SNR) interval to provide overall adequate learned parameters. Thus, in the context of DL-SEP, learned parameters are only dependent on the prior information  $I_A$  (or equivalently, the prior covariance  $v^{p(\tau)}$ ). In this section, we explore the effects adapting parameters to the operating point conditions by making learned hyper-parameters also SNR-dependent. Hence the learning procedure is changed to use a *fixed* noise variance, in order to have a set of learned parameters  $\beta^{(s)}(I_A, \sigma_w^2)$  tabulated as a function of  $I_A$  and  $\sigma_w^2$ .

In Figure 6 we compare the PER performance obtained with CE loss function in the conventional approach with parameters obtained through learning with SNR-dependent CE. The obtained improvements with the SNR-dependent parameters is less than 0.025 dB and thus we can conclude that the originally proposed framework which solely uses the prior information  $I_A$  for parameter adaptation is robust. Indeed, as the feedback from the decoder naturally incorporates some information about the state of the SNR, this learning framework appears to be attractive for optimizing SISO detectors.

## 4 Conclusion

The use of deep unfolding on iterative physical layer algorithms enables to overcome their modelling or complexity limitations by exploiting the powerful optimization capabilities of stochastic training strategies. In this paper, we aim to get a better grasp of unfolded turbo detection techniques that are optimized with hybrid-AI by further analysing the response of the proposed receiver to different learning parameters.

Our complementary investigations let us think that the promising soft BER loss functions, which provided reduced packet error rates in decoding applications, is not well adapted for turbo detection, while cross entropy on extrinsic soft bits seems to match better to the actual PER behaviour. Moreover, choosing the right loss function is fundamental also for reducing the complexity of the receiver. The cross entropy loss function matches

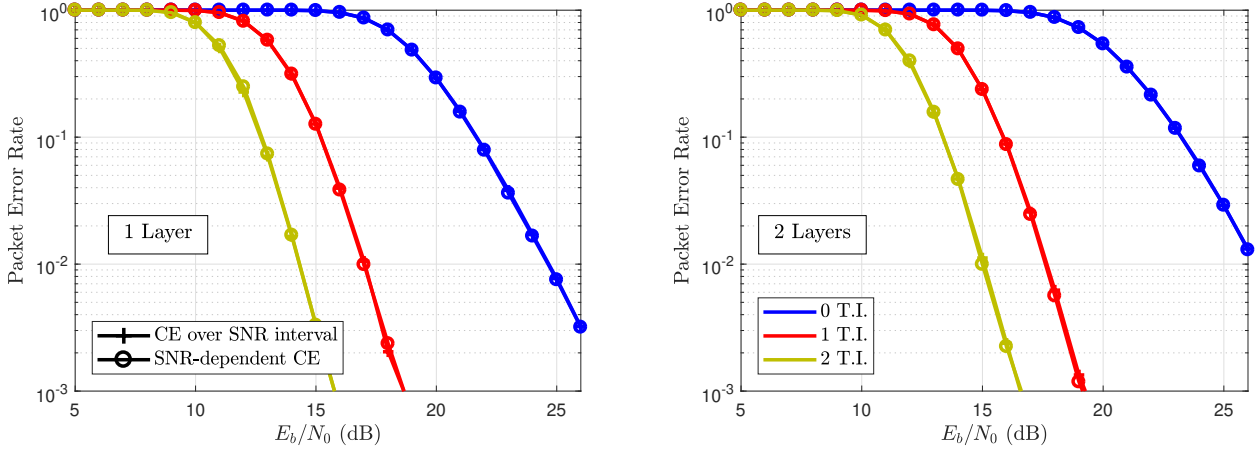


Figure 6 – Comparison of SNR-adaptative CE-based learned parameters with SNR-invariant CE-based learned parameters.

well with extrinsic information behaviour at the output of the demapper, and hence it allows to dynamically select optimal damping parameters only as a function of the average mutual information from the decoder, while adding SNR information is not necessary and brings no significant improvement.

Finally, by using deep unfolding, the neural network implemented at the receiver inherits the structure and fundamental behaviour of the underlying EP-based Bayesian inference algorithm, thus considerably simplifying the interpretation of the impact of the learned parameters on the receiver behaviour.

## 5 References

- [1] O. Simeone, “A very brief introduction to machine learning with applications to communications systems,” *IEEE Transactions on Cognitive Communications*, vol. 4, pp. 648 – 664, Dec. 2018.
- [2] A. Balatsoukas-Stimming and C. Studer, “Deep unfolding for communications systems: a survey and some new directions,” *a*, vol. abs/1906.05774, June 2019.
- [3] W. Guo, “Explainable artificial intelligence (xai) for 6g: Improving trust between human and machine,” *a*, vol. abs/1911.04542, Sept. 2019.
- [4] J. R. Hershey, J. Le Roux, and F. Weninger, “Deep unfolding: Model-based inspiration of novel deep architectures,” Tech. Rep. TR2014-117, Mitsubishi Electric Research Labs, 2014. Version 12.0.1.
- [5] C. Douillard, M. Jézéquel, C. Berrou, A. Picart, *et al.*, “Iterative correction of intersymbol interference: Turbo-equalization,” *Eur. Trans. Telecomm.*, vol. 6, pp. 507–511, Sept. 1995.
- [6] M. Tüchler and A. C. Singer, “Turbo equalization: An overview,” *IEEE Trans. on Inf. Theory*, vol. 57, pp. 920–952, Feb. 2011.
- [7] H. Loeliger, J. Dauwels, J. Hu, S. Korl, L. Ping, and F. R. Kschischang, “The factor graph approach to model-based signal processing,” *Proceedings of the IEEE*, vol. 95, pp. 1295–1322, June 2007.
- [8] M. Senst *et al.*, “How the framework of expectation propagation yields an iterative IC-LMMSE MIMO receiver,” in *IEEE 54th GLOBECOM*, Dec. 2011.
- [9] S. Şahin, C. Poulliat, A. M. Cipriano, and M.-L. Boucheret, “Doubly iterative turbo equalization: Optimization through deep unfolding,” in *IEEE 30th PIMRC*, pp. 1–6, Sept. 2019.
- [10] J. Ma and L. Ping, “Orthogonal AMP,” *IEEE Access*, vol. 5, pp. 2020–2033, Jan. 2017.
- [11] S. Şahin, A. M. Cipriano, C. Poulliat, and M.-L. Boucheret, “A framework for iterative frequency domain EP-based receiver design,” *IEEE Transactions on Communications*, vol. 66, pp. 6478–6493, Dec. 2018.
- [12] E. Nachmani, Y. Be’ery, *et al.*, “Learning to decode linear codes using deep learning,” in *54th Annual Allerton Conf.*, pp. 341–346, Sept. 2016.
- [13] M. Borgerding *et al.*, “AMP-inspired deep networks for sparse linear inverse problems,” *IEEE Transactions on Signal Processing*, vol. 65, pp. 4293–4308, Aug. 2017.
- [14] S. Ten Brink, “Designing iterative decoding schemes with the extrinsic information transfer chart,” in *AEU Int. JEC*, vol. 54, Jan. 2000.
- [15] D. P. Kingma and J. Ba, “Adam: a method for stochastic optimization,” in *Proc. Int. Conf. Learn. Represent.*, May 2015.
- [16] M. Lian, F. Carpi, C. Häger, and H. D. Pfister, “Learned belief-propagation decoding with simple scaling and snr adaptation,” *a*, vol. abs/1901.08621, Jan. 2019.

# Performance Evaluation of SWIPT-enabled Cellular Networks with Adaptive Modulation - A Stochastic Geometry Approach

*L'évaluation des performances des réseaux cellulaires compatibles SWIPT avec modulation adaptive - Une approche de la géométrie stochastique*

---

**Lam-Thanh Tu<sup>1</sup>, Abbas Bradai<sup>2</sup>, and Yannis Poussset<sup>3</sup>**

<sup>1</sup> XLIM, University of Poitiers, lam.thanh.tu@univ-poitiers.fr

<sup>2</sup> XLIM, University of Poitiers, abbas.bradai@univ-poitiers.fr

<sup>3</sup> XLIM, University of Poitiers, yannis.poussset@univ-poitiers.fr

---

**Keywords:** SWIPT, Adaptive Modulation, Performance Analysis, Stochastic Geometry

**Mots clés :** SWIPT, Modulation adaptive, Analyse de performance, Géométrie stochastique

---

## Abstract:

The performance of simultaneous wireless information and power transfer (SWIPT)-enabled cellular networks by utilizing adaptive modulation are investigated. In particular, the coverage probability (Pcov), the occurrence probabilities of different mode of modulations and the achievable spectral efficiency (ASE) are provided by leveraging tools from stochastic geometry. It should be noted that different from works in the literature which are ignored the spatial-correlation between base stations (BSs) as well as the correlation between information decoding and harvested energy at the end-devices (EDs), we take these into considerations by yielding the recent definition of the coverage probability. Finally, our numerical results show that employing adaptive modulation in SWIPT-enabled ED is a promising way to improve both spectral efficiency (SE) and energy efficiency (EE) of cellular networks.

## Résumé :

Les performances des réseaux cellulaires activée par SWIPT ( Simultaneous wireless Information and Power Transfer) en utilisant la modulation adaptative sont étudiées. En particulier, la probabilité de couverture (Pcov), les probabilités d'occurrence des modes configurations de modulation différentes et l'efficacité spectrale souhaitée (ASE) sont fournies en exploitant des approches de la géométrie stochastique. Il convient de noter qu'à la différence des travaux de la littérature qui ignorent la corrélation spatiale entre les stations de base (BS) ainsi que la corrélation entre le décodage des informations et l'énergie récoltée au niveau des dispositifs finaux (ED), nous les prenons en considération en donnant la définition récente de la probabilité de couverture. Enfin, nos résultats numériques montrent que l'utilisation de la modulation adaptative dans les ED compatibles SWIPT est un moyen prometteur d'améliorer à la fois l'efficacité spectrale (SE) et l'efficacité énergétique (EE) des réseaux cellulaires.

## 1 Introduction

Nowadays, one of main challenges of end-devices (EDs) is how to prolong its operation over a reasonable amount of time. At the first attempt, a larger battery seems to be an appropriate solution, it, however, typically leads to the devices itself too bulky. In addition, some special EDs may even not be able to re-charge its battery, such as sensor nodes that operate under harsh environment. In this context, energy harvesting (EH) is regarded as a promising technology to address this problem. Among all available EH techniques, the simultaneous wireless information and power transfer (SWIPT) is emerging as a suitable solution for end-devices thanks to its cost-effective and utilizing the available energy sources like interference from other concurrent transmission, compared with other EH solutions, i.e., power beacon, solar and/or wind energy sources. In particular, in SWIPT, the radio frequency (RF) signals are utilized to not only convey information but also to replenish the battery of the EDs by installing a complement low-cost energy harvester along with the traditional receiver [1].

On the other hand, adaptive modulation is a mature technology which has been proven as a key technique to improve spectral efficiency (SE). Particularly, based on the practical channel conditions, the transmitter actively adjusts its modulation schemes, i.e., BPSK, QPSK, 8PSK and so on, to maximize the data rate thus improving the spectral efficiency, for example, the lower the signal-to-interference-plus-noise ratio (SINRs) is, the smaller the modulation scheme is yielded. As a result, in this work, we investigate the performance of cellular networks at system-level by applying both SWIPT and adaptive modulation. It should be noted that different from the traditional approach which uses system simulator to obtain the results at system-level. Our work, on the other hand, studies the performance of system-level cellular networks by leveraging the advantages of tools from stochastic geometry (SG) which is proven to be more tractable and consuming less resources compared with the system simulator approach [2].

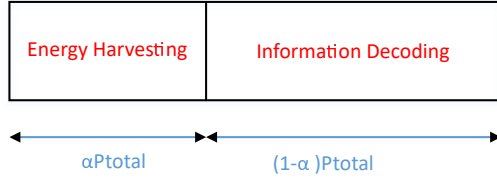


Figure 1 – Illustration of the power-splitting (PS) protocol of SWIPT-enabled receiver.

### 1.1 Related works

In this section, the state-of-the-art of both SWIPT and adaptive modulation at system-level cellular networks are discussed. In [3] the energy efficiency (EE) of SWIPT-enabled multi-cell multiple-input single-output (MISO) networks was investigated. In particular, a centralized beamforming scheme is designed by using the semi-definite relaxation and successive convex approximation technique to maximize the EH efficiency. The ergodic capacity of SWIPT hybrid non-orthogonal multiple access (NOMA) system was addressed in [4]. This work, however, merely studied the performance at link-level instead of system-level. Furthermore, the interference-free system is considered which is not true in practical cellular networks. The outage probability of SWIPT NOMA system with transmit antenna selection was taken into consideration in [5]. Nevertheless, this work also ignores the presence of interference as well as no adaptive modulation is considered.

The performance of both mmWave and computational radio frequency identification networks were provided in [6, 7]. Although stochastic geometry is utilized to modelling the EDs in [6], the metrics of interest, nonetheless, are the power condition and information condition instead of either coverage probability (Pcov) or achievable spectral efficiency (ASE) as in our work. Compared with [7], we do not consider the help of relay but adaptive modulation is taken into account.

One of the seminal works that investigates the performance of adaptive modulation in cellular networks was [8], in this work, however, energy harvesting is not considered and the networks was modelled by rectangular grid modelling which is too ideal to model the cellular networks. Other works, i.e., [9, 10], investigated different aspects of cellular network with adaptive modulation. To be more specific, the EE of two-tier multiple-input multiple-output (MIMO) cellular networks was investigated in [9] while [10] studied the performance of adaptive multicast mechanism. Our work, on the contrary, is considered different scenarios. The main contributions as well as novelties are provided in the sequel.

### 1.2 Main contributions and novelties

In this paper, different to the above-mentioned works, we study the performance of SWIPT-enabled cellular networks at system-level by applying adaptive modulation. Particularly, the main contributions and novelties of this manuscript are summarized as follows:

- Tools from stochastic geometry are used to modelling the distributions of both EDs and base stations (BSs).
- Nakagami- $m$  fading is taken into account instead of Rayleigh fading to better modelling the channel coefficient.
- Power-splitting (PS) SWIPT protocol is taken into consideration.
- Adaptive modulation is utilized to actively exploit the channel state information (CSI) at the BS.
- Three performance metrics are investigated, namely, the coverage probability, the occurrence probabilities of different modulation schemes, and the achievable spectral efficiency are studied and compared with the baseline system, fixed modulation.
- A recent definition of coverage probability is yielded which is able to take into consideration both harvested energy and information decoding.
- Different to the works in the literature, spatial-correlation are considered via the harvested power and information decoding.

## 2 Systems models

### 2.1 Cellular Network Modelling

Let us consider a downlink cellular networks where the BSs are modelled according to a homogeneous Poisson point process (PPP) denoted by  $\Psi_{\text{BS}}$  with density  $\lambda_{\text{BS}}$ . The EDs, in addition, is also modelled by

another homogeneous PPP which is independent of  $\Psi_{\text{BS}}$  and denoted by  $\Psi_{\text{ED}}$  with density  $\lambda_{\text{ED}}$ . It should be emphasized that in this paper, the general scenario is considered rather than fully-loaded as most of the work in the literature [11].

The performance is measured at the typical ED denoted by,  $\text{ED}_0$ , which is located at the origin of the two-dimensional plane. According to Palm theory [12], the results measure at  $\text{ED}_0$  can be applied to other EDs of the networks. The total receive power at the  $\text{ED}_0$ , which includes both intended and interference BS, is divided into two different parts thanks to power-splitting (PS) protocol as illustrated in Fig. 1. Let us denote  $P_{\text{total}}$  at the total receive power at  $\text{ED}_0$ . A fraction of the receive power,  $\alpha P_{\text{total}}$ ,  $\alpha \in (0, 1)$ , is put into the energy harvester to charge the battery, where  $\alpha$  is the power splitting ratio. The remain part, i.e.,  $(1 - \alpha) P_{\text{total}}$ , is used to decode the incoming information from the serving BS denoted by  $\text{BS}_0$ . It is noted that depending on the channel gain which can be obtained via the simultaneous and error-free channel state information<sup>1</sup>,  $\text{BS}_0$  selects an appropriate modulation scheme to transmit to the  $\text{ED}_0$ . Moreover, the results can also be extended straightforwardly to time switching (TS) and antenna switching (AS) protocols, respectively [13, Section. 1.5.1]. In this work, we assume that orthogonal resources allocations are considered inside each-cell. It means that there is no intra-interference in each cell, nevertheless, other-cell interference, of course, is considered.

## 2.2 Small-scale fading and large-scale path-loss modelling

Let us consider the generic link from BS-to-ED. The wireless signal is degraded by both small-scale fading and large-scale path-loss. The impact of shadowing is studied implicitly by modifying the density of the BS [14].

### 2.2.1 Small-scale fading

The small-scale fading of the generic link from BS-to-ED is assumed to follow Nakagami- $m$  fading with shape and spread parameters denoted by  $m$  and  $\Omega$ , respectively. The channel gain, as a result, denoted by  $h_n$ , is followed Gamma distribution with shape and scale meters denoted by  $k$  and  $\theta = \frac{\Omega}{m}$ .

### 2.2.2 Large-scale path-loss

Let us consider the generic link between an arbitrary BS and ED. The large-scale path-loss, denoted by  $L_n$ , is computed by applying unbounded path-loss model and is formulated as follows:

$$L_n = l(r_n) = \mathcal{K}_0 r_n^\beta \quad (1)$$

where  $\mathcal{K}_0$  is the path-loss constant and is computed as  $\mathcal{K}_0 = \left(\frac{4\pi f_c}{3 \times 10^8}\right)^2$ , where  $f_c$  is the carrier frequency and the number  $3 \times 10^8$  (in meter per second) is the speed of light;  $\beta > 2$  is the path-loss exponent.

It is apparent that general path-loss models, such as, the bounded path-loss model and/or the multiple path-loss exponent and so on, can be taken into consideration. Nonetheless, in this work, for simplicity, the basic and widely applied path-loss model is yielded.

### 2.2.3 Cell association

As far as the cell association is concerned, the smallest path-loss denoted by  $L^{(0)}$ , is utilized as a criteria to select the serving BS,  $\text{BS}_0$ , and is formulated as

$$L^{(0)} = \min_{n \in \Psi_{\text{BS}}} \{l(r_n)\} \quad (2)$$

The core reason for applying this criteria instead of other advanced standards, i.e., the highest received power, is that it consumes less power at the ED since the ED does not always keep measuring the channel coefficient from all BSs. In fact, it requires only the distance from the ED to the BS.

## 2.3 Adaptive Discrete Modulation

Adaptive discrete modulation is one of key solutions to improve spectral efficiency by actively exploiting the advantages of channel state information at the transmitter (CSIT). Under the considered networks, we assume that this information is error-free and no delay as well. In particular, depending on the signal-to-interference-plus-noise ratio (SINR) at the receiver, the BS chooses the most appropriate modulation scheme to transmit

---

<sup>1</sup>In general, this assumption is idealistic, thus, the results in this paper can be deemed to represent the upper-bound of the practical scenarios.

information. Let us split the entire range of SINR into  $\mathcal{A} \in \mathbb{N}$  non-overlapping region and the boundary of each interval is denoted by  $\gamma_T^a$ ,  $a \in \{0, \dots, \mathcal{A}\}$ , as follows:

$$0 = \gamma_T^0 < \gamma_T^1 < \dots < \gamma_T^a < \dots < \gamma_T^{\mathcal{A}} = +\infty \quad (3)$$

In this work, the popular  $M$ -QAM modulation scheme is taken into account. In particular,  $M_k = 2^k$ -QAM modulation is selected if the SINR drops into the interval  $[\gamma_T^k, \gamma_T^{k+1})$ ,  $k \in \{1, \dots, \mathcal{A}-1\}$ . In addition, if the SINR is extremely small or it belongs to the region  $[\gamma_T^0 = 0, \gamma_T^1)$ , BS stops transmitting and the outage event appears.

In order to identify the boundary values, the bit error rate of  $M$ -QAM with Gray coding over AWGN channel is applied as follows [15]:

$$\text{BER}_T = \varsigma_k Q\left(\sqrt{\tau_k \gamma_T^k}\right) \Rightarrow \gamma_T^k = \frac{1}{\tau_k} \left[ Q^{-1}\left(\frac{\text{BER}_T}{\varsigma_k}\right) \right]^2, \quad k \in \{1, \dots, \mathcal{A}-1\}, \quad (4)$$

where  $Q(\cdot)$  and  $Q^{-1}(\cdot)$  are the Gaussian Q function and the inverse Gaussian Q function, respectively;  $\text{BER}_T$  is the intended bit error rate threshold; and

$$\varsigma_k = \begin{cases} 1 & m_k = 1, 2 \\ 4/m_k & m_k \geq 3 \end{cases}, \quad \tau_k = \begin{cases} 2/m_k & m_k = 1, 2 \\ 3/(2^{m_k} - 1) & m_k \geq 3 \end{cases} \quad (5)$$

where  $m_k = \log_2(M_k)$ .

## 2.4 Energy Harvesting

The harvested energy denoted by  $\mathcal{EH}$  (in Joule), is the total received power from all active BSs at the ED and is formulated as follows [16]:

$$\mathcal{EH} = \alpha \eta \left( P_{\text{BS}} \sum_{i \in \Psi_{\text{BS}}^{(\text{A})}} \frac{h^{(i)}}{L^{(i)}} \right). \quad (6)$$

Here  $\eta \in [0, 1]$  is the energy conversion coefficient;  $P_{\text{BS}}$  is the transmit power of the BSs;  $\Psi_{\text{BS}}^{(\text{A})}$  is the set of active BS which is also considered as an homogeneous PPP with density  $\lambda_{\text{BS}}^{\text{A}} = \left(1 - \left(1 + \frac{1}{3.5} \frac{\lambda_{\text{ED}}}{\lambda_{\text{BS}}}\right)^{-3.5}\right) \lambda_{\text{BS}}$  [17]. Under the considered networks, the BS is considered as active if at least one MT is located at its Voronoi cell.  $h^{(i)}$  and  $L^{(i)}$  are the small-scale fading and the large-scale path-loss from the  $i$ -BS to the typical ED, respectively. In Eq. (6), the AWGN noise at the receiver is ignored since the power harvests from noise is not comparable with the interference.

## 2.5 Signal-to-Interference-Plus-Noise Ratio

The SINR at  $\text{ED}_0$  is formulated as follows

$$\gamma_{\Delta} = \frac{P_{\text{BS}} \frac{h^{(0)}}{L^{(0)}}}{P_{\text{BS}} \sum_{j \in \Psi_{\text{BS}}^{(\text{A})} \setminus \{0\}} \frac{h^{(j)}}{L^{(j)}} + \sigma_{\text{N}}^2 + \sigma_{\text{C}}^2} \quad (7)$$

where  $\sigma_{\text{N}}^2 = -174 + \text{NF} + 10\log_{10}(\text{BW})$  (in dBm) is the AWGN noise variance at the  $\text{ED}_0$ ; BW is the transmission bandwidth; NF is the noise figure at the ED;  $\sigma_{\text{C}}^2 = \frac{\sigma_{\text{cov}}^2}{(1-\alpha)}$  [18], where  $\sigma_{\text{cov}}^2$  refers to the noise introduced during the conversion from radio frequency (RF) signal to baseband; and  $h^{(s)}$ ,  $L^{(s)}$ ,  $s \in \{0, j\}$ , are the small-scale fading and the large-scale path-loss from the BS<sub>s</sub> to  $\text{ED}_0$ ;  $\Psi_{\text{BS}}^{(\text{A})} \setminus \{0\}$  is a set of active BS except for BS<sub>0</sub>.

## 3 Performance Metrics

### 3.1 Coverage Probability

In this section, three performance metrics are investigated, i.e., the coverage probability, the occurrence probabilities of different modulation schemes, and the achievable spectral efficiency of each ED. In particular, the coverage probability,  $\text{Pcov}$ , is defined as the number of successful transmission over the total transmission.

TABLE I: Setup of parameters (unless otherwise stated)

Parameters [Unit]	Values
$R_{\text{cell}} = \frac{1}{\sqrt{\pi \lambda_{\text{BS}}}}$ [m]	40
$\text{RED} = \frac{1}{\sqrt{\pi \lambda_{\text{ED}}}}$ [m]	100
$P_{\text{BS}}$ [dBm]	30
$\text{BER}_T$	$10^{-3}$
$\gamma_E$ [dBm]	-80
BW [kHz]	250
$\eta$	0.7
$\alpha$	0.3
$\mathcal{A}$	5
NF [dB]	10
$\sigma_{\text{cov}}^2$ [dBm]	-70
$m$	4.5
$\Omega$	12.5
$\beta$	3.5
$f_c$ [GHz]	2.1

However, different from most of works in the literature, the  $\text{Pcov}$  under the considered cellular networks occurs providing that two following conditions are satisfied simultaneously: i) The probability that the harvested energy is greater than an activation threshold; ii) The probability that the receive SINR is greater than  $\gamma_T^1$  and is formulated as follows:

$$\text{Pcov} = \Pr \{ \mathcal{E}\mathcal{H} \geq \gamma_E, \gamma_\Delta \geq \gamma_T^1 \} \quad (8)$$

Here  $\gamma_E$  is the predefined energy threshold so that the ED is activated. It is apparent that Eq. (8) is recently proposed. The benefits of this recent definition is that it takes into account both energy harvesting and SINR together in lieu of separately.

### 3.2 Occurrence probabilities of each modulation scheme

The probability that the  $\text{BS}_0$  transmits at  $k$  modulation scheme refers to the occurrence probabilities denoted by  $\Upsilon_k$  and is computed as

$$\Upsilon_k = \Pr \{ \mathcal{E}\mathcal{H} \geq \gamma_E, \gamma_T^k \leq \gamma_\Delta \leq \gamma_T^{k+1} \}, \quad k \in \{1, \dots, \mathcal{A} - 1\}. \quad (9)$$

It should be noted the sum of  $\Upsilon_k$  where  $k \in \{0, \dots, \mathcal{A} - 1\}$  is equal to one. Mathematical speaking, we have

$$\sum_{k=0}^{\mathcal{A}-1} \Upsilon_k = 1. \quad (10)$$

### 3.3 Achievable Spectral Efficiency (ASE)

Under adaptive modulation system, the average link achievable spectral efficiency (ASE) (in bits/s/Hz) can be computed as a weighted sum of the data rate associated with  $\mathcal{A}$  region as follows [19]:

$$\text{ASE} = \sum_{k=1}^{\mathcal{A}-1} m_k \Upsilon_k. \quad (11)$$

## 4 Numerical Results

In this section, numerical results are provided to measure the performance of these above metrics, i.e.,  $\text{Pcov}$  and ASE. Without loss of generality, the simulation parameters are provided in Table I. In Table I,  $R_{\text{cell}}$  and  $\text{RED}$  are the inter-site distance between BSs and average distance between two EDs, respectively. In this work, five adaptive modulation scheme are applied as [19], namely, no transmission, BPSK, QPSK, 16QAM and 64QAM, respectively. It should be noted that different kinds of modulations as well as higher modulation levels can be employed straightforwardly.

Fig. 2 reveals the behaviour of  $\text{Pcov}$  respect to both energy harvesting threshold,  $\gamma_E$ , and BER threshold, i.e.,  $\text{BER}_T$ . We experience that the  $\text{Pcov}$  is a concave function of both variables. In addition, the  $\text{Pcov}$  is

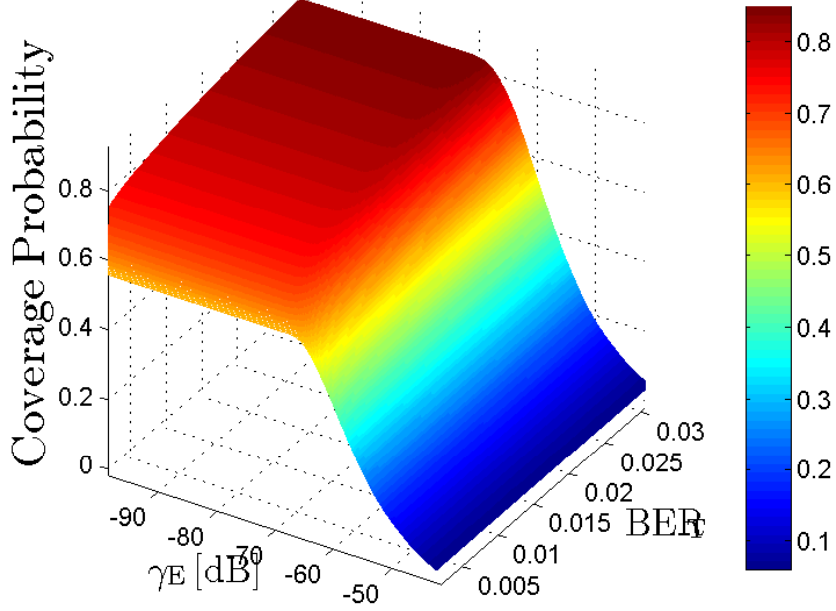


Figure 2 –  $P_{cov}$  as a function of both energy harvesting threshold,  $\gamma_E$ , and BER threshold,  $BER_T$ .

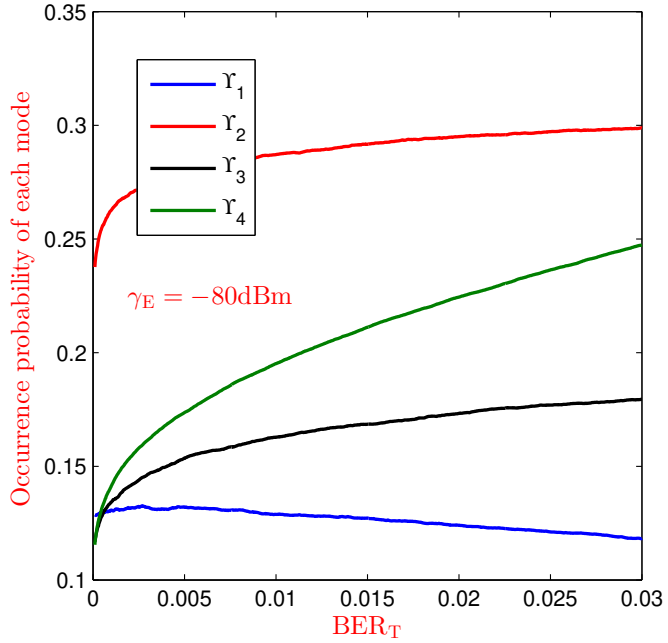


Figure 3 – Occurrence probabilities vs BER threshold,  $BER_T$ .  $\Upsilon_k = \{\text{BPSK, QPSK, 16QAM, 64QAM}\}$ ,  $k \in \{1, 2, 3, 4\}$ .

monotonically decreasing with  $\gamma_E$  providing that  $BER_T$  is constant. The same pattern can be obtained if  $\gamma_E$  is fixed and  $BER_T$  reduces.

The occurrence probabilities,  $\Upsilon_k$ , is shown in Fig. 3 versus the bit error rate threshold,  $BER_T$ . The results show that  $\Upsilon_2$  or QPSK always outperforms others modulation schemes. Furthermore, it is obvious that the lower the  $BER_T$  threshold is, the higher the probability of 64QAM or  $\Upsilon_4$  is attained.

Fig. 4 illustrates the performance of ASE as a function of energy requirement. It is no doubt that ASE is monotonically decreasing with  $\gamma_E$ . Furthermore, it is easy to recognize that the proposed adaptive modulation outperforms all fixed modulations from BPSK to 64QAM. To be specific, the performance of the proposed scheme is almost two-fold compared with 16QAM modulation and around three-times if BPSK is used. Finally, it is apparent that increasing BER threshold will reduce the ASE as expected.

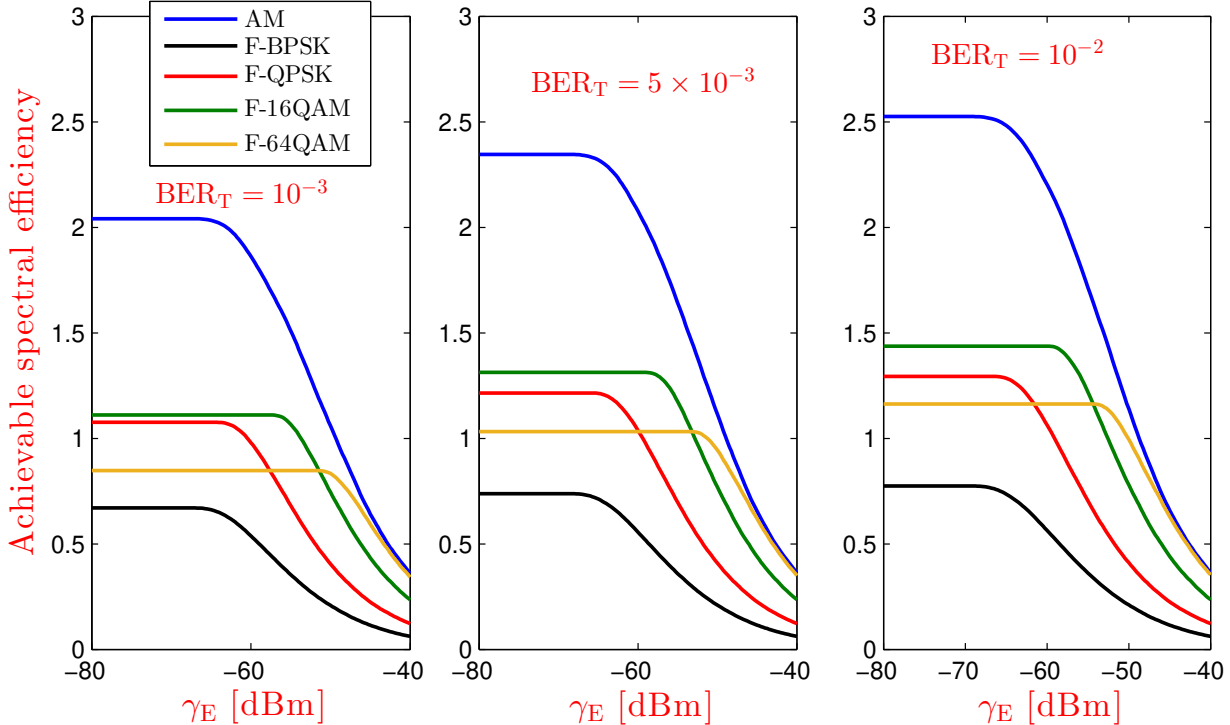


Figure 4 – Achievable spectral efficiency of the proposed adaptive modulation and fixed modulation versus energy harvesting threshold  $\gamma_E$  with various value of  $BER_T$ . Here, AM denotes the proposed adaptive modulation;  $F-k$ ,  $k \in \{BPSK, QPSK, 16QAM, 64QAM\}$  denotes fixed  $k$  modulation, i.e.,  $F\text{-}BPSK$  is fixed BPSK modulation.

## 5 Conclusion

In this paper, the performance of cellular networks is investigated with three metrics, coverage probability, occurrence probabilities and achievable spectral efficiency, correspondingly. In particular, five discrete modulation schemes are considered, no transmission, BPSK, QPSK, 16QAM and 64QAM respectively. The results show that by applying adaptive modulation as well as the energy harvesting, we are able to increase both spectral efficiency and energy efficiency. These performances can be enhanced significantly by considering network slicing with the current infrastructure [20] or using deep learning combined with mathematical modelling [21].

## 6 References

- [1] J. Huang, C.-C. Xing, and C. Wang, “Simultaneous wireless information and power transfer: Technologies, applications, and research challenges,” *IEEE Commun. Magazine*, vol. 55, pp. 26–32, Nov. 2017.
- [2] M. Haenggi, *Stochastic Geometry for Wireless Networks*. Cambridge University Press, 2012.
- [3] S. Jang, H. Lee, S. Kang, T. Oh, and I. Lee, “Energy efficient swipt systems in multi-cell miso networks,” *IEEE Trans Commun.*, vol. 17, pp. 8180–8194, Dec. 2018.
- [4] S. K. Zaidi, S. F. Hasan, and X. Gui, “Evaluating the ergodic rate in swipt-aided hybrid noma,” *IEEE Commun. Lett.*, vol. 22, pp. 1870–1873, Sep. 2018.
- [5] T. N. Do, D. B. Costa, T. Q. Duong, and B. An, “Improving the performance of cell-edge users in miso-noma systems using tas and swipt-based cooperative transmissions,” *IEEE Trans. Green Commun. Netw.*, vol. 2, pp. 2473–2400, Mar. 2018.
- [6] Y. Kim, T. J. Lee, and D. I. Kim, “Joint information and power transfer in swipt-enabled crfid networks,” *IEEE Wireless Commun. Lett.*, vol. 7, pp. 186–189, Apr. 2018.
- [7] S. Biswas, S. Vuppala, and T. Ratnarajah, “On the performance of mmwave networks aided by wirelessly powered relays,” *IEEE J. Sel. Areas Commun.*, vol. 10, pp. 1522–1537, Dec. 2016.
- [8] X. Qiu and K. Chawla, “On the performance of adaptive modulation in cellular systems,” *IEEE Trans. Commun.*, vol. 47, pp. 884–895, Jun. 1999.

- [9] R. H. Aquino, S. A. R. Zaidi, D. McLernon, and M. Ghogho, "Energy efficiency analysis of two-tier mimo diversity schemes in poisson cellular networks," *IEEE Trans. Commun.*, vol. 63, pp. 3898–3911, Oct. 2015.
- [10] M. Li and Y. H. Wu, "Performance analysis of adaptive multicast streaming services in wireless cellular networks," *IEEE Trans. Mobile Comput.*, vol. 18, pp. 2616–2630, Nov. 2019.
- [11] J. G. Andrews, F. Baccelli, and R. K. Ganti, "A tractable approach to coverage and rate in cellular networks," *IEEE Trans. Commun.*, vol. 59, pp. 3122–3134, Nov. 2011.
- [12] M. Haenggi, *Stochastic Geometry for Wireless Networks*. Cambridge University Press, 2013.
- [13] L. T. Tu, *New Analytical Methods for the Analysis and Optimization of Energy-Efficient Cellular Networks by Using Stochastic Geometry*. PhD thesis, University of Paris-Sud, 6 2018.
- [14] M. D. Renzo, A. Zappone, L.-T. Tu, and M. Debbah, "System-level modeling and optimization of the energy efficiency in cellular networks – a stochastic geometry framework," *IEEE Wireless Commun.*, vol. 17, pp. 2539–2556, Apr. 2018.
- [15] V. N. Q. Bao and H. Y. Kong, "Joint adaptive modulation and distributed switch-and-stay for partial relay selection networks," *IEICE Trans. Commun.*, vol. 95, pp. 668–671, Feb. 2012.
- [16] L.-T. Tu, M. D. Renzo, and J. P. Coon, "System-level analysis of swipt mimo cellular networks," *IEEE Commun. Lett.*, vol. 20, pp. 2011–2014, Oct. 2016.
- [17] S. M. Yu and S.-L. Kim, "Downlink capacity and base station density in cellular networks," in *IEEE Workshop on Spatial Stochastic Models for Wireless Networks*, pp. 1–7, 5 2013. [Online]. Available: <http://arxiv.org/pdf/1109.2992.pdf>.
- [18] L.-T. Tu, M. D. Renzo, and J. P. Coon, "System-level analysis of receiver diversity in swipt-enabled cellular networks," *IEEE/KICS J. Commun. Netw.*, vol. 18, pp. 926–937, Dec. 2016.
- [19] M. S. Alouini and A. Goldsmith, "Adaptive modulation over nakagami fading channels," *Wireless Pers. Commun.*, vol. 13, pp. 119–143, May. 2000.
- [20] S. Dawaliby, A. Bradai, and Y. Pousset, "Distributed network slicing in large scale iot based on coalitional multi-game theory," *IEEE Trans. Netw. Service Manag.*, vol. 16, pp. 1567 – 1580, Dec. 2019.
- [21] A. Zappone, M. D. Renzo, M. Debbah, L. T. Tu, and X. Qian, "Model-aided wireless artificial intelligence: Embedding expert knowledge in deep neural networks for wireless system optimization," *IEEE Veh. Technol. Mag.*, vol. 14, pp. 60–69, Sep. 2019.

# **Electromagnetic Compatibility Issues**

## Caractérisation de matériaux diélectriques jusqu'à 330GHz : une technique de mesure en espace libre sans filtrage temporel

***Dielectric material characterization up to 330 GHz : a free space S-parameter measurement technique without time domain gating***

**Daniel Bourreau, Alain Péden**

Lab-STICC, UMR 6285 CNRS, IMT Atlantique, technopôle Brest-Iroise, CS 83818, 29238 Brest Cedex 3

[daniel.bourreau@imt-atlantique.fr](mailto:daniel.bourreau@imt-atlantique.fr) [alan.peden@imt-atlantique.fr](mailto:alan.peden@imt-atlantique.fr)

**Mots clés :** caractérisation de matériaux, espace libre, ondes millimétriques  
material characterization, free space, millimeter wave

### Résumé/Abstract

This paper presents the implementation of free space S-parameter measurement setups in the Ka, W and J bands. The complex permittivity extraction is performed without any specific processing on the S-parameters from 26 up to 330 GHz. The comparison between the measured and simulated four S-parameters (magnitude and phase) shows very good agreement and validates the test benches as well as the calibration procedure.

### 1 Introduction

Millimeter waves up to THz are increasingly being used or foreseen in various applications such as 5G (backhaul), RFID tags to analyze the risks associated with aging structures, imaging (non-destructive control, security), automotive radars, radiometry, ... Regardless of the application, the complex dielectric permittivity of materials is a key parameter in the design and optimization of microwave devices and systems. Moreover, the study of the propagation and the interactions of waves with the environment also requires a precise knowledge of these characteristics.

This paper presents the implementation of tests benches from 26 GHz to 330 GHz in 3 normalized frequency bands: Ka, W and J. The measured S-parameter of a dielectric material slab are used to extract the complex permittivity and the validation of the extraction results is carried out by the comparison with the four S-parameter analytical model, in magnitude and phase.

### 2 Test bench description

The "quasi-optical" test benches allows us to measure the free space S-parameters of a dielectric slab placed between two GOLA (Gaussian Optic Lens Antenna), as shown in Fig. 1 and 2 [1] [2] [3] [4].

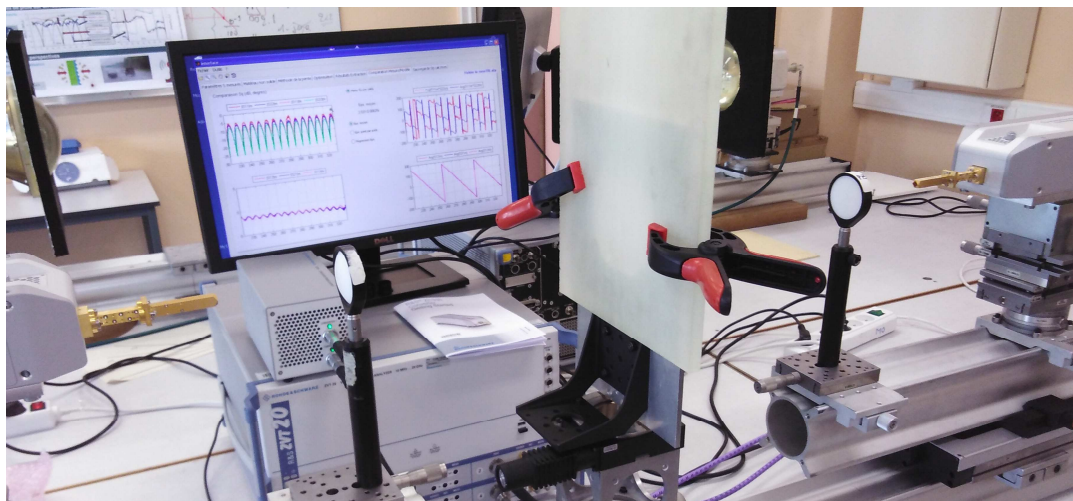


Fig. 1 : Quasi-optical test bench in the J band with a Rexolite slab under test

Such specific antennas are realized using a horn and a lens [1] [2] to obtain a focused or paraxial gaussian beam depending on the waist to wavelength ratio.

The higher the ratio, the more paraxial the beam. Therefore, the waist is the optimal position for the free space S-parameter measurement of a device under test (dielectric slab, frequencies selective surfaces, polarizer, etc.) without filtering and time gating [3] [4].

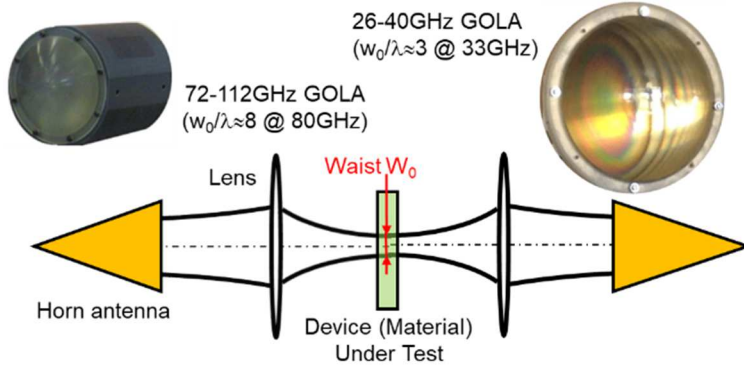


Fig. 2 : Gaussian beam focused to obtain the waist

### 3 Material characterization

The permittivity extraction is carried out using the analytical model of a dielectric slab whose parallel faces are under normal incidence of a plane wave (see Fig 3 : dielectric slab model). The free space Thru-Reflect-Line (TRL) technique is used for the setup calibration as described in [3] [4].

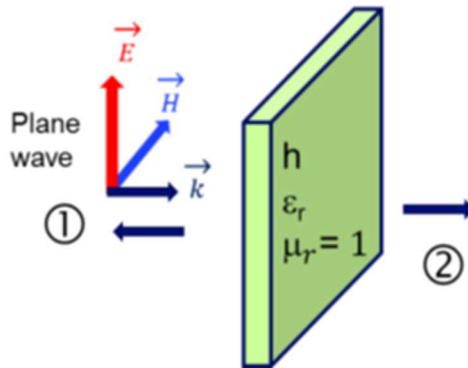


Fig 3 : dielectric slab model

As the slab thickness is measured with a caliper, the relative complex permittivity can be extracted at each frequency point only from the measured  $S_{12}$  and  $S_{21}$  parameters (magnitude and phase). The  $S_{11}$  and  $S_{22}$  coefficients are used to refine the slab thickness by comparing the measured and simulated S-parameters [3] [4]. The extraction result performed in the Ka, W and J bands for a 12.815 mm Rexolite slab is shown in Fig 4.

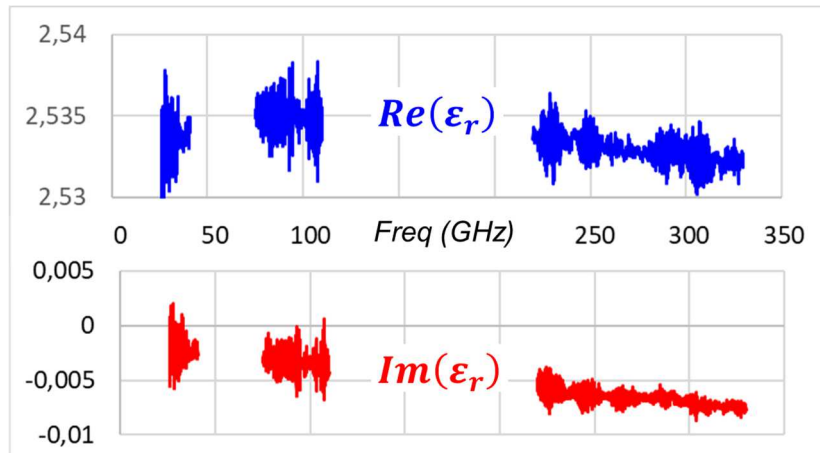


Fig 4 : Extracted permittivity (real and imaginary parts) of a Rexolite slab

Given the very small change of the permittivity over the frequency bands, the mean values with their standard deviations are calculated. Some materials have frequency-dependent complex permittivity. For such materials, a linear regression or a Debye model can be fitted [5].

#### 4 Validation results

To validate the permittivity extraction, as well as the S-parameter measurement, we performed the comparison in magnitude and phase between the simulated and measured S-parameters. As an example, Fig 5 shows the results obtained using the mean values extracted in the J band. We also analyze the linear regression of the permittivity and if necessary we can extract a model (Debye, ...).

Very good agreement is demonstrated without any preliminary data processing of the calibrated S-parameters.

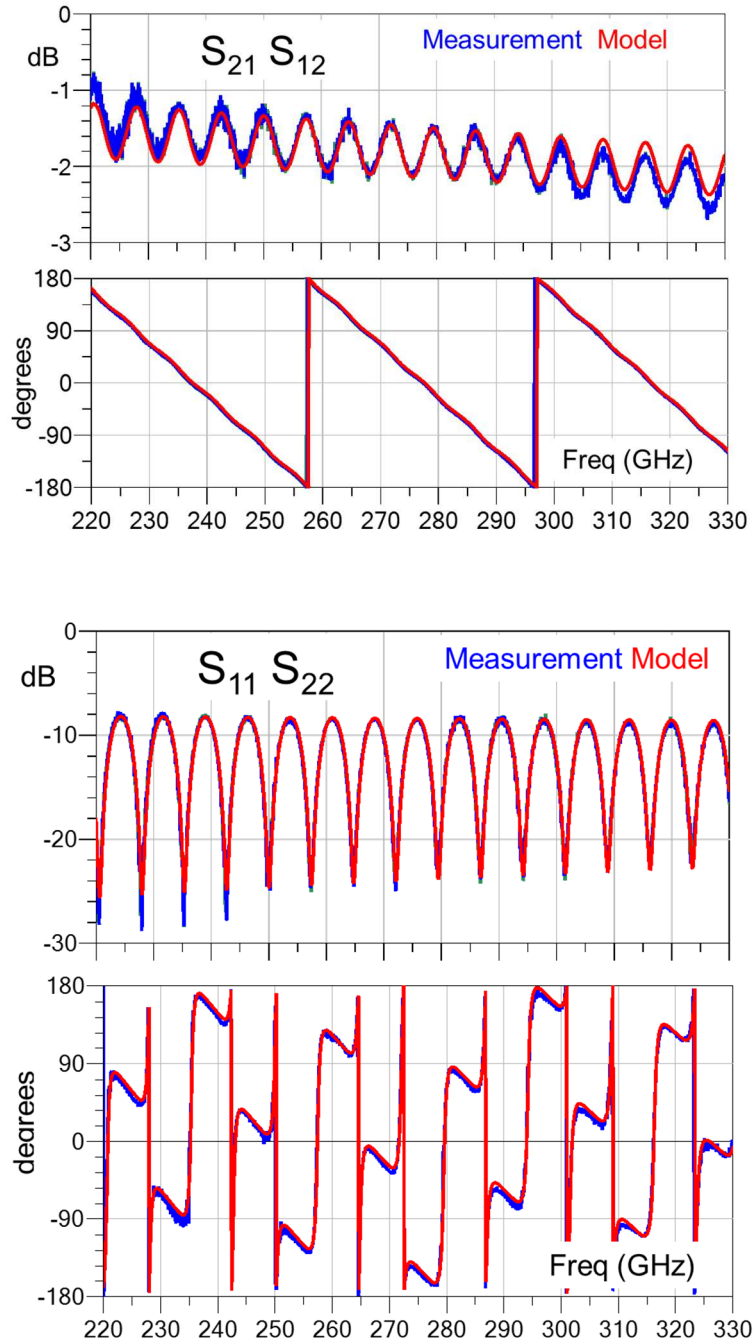


Fig 5 : Comparison between measured and simulated S parameters of the Rexolite slab in the J band

## 5 Current developments

Processes use powders and liquids to make a solid material. We could use the same characterization method to extract the dielectric properties for non-solid materials (powder or liquids) [5]. It is then possible to define a database or a model to predict the desired property.

Multi-layers materials is be also tested but painted materials have very low thickness and the method is very sensitive. As well as S-parameter measurement under incidence angle of the beam, we investigated multilayer properties extraction.

The ACC radar operates around 77 GHz. In these frequency ranges, rain has high propagation losses which disturb the operation of the radar. In addition, the runoff of water on a bumper (radome) disrupts its transfer function. In our laboratory we have made such measurements that we will model in order to integrate this phenomenon in a radar simulator [6].

## 6 Conclusion and perspectives

We present a free space S-parameter measurement technique in the Ka, W and J bands. Very good results, repeatability and precision are demonstrate through the comparison with the theoretical model.

The D band setup (110-170 GHz) is also under progress. FSS (Frequency Selective Surfaces) and metamaterial can also be measured.

## Bibliography

- [1] P.F. Goldsmith “**Quasi-optical techniques**” Proceedings of the IEEE Vol. 80, Issue: 11, Nov 1992
- [2] Le Goff M., Le Bras J.L., Deschamps B., Bourreau D., Peden A. “**Ka band quasi optical test bench using focusing horns**”. 29th EUMC, 1999
- [3] Le Bras J.L, Le Goff M., Deschamps B., Peden A., Bourreau D., Toutain S. “**Quasi optical circuit measurements method in W band**”. ESA workshop, 1998
- [4] Bourreau D., Péden A., Le Maguer S., “**A quasi-optical free-space measurement setup without time-domain gating for material characterization in the W-band**”. IEEE transactions on instrumentation and measurement, december 2006, vol. 55, n° 6, pp. 2022-2026
- [5] DanielBourreau, Alain Péden “**Characterization of non-solid materials in the W-Band**” 15èmes Journées de Caractérisation Microondes et Matériaux Paris, 19-21 Mars 2018
- [6] Daniel Bourreau, Alain Péden “**Caractérisation et modélisation de l'environnement de propagation (radômes et conditions extérieures) des systèmes radios aux ondes millimétriques et submillimétriques**” XXIèmes JNM 14-17 mai 2019 – Caen

## Statistique de l'efficacité de blindage de matériaux composites pour la 5G: méthodes avancées d'échantillonnage

---

*Sébastien Lalléchère<sup>1</sup>, Sébastien Girard<sup>1</sup>, Jérôme Rossignol<sup>2</sup>, Didier Stuerga<sup>2</sup>, and Gilles Clément<sup>3</sup>*

<sup>1</sup>Université Clermont Auvergne, Institut Pascal, SIGMA Clermont, CNRS UMR 6602, sebastien.lallechere@uca.fr

<sup>2</sup>Université de Bourgogne, ICB, Equipe GERM, jerome.rossignal@u-bourgogne.fr

<sup>3</sup>Tresse Industrie, Texprotec, g.clement@tresse.com

---

**Mots-clés :** blindage électromagnétique, méthode d'homogénéisation, statistique, matériaux composites, fibres de carbone

### Résumé :

Cette proposition présente une méthodologie pour l'estimation statistique du niveau de protection offert par des matériaux composites constitués par des fibres de carbone sur une large gamme de fréquences contenant la bande 5G. La variabilité géométrique des nanostructures de carbone (essentiellement en termes de formes et de dimensions) impose, dans un premier temps, une caractérisation fréquentielle précise de la distribution statistique des propriétés diélectriques des matériaux. La propagation, dans un second temps, des incertitudes précédentes au niveau de l'efficacité de blindage des matériaux apporte des contraintes particulières quand aux méthodes statistiques à mettre en œuvre. Ainsi, cette contribution vise à démontrer l'apport de méthodes de “clustering” pour réduire la complexité de problèmes impliquant un nombre important de paramètres aléatoires corrélés. L'estimation des niveaux de protection électromagnétique de matériaux composites pour des fréquences 5G sub-6GHz permettra de valider l'approche proposée.

## 1 Introduction

Le futur déploiement des systèmes de communication de cinquième génération (5G) et la part croissante prise par les objets communicants (internet des objets, IoT en anglais) complexifient l'analyse de la compatibilité électromagnétique (CEM) des systèmes électroniques. En effet, les modifications imposées sur la nature des sources de rayonnement électromagnétique (types, niveaux, usages), les chemins de couplages et les victimes potentielles des perturbations nécessitent une analyse fine de la CEM de ces systèmes [1]. Dans le cadre de la protection des victimes, l'utilisation de fibres et de nanotubes de carbones (CNT en anglais) pour les matériaux composites a connu un intérêt croissant ces quinze dernières années [2]. Ainsi, les travaux initiés dans [3] ont permis de montrer l'importance d'une caractérisation multi-échelles et multi-physiques pour des applications de blindage électromagnétique large bande.

## 2 Problème considéré

Dans cette contribution, on s'intéresse à la réalisation d'un mélange entre des fibres de carbone et une matrice en PMMA (Polyméthacrylate de méthyle, basé sur un modèle de Debye). Pour les besoins de la démonstration, le choix des matrices (PMMA) et inclusions (fibres de carbone) se base sur le cas déterministe explicité dans [2]. L'étude récente des propriétés pour une application en protection des systèmes électroniques fait apparaître des composites différents et l'utilisation de PET (Polytéraphthalate d'éthylène) et de CNTs [3], plus en phase avec les propriétés d'usage (niveau matériau) pour la réalisation de tresses de protection EM [4]. Dans la suite, on supposera que les fibres de carbone présentent des dimensions micrométriques avec une forme générique cylindrique. On considère dans la suite que les mélanges réalisés incluent une part d'incertitudes quant à la répartition des classes de fibres aux dimensions variables (longueur  $L$  et diamètres  $2*R$ ), et le niveau d'incertitude des longueurs/diamètres de fibres (voir la Fig. 1).

### 2.1 Méthodologie

La méthodologie suivie dans cette étude est synthétisée suivant les quatre étapes représentées dans les figures 1 et 2 :

- Étape A : génération de collections d'échantillons (plusieurs milliers, dizaines de milliers :  $n_{mc}$ ) comprenant des classes de fibres de carbone dont les paramètres sont définis aléatoirement (voir Fig. 1). La Fig. 3(1)

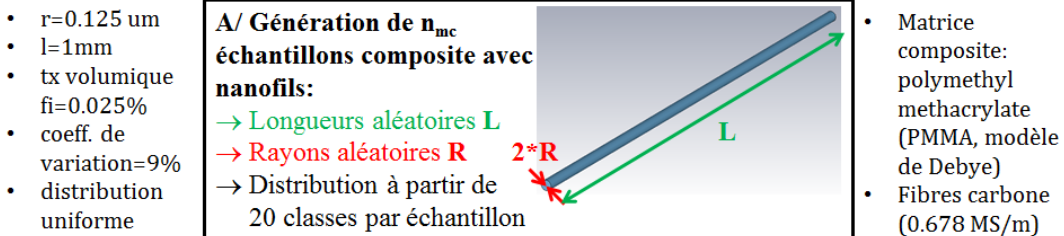


Figure 1 – Méthodologie : description de la génération des échantillons composites (étape A).

donne une représentation d'un échantillon de matériau composite contenant quatre classes de fibres aux longueurs et diamètres aléatoires dans les limites évoquées précédemment. L'effet sur la distribution de la permittivité complexe est illustrée dans la Fig. 3(2) avec les parties réelle [A] et imaginaire [B].

- Étape B : évaluation des propriétés diélectriques des composites selon [2].
- Étape C : définition des plans d'expériences classiques (étape C1 dans la Fig. 2 ; choix aléatoires de  $n_{boot}$  réalisations parmi les  $n_{mc}$  de la population initiale (étape A)) ou optimums (étape C2 dans la Fig. 2 ; SROM,  $n_{srom}$ ).
- Étape D : Post-traitement final (estimation de l'efficacité de blindage du matériau soumis à une onde plane en incidence normale : moyenne et écart-type).

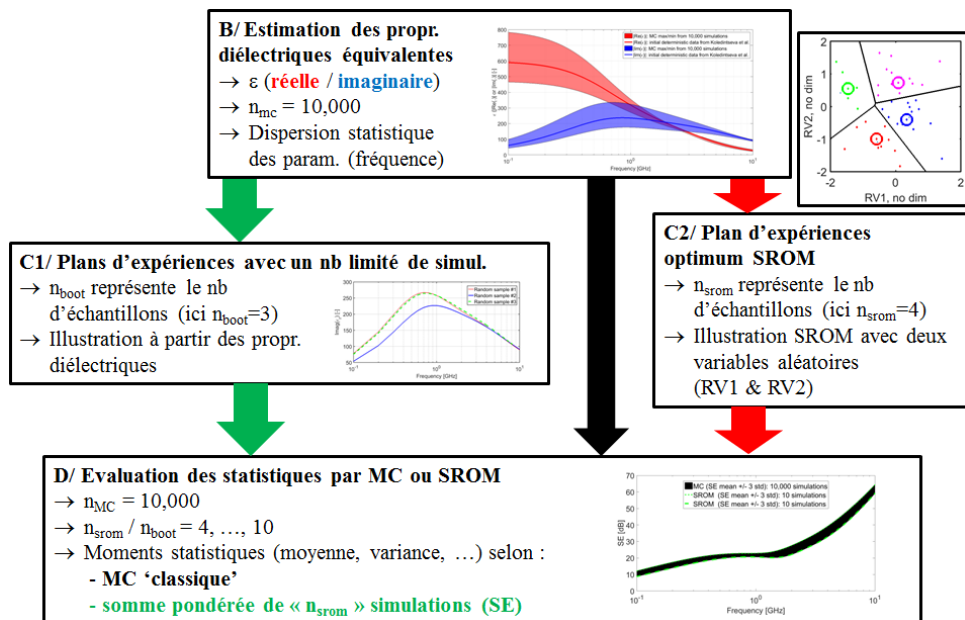


Figure 2 – Méthodologie : choix des échantillons et post-traitements (étapes B-D).

Comme évoqué précédemment, on constate que les différentes contraintes aléatoires (taille des fibres de carbone, définition de classes de fibres de tailles différentes pour un même échantillon) entraînent des variations importantes des propriétés diélectriques du matériau en fonction de la fréquence (voir Fig. 3(2)). On constate ainsi, pour trois fréquences distinctes (à savoir  $f_1 = 100\text{MHz}$ ,  $f_2 = 1\text{GHz}$ , et  $f_3 = 2.5\text{GHz}$ , données non représentées ici) une distribution des parties réelles et imaginaires de la permittivité diélectrique très variable incluant des distributions de type Weibul, normale, et/ou log-normale. Ceci impose, a priori, de traiter ce problème de quantification d'incertitudes selon deux stratégies bien distinctes :

- Fréquence par fréquence : il faut pour cela traiter l'identification des paramètres des lois de distribution de la permittivité complexe (parties réelle et imaginaire) pour chaque fréquence ; des stratégies peuvent alors être mises en œuvre incluant ou non le recours à Monte-Carlo. Cette méthodologie est bien adaptée si le calcul des propriétés de protection CEM (shielding effectiveness an anglais) inclut un code fréquentiel.
- En tenant compte de l'ensemble des données fréquentielles. Dans ce cas, l'utilisation de codes de calculs temporels est envisageable en intégrant la dépendance concernant les propriétés diélectriques du matériau

d'une fréquence à une autre. C'est cette méthodologie qui est privilégiée en s'appuyant sur la technique SROM (voir dans la suite).

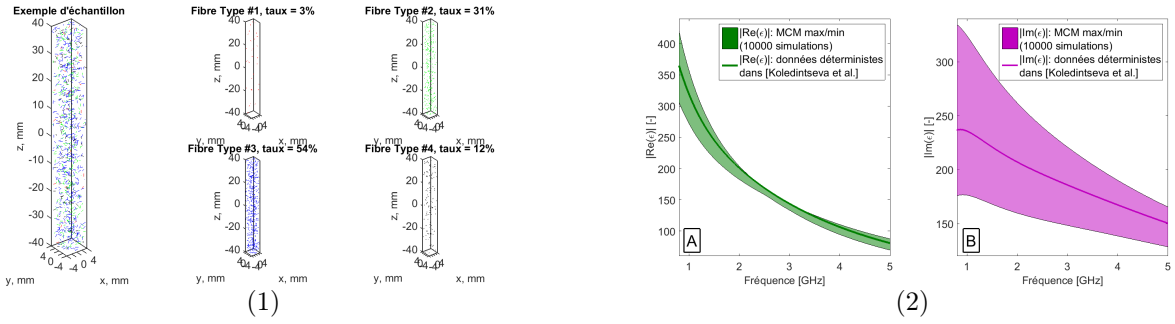


Figure 3 – (1) Distribution aléatoire des fibres dans l'échantillon composite. (2) Distribution de la permittivité complexe du matériau composite : parties réelle [A] et imaginaire [B].

## 2.2 Méthode d'échantillonnage : technique SROM

Les constatations précédentes (Fig. 3) justifient l'intérêt de proposer une stratégie alternative à la méthode Monte-Carlo (MC) permettant de tenir compte naturellement de paramètres aléatoires sur une large gamme de fréquences (les distributions évoluant en fonction de la fréquence). La méthode retenue est basée sur l'approche SROM (stochastic reduced order method) d'échantillonnage avancé (voir son utilisation dans le domaine des mathématiques appliquées dans [5]) et permet de sélectionner le plan d'expérience optimal pour un nombre de simulations réduit (10 maximum ici).

La méthodologie développée autorise un choix automatisé de l'ensemble de données  $(\hat{x}_i, w_i)$  avec  $i = 1, \dots, n_{srom}$ ,  $\hat{x}_i$  le numéro d'échantillon à partir de l'ensemble initial de taille  $n_{mc}$ . Le choix est basé en considérant chaque valeur des parties réelle et imaginaire de la permittivité diélectrique en fonction de la fréquence comme une variable aléatoire à part entière (ici 202 variables, 101 fréquences étant discrétisées entre 100MHz et 5GHz). Au final, on calcule la valeur moyenne de la grandeur d'intérêt (à savoir l'efficacité de blindage EM, notée  $S$  ici) selon :

$$\langle S(f) \rangle = \sum_{i=1}^{n_{srom}} w_i S_{\hat{x}_i}(f), \quad (1)$$

où  $\langle S(f) \rangle$  est la donnée moyenne de l'efficacité de blindage à la fréquence  $f$ , et  $S_{\hat{x}_i}(f)$  représente l'efficacité de blindage calculée à partir de la simulation avec le composite numéro  $\hat{x}_i$  (généré lors de l'étape A du processus, voir Fig. 1).

L'évaluation de la variance de l'efficacité de blindage fait intervenir les paires pondérées SROM  $(\hat{x}_i, w_i)$  comme dans le cas de la relation (1) :

$$var(S(f)) = \sum_{i=1}^{n_{srom}} w_i (S_{\hat{x}_i}(f) - \langle S(f) \rangle)^2. \quad (2)$$

## 3 Résultats numériques

Afin d'estimer la qualité des résultats fournis par SROM, on propose de réaliser deux types de traitements :

- une sélection aléatoire d'un nombre réduit ( $n_{boot} = 10$ ) d'échantillons générés initialement (i.e. parmi  $n_{mc} = 10000$ ) avec une répétition du choix des échantillons (voir l'étape C1 dans Fig. 2),
- la sélection des  $n_{srom} = 10$  échantillons les plus représentatifs de la population initiale ( $n_{mc} = 10000$ ).

Le calcul qui en découle de l'efficacité de blindage permet d'estimer l'erreur relative par rapport à la moyenne et à l'écart-type obtenu par MC (respectivement suivant les relations 1 et 2).

La Fig. 4 donne une vue de l'estimation des moyennes [C] et écart-types [A-C] obtenus par MC et SROM. On constate le très bon accord entre la méthode SROM et les données MC (même pour l'estimation de l'écart-type). On notera également que l'erreur relative de la méthode SROM est trente fois plus faible que celle obtenue en choisissant au hasard un même nombre de réalisations dans la population initiale MC (voir Fig. 4[B]).

Enfin, la comparaison des données issues de MC ( gabarit impliquant moyenne  $\pm 3$  écart-types de l'efficacité de blindage) souligne la qualité des résultats SROM.

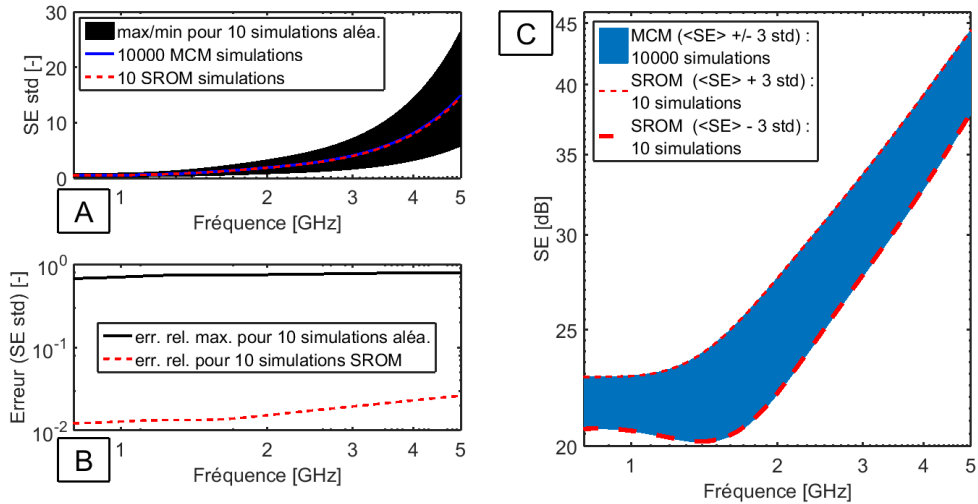


Figure 4 – [A] Ecart-type (std) SE par MC (référence et tirages aléatoires de 10 simulations, respectivement en bleu et noir) et SROM (rouge). [B] Erreur par tirage aléatoire de 10 simulations (noir) et SROM (rouge). [C] Évaluation statistique (moyenne  $\pm$  3 écart-types) de l'efficacité de blindage (SE) du matériau composite par MC (10000 simulations en bleu) et par SROM (10 simulations en rouge, traits discontinus).

#### 4 Conclusion

Cette contribution a permis de détailler l'utilisation de la méthode SROM dans le contexte de la caractérisation des niveaux de protection induits par des matériaux composites jusqu'à 5GHz. La quantification des incertitudes liées à des aléas géométriques (tailles des fibres de carbone) a été réalisée sur une gamme de fréquence allant de 100MHz à 5GHz. La diversité des distributions statistiques caractérisant la permittivité diélectrique équivalente des échantillons composite a été prise en compte naturellement à travers la méthode SROM. La capacité naturelle de la méthode à intégrer la dépendance entre les variables aléatoires offre des perspectives intéressantes pour la simulation de ces matériaux dans des codes de calculs temporels permettant conjointement d'accéder à des résultats sur une large gamme de fréquences avec un degré de réalisme appréciable comparativement à des simulations Monte-Carlo. Le gain en temps de calcul (facteur 1000 ici) et l'estimation de l'erreur relative (1 à 3% pour l'estimation de la variance) produits par l'utilisation des plans d'expériences SROM offre des perspectives très intéressantes pour l'intégration de ces modèles dans des simulations "Full-wave".

#### 5 References

- [1] J. Vikstedt, The 5G New Radio - Implications for EMC and Antenna Testing, in proc. 2018 IEEE Symposium on EMC, SI & PI, Aug. 2018
- [2] M. Koledintseva, Engineering of composite media for shields at microwave frequencies, in proc. IEEE Int. Conf. on EMC, 2005
- [3] M. Michel, Élaboration d'un fil nanocomposite PET – nanotubes de carbone pour le blindage électromagnétique. Suivi de la microstructure induite par le procédé d'étirage et caractérisations des basses fréquences aux hyperfréquences (in French), PhD Thesis, Université de Bourgogne, Dijon, France, Oct. 2019
- [4] P. Omerin, G. Omerin, G. Clément, Gaine de blindage électromagnétique, à diamètre extensible (in French), Patent EP1348247B1, European Patent, 2009.
- [5] M. Grigoriu, Reduced order models for random functions. Application to stochastic problems, Appl. Math. Model., 2009

## Design of 3.6-GHz 5G NGD passive circuit

**B. Ravelo<sup>1</sup>, S. Lallechère<sup>2</sup>**

<sup>1</sup> NUIST, Nanjing, China {blaise.ravelo}@nust.edu.cn

<sup>2</sup> Université Clermont Auvergne, Institut Pascal, SIGMA Clermont, {sebastien.lallechere}@uca.fr

**Keywords:** Negative Group Delay (NGD), Microstrip circuit, Design, NGD analysis, NGD synthesis

### Abstract/Résumé

This paper introduces a design of bandpass NGD circuit with 3.6-GHz centre frequency. The NGD passive topology consists of parallel resistance associated with an open-ended microstrip stub. The S-matrix and group delay (GD) model of the topology are established. A microstrip proof of concept is designed and simulated to validate the theoretical approach. The simulated circuit operates with -0.34 ns NGD around 3.6 GHz centre frequency over 0.32 GHz bandwidth and only 3 dB attenuation loss. This NGD circuit can be useful for the improvement of phase linearity and GD equalization of future 5G microwave devices.

### 1 Introduction

The 5G technology is a promising solution for the future RF/microwave system [1]. However, the system may suffer from the data synchronisation in order to satisfy the master word target wireless connection “anything, anywhere and anytime”. In this context, the design of electronic and power systems will require enhanced works [2]. The future 5G device performances depend on the delays between the multiple transmitter (Tx) and receiver (Rx) positions. To reduce the delay effect, we propose an innovative solution based on the bandpass (BP) negative group delay (NGD) function [3-5]. Because of the unfamiliarity of RF/microwave design engineers and also research communities to this fascinating function, it would be necessary to have a brief recall on its functioning with a simple topology. For this reason, the present paper introduces a design of a BP NGD cell with 3.6 GHz centre frequency.

### 2 Design method of NGD circuit

This section describes the theoretical approach of the BP NGD circuit.

#### 2.1 Topological description and S-matrix modelling

Fig. 1 represents the topology of NGD passive two-port circuit. It is composed of a parallel resistance  $R$  ended by an lossless open-ended stub  $TL(Z, \tau_0)$  which is defined by characteristic impedance  $Z$  and delay  $\tau_0$ . Acting as a symmetric passive circuit, the equivalent S-matrix must be written as  $S_{11}=S_{22}$  and  $S_{12}=S_{21}$ .

By denoting the reference impedance  $R_0=50 \Omega$  and the angular frequency variable  $\omega$ , the S-matrix model of this circuit can be written as:

$$\begin{cases} S_{11}(j\omega) = \frac{-jR_0 \tan(\omega\tau_0)}{2Z + (2R + R_0) \tan(\omega\tau_0)} \\ S_{21}(j\omega) = \frac{2(Z + R) \tan(\omega\tau_0)}{2Z + (2R + R_0) \tan(\omega\tau_0)} \end{cases} \quad (1)$$

The associated group delay (GD) model is defined by:

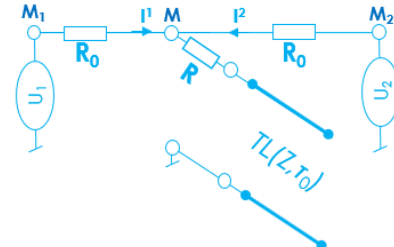


Figure 1: NGD passive circuit

$$GD(\omega) = \frac{-\partial \arg[S_{21}(j\omega)]}{\partial \omega} \quad (2)$$

It can be derived from the transmission coefficient given in (1) that:

$$GD(\omega) = \frac{R_0 Z \tau_0 [1 + \tan^2(\omega\tau_0)] [2Z^2 - R(2R + R_0) \tan^2(\omega\tau_0)]}{[Z^2 + R^2 \tan^2(\omega\tau_0)] [2Z^2 + (2R + R_0)^2 \tan^2(\omega\tau_0)]} \quad (3)$$

## 2.2 NGD analysis and synthesis

The NGD analysis consists in proving that the proposed topology is capable to operate as a bandpass NGD function. Doing this, we intuitively have the NGD centre frequency:

$$f_0 = \omega_0 / (2\pi) = 0.25 / \tau_0 \quad (4)$$

At this frequency, the S-parameters and GD established in (1) and (2) become, respectively:

$$\begin{cases} |S_{11}(j\omega_0)| = R_0 / (2R + R_0) \\ |S_{21}(j\omega_0)| = 2R / (2R + R_0) \end{cases} \quad (5)$$

$$GD(\omega_0) = -R_0 Z \tau_0 / [R(R_0 + 2R)] \quad (6)$$

The associated NGD bandwidth is given by:

$$\Delta f = \left\{ \frac{\omega_0}{\pi} - \frac{2}{\tau_0} \arctan \left[ \frac{Z\sqrt{2}}{\sqrt{R(R_0 + 2R)}} \right] \right\} \quad (7)$$

The NGD design equation can be established from the desired NGD centre frequency, NGD value and return loss  $a$ , by solving the system of equations:

$$\begin{cases} S_{11}(f_0) = a \\ GD(f_0) = -t \end{cases} \quad (8)$$

Therefore, we have:

$$\begin{cases} \tau_0 = 0.25 / f_0 \\ R = 0.5R_0(1-a) / a \\ Z = 0.5R_0(1-a)t / a^2\tau_0 \end{cases} \quad (9)$$

## 3 Validation results

A proof of concept and comparison between the model and microstrip simulation is discussed in this section to validate the previous BP NGD theory.

### 3.1 POC description

Table 1 addresses the desired NGD specifications to design the 5G NGD POC. By using design equations (9), we obtain the NGD parameters of Table 1.

Specifications	Designation	$f_0$	$t$	$a$
	Value	3.6 GHz	0.34 ns	10 dB
NGD ideal parameters	Designation	$\tau_0$	$R$	$Z$
	Value	69 ps	60 Ω	1 kΩ

Table 1: NGD specifications and calculated parameters

A microstrip circuit illustrated in Fig. 2(a) was designed and simulated to validate more concretely the modelled S-parameters. The dielectric substrate with thickness  $h$  is Cu metallized with physical width  $d$ , length  $d$  and thickness  $x$ . Fig. 2(b) shows the 3D design of the NGD circuit POC constituted by a resistor  $R$ , open-ended TL( $w, d$ ) and access line TL<sub>a</sub>( $w_a, d_a$ ). After calculations and slight optimization, the specifications of the Kapton substrate and the NGD POC physical parameters are indicated in Table 2.

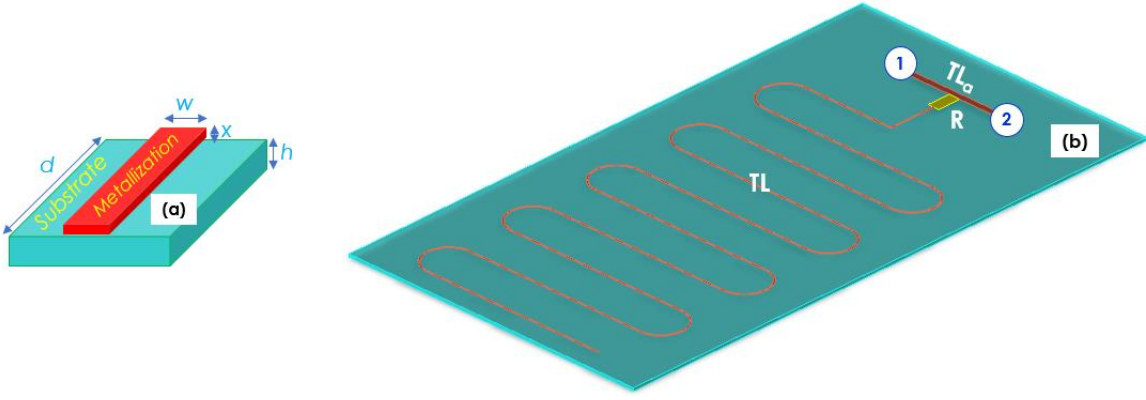


Figure 2: (a) Microstrip design and (b) NGD circuit POC 3D design

Substrate	$\epsilon_r$	$\tan(\delta)$	$x$	$h$	$\sigma$
	3.3	0.002	17 $\mu\text{m}$	125 $\mu\text{m}$	58 MS/s
NGD POC	$w$	$d$	$w_a$	$d_a$	$R$
	62 $\mu\text{m}$	23.4 cm	277 $\mu\text{m}$	2 mm	60 $\Omega$

Table 2: Specifications of the NGD microstrip circuit

### 3.2 Discussion on NGD results

As an ideal model, Matlab calculations of equations (1) and (3) have been realized. Then, the distributed microstrip circuit introduced in Fig. 2(b) was simulated with the commercial tool ADS® from Keysight Technologies® schematic simulation. Figs. 3 display the compared results from calculations (“Calc.”) and ADS® simulations (“Simu.”). As expected theoretically, bandpass NGD function is observed as depicted in Fig. 3(a). Table 3 summarizes the differences between the calculated and simulated results.

Characteristics	$f_0$	$GD(f_0)$	$\Delta f$	$S_{21}(f_0)$	$S_{21}(f_0)$
Ideal	3.6 GHz	-0.34 ns	327 MHz	-3.025 dB	-10.63 dB
Simu.	3.599 GHz	-0.298 ns	172 MHz	-2.35 dB	-12.67 dB

Table 3: Characteristic of ideal and simulated NGD POCs

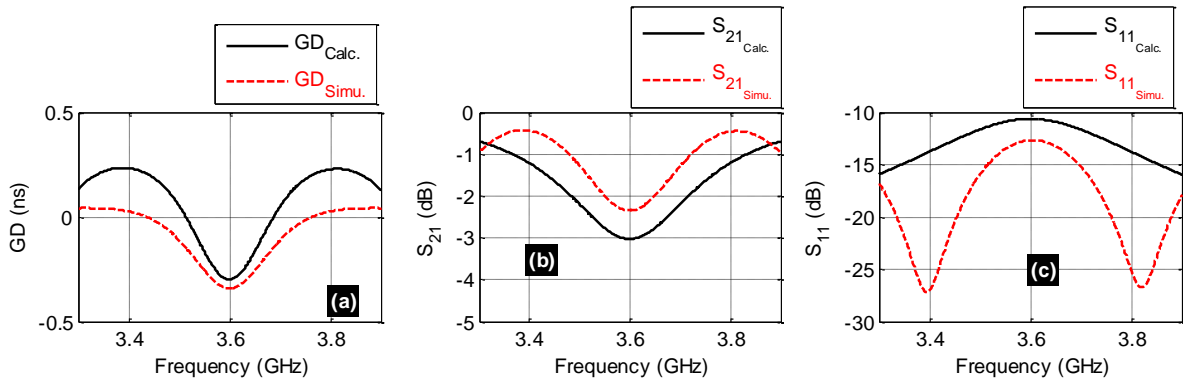


Figure 3: Calculated and simulated (a) GD, (b)  $S_{21}$  and (c)  $S_{11}$  of 3.6 GHz 5G NGD circuit

## 4 Conclusion

A pedagogical BP NGD theory is investigated. The NGD circuit is constituted by a shunt parallel resistor ended by an open-ended stub. The NGD analysis and synthesis equations have been established from the S-matrix equivalent model. The feasibility of the NGD theory was verified with design of ideal and microstrip POCs. As expected, BP NGD responses operating around the 5G frequency 3.6 GHz were obtained and discussed. This

innovative NGD function can be a potential solution for future 5G networks (Fig. 4) [6]. An example of wireless sensor (WS) scenario and NGD delay effect reduction [7] is illustrated in Fig. 5.

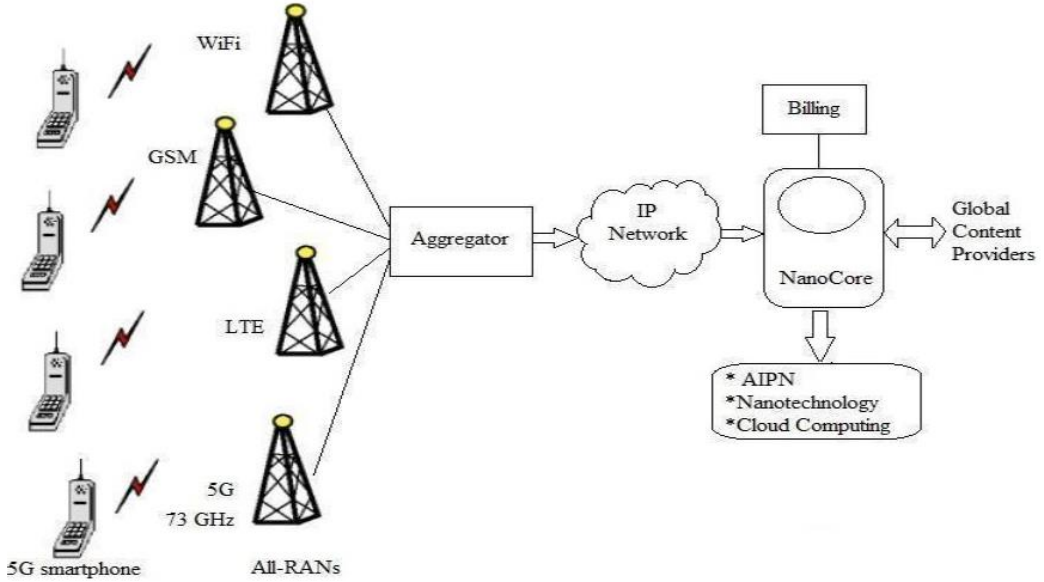


Figure 4: Network Architecture for 5G [6]

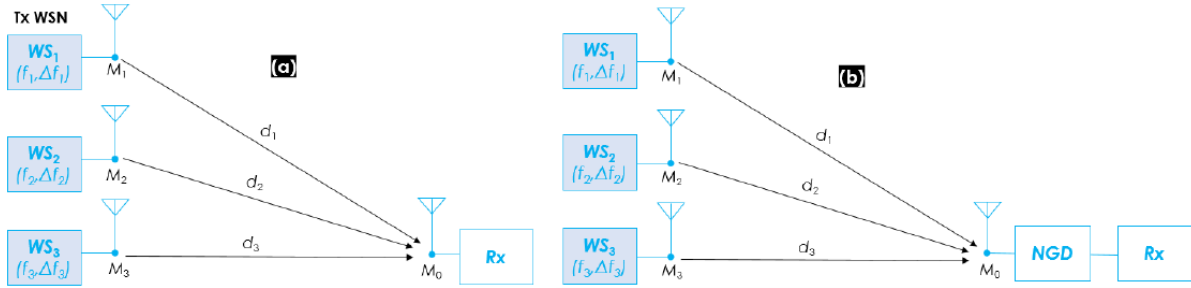


Figure 5: Configuration NGD delay reduction [7]

## References

- [1] V. Tikhvinskiy et al., "Experimental test results of EMC between 5G and Radio relay links in millimeter band", in proc. EMC Europe 2019, Barcelona, Spain, 2-6 Sept. 2019, pp. 220-225.
- [2] Q. Yu, "The era of 5G and its impacts on EMC Design and Testing", in proc. IEEE Int. Symp. On EMC, SI/PI, Washington, DC, 2017.
- [3] B. Ravelo, "Theory and Design of Analogue and Numerical Elementary NGD Circuits: Theoretical Characterization of Analogue and Numerical NGD Circuits", LAP Lambert Academic Publishing, Germany, 2012.
- [4] B. Ravelo, "Negative Group Delay Devices: From concept to applications", IET Materials, Circuit and Devices Series 43, Publisher Michael Faraday House, UK, 2018.
- [5] B. Ravelo, "On the low-pass, high-pass, bandpass and stop-band NGD RF passive circuits", URSI Radio Science Bulletin, Vol. 2017, No. 363, Dec. 2017, pp. 10-27.
- [6] S. Arunachalam, S. Kumar, H. Kshatriya and M. Patil, "Analyzing 5G: Prospects of Future Technological Advancements in Mobile", International Conference on Innovative and Advanced Technologies in Engineering", IOSR Journal of Engineering, pp. 6-11.
- [7] F. Wan, N. Li, W. Rahajandraibe and B. Ravelo, "Reduction Technique of Differential Propagation Delay with Negative Group Delay Function", Accepted for communication, IEEE EuCAP 2020, Copenhagen, Denmark, 15-20 March 2020, pp. 1-5.

# **Exposition and Dosimetry in the 5G context**

# Massive MIMO Network Downlink Exposure Evaluation Using Stochastic Geometry

---

*Maarouf Al Hajj<sup>1</sup>, Shanshan Wang<sup>1</sup>, Philippe de Doncker<sup>2</sup>, Claude Oestges<sup>3</sup>, Joe Wiart<sup>1</sup>*

<sup>1</sup> Télécom Paris, Institut Polytechnique de Paris, {maarouf.alhajj, shanshan.wang, joe.wiart}@telecom-paris.fr

<sup>2</sup> Université libre de Bruxelles, pdedonck@ulb.ac.be

<sup>3</sup> Université catholique de Louvain, claude.oestges@uclouvain.be

---

**Keywords:** 5G, Stochastic Geometry, Massive MIMO, RF Exposure.

## Abstract

This paper aims to estimate the exposure in 5G massive MIMO networks using a stochastic geometric approach. The paper investigates the effect of beamforming, and the effect of multi-user massive MIMO on the exposure of a 5G network. The massive MIMO antenna pattern distribution is obtained by fitting the radiation pattern obtained by running a large amount of channel simulations on NYUSIM. The distribution is then implemented into an analytical framework based on stochastic geometry, so we can obtain an analytical expression of the downlink exposure.

## 1 Introduction

5G systems are being designed to be extremely flexible in terms of both the antennas used, the resource allocation, and the cellular system architecture. New Radio will have major differences in handling data transmission and reception. And while the exact architecture and models are still not yet complete, and each constructor/operator can develop vastly different technologies of antennas and RAN architecture due to the huge flexibility of the 5G technology, the characterization of the emission can be hard, and it may depend on lots of variables[1].

The exposure of 5G antennas proved to be a large problem for regulatory bodies since the configuration and implementation can vary largely between networks, thus making isolated antenna measurements more difficult to use as prediction. And since massive MIMO antennas are not yet deployed, simulating the behavior of the 5G network becomes the sole way to model the exposure.

Stochastic geometry studies the random spatial patterns such as point processes which are often considered the main subject of stochastic geometry[2]. This approach can be used in wireless and cellular networks due to the uncertainty in the deployment of wireless nodes, especially in 5G networks.

The antenna pattern is produced using the NYUSIM channel simulator[3], which is based on measurements in mmWave in the city of New York. The simulator spatially divides the paths of transmission into lobes depending on the angle-of-departures of each path.

## 2 System Description

We consider a 5G cellular network where the base stations are distributed in a 2D plain as a Poisson point process  $\Phi_{BS}$  and with density  $\lambda$ . The users are assumed to be uniformly distributed in the cell. The system is assumed to be in full buffer mode, which is an acceptable conservative assumption for exposure estimation, and users are being served over the whole transmission period. Therefore, the power allocated to each user is the same due to the lack of downlink power control.

As a simplistic approach, we assume a free-space path loss model,  $L = r^{-\alpha}$ . Where,  $\alpha$  is the path loss exponent and is assumed as  $\alpha = 4$ . We also assume that there is no shadowing, and no background noise. The antenna is simulated in line-of-sight mode to insure maximum directed beamforming gain, which will produce the maximum exposure.

### 3 Distribution of Antenna Pattern

We run a large number of channel simulations using the NYUSIM simulator with the characteristics summarized in Table 1.

**Table 1.** List of channel parameters used in NYUSIM

Notation	Value	Meaning
f	28 GHz	Carrier Frequency
N <sub>TX</sub>	64	Number of transmit antenna elements
Scenario	UMi	BS deployment scenario
Environment	LOS	Link type between the Tx and Rx
Antenna spacing	0.5	Antenna element spacing per wavelength
Polarization	Co-Pol	Polarization of the Tx
$\alpha$	4	Path loss exponent

A generalized gain distribution can also be determined from the simulations Figure 1 and for this example, the gain has been fitted into a multimodal normal distribution where the pdf can be written as in (1)

$$y = p \frac{1}{\sigma_1 \sqrt{2\pi}} e^{-0.5(\frac{x-\mu_1}{\sigma_1})^2} + (1-p) \frac{1}{\sigma_2 \sqrt{2\pi}} e^{-0.5(\frac{x-\mu_2}{\sigma_2})^2} \quad (1)$$

Where  $p, \sigma_1, \sigma_2, \mu_1, \mu_2$  are the fitted parameters and have the respective values [0.6, 16.35, 41.67, 6.68, 8.63]. The two observed peaks in the gain distribution can be attributed to the cases where multiple beams are formed (Multi-user MIMO) versus the single user case.

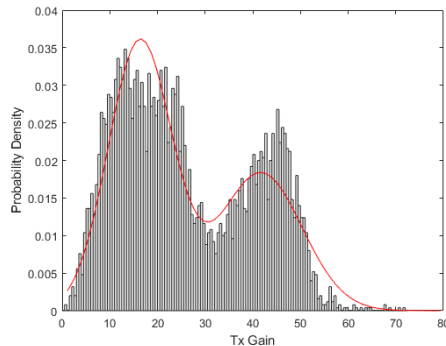


**Figure 1.** Fitting of the gain distribution obtained from NYUSIM

To simplify the analytical formulation and to better allow the comparison of cases, we fit separate distribution for each case of single or multi-user usage and we approximate the distribution to fit a rectangular distribution with the peak as the average gain in the beam's angle, and the width as the average HPBW of the beam. The gain distribution for single user MIMO is presented in Figure 2, and the gain distribution for 2-beam configuration is presented in Figure 3.

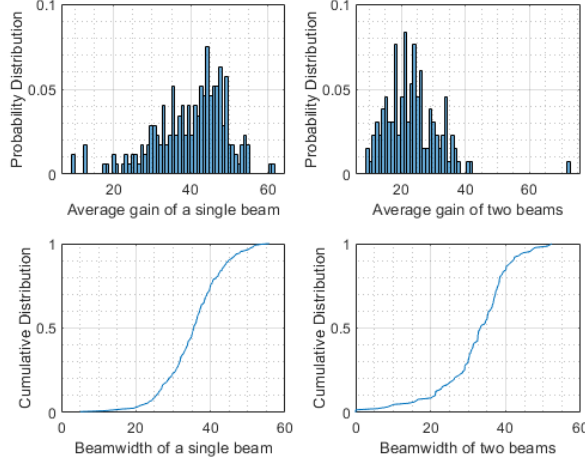


**Figure 2.** Gain and HPBW distributions for one and two-beam cases

The gain can then be expressed by as the product of the average gain per path and half-power beamwidth as expressed in (2).

$$G = G_{avg} \times HPBW_{avg} \quad (2)$$

#### 4 Analytical Formulation Using Stochastic Geometry

We assume that the base stations are distributed following a Poisson point process  $\Phi_{BS}$ , a simple path loss model  $r^{-\alpha}$  where  $\alpha$  is the path loss exponent, and  $m$  is the minimum distance from the BS to avoid infinite exposure. The exposure can be calculated by summing the received power at a certain point in space from the serving base station and from all other interferers.

Where  $\phi(t) = E\{\exp(jtX)\}$  is the characteristic function of the exposure. It can also be written as in (3).

$$\begin{aligned} \phi(t) &= E \left\{ \exp \left( jt \sum_{r_i \in \Phi_{BS}} P_{tx} |h|^2 G_{Tx}(\theta) r^{-\alpha} \right) \right\} \\ &= E_r \left\{ E_{|h|^2} \left\{ \prod_{x \in \Phi_{BS}} \int \exp (j t P_{tx} |h|^2 G(\theta) r^{-\alpha} d\theta \right\} \right\} \end{aligned} \quad (3)$$

The close-form equation can then be expressed by (4):

$$\phi(t) = \exp \left( -2\pi\lambda BW G P_G \frac{jtP_{tx}G\bar{y}m^{2-\alpha}}{\alpha-1} {}_2F_1 \left( 1, \frac{\alpha-2}{\alpha}, 2-\frac{2}{\alpha}, jtP_{tx}G BW P_G \bar{y}m^{-\alpha} \right) \right) \quad (4)$$

Where,  $\alpha$  is the path loss exponent,  $BW$  is the beamwidth,  $\lambda$  is the PPP intensity,  $G$  is the average gain,  $P_{tx}$  the transmit power, and  $m$  the minimum separation distance.

#### 5 Results

The CDF of the exposure can be determined using the Gil-Peleaz theorem [4] represented by (5).

$$F(x) = \frac{1}{2} - \frac{1}{\pi} \int_0^\infty \frac{\text{Im}[e^{-jtx}\phi(t)]}{t} dt \quad (5)$$

The CDF produced from the stochastic-geometric framework is then compared with a Monte-Carlo simulation for both the case of a single emitted beam, and the case of two emitted beams, as shown in Figure 3 and Figure 4.

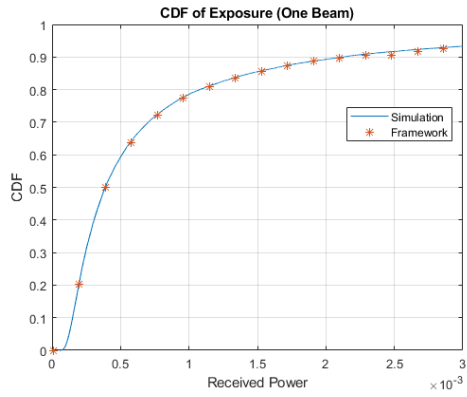


Figure 3. CDF of the exposure (Simulation vs Framework) for one beam case

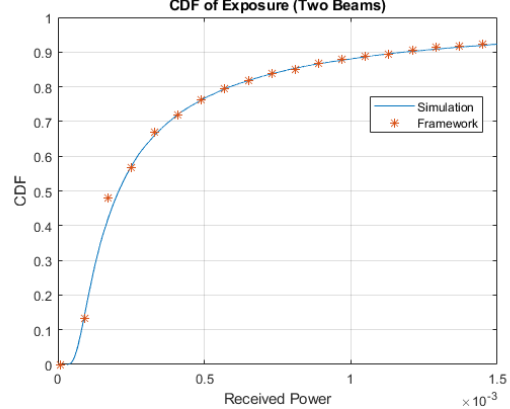


Figure 4. CDF of the exposure (Simulation vs Framework) for two beam case

These two figures clearly show the difference between operating the antenna with a single beam and multiple beams. The difference in the exposure is attributed to the division of the antenna elements into two parts to form two different beams, which reduces the gain of the lobe serving a certain user.

## 6 Conclusion

In this paper, we have presented an accurate framework to analytically estimate the exposure in a massive MIMO network using stochastic geometry.

We have also made the comparison between the different implementation cases of a massive MIMO antenna which can be significant and confirms the interest of the study in this domain.

Future work will focus on producing more accurate and representative models in order to better study the variability of massive MIMO networks, and the effects the changes of the characteristics and the network usage on the exposure in addition to the spatio-temporal behavior of antenna.

## 7 References

- [1] P. Baracca, A. Weber, T. Wild, and C. Grageat, “A Statistical Approach for RF Exposure Compliance Boundary Assessment in Massive MIMO Systems,” 2018.
- [2] M. Haenggi, *Stochastic geometry for wireless networks*, vol. 9781107014. 2009.
- [3] S. Sun, G. R. Maccartney, and T. S. Rappaport, “A novel millimeter-wave channel simulator and applications for 5G wireless communications,” *IEEE Int. Conf. Commun.*, vol. 10, no. 1, pp. 1–7, 2017.
- [4] J. GIL-PELAEZ, “Note on the inversion theorem,” *Biometrika*, vol. 38, no. 3–4, pp. 481–482, 1951.

## **Proposal for simplified RF exposure assessment formula updates for millimetre wave small cells using beamforming**

---

**Kamil Bechta<sup>1</sup>, Christophe Grangeat<sup>2</sup>**

<sup>1</sup>Nokia, kamil.bechta@nokia.com

<sup>2</sup>Nokia, christophe.grangeat@nokia.com

---

**Keywords:** 5G, beamforming, millimetre wave, radio frequency exposure, small cell

### **Abstract/Résumé**

Together with introduction of 5<sup>th</sup> generation (5G) of mobile communication system the millimetre wave (mmWave) frequency range is started to be utilized for personal mobile communication. Small cells deployment is typically assumed for mmWave as well as beamforming and beam steering of antenna radiation pattern. All this together enforce updates in current approaches for evaluation of radio frequency (RF) exposure, which were established and optimized for legacy systems. This paper proposes updates of simplified evaluation methods determined by International Electrotechnical Commission (IEC) for radio equipment working in frequency range between 2 GHz and 100 GHz covering mmWave. Proposed updates allow to improve the accuracy of simplified evaluation of compliance distances from mmWave small cell antennas which are capable to perform beamforming and beam steering.

### **1 Introduction**

5<sup>th</sup> generation of mobile communication system (5G) starts utilization of millimetre wave (mmWave) frequency range for personal mobile communication. On top of that 5G introduces common use of beamforming with narrow-beam directional antennas and continues deployment of small cells for improvement of network capacity. Due to challenging propagation conditions in mmWave the most common deployment for this frequency range is small cell with high-gain directional antennas and beamforming, which creates a new study case from the perspective of radio frequency (RF) exposure assessment. International Electrotechnical Commission (IEC) in [1] and [2] defines simplified evaluation process of RF exposure from base stations (BS) of different classes, including low power small cells, which is based on International Commission on Non-Ionizing Radiation Protection (ICNIRP) [3] general public limits. This paper proposes update of approach presented in [1] and [2], which allows to minimize the simplified evaluation error in case of mmWave small cells with high-gain directional antennas and beamforming. Therefore, Section 2 discusses current versions of formulas for simplified evaluation of compliance distances according to [1] and [2]. Section 3 presents results of this simplified evaluation in reference to simulation results obtained from comprehensive computation model, whereas section 4 proposes how to improve the accuracy of simplified approach by minimization of evaluation error. Section 5 summarizes and concludes the paper.

### **2 Current small cell installation guidance with simplified verification process**

IEC in section 6.2.4 of [1] defines simplified product installation evaluation process which applies to wide range of BS classes. Each class represents BSs with given range of applicable equivalent isotropic radiated power (EIRP), based on which the product installation criteria are defined. Currently, the simplified guidance of [1] are used with general public ICNIRP-based [3] exposure limits, however IEC is working on extended guidance that is applicable to other exposure limits than ICNIRP.

For frequency range between 2 GHz and 100 GHz, which includes mmWave range, the IEC recommends the minimum height ( $H_m$ ) of the lowest radiating part of the beamforming antenna(s) above the general public walkway and the minimum distance ( $D_m$ ) to areas accessible to the general public in the main lobe direction, as specified below by (1) and (2), respectively.

$$H_m = \max \begin{cases} 2 + \sqrt{\frac{EIRP \cdot A_{sl}}{10\pi}} \\ 2 + \sqrt{\frac{EIRP}{10\pi}} \sin(\alpha + 1.129\theta_{bw}) \end{cases} \quad (1)$$

$$D_m = \sqrt{\frac{EIRP}{10\pi}} \quad (2)$$

where:

- $A_{sl}$  is the side lobe suppression value in linear domain,
- $\alpha$  is the total downtilt in [rad],
- $\theta_{bw}$  is the vertical half power beamwidth (HPBW) in [rad].

As can be noticed, the outcome compliance distances from (1), i.e.  $H_m$ , depends on the way how the radiating directional antenna is forming the radiation pattern towards the point of investigation below the antenna. If the evaluated exposure is caused by the side lobes of static beam then the upper part of (1) applies. However, if the antenna is performing beam steering and is capable to tilt the beam towards the general public walkway, the lower part of (1) applies.

Because beamforming with beam steering are key features of 5G, the lower part of (1) will be investigated in further part of this paper, where updates of (1) and (2) are proposed to improve the accuracy of simplified evaluation of compliance distances for 5G mmWave small cells with beamforming and beam steering.

### 3 Simulations of RF exposure assessment for 5G mmWave small cell

To assess accuracy of simplified approach presented by (1) and (2) the realistic RF exposure was calculated using the synthetic model method defined by IEC in section B.4.4.1 of [1] and [4] and disclosed by (3) below. This model allows to determine the electric field strength at a point of investigation as a vector sum of  $n$  small patches of the antenna treated as separate sources.

$$E = \sum_n \alpha_n \frac{\sqrt{30 \times P_n \times G_n}}{r_n} e^{j(\gamma_n + \frac{2\pi r_n}{\lambda})} \quad (3)$$

where:

- $E$  is the electric field strength in [V/m],
- $r_n$  is the distance between the observation point and reference point of patch  $n$  in [m],
- $P_n$  is the input power to patch  $n$  in [W],
- $\gamma_n$  is the relative phase of applied voltage at antenna patch  $n$  in [rad],
- $G_n$  is the gain of patch  $n$  towards the point of investigation relative to an isotropic antenna in linear domain,
- $\alpha_n$  is the weighting coefficient,
- $\lambda$  is the wavelength in [m].

Calculations were performed with the “EMF Visual” software release 4.0 [5] based on methods developed in [4]. RF exposure has been simulated for typical 5G mmWave (28 GHz and 39 GHz) small cell BSs with realistic RF parameters to increase the practicality of outcome results. Table 1 contains main RF parameters of BSs used for simulations, whereas Table 2 and Table 3 present compliance distances obtained from simulations for 28 GHz and 39 GHz cases, respectively. Table 2 and Table 3 include also simplified evaluations of  $D_m$  and  $H_m$  for parameters from Table 1 obtained according to (1) and (2) derived from [1].

As can be noticed, calculation results according to simplified approach (1) and (2) demonstrate overestimation of compliance distance in reference to simulation results based on synthetic model (3). In case of  $H_m$  the estimation error increase from around 20% to 120% in assumed range of EIRP. For both frequency cases, i.e. 28 GHz and 39 GHz,  $H_m$  estimation error is similar, however it increases together with the increase of downtilt, which has been illustrated in Figure 1.

In case of  $D_m$  the estimation error is above 100% in full range of assumed EIRP, whereas, for 39 GHz frequency and lower values of EIRP, it can be as high as 150-200%. More detailed illustration of  $D_m$  estimation error is presented in Figure 1.

It should be noted, that more comprehensive study with larger number of calculation results and wider range of frequencies would be needed to finally assess the accuracy of simplified approach, however results presented in this paper give already an overview on the range of possible estimation errors.

*Table 1 : Main RF parameters of BS used for simulations of RF exposure*

Parameter	Value							
Antenna array configuration	8(V) x 8(H) x 2(Pol)							
Frequency [GHz]	28					39		
Vertical HPBW ( $\theta_{bw}$ ) [ $^{\circ}$ ]	12.5					10.0		
Max total downtilt ( $\alpha$ ) [ $^{\circ}$ ]	30	45		30	45		30	45
EIRP [dBm]	44, 54, 64, 70	50, 54, 60, 64, 70	44, 54, 64, 70	50, 54, 60, 64, 70	44, 54, 64, 70	50, 54, 60, 64, 70	44, 54, 64, 70	50, 54, 60, 64, 70

*Table 2: Simulation results and simplified calculations of compliance distances for 28 GHz case*

Compliance Distance (28 GHz)									
EIRP [dBm]	44	50	54	54	60	64	64	70	70
Downtilt [ $^{\circ}$ ]	30	45	30	45	45	30	45	45	30
<i>Synthetic method results using (3)</i>									
$D_m$ [m]	<b>0.4</b>	<b>0.9</b>	<b>1.4</b>	<b>1.4</b>	<b>2.8</b>	<b>4.5</b>	<b>4.5</b>	<b>9.0</b>	<b>9.0</b>
$H_{u,d}$ [m]	0.1	0.5	0.7	0.8	1.7	2.2	2.7	5.7	4.6
$H_m$ [m]	<b>2.1</b>	<b>2.5</b>	<b>2.7</b>	<b>2.8</b>	<b>3.7</b>	<b>4.2</b>	<b>4.7</b>	<b>7.7</b>	<b>6.6</b>
<i>Simplified calculations using (1) and (2)</i>									
$D_m$ [m]	0.9	1.8	2.9	2.9	5.7	9.0	9.0	17.9	17.9
$D_{m\_adj}$ [m]	<b>0.5</b>	<b>0.9</b>	<b>1.4</b>	<b>1.4</b>	<b>2.9</b>	<b>4.5</b>	<b>4.5</b>	<b>9.0</b>	<b>9.0</b>
$H_m$ [m]	2.7	3.6	4.0	4.5	6.9	8.3	9.7	17.3	14.5
$H_{m\_adj}$ [m]	<b>2.3</b>	<b>2.6</b>	<b>2.8</b>	<b>3.0</b>	<b>3.9</b>	<b>4.5</b>	<b>5.0</b>	<b>8.0</b>	<b>6.9</b>

*Table 3: Simulation results and simplified calculations of compliance distances for 39 GHz case*

Compliance Distance (39 GHz)									
EIRP [dBm]	44	50	54	54	60	64	64	70	70
Downtilt [ $^{\circ}$ ]	30	45	30	45	45	30	45	45	30
<i>Synthetic method results using (3)</i>									
$D_m$ [m]	<b>0.3</b>	<b>0.6</b>	<b>1.2</b>	<b>1.2</b>	<b>2.8</b>	<b>4.4</b>	<b>4.4</b>	<b>9.0</b>	<b>9.0</b>
$H_{u,d}$ [m]	0.2	0.5	0.6	0.8	1.7	2.1	2.7	5.3	4.3
$H_m$ [m]	<b>2.2</b>	<b>2.5</b>	<b>2.6</b>	<b>2.8</b>	<b>3.7</b>	<b>4.1</b>	<b>4.7</b>	<b>7.3</b>	<b>6.3</b>
<i>Simplified calculations using (1) and (2)</i>									
$D_m$ [m]	0.9	1.8	2.9	2.9	5.7	9.0	9.0	17.9	17.9
$D_{m\_adj}$ [m]	<b>0.5</b>	<b>0.9</b>	<b>1.4</b>	<b>1.4</b>	<b>2.9</b>	<b>4.5</b>	<b>4.5</b>	<b>9.0</b>	<b>9.0</b>
$H_m$ [m]	2.6	3.5	3.9	4.4	6.7	7.9	9.5	16.9	13.8
$H_{m\_adj}$ [m]	<b>2.3</b>	<b>2.6</b>	<b>2.8</b>	<b>3.0</b>	<b>3.9</b>	<b>4.3</b>	<b>4.9</b>	<b>7.9</b>	<b>6.6</b>

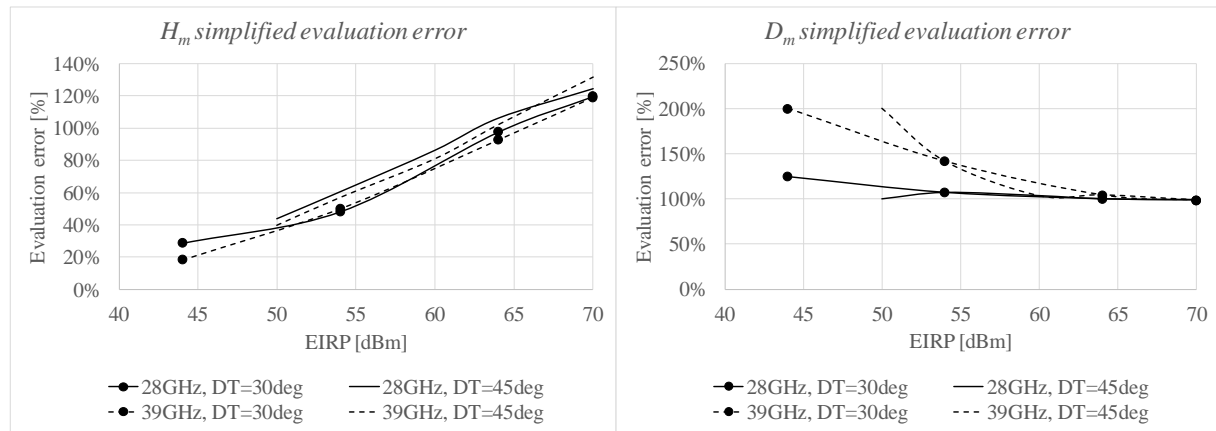


*Figure 1 : Plots of simplified evaluation error in function of EIRP and downtilt*

#### 4 Modified small cell installation guidance with simplified verification process

As can be noticed, Table 2 and Table 3 contain also adjusted values of  $D_m$  and  $H_m$ , marked as  $D_{m\_adj}$  and  $H_{m\_adj}$ . Adjustment means that (1) and (2) have been modified to provide compliance distance aligned with results of exposure assessment simulations based on synthetic model method (3). Updated forms of (1) and (2) are presented below as (4) and (5), respectively. Increased have been constant factors for EIRP calibration, which has been changed from 10 to 65 and from 10 to 40 for  $H_m$  and  $D_m$ , respectively.

$$H_m = 2 + \sqrt{\frac{EIRP}{65\pi}} \sin(\alpha + 1.129\theta_{bw}) \quad (4)$$

$$D_m = \sqrt{\frac{EIRP}{40\pi}} \quad (5)$$

Updated formulas for simplified approach demonstrate reduced error in compliance distance evaluations. In case of  $H_m$  the estimation error is below 10% for all investigated cases, whereas  $D_m$  estimation error has been reduced by at least four times in comparison to results obtained by (2). Illustration of estimation errors for updated formulas is presented in Figure 2.

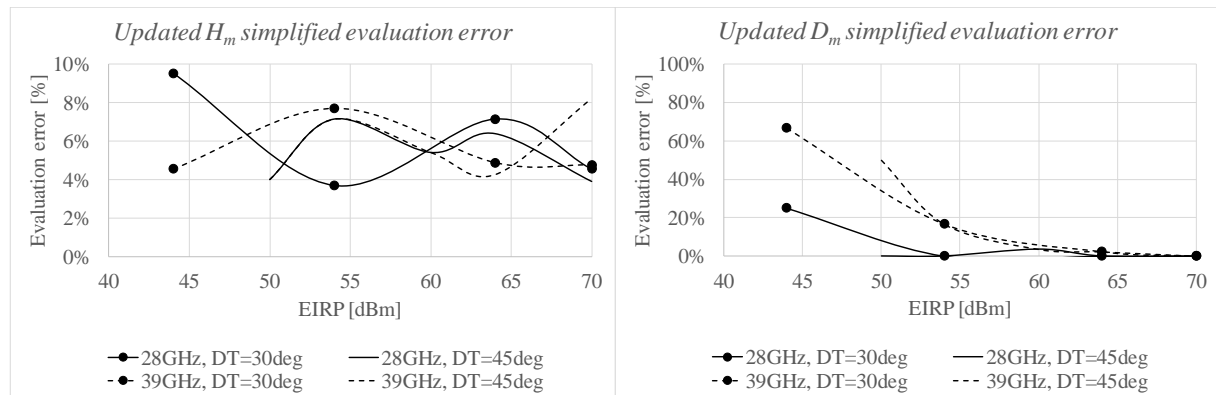


Figure 2 : Plots of updated simplified evaluation error in function of EIRP and downtilt

#### 5 Conclusion

Modifications of simplified formulas introduced in [1] for product installation guidance have been proposed, which after additional verification can be part of future extensions of this guidance towards 5G mmWave small cell equipment with beamforming. Verified update is proposed for inclusion in future EMF exposure standards updates e.g. [1] and [6]. It is particularly important in the light of recent decisions made by World Radiocommunication Conference of 2019 (WRC-19) [7] on allocation of new mmWave frequency bands, e.g. 26 GHz, 39 GHz or 48 GHz, for 5G deployment. Updated formulas demonstrate reduced estimation error of compliance distances in comparison to current version of [1], but remain conservative compared to results obtained by synthetic model method.

#### References

- [1] IEC 62232:2017, “Determination of RF field strength, power density and SAR in the vicinity of radiocommunication base stations for the purpose of evaluating human exposure”, September 2017.

- [2] IEC TR 62669, “Case studies supporting IEC 62232 – Determination of RF field strength and SAR in the vicinity of radiocommunication base stations for the purpose of evaluating human exposure”.
- [3] International Commission on Non-Ionizing Radiation Protection (ICNIRP), “Guidelines for limiting exposure to time-varying electric, magnetic, and electromagnetic fields (up to 300 GHz)”, Health Phys 74: 494-522.2 1998.
- [4] Z. Altman, B. Begasse, C. Dale, A. Karwowski, J. Wiart, M.F. Wong, and L. Gattoufi, “Efficient models for base station antennas for human exposure *assessment*”, IEEE Trans. Electromagn. Compat. Nov 2002, vol.44, pp. 588-592.
- [5] Microwave Vision Group (MVG), “EMF Visual User Manual”, SEWB/EMF-VISUAL-UM.1/v2020.0.
- [6] ITU-T Recommendation K.52, “Guidance on complying with limits for human exposure to electromagnetic fields”.
- [7] <https://news.itu.int/wrc-19-agrees-to-identify-new-frequency-bands-for-5g/>

## RF-EMF exposure assessment in the new incoming 5G indoor exposure scenarios

**Marta Bonato<sup>1,2</sup>, Laura Dossi<sup>1</sup>, Emma Chiaramello<sup>1</sup>, Serena Fiocchi<sup>1</sup>, Silvia Gallucci<sup>1</sup>, Gabriella Tognola<sup>1</sup>, Paolo Ravazzani<sup>1</sup> and Marta Parazzini<sup>1</sup>**

<sup>1</sup> Institute of Electronics, Computer and Telecommunication Engineering, CNR, Milano, Italy,  
[marta.bonato@ieiit.cnr.it](mailto:marta.bonato@ieiit.cnr.it), [emma.chiaramello@ieiit.cnr.it](mailto:emma.chiaramello@ieiit.cnr.it), [serena.fiocchi@ieiit.cnr.it](mailto:serena.fiocchi@ieiit.cnr.it), [laura.dossi@ieiit.cnr.it](mailto:laura.dossi@ieiit.cnr.it),  
[silvia.gallucci@ieiit.cnr.it](mailto:silvia.gallucci@ieiit.cnr.it), [gabriella.tognola@ieiit.cnr.it](mailto:gabriella.tognola@ieiit.cnr.it), [paolo.ravazzani@ieiit.cnr.it](mailto:paolo.ravazzani@ieiit.cnr.it),  
[marta.parazzini@ieiit.cnr.it](mailto:marta.parazzini@ieiit.cnr.it)

<sup>2</sup> Department of Electronics, Information and Bioengineering, Polytechnic of Milano, Italy

---

**Keywords:** indoor 5G scenario, RF-EMF exposure assessment

---

### Abstract

In the next years the development of the incoming 5G networks will drastically change the level of exposure of the population to RF-EMF. For this reason, there is a need to promptly conduct an adequate exposure assessment. In the present work a specific case of a user exposure scenario is evaluated, where the user is placed in a room where a 5G access point is located. More in details, the exposure of two 8x8 multi-element antenna planar arrays are examined in an indoor environment and correctly modelled at 3.7 GHz and 27 GHz. The user exposure assessment will be conducted using the FDTD solver implemented in Sim4Life platform. In specific, the user will be described by the head of Ella model from the Virtual Family, who will be placed at a distance of 50 cm from the antenna array, simulating two different worst cases of exposure scenario. The quantities that will be analyzed for determining the exposure levels are the specific absorption rate (SAR) and the transmitted power density ( $S_{tr}$ ), as indicated in the basic restrictions of the ICNIRP guidelines.

### 1 Introduction

The next incoming generation of 5G mobile networks will be implemented to provide new services and utilities to all the population. Among them, the most innovative aspects will regard the automotive, health and industry sectors. The 5G networks will in fact develop the concept of future smart societies, smart cities and smart homes characterized by the idea of Internet of Things devices' connections [1, 2]. To support these high-performing applications the new networks will have to provide transmissions with a significant data rate increase w.r.t. the actual 4G networks and very low latency, thus new technologies will be necessary to satisfy these unprecedented demands. In particular, one of key 5G technologies outlined in the last Releases of the standardization group 3GPP (3rd Generation Partnership Program) is the use of millimeter (mm)-Wave MIMO (Multiple-Input-Multiple Output) links, requiring the deployment of multi-element antenna arrays operating at these frequencies never used before for mobile applications. In Italy, the first new licensed frequency ranges are 3.6 – 3.8 GHz and 26.5 – 27.5 GHz [3]. The use of these higher frequencies, suffering of very high path loss, will require the use of smaller cells and consequently an increment of the number of base stations (BS), and also the use of directive antennas able to focus the radiation in highly directional beams, i.e. antenna array with a great number of antenna elements. Such technology in 5G networks will be adopted not only at the outdoor BSs (positioned on the roof of high building) but also at radio units at lower height (e.g. on top of traffic lights) for the coverage in urban areas and in indoor scenario. In fact, only the intensive use of new frequencies and multi-element array antennas with high beamforming capability to countermeasure the increased path loss while reducing the interference, will be able to improve the performance in connectivity as foreseen for 5G new applications [4]. However, all these innovations will also drastically change the exposure conditions of a user to the RF-EMF and for this reason it became evident the need of conduction promptly an exposure assessment to these new 5G networks. Consequently, the present work will focus specifically to an example of exposure assessment of a user in downlink scenario at an indoor environment, simulating the presence in the room of a 5G access point. The details of the chosen scenario and of the work are described in the following paragraph.

## 2 Materials and Methods

In this preliminary work two different examples of indoor planar 8x8 antennas arrays were modelled and tested to simulate the presence of a 5G access point in the room. The selected working frequency for the two antennas arrays was one at 3.7 GHz and one at 27 GHz, which represent the frequencies of the first frequencies ranges that will be implemented in 5G Italy networks. Each of the 64 elements of antennas arrays was modelled as a simple patch antenna, whose dimensions and properties were chosen according to literature [5]. The spacing between the elements was set equal to  $\lambda/2$  for both the arrays. To evaluate the exposure levels, it was considered the worst-case exposure levels, where all the elements of the array have a phase shift of  $0^\circ$ , resulting in a central frontal beam perpendicular to the plan of the array. The user was simulated with the model Ella from the Virtual Family and her head was placed at the center height of the antennas array, at a distance of 50 cm. Three different configurations will be examined for both the antennas arrays, one where the user is in front of the antennas array one where the user is placed from the side and the last where the back of the user head is in front of the antenna arrays, as it can be seen from Fig.1.

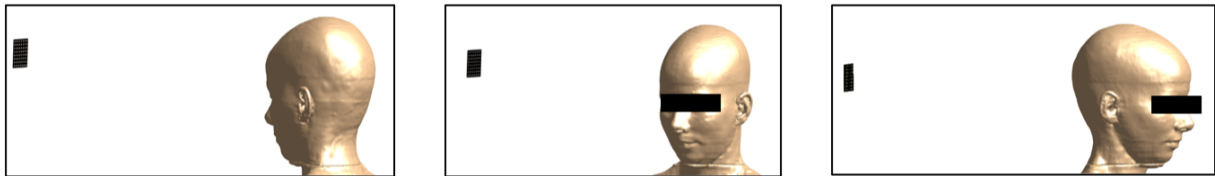


*Figure 1: Scheme of the three different user's configurations that will be analysed for each antennas array. Note that in this figure is represented the antenna array dimensions at 27 GHz.*

Due to computational cost for the 27 GHz frequency, the simulation domain will be limited to the region where the head of the model is present, not considering the rest of the body. The simulations will be conducted using the Sim4Life platform, where the FDTD solver is implemented. The tissues dielectric proprieties of the Ella model were chosen according to literature [6, 7]. For the boundaries of the simulations, it was applied an absorbing condition with perfectly matched layer (PML) and at last each single element of the two arrays was excited by a gaussian signal centred in the two chosen frequencies normalized for a total of 100 mW input power. Data on specific absorption rate (SAR) and transmitted power density ( $S_{tr}$ ), as suggested from the ICNIRP guidelines [8], will be analyzed for the exposure assessment.

## 3 Results

In the present paragraph are reported only some preliminary results about the complete analysis that will be conducted for the three different configurations for the indoor planar 8x8 antennas array at 3.7 GHz and at 27 GHz.

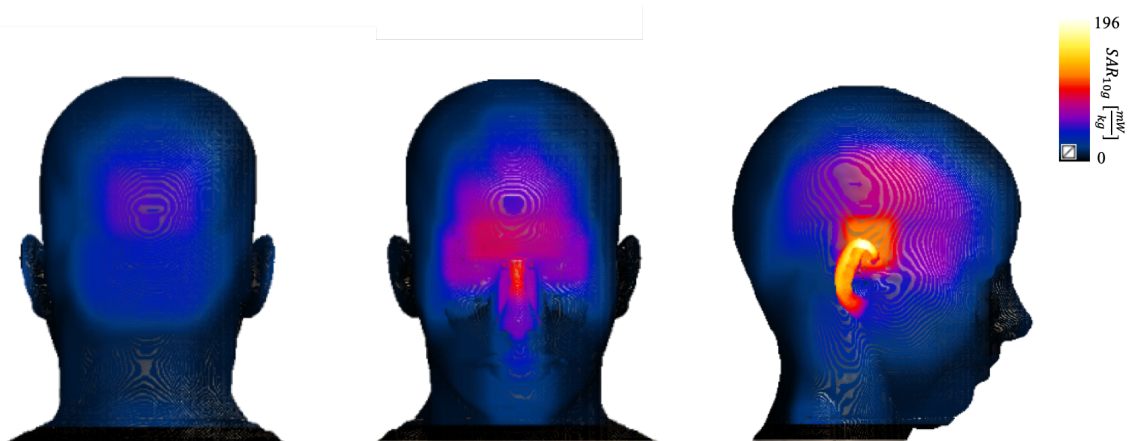


*Figure 2: Distribution of  $SAR_{10g}$  induced on the head skin model by the 8x8 planar antenna array at 3.7 GHz with a total of 100 mW input power. At the left for the posterior configuration, in the middle for the frontal one and at the right for the lateral one.*

In Fig.2 it is in fact illustrated the SAR, averaged on 10 g of skin tissue ( $SAR_{10g}$ ), for the three different configurations obtained from the exposure to the 8x8 planar antenna array at 3.7 GHz with an input power of 100 mW. As it can be seen for the figure, the configuration that caused the highest values of exposure is the lateral one, principally in the ear skin area, with a peak of  $SAR_{10g}$  equal to 196 mW/kg, well below the ICNIRP limit of 2 W/kg for the average head and torso exposure. The peak  $SAR_{10g}$  for the frontal configuration is a bit lower and equal to 104 mW/kg, whereas the lowest values of exposure are obtained for the posterior configuration, where the highest value of  $SAR_{10g}$  is equal to 51 mW/kg, almost a quarter of the peak value of the frontal configuration. The next work steps will involve a detailed analysis to assess the exposure levels on different tissues in the head model. The same analysis will be replied also for the configurations with the 8x8 array antenna at 27 GHz.

## 4 Conclusion

The presented work will mainly focus on some downlink exposure cases in indoor environment, characterizing a single user exposure levels changes that will occur with the introduction of the multi-element antennas array with beamforming capability in the mm-wave frequency range. The exposure assessment will be evaluated principally based on ICNIRP guidelines.

Future works will also involve the use of stochastic methods and machine learning [9, 10] approaches combining with deterministic dosimetry to face the high variability of scenarios that will characterize the 5G networks.

## Acknowledgment

The authors wish to thank Schmid and Partner Engineering AG ([www.speag.com](http://www.speag.com)) for having provided the simulation software SEMCAD X/SIM4Life.

## References

- [1] J.G. Andrews, S. Buzzi, W. Choi, S.V. Hanly, A. Lozano, A.C. Soong, J.C. Zhang, "What will 5G be?". In IEEE Journal on selected areas in communications. 2014 Jun 3;32(6):1065-82.
- [2] Boccardi F, Heath RW, Lozano A, Marzetta TL, Popovski P. Five disruptive technology directions for 5G. IEEE Communications Magazine. 2014 Feb 12;52(2):74-80.
- [3] Recommendations, ITU-T. K-Series. "5G technology and human exposure to RF EMF." (2017).
- [4] Larsson EG, Edfors O, Tufvesson F, Marzetta TL. Massive MIMO for next generation wireless systems. IEEE communications magazine. 2014 Feb 12;52(2):186-95
- [5] Shikhantsov, Sergei, et al. "STATISTICAL APPROACH FOR HUMAN ELECTROMAGNETIC EXPOSURE ASSESSMENT IN FUTURE WIRELESS ATTO-CELL NETWORKS." Radiation protection dosimetry 183.3 (2018): 326-331.
- [6] C. Gabriel, S. Gabriel and Y.E. Corthout, "The dielectric properties of biological tissues: I. Literature survey," Physics in Medicine & Biology, 1996, 41(11), 2231.
- [7] S. Gabriel, RW. Lau, and C. Gabriel, "The dielectric properties of biological tissues: II. Measurements in the frequency range 10 Hz to 20 GHz", Phys Med Biol, vol. 41, pp. 2251-2269, 1996.
- [8] International Commission on Non-Ionizing Radiation Protection, "ICNIRP guidelines for limiting exposure to time-varying electric, magnetic and electromagnetic fields (up to 300 GHz)", Health Phys, vol. 74, pp. 494-522, 1998.
- [9] E. Chiaramello, S. Fiocchi, M. Parazzini, P. Ravazzani, J. Wiart, "Stochastic Dosimetry for Radio-Frequency Exposure Assessment in Realistic Scenarios". In Uncertainty Modeling for Engineering Applications 2019 (pp. 89-102). Springer, Cham.
- [10] G. Tognola, M. Bonato, E. Chiaramello, S. Fiocchi, I. Magne, M. Souques, M. Parazzini, and P. Ravazzani, Use of Machine Learning in the analysis of indoor ELF MF exposure in children", Int J Environ Res Public Health, vol. 16, p. 1230-1243, 2019.

# Artificial Neural Networks for Uncertainty Quantification in RF Radiation Modeling

---

**X. Cheng<sup>1</sup>, C. Henry<sup>2</sup>, F. Andriulli<sup>3</sup>, C. Person<sup>4</sup>, and J. Wiart<sup>5</sup>**

<sup>1</sup>Chaire C2M, LTCI, Télécom ParisTech, Université Paris-Saclay, France, xi.cheng@telecom-paris.fr

<sup>2</sup>Department of Electronics and Telecommunications, Politecnico di Torino, Turin, Italy, clement.henry@polito.it

<sup>3</sup>Department of Electronics and Telecommunications, Politecnico di Torino, Turin, Italy, clement.henry@polito.it

<sup>4</sup>IMT Atlantique / lab-STICC UMR CNRS 6285, Technopole Brest Iroise, France, christian.person@imt-atlantique.fr

<sup>5</sup>Chaire C2M, LTCI, Télécom ParisTech, Université Paris-Saclay, France, joe.wiart@telecom-paris.fr

---

**Keywords:** Artificial neural network, electroencephalography, uncertainty quantification

**Abstract:**

This paper focuses on quantifying the uncertainty in the outputs of numerical simulations produced by uncertain positions of the electrodes placed on patient's scalp. In order to avoid running thousands of simulations, an architecture which combines two different artificial neural networks (ANNs) for uncertainty quantification (UQ) is proposed in this paper. The overall aim of this work is to develop a surrogate model for UQ involving high-dimensional data. The proposed method is demonstrated to be an attractive alternative to conventional UQ methods since it shows considerable advantage in the computational expense and speed.

## 1 Introduction

The final goal of ANSES ECLAIR project is to design a system allowing high resolution EEG recordings in the presence of an RF radiating source and taking electromagnetic field deformation into account. Achieving this goal requires understanding well the interaction between the metallic part of the EEG recordings and the RF source. Since measurement is time consuming and expensive, numerical modeling is an effective alternative method to investigate the physical properties of the proposed system. The modeling of the radiating source, head, and EEG device relies on sets of input parameters which can affect the electromagnetic field, and then affect specific absorption rate (SAR) values in brain. In practice, the exact values of the random inputs can not be found, which produces uncertainties in simulation results. Uncertainty quantification (UQ) is an indispensable part when the acceptability of the simulation results is considered. In this paper, UQ is concentrated on uncertain positions of the electrodes in a EEG helmat.

## 2 Design of the experiment (DoE)

The head model is a 3-layer sphere, and the electrodes is formed by triangles on the sphere. In this case, the position of each electrode can be represented by  $(r, \theta_p, \phi_p)$  ( $p = 1, \dots, L$ ) in a spherical coordinate system and  $(P_p^x, P_p^y, P_p^z)$  in a Cartesian coordinate system, respectively, where  $r$  is the radius of the sphere,  $\theta_p$  is polar angle,  $\phi_p$  is azimuthal angle, and  $L$  is the number of electrodes. The coordinates of the two systems can be transformed into each other. The original Cartesian coordinate of a electrode  $(P_p^x, P_p^y, P_p^z)$  is obtained by a toolbox, and they are used in the numerical simulations. The uncertainties in the positions of the electrodes are modeled in a spherical coordinate system, and the coordinates with uncertainties required to be transformed into Cartesian coordinates. In a spherical coordinate system, the center of each electrode moves in a square, and the size of the square is controlled by  $\Delta$ . For each electrode, there are 9 possible positions represented by 9 indexes. When  $\Delta$  is determined, the uncertainty of the position of an electrode can be modeled by the 9 indexes which is a discrete random variable. In the above case, the electrodes positions are changed independently of one another, and the number of combination is  $9^L$ .

## 3 Acknowledgement

This research is supported by the French Agency for Food, Environmental and Occupational Health Safety (ANSES): Project ECLAIR (ANSES ECLAIR EST-2016-2-RF-23).

## Assessment Of Temporal Uplink Emitted Power Variation For VoLTE Calls

Amirreza Chobineh<sup>1</sup>, Emmanuelle Conil<sup>2</sup> and Joe Wiart<sup>1</sup>

<sup>1</sup>Telecom Paris, Chair C2M, Palaiseau, France, {amirreza.chobineh@telecom-paris.fr}

<sup>2</sup>ANFR, Maison-Alfort, France

Exposure, VoLTE, Temporal,

### 1 Abstract

Voice over LTE (VoLTE) is a technology used by operators to offer voice calls over LTE technology. In this study the temporal variation of power emitted by UE during a VoLTE voice call is investigated through measurements in a human exposure point of view. The effect of Semi-Persistent-Scheduling (SPS) and voice activity detection (VAD) algorithms on emission duration is assessed and the temporal occupation rate of the uplink emitted power of UE during a VoLTE call is presented.

### 2 Introduction

People now use their mobile phone for a large variety of uses such as browsing, checking emails, social media, streaming etc., however, voice communication stays as one of the main mobile phone uses. Voice over IP (VoIP) applications such as Skype and WhatsApp have become very popular since they can be used on mobile phones. Since LTE systems only support packet services, the voice service will use Voice over LTE (VoLTE) other than classical circuit-switched voice technology as in GSM and UMTS. Despite the wide use of smartphones, public concerns exist about the mobile phone EMF exposure during wireless calls. Regarding voice calls, the exposure depends on various parameters such as the design of the mobile phone, the position of the mobile phone and its antenna according to the head and the emitted power of the device during a voice call. The influence of the design of the mobile phone, as well as the effect of the position on RF exposure, has been carried out in previous studies[1]. The emitted power by users equipment (UE), however, is a highly variable parameter that depends on the technology and algorithms through which voice communication is performed such as power control algorithms, voice activity detection (VAD), compression and encapsulation algorithms, conversation rate, distance from the base station etc.[2] In this study, the temporal variation of emitted power and UE during a 6 minutes VoLTE call is studied.

### 3 VoLTE

VoLTE is a packet switching IP based technique allowing high-quality voice calls and simultaneous data and call transfer. Since VoLTE is a native LTE application, it has the luxury to guarantee the physical resources block (PRBs) allocation to achieve an acceptable quality of service. Semi-Persistent-Scheduling (SPS) is a method used in LTE to minimize granting overhead for real-time applications such as voice calls. It takes advantage of the consistent and predictable transmission pattern of VoLTE packets (constant periods, predictable number of packets etc.) to make a persistent grant of uplink PRBs rather than scheduling the user in every cycle. A VoLTE call can be in two different states: the active state where the voice activity detection (VAD) algorithms detects the existence of voice/sound and UE sends packets in a fast frequency and the idle state during which VAD algorithms do not detect any voice/sound and the UE transmit power in a lower frequency.

### 4 Methods and materials

In order to characterize the power emission and emission time during a voice call, a series of measurements have been performed in an indoor urban office environment. The measurements have been performed at the 1800 MHz frequency band for LTE. A Nemo Handy handheld trace mobile solution[3] installed on a Sony Xperia XZ Premium mobile phone has been used in order to monitor and record network parameters while connected to a French commercial cellular network operator and is placed in cheek position to a SAM head full of absorbent liquid and an absorbent dummy hand. An antenna has been mounted near the trace mobile phone in order to perform relative measurements of the time variation of the emitted power and a Tektronix TDS6124C Digital Storage Oscilloscope is used to monitor and store the emitted power variation by mobile phone during a trial. The distance between the receiver antenna and the trace mobile is 2 cm. Figure 1 illustrates the measurement configuration.

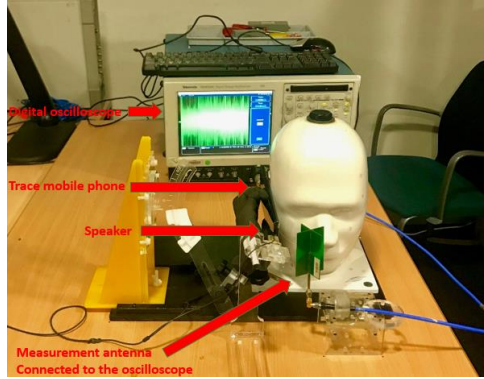


*Figure 1, Measurement configuration*

A 6 minutes voice speech file has been prepared which is a collection of multiple pieces of randomly chosen French audiobooks. The conversation rate of the audio file is 60%. During the measurement, the speech file has been played through a speaker, placed near the trace mobile microphone. The entire system has been caged by wave absorbents during the measurements in order to minimize the environmental noise. The sampling rate of the oscilloscope is 20kS/s.

## 5 Results and discussion

Measurement results performed by oscilloscope show that in active state, the UE transmits every 20 ms and in idle state every 160 ms. (figure 2). During 6 minutes of VoLTE call, UE transmits power, 4% of the time in speech mode and 0.6% of the time in silent mode.

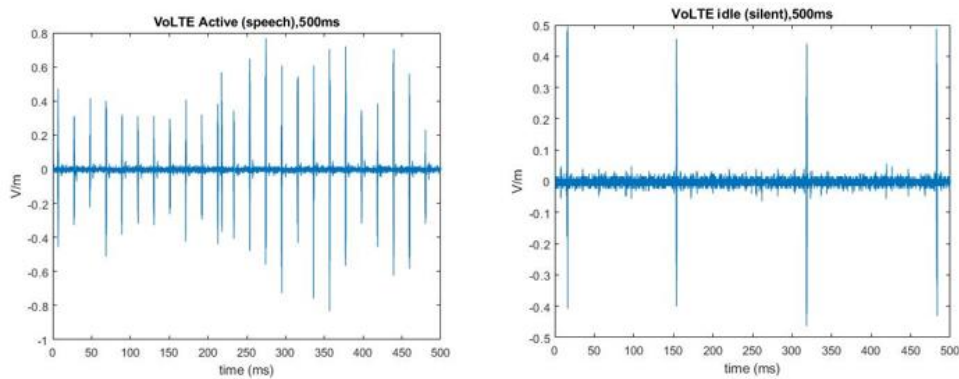


*Figure 2, UE emitted power variation during 500 ms call for idle and active states*

The duration of each transmission is 1ms. These results demonstrate that in case of VoLTE calls, the temporal variation of uplink emitted power is different from the temporal variation of uplink emitted power in data mode. In case of voice calls, the emission power frequency is fixed and the UE does not transmit power most of the time.

It should be noted that the frequency of power transmission in active and idle states is defined by network and can be different from one operator to another.

These results are especially interesting, in case of using trace mobile phones to assess the emitted power by UE. Since Trace mobile phones, report the emitted power in a once or twice per second, these results can help to assess the total power transmission duration and average emitted power over time correctly. The assessment of the temporal variation of uplink emitted power for other technologies and VoIP applications will be investigated in future.

- [1] A. Krayni, A. Hadjem, A. Sibille, C. Roblin, and J. Wiart, “A Novel Methodology to Evaluate Uplink Exposure by Personal Devices in Wireless Networks,” *IEEE Transactions on Electromagnetic Compatibility*, vol. 58, no. 3, pp. 896–906, Jun. 2016.
- [2] J. Wiart, C. Dale, A. V. Bosisio, and A. Le Corne, “Analysis of the influence of the power control and discontinuous transmission on RF exposure with GSM mobile phones,” *IEEE Transactions on Electromagnetic Compatibility*, vol. 42, no. 4, pp. 376–385, Nov. 2000.
- [3] “Nemo Handy Handheld Measurement Solution | Keysight (formerly Agilent’s Electronic Measurement).” [Online]. Available: <https://www.keysight.com/en/pd-2767485/nemo-handy?cc=FR&lc=fre>. [Accessed: 08-Mar-2019].

## Evaluation of exposure induced by a 5G antenna in the 3,4 - 3,8 GHz band.

*Emmanuelle Conil<sup>1</sup>, Jean-Benoît Agnani<sup>2</sup>*

<sup>1</sup>ANFR, *Emmanuelle.Conil@anfr.fr*

<sup>2</sup>ANFR, *Jean-Benoit.Agnani@anfr.fr*

*Keywords:* 5G trials, EMF exposure

### Abstract

This paper presents the exploratory measurements performed by ANFR during the first 5G trials in the band 3400-3800 MHz in order to better understand 5G signals, to anticipate the need to update the in situ measurement protocol and to work on the definition of a new indicator of the exposure. The paper focuses on a case: the trial of Bouygues Telecom at Bordeaux-Mérignac with a Huawei antenna.

### Résumé

Cet article présente les mesures exploratoires réalisées par l'ANFR lors des premiers essais 5G dans la bande 3400-3800 MHz afin de mieux comprendre les signaux 5G, d'anticiper la nécessité de mettre à jour le protocole de mesure in situ et travailler sur la définition d'un nouvel indicateur de l'exposition. L'article porte sur un cas: le pilote de Bouygues Telecom à Bordeaux-Mérignac avec une antenne Huawei.

### 1 Introduction

The key elements of 5G, for exposure, in the new frequency bands are steerable beam antennas to users, wider frequency bands, finer beams and alternating exposure (Time Division Duplex, TDD mode). And the expected consequences are a lower level of exposure outside the beams, a higher exposure level in the beam, a shorter exposure time.

The French National Agency of Frequencies (ANFR) carried out exploratory exposure measurements during the first trials in collaboration with the operator and the antenna manufacturer in order to better understand 5G signals, to anticipate the need to update the in situ measurement protocol and to work on the definition of a new indicator.

In this paper, we are focused on the trial of Bouygues Telecom at Bordeaux-Mérignac with a Huawei antenna.

### 2 5G trial of Mérignac

On this site (cf. Figure 1), a 64T64R (64 transmission and 64 reception antennas) station is installed at 12 meters of height in a false tree and the traffic is generated using a CPE “customer premise equipment” as a receiver.



Figure 1 : on the left, satellite view of the 5G site at Bordeaux-Mérignac, position of the CPE receiving the data and axis of measurements; and on the right, CPE custom premise equipment used to receive the 5G data.

The main characteristics of the 5G signals used on that site are in the Table 1:

Parameter	Values	Parameter	Values
<b>Central frequency</b>	3650 MHz	<b>Centrale frequency of SSB*</b>	3650 MHz
<b>Bandwidth</b>	100 MHz	<b>SSB periodicity</b>	20 ms
<b>Space subcarriers</b>	30 kHz	<b>Number of SSB</b>	7
<b>Frame format</b>	DDDSU	<b>Rated power</b>	200 W
<b>TDD factor</b>	75% downlink		

Table 1 : main 5G characteristics of the site of interest in this paper located in Mérignac

\*SSB : synchronisation signal block

The measurements are performed with a Narda SRM 3006 and a tri-axial probe. Channel power are performed over 100 MHz at a height of 1,5 meter above the ground and 6 minutes time-averaged values are recorded.

## 2.1 Results with no traffic

In the absence of traffic, only signaling signals are transmitted. Figure 2 illustrates the spectrum observed in the absence of traffic. The colors indicate the occurrence of the power levels, indicated on a logarithmic scale on the ordinate, as a function of the frequency on the abscissa (120 MHz around the central frequency of the antenna emission band). The most frequently measured level is shown in yellow and corresponds to the noise level in the band: in fact, most of the time, in the absence of traffic, there is no emission. More rarely, the signaling signals are emitted (blue color in the figure). These signaling signals consist of SSB which occupy a bandwidth of 20 block resources (BR), that is to say 7.2 MHz and are located in the center of the band. The other signals are other reference signals RS (reference signal).

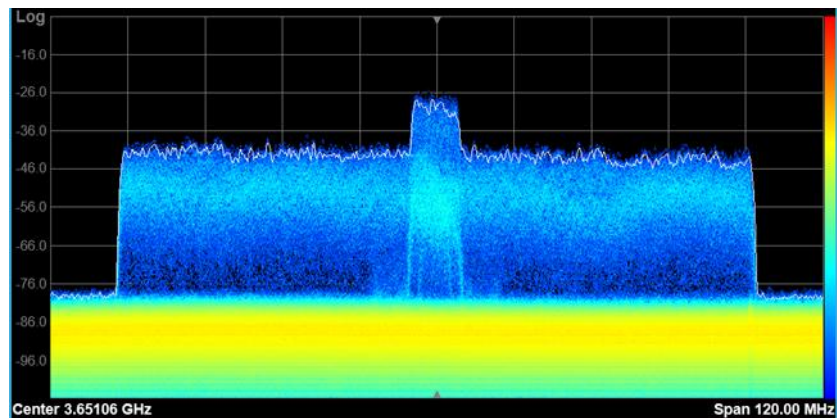


Figure 2: Spectrum (Huawei – Bouygues Telecom – Mérignac)

The average electric field level measured at distances from 35 m to 200 m from the 5G antennas, in the absence of traffic, on the 100 MHz frequency band of the transmitters, is between 0.01 V/m and 0.6 V/m.

## 2.2 Results in continuous transmission in one direction

In that test configuration, the antenna is fully loaded and is transmitting continuously towards a unique receiver. It is worth pointing out that this configuration is not realistic but has the advantage to be well defined, stable in time and reproducible.

In such configuration, the maximum electric field level was measured on this site at almost 9 V/m near the CPE served by the antenna. As a reminder, the regulatory limit in the considered frequency band is 61 V/m. Figure shows, on the left, the electric field level measured at different distances from the 5G antenna, in the axis of the CPE. Reflections on the ground lead to constructive and destructive combinations of the field which explain the field level of only 4 V/m at 120 m from the antenna and the field level of 8.5 V/ m at 90 m from the antenna.

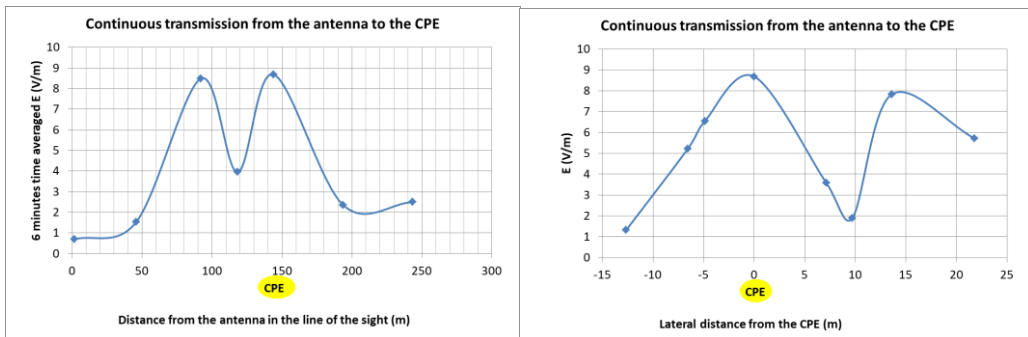


**Figure 3:** levels of time-averaged E-field measured over 100 MHz at 1.5 meters above the ground when antenna is transmitted continuously toward a CPE placed at 145 meters from the antenna.

On the right of the Figure 3, the beam width is illustrated at 1.5 m from the ground and at a distance of 150 m from the antenna. As you move away from the CPE which is served by the antenna, the average field level decreases rapidly (by a factor of 2 to 7.5 m on each side of the CPE). We observe on one side of the CPE the reflection of the field on the large building, this reflection induces a field level of 8 V / m at about 15 m from the CPE against a little more than 1 V/m at the same distance from the CPE, but on the other hand, in the absence of reflection.

### 2.3 Results with download of files

As a more realistic configuration, the 6 minutes time averaged E fields has been measured during the download of files with different sizes. In that case, the CPE was not able to receive more than 140 RB compared to the 273 RB available at the antenna. During the transmissions, the antenna was loaded at about 50% of its maximum. Results are in the Table 2. As expected, the level of the time averaged E field is strongly dependant of the configuration.

Duration of download	File size	6 minutes time averaged E-field
No download	0 MB	0,2 V/m
2 s	150 MB	0,5 V/m
7 s	500 MB	0,8 V/m
15 s	1 GB	1,1 V/m
150 s	10 GB	3,9 V/m
Infinite	Infinite	6,5 V/m

**Table 2 :** results of 6 minutes time averaged E field corresponding to the download of files of different sizes.

These measurements made it possible to observe the frequency spectrum and the temporal occupation of the first 5G signals. They also highlighted the variation in the level of exposure as a function of usage and led to the proposal of a new indicator making it possible to better reflect the real exposure created by 5G networks with orientable beams. This indicator is based on a predictable usage pattern for 5G, which results in the sending, in a given direction, of one gigabyte of data every 6 minutes. With an assumption of an average speed of 500 Mbps, the antenna then transmits in the given direction about 15 seconds every 6 minutes (about 4% of the time). The hypotheses to define this indicator will be compared with the measurements of exposure carried out in the field, for 5G commercial networks. They will be revised if necessary.

This indicator results in a reduction factor which makes it possible to calculate the exposure under real conditions from the theoretical maximum power of the antennas. Field levels at 100 meters from a 5G antenna resulting from the application of the indicator appear comparable to those found at the same distance from a 4G antenna.

<b>4G</b>	<b>Current</b>	<b>Future</b>
Power	60 W	160 W
Gain	18 dBi	18 dBi
Attenuation over 6 minutes	- 4 dB	- 4 dB
Glazing	- 2 dB	- 2 dB
<b>Estimated E field at 100 m</b>	<b>1,7 V/m</b>	<b>2,8 V/m</b>

Table 3: estimation of the electric field level at 100 meters from a 4G antenna inside a building with an assumption of typical current transmitting power and an assumption of future transmitting power.

<b>5G</b>	<b>Low assumption</b>	<b>High assumption</b>
Power	80 W	200 W
Gain	24 dBi	24 dBi
Attenuation over 6 minutes	- 13,5 dB	- 13,5 dB
Glazing	- 2 dB	- 2 dB
TDD	- 1,25 dB	- 1,25 dB
<b>Estimated E field at 100 m</b>	<b>1,1 V/m</b>	<b>1,8 V/m</b>

Table 4: estimation of the electric field level at 100 meters from a 5G antenna inside a building with a low power and a high transmitting power assumption.

However, in 4G, the reduction factor applies to the maximum value of the antenna gain which is only observed in the main direction of the antenna: outside this main direction, the field level will be lower. However, with the 5G steerable beam antennas, the exposure calculated from the indicator will be valid in a larger number of directions.

### 3 Conclusion

This process of exposure evaluation has been set up on different 5G trials to cover different configurations (operator, manufacturer and 5G characteristics). The results have also been used to work on a new indicator of exposure as in situ measurement aims also at providing information on daily exposure.

## On the use of ERCs for 5G measurements *De l'utilisation des chambres réverbérantes électromagnétiques pour les mesures 5G*

---

Lars Ole Fichte<sup>1</sup>, Sébastien Lalléchère<sup>2</sup>, Chaouki Kasmi<sup>1</sup>, Marcus Stiemer<sup>1</sup>

<sup>1</sup>Helmut Schmidt University, Hamburg, Germany, mailto: lo.fichte@hsu-hh.de

<sup>2</sup>Université Clermont Auvergne, Institut Pascal, SIGMA Clermont, CNRS UMR 6602, Clermont-Fd, France

---

**Keywords ; mots-clés:** 5G Networks, Electromagnetic Reverberation Chamber, Susceptibility Tests; réseaux 5G, chambre réverbérante électromagnétique, tests de susceptibilité.

---

### Abstract/Résumé

Electromagnetic reverberation chambers (ERCs) have demonstrated their cost-effectiveness over the years as a viable alternative to classical electromagnetic compatibility (EMC) environments. Their ability to deal with EMC, safety-, or security risk analysis connected with 5G applications is just limited by the lack of knowledge and control of transient fields. The technological spectrum of ERCs will be extended to examine effects of life-like electromagnetic transient fields, targeting EMC risk assessment and mitigation (reliable and safe communication). This paper will outline the usability of ERCs for various areas.

### 1 Introduction

The increasing degree of interconnectedness of all kinds of electrical devices is currently modifying the challenges on safe and secure technical engineering. This requires the establishment of new engineering procedures and tools that enable an integrated and simultaneous analysis of risks inherent to the massive use of electronic devices and facilities. Especially the introduction of 5G networks requires re-validation of EMC properties and biological compatibility because of a much larger parameter space (e.g. frequency range and power density), and particularly, transient effects.

### 2 ERCs for Susceptibility and Dosimetry Tests

Due to their cost-effectiveness and simple usability, ERCs have become a viable alternative to classical EMC environments such as Open Area Test Sides and Anechoic Chambers. This development has become possible by research carried out during the last 20 years leading to an understanding how the electrical fields are distributed in these resonators with a moving geometry and how characteristic data of a device under test can be derived via suitable measurement procedures including hardness tests, emissivity tests, and the measurement of a device's shield damping capacity. For a comprehensive introduction to the field, see [1].

Measurements in ERCs become increasingly interesting for wireless applications: These environments came into the focus of research some years ago due to their advantages, comprising the suitability for fully automated measurements, the capacity to provide complicated field patterns, or the possibility to generate a high field intensity with relatively inexpensive amplifiers. Additionally, their easy handling makes ERCs an area of interest for various applications. Consequently, the biological community is continuing to use ERCs for exposure test (the topic was discussed at BioEM 2017 conference, June 2017, Hangzhou, China) e.g. [2, 3]. **In particular**, many questions arising within the spectrum of future 5G applications can be examined by ERCs, including biological and electromagnetic compatibility issues due to field patterns resulting from massive MIMO, beamforming, and the enormous density (co-location) of devices, such as the expected high background noise

power and unnegelectable interference problems. The requirement of a statistical analysis to assess these new technologies has been pointed out, e.g., in [4]. EMC research groups are hence exploring their behavior both with deterministic, statistical, stochastic, and “chaotic” approaches [5, 6, 7, 8, 9].

The relevant international standard IEC 61000-4-21 [IEC11] unfortunately recommends a minimum volume of  $70 \text{ m}^3$  for an ERC, which exceeds the space available in most EMC laboratories and consequently restricts their applicability (see Fig. 1 for a typical example of a “small” ERC). Additional research on small scale ERCs will therefore provide smaller companies with an affordable test method. Numerical simulations of the electric fields in a small ERC are presented in [10].



Fig.1: Small size ERC used for testing.

## 2.1 Susceptibility tests

Any relevant investigation on the susceptibility of DUTs to interference from external electromagnetic fields must include a test that delivers information on the coupling frequencies, i.e. frequencies at which the DUT can receive power from the signal environment as a function of frequency. To facilitate this, we use a method which allows for the identification of critical coupling frequencies of an unknown electronic device by nondestructive measurement based on an electromagnetic reverberation chamber (ERC), which is in accordance with the appropriate standard IEC 61000-4-21 in terms of size, calibration, and stirrer efficiency. Basically, the idea of microwave spectroscopy is transferred to detect possible resonances of electronic devices. For this method, the use of an ERC is highly favorable, since other test environments cannot guarantee that every combination of field direction and polarization is included. This kind of spectroscopic applications of ERCs have been initialized by L. O. Fichter et al. [11] and since then further developed [12, 13]. A simulation-based assessment of the suitability of small ERCs has been presented, e.g., in [10] by analysis of their field statistics.

The spectroscopic method is based on the power consumption (i.e. absorbing cross section, ACS) of a device in an ERC, monitored as a function of the applied frequency. Hardware improvements to reduce noise and to increase the signal to noise ratio as well as procedures to reconstruct the signal from the measured data in high quality had to be considered. Currently, the limits of the method are analyzed, e.g., by a comparison of the coherence time of the eigenmodes of an ERC to the coherence time of a device under test. Another area, the power spectroscopy method will be extended to, are testing methods showing whether a system is susceptible to data security issues for certain types of disturbances. Such techniques are of paramount importance, especially regarding 5G framework for TRP (Tx/Rx point) characterization in realistic environments. The complete power budget (including both scattered and absorbed power in an ERC) provides reliable information considering functional safety of next generation electronics devices. Moreover, newest and next generation of electronic devices rely on very high frequencies; in that way, the ambience seen by the components or the PCB is statistical in nature. Indeed, their respective containers (boxes, bays or shelters) act by themselves as ERCs.

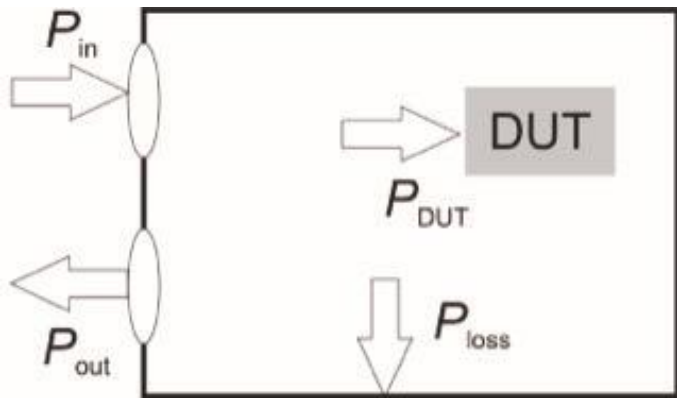


Fig.2: Power fluxes in a loaded ERC.

In detail the power absorption of the device (as a function of frequency) is determined from comparing the power losses of an empty ERC with the losses measured after loading the chamber with the DUT (see. Fig. 2 for power fluxes). The losses can be determined by subtracting output from input power, under the assumption that loss mechanisms are unchanged after loading the chamber with a DUT. The power measurement is performed with a (rather expensive) Vector Network Analyzer (VNA), but earlier experiments successfully employed power meters; the cost of the self-constructed ERC is negligible. Testing for critical coupling paths can therefore be executed with simple means, on the spot, and is even feasible for ammunition. With a correct implementation, we are able to fully automate the test procedure with the only exception of changing the DUT.

The method has been successfully validated with linear DUTs chosen for their known resonant frequencies, and with more complex devices. The precision of measurement is estimated below 5%, e.g. [13]. Note that the dimension of the DUT is only limited by the size of the ERC, so system level tests (e.g. for cars or trucks) are possible in larger ERCs.

## 2.2 Biological dosimetry

For biological reverberation chambers a dosimetry in terms of the specific absorption rate (SAR) has been developed, that has also been transferred to biological exposition experiments with open wave guides [14]. Consideration of pulsed fields and, more generally, of transient effects in ERCs is a completely new subject with promising perspectives and interesting scientific questions. Such new applications rely on a deepened insight into the statistical distribution of electromagnetic properties, as examined, e.g., in [15, 16].

In order to estimate the impact of emitting devices on biological tissue, a dosimetry for continuous and pulsed fields is required. In this context, figures that reflect the impact of such fields on the load of the chamber become relevant. One of the characteristic figures is the specific absorption rate (SAR), which indicates the mass related absorbed power. A dosimetry requires knowledge of how the chamber interacts with a load. This can be derived by measurements inside an ERC and can be validated by physical modelling.

Depending on their amplitude and duration, electromagnetic pulsed and continuous waves (CWs) may generate adverse health effects (i.e. heating of the tissues) or contribute to thermal and non-thermal therapeutic applications (i.e. electrochemotherapy or gene transfer). Thermal effects are well known and correctly documented in the safety standard. On the contrary, non-thermal effects are still studied and badly documented. Biologists are still expecting solutions from physicists to generated pulsed electromagnetic waves in biological samples. In that way, an ERC with a high confidence in the level and homogeneity of fields and of the SAR is highly appreciated [17].

## 3 Advantages of ERCs at higher frequencies

In addition to the obvious advantages of ERCs they face the same problems as conventional EMC test procedures (like semi-anechoic chambers or GTEM cells) with regard to being RF proof. Yet, ERCs do not require any absorbers and therefore avoid the installation of costly broadband absorbing devices; possibly they can cover the full frequency range of 5G tests. While time-gating can be applied in every test environment at

very high frequencies to mitigate additional reflections at not perfectly absorbing boundaries, ERCs might be able to provide better results after being investigated for excitation with transient signals.

The minimum volume of 70 m<sup>3</sup> for an ERC recommended by IEC 61000-4-21 (as discussed above) applies also for chambers designed for 5G related test. Yet, since the size of an ERC – more precisely its volume – is defined by the lowest usable frequency (LUF), and ERCs intended for measurement at 5G frequencies will be a lot smaller than the conventional chambers recommended by IEC. As a consequence, it will be possible to design small ERCs – smaller than an average refrigerator or even as small as a desktop computer - for very cost-efficient EMC test. Last but not least, measurements based on ERCs can be easily automated, yielding a higher efficiency for performing the large number of tests required by the new wireless technologies expected.

## References

- [1] P. Besnier and B. Démoulin, Electromagnetic Reverberation Chambers. Wiley & Sons, 2011
- [2] A. Vian et al., Plant response to high frequency electromagnetic fields, BioMed Research Internat., 2016
- [3] S. Lalléchère et al., Mode stirred reverberation chamber (MSRC): a large and efficient tool to lead high frequency bioelectromagnetic in vitro experimentation, Progress in Electromagnetic Research B, 2010
- [4] K. Wiklundh and P. Stenumgaard, **EMC Challenges of the Internet of Things**, Electronic Environment, 2017, <https://www.electronic.nu/2017/05/05/emc-challenges-of-the-internet-of-things/>
- [5] V. M. Primiani and F. Moglie, Reverberation chamber performance varying the position of the stirrer rotation axis, IEEE TEMC, 2014
- [6] S. Baranowski et al., Evaluation of the Electric Field Amplitude in a MSRC from Power Measurement with a Monopole. In: 2<sup>nd</sup> AT-RASC, Spain, May 2018
- [7] V. Houchouas et al., Experimental comparison of mode-stirrer geometries for EMC. In: ASIAEM 2015
- [8] P. Bonnet et al., Numerical simulation of a reverberation chamber with a stochastic collocation method, CRAS, 2009
- [9] K. Selemani et al., Energy localization effects within a reverberation chamber and their reduction in chaotic geometries, IEEE TEMC, 2017
- [10] I. Barbary et al., Simulation based analysis of electric field distributions in small reverberation chambers. In: 2017 International Symposium on Electromagnetic Compatibility - EMC EUROPE, Angers, 2017
- [11] L. O. Fichte et al., Modenverwirbelungskammer zur Prüfung elektronischer Schaltungen, German Patent DE102012024373 A1, 2014
- [12] C. H. Schlie et al., Constructive adjustment of characteristic parameters of a mode-stirred reverberation chamber for EMC tests and power spectroscopy. In: 2017 International Conference on Electromagnetics in Advanced Applications (ICEAA), p. 1079-1082, 2017
- [13] M. Stiemer et al., Power spectroscopy with electrical reverberation chambers for EMC. In: 19ème Colloque International et Exposition sur la Compatibilité ÉlectroMagnétique (CEM), Paris, 2018
- [14] A. Lamkowski et al., Gene Expression Analysis in Human Peripheral Blood Cells after 900 MHz RF-EMF Short-Term Exposure. Radiation Research, 189(5) 529–540, 2018
- [15] M. Hagel et al., Investigation of Shielding Effectiveness of Cables using Stochastic Methods. In: 4th Workshop on Uncertainty Modeling for Engineering Applications (UMEMA 2018), Split, Croatia, December 2018
- [16] S. Lalléchère et al., Assessing probability distributions of transfer impedance from direct integration and stochastic reduced order method. In: Proc. EMC Sapporo & APEMC 2019
- [17] N. Albuisson and JC Joly, Quick numerical approach for specific absorption rate determination in a reverberating environment - Application to an EM stopping vehicle project. In: EUROEM London, UK, 2016

# Estimation of network densification impact on EMF exposure using stochastic geometry

---

***Q. Gontier<sup>1</sup>, L. Petrillo<sup>1</sup>, H. Nguyen<sup>1</sup>, C. Oestges<sup>2</sup>, J. Wiart<sup>3</sup>, and Ph De Doncker<sup>1</sup>***

<sup>1</sup> Wireless Communications Group, Université libre de Bruxelles

<sup>2</sup> ICTeam dpt., UCLouvain

<sup>3</sup> C3M dpt., Télécom Paris

---

**Keywords:** EMF exposure, stochastic geometry, cellular networks

**Abstract:**

EMF exposure in Brussels, Belgium, is studied in the framework of stochastic geometry. Poisson point processes with realistic intensity are randomly generated to model base stations. Electric field level at random location is deduced from a simple path loss law. Statistical results are compared to experimental data's in order to optimize the model. The impact of network densification is analyzed and probabilities of exceeding exposure thresholds are derived.

## 1 Introduction

Electro-Magnetic Field (EMF) level due to cellular networks is difficult to calculate deterministically in a reasonable time, and it is subject to many uncertainties (due to the number of base stations in operation, the environment geometry, the presence of people and vehicles causing shadowing...). Instead, it is preferable to look for statistical values over a representative area  $P$  where the base stations (BS) density  $\lambda[\frac{\text{BS}}{\text{km}^2}]$  can be considered uniform. In the stochastic geometry approach [1] considered here, the BS pattern is modeled as an homogeneous Poisson Point Process (PPP). In section II, it is shown that exposure at an arbitrary location, for a given PPP, can then be deduced from an attenuation model for the electric field. By comparing simulated and experimental data's for the centre of Brussels, optimal values for the model parameters are found in Section III. Finally, in section IV, the impact of network densification is deduced from the stochastic approach.

## 2 Method

We focus on modeling exposure in the centre of Brussels, also known as the Pentagon area. This region  $P$  is chosen because the BS intensity can be considered uniform, and because experimental values of the equivalent 900MHz electric field are available (see [4] experimental set-up). The equivalent 900MHz electric field is defined as the total electric field summed up over the cellular bands with weights depending on frequency according to ICNIRP reference levels [4]. In  $P$ , the BS intensity for the whole set of services and providers is  $\lambda = 25.8 \pm 2.5 \frac{\text{BS}}{\text{km}^2}$ .

Knowing  $\lambda$ , realizations of an homogeneous PPP can be generated to serve as basis to evaluate the statistical properties of the equivalent 900MHz E-field. The area where the PP is generated is a square of  $1\text{km}^2$ , as seen in Fig.1, and the calculation point  $u$  is at the centre of the square, without lost of generality.

To estimate exposure, a model for the amplitude of the equivalent 900MHz electric field  $E$  at distance  $d$  from the computation point  $u \in P$  to a given BS is needed. Single-slope and multi-slope models were tested. The one that gave the best results when compared to the experimental data's is a generalized Friis law:

$$E(d) = A \frac{\sqrt{30 \text{ EIRP}}}{(d^2 + h^2)^{\frac{n}{4}}} \quad (1)$$

where  $n$  the *path loss exponent*, equal to 2 in free-space, and  $h$  the height of the BS antenna, assumed the same for all BS.  $A$  is a scaling factor with dimensions  $[\text{m}^{\frac{n}{2}-1}]$ , and EIRP is set to 61dBm, to initiate the model with a realistic value without losing generality (through fitting of  $A$  in the next section).

At this point, we can consider two cases. Given a calculation point  $u$ , either (a) we consider only the electric field due to the nearest BS or (b) we consider the quadratic sum of the electric fields emitted by all BS present in a disc of radius  $R$  to be defined, assuming that the BS are uncorrelated.

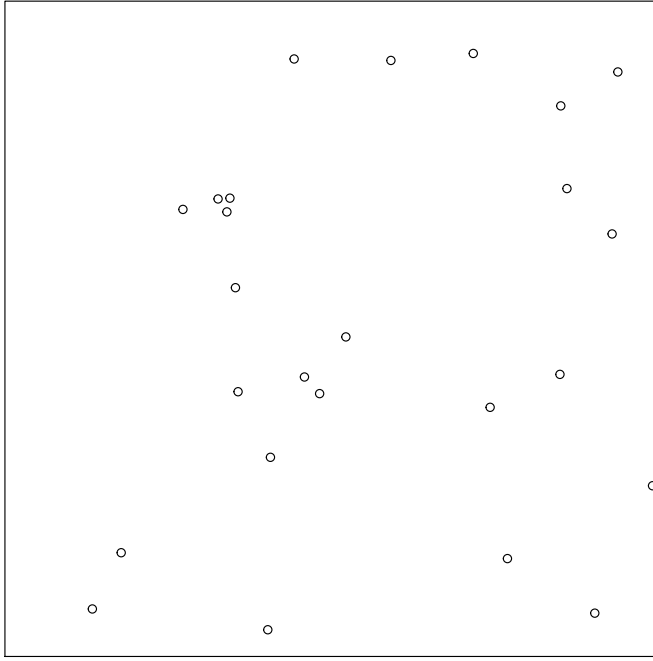


Figure 1 – Example of PPP generated on a square of  $1\text{km}^2$  with intensity  $\lambda = 25 \frac{\text{BS}}{\text{km}^2}$

### 3 Comparison with experimental data's

Sets of unknown parameters  $\{A, h, n\}$  in (1) were tested for fitting. For each given set,  $10^5$  PPP with  $\lambda = 25 \frac{\text{BS}}{\text{km}^2}$  were generated in order to obtain a simulated distribution of  $E$  using equation (1), for cases (a) and (b). Then, statistical values such as the mean  $\mathbb{E}[E] = \mu$ , the median  $Q_2(E)$ , the quartiles  $Q_1$  and  $Q_3$  and the standard deviation  $\sigma(E)$  were computed but also the parameters  $\mu_{LN}$  and  $\sigma_{LN}$  of the log-normal approximation of the distribution of  $E$ . These values were compared to the drive-test (DT) experimental values in order to find the set  $\{A, h, n\}$  that fits best.

Optimal values of the parameters are listed in table 1. For case (b),  $R$  was chosen equal to  $400m$ . This value is large enough to contain at least one BS, but also not too large to avoid prohibitive computation times. BS outside this disk actually have a very small impact on  $E$  as compared to the BS inside. The probabilities of reaching some thresholds for  $E$  are also added in this table. Method (b) gives slightly better results and has so to be preferred to assess exposure.

Table 1 – Numerical and experimental values of the total equivalent 900MHz electric field.

	Case (a)	Case (b)	DT
$h$	15	15	
$n$	2.35	2.95	
$A$	0.39	0.90	
$Q_1 [\text{V/m}]$	0.24	0.25	0.24
$Q_2 [\text{V/m}]$	0.36	0.35	0.45
$\mu [\text{V/m}]$	0.50	0.50	0.51
$Q_3 [\text{V/m}]$	0.58	0.56	0.66
Max [V/m]	3.14	3.30	3.33
$\sigma [\text{V/m}]$	0.44	0.44	0.35
$\mu_{LN} [\text{dBV/m}]$	-8.16	-8.08	-7.92
$\sigma_{LN} [\text{dBV/m}]$	5.82	5.56	6.19
$\mathbb{P}[E > 1\text{V/m}] [\%]$	10.05	7.59	8.08
$\mathbb{P}[E > 3\text{V/m}] [\%]$	0.17	0.25	0.02
$\mathbb{P}[E > 6\text{V/m}] [\%]$	0.00	0.00	0.00

## 4 Impact of network densification

Let us consider an increasing value of  $\lambda$ , which can for instance simulate the expansion of current networks such as for the release of 5G. Table 2 lists the probabilities to reach the thresholds if the BS intensity increases. It can be concluded that, even by tripling the BS density, the probability of reaching the threshold 6 V/m imposed by the city of Brussels is negligible.

Table 2 – Evolution of the probabilities with the increase of the intensity

	$\lambda \left[ \frac{\text{BS}}{\text{km}^2} \right]$	25	40	75
Case (a)	$\mathbb{P}[E > 1V/m [\%]$	10.05	15.65	27.27
	$\mathbb{P}[E > 3V/m [\%]$	0.17	0.21	0.44
	$\mathbb{P}[E > 6V/m [\%]$	0.00	0.00	0.00
Case (b)	$\mathbb{P}[E > 1V/m [\%]$	7.59	12.94	27.05
	$\mathbb{P}[E > 3V/m [\%]$	0.25	0.40	1.08
	$\mathbb{P}[E > 6V/m [\%]$	0.00	0.00	0.00
DT	$\mathbb{P}[E > 1V/m [\%]$	8.08		
	$\mathbb{P}[E > 3V/m [\%]$	0.02		
	$\mathbb{P}[E > 6V/m [\%]$	0.00		

## 5 Conclusions

Knowing the intensity of base stations inside Brussels,  $\lambda = 25.8 \pm 2.5 \frac{\text{BS}}{\text{km}^2}$ , and fitting a model giving the magnitude of the equivalent 900 MHz E-field as a function of distance to the transmitting BS, PPP were used to model exposure to EMF. Statistical results were compared with experimental values. The agreement between stochastic geometry and measurements is very good showing the potentiality of this method to assess exposure.

## Acknowledgments

The authors would like to thank the financial supports of FNRS (EOS MUSE-WINET program), and of Icity.Brussels (FEDER/EFRO grant).

## 6 References

- [1] F. Bacelli, B. Blaszczyszyn, “*Stochastic Geometry and Wireless Networks*”, Volume I, B. NoW Publishers, Foundations and Trends in Networking Vol. 3: No 3-4, pp. 249-449, 2009.
- [2] A. Baddeley, E. Rubak and R. Turner, “*Spatial Point Patterns: Methodology and Applications with R*”, Chapman and Hall/CRC Press, London, 2015.
- [3] J. F. C. Kingman, “*Poisson processes*”, Oxford Studies in Probability, Vol. 3, The Clarendon Press Oxford University Press, New York, 1993.
- [4] T. Lemaire, J. Wiart, P. De Doncker, “*Variographic analysis of public exposure to electromagnetic radiation due to cellular base stations*”. Bioelectromagnetics, 37(8), 557-562, 2016

## Numerical dosimetry in human model for 5G and beyond *Dosimétrie numérique dans le modèle humain pour la 5G et au-delà*

**Abdelrahman Ijjeh<sup>1</sup>, Marylène Cueille<sup>1</sup>, Jean-Lou Dubard<sup>1</sup>, Michel Ney<sup>2</sup>**

<sup>1</sup> LEAT, UMR-CNRS 7248, Université Côte d'Azur, 930 route des Colles, 06903 Sophia Antipolis, France

<sup>2</sup> Lab-STICC/IMT-Atlantique, CS 83818, 29238 Brest Cedex 3, France, [michel.ney@imt-atlantique.fr](mailto:michel.ney@imt-atlantique.fr)

*Keywords (in English and French):*

SAR computation, sub-gridding, time-domain computational methods, complex media.

*Calcul de DAS, sous-maillage, méthodes de calcul dans le domaine temporel, milieux complexes.*

### Abstract/Résumé

To design any new EM-device, it is of great importance to have a good estimation of the specific absorption rate (SAR) distribution or the Power Density (PD) it induces in users or people in its proximity. Respecting the recommended SAR limits is mandatory for any new technology to go public. Moreover, the good knowledge of SAR/PD is critical in any electromagnetic compatibility (EMC) study between EM-devices with lossy media. From numerical analysis point of view, as frequencies go higher and higher e.g. from 5G to millimetric or even terahertz applications, the computational problem becomes exhaustive in size. Note that at higher frequencies, the transmitting devices get normally smaller in size. In this article, we will study the effect of considering only the tissues (the part of the human model) adjacent to the transmitter vs. including the full human model in the computation domain. For a good spatial representation, the block-meshing scheme can be applied to finely mesh the antenna system and the tissues close to it. Numerical examples show the SAR distributions at 3.5 GHz in human head and the entire body, in addition to show the validity and CPU-time/memory gain obtained when considering part of the human model instead of the entire model. Moreover, we show the effects of human head presence on the antenna performance in its proximity.

### 1 Introduction

In the last few decades, one can observe the constant and rapid increase in operating frequencies of EM-devices. The reasons behind that is to increase the data rate (bandwidth), downsize antenna systems, and to allocate new unused frequency bands, in addition to other applications such as spectroscopy and imaging techniques. For such devices, the SAR/PD levels estimation is mandatory. However, at such high frequencies (5G and beyond) experimental measurements are very difficult to conduct [1] [2]. Even numerical simulations are very challenging in several scenarios [1] [2]. As the frequency goes higher the size of the computational domain becomes higher, hence the memory requirements and CPU time become higher as well. For instance at frequencies greater than 10 GHz, volumic simulations including human body are extremely huge and parallel big machines are necessary to perform the computations. It is worth mentioning that if we go the other way in the spectrum for instance to study the SAR at frequencies less than 10 MHz we face another problem; a huge number of iterations is necessary to cover the low frequency band of interest. Therefore, the easiest SAR computations with reasonable computational costs are for the range of frequencies between few tens of MHz until few GHz.

In this article, we are going to present a general methodology to perform SAR full-wave computations, as well as, focusing attention on the complexity of the problem, the different challenges and the practical computational limitations. Moreover, sub-gridding feature (it is much more efficient than structured irregular meshing that is used in the up-to-date commercial solvers) can be applied when dealing with a multi-scale scenario (ex. an antenna with very small details). Finally, we will study the effects of truncating the computational problem by keeping the antenna system and the human tissues in its proximity and excluding everything else.

### 2 Mathematical model

As a computational scheme, we are going to use the Transmission-Line Matrix method (TLM) in time-domain (TD). The TLM method is a full-wave computational method that has some very attractive features:

- 1) Can handle any linear anisotropic dispersive heterogeneous media [3].
- 2) Very efficient in highly heterogeneous structures (mesh or media), as compared to other TD methods.
- 3) One can do the sub-gridding for any mesh ratio, and in any heterogeneous media. Thanks to the ideal transformer model, that allows smooth, lossless and stable transition between fine and coarse meshes [4].

- 4) Can handle any lumped element (source, passive or active element). Thus, at any point (or region) we can define a port for example and control exactly how much power is supplied.

For more details concerning the mathematical representation of TLM method, we refer the reader to [3] [4]. As a human model, we used the heterogeneous Duke voxel model. Media properties for different tissues in are represented as a summation of four Cole-Cole expressions [5]:

$$\varepsilon(\omega) = \varepsilon_\infty + \sum_{i=1}^4 \frac{\Delta\varepsilon_i}{(1+j\omega\tau_i)^{(1-\alpha_i)}} + \frac{\sigma}{j\omega\varepsilon_0} \quad (1)$$

where  $\varepsilon_\infty$  is the permittivity at very high frequencies,  $\sigma$  the conductivity,  $\tau_i$ ,  $\alpha_i$  and  $\Delta\varepsilon_i$  are different parameters used by Cole-Cole model. In TD simulations, the dispersive media properties are translated into TD-filters.

### 3 SAR computation in realist scenarios

As frequencies go higher, the wavelength  $\lambda$  gets smaller. Finer meshes are required to represent the computational domain ( $\Delta l \leq \lambda / 10\sqrt{\varepsilon_r}$ ). To show the complexity of the problem when working at higher frequencies we can make this rough estimation of the problem size. It is desired to simulate a human model exposed to a signal at 10 GHz ( $\lambda = 3$  cm). Assuming the human model is mainly water ( $\varepsilon_r \approx 70$ ) at 10 GHz and at 37 °C, the mesh size is  $dl \leq 0.36$  mm. Now for Duke model of dimensions 177 cm × 61 cm × 31 cm, one needs around 7.17 billion cells. To perform a convergence test for instance by doubling the resolution in every dimension, the problem size explodes to 57 billion of cells. For the 5G frequency band at 60 GHz the previous number of cells reaches few Tera cells. At millimetric (110 GHz to 300 GHz) and terahertz (0.3 THz to 30 THz) frequencies, cell numbers are much higher.

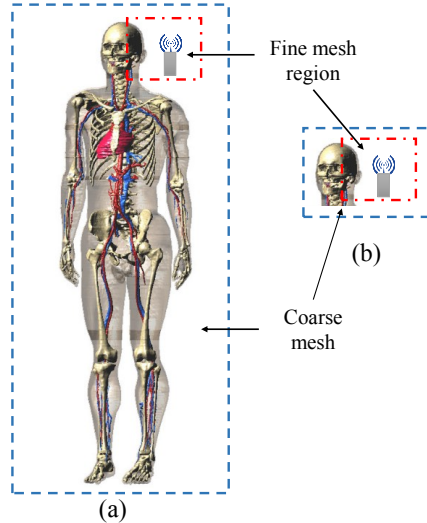


*Figure 1: Duke model exposed to EM waves, (a) the full body is included in the computational domain, block meshing is used around the antenna system and the human tissues close to it. (b) Only the head is considered, fine resolution is used around the antenna and the tissues in its proximity.*

As shown in figure 1, we are going to study the effect of considering only the part of Duke model that is close to the antenna system, for example the head in figure 1b. Comparison will be made with the scenario when the full body is present (figure 1a). The objective is to compute the impact of truncating the computational domain on the SAR distribution in human head and on the antenna performance. Such analysis can be very beneficial when dealing with devices that produce localized power in small regions such as medical sensors and RFIDs, smart lenses, or other wearable devices. Sub-gridding feature in TLM can be used to give a good geometrical representation of the antenna system/circuit and the nearby human tissues. Finally, as frequencies go higher, the skin effect obliges us to use fine resolution in the first few skin depths in lossy media to accurately capture the rapidly decaying EM fields.

### 4 Results and discussions

In this section, we present three scenarios for SAR computation at 3.5 GHz frequency. In the first experiment, we study the effects of plane-wave excitation on the head of Duke voxel model for two spatial resolutions (mesh

sizes), namely, at  $\Delta x = 1$  mm and at  $\Delta x = 0.667$  mm. In the second experiment, the SAR distribution is shown when Duke' head is excited by a half-wavelength dipole antenna ( $\lambda = 8.6$  cm) at the aforementioned resolutions. In addition, the impact of human head presence on the antenna input impedance is presented. Finally, an experiment of SAR computation again at 3.5 GHz is provided for plane wave excitation with both the head alone, and the entire body. The objective of this experiment is to show the effects of exclusion the rest of the body on the accuracy in SAR distributions in the head. To reduce the computer expenditures, we used a resolution of 2 mm for the last experiment, since the entire human model was very huge to simulate at 1 mm or finer. In all experiments cubic cells were used everywhere, with maximum time-step. Modulated-Gaussian pulse ( $t_o = 6.67$  ns,  $\sigma = 1.33$  ns and  $f_o = 3.5$  GHz) was used as an excitation. All simulations were performed on a TLM parallel solver developed in collaboration between LEAT laboratory and IMT-Atlantique [6].

#### 4.1 Duke' head excited by a plane wave

Consider the configuration in Figure 2 below with the head of Duke' model illuminated by a plane wave. Huygens box for is used as a source of plane wave excitation. The TEM wave is vertically polarized propagating towards the face of Duke.

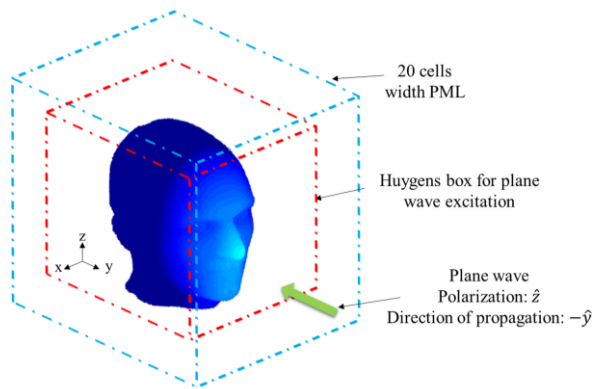


Figure 2: Duke voxel model excited by a plane-wave using Huygens box

The SAR distribution was initially computed at 1 mm resolution, then as a convergence test was conducted by repeating the same simulation with a 0.667 mm mesh-size. As shown in figure 3 below both SAR distributions are in good matching.

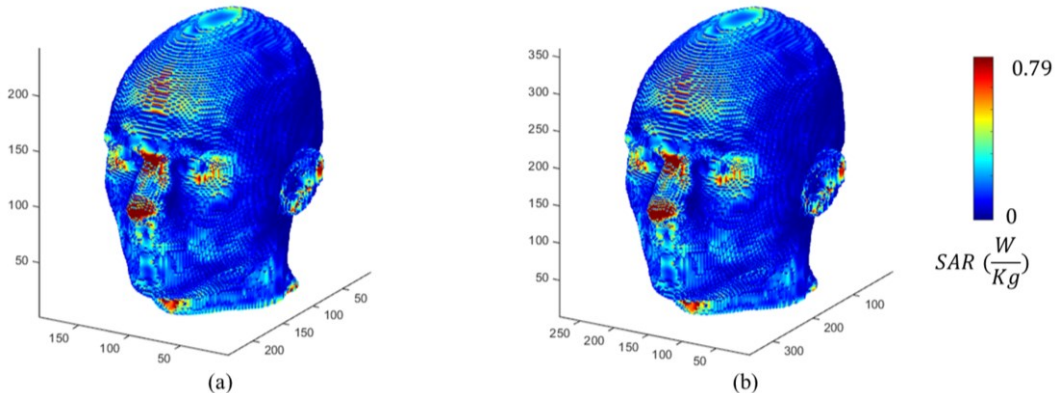


Figure 3: SAR distributions for plane wave excitation at 3.5 GHz, (a) resolution 1 mm, (b) resolution 0.667 mm.

Table 1 below shows the computational expenditures for both simulations shown in figure 3. Where  $N_c$  is the number of TLM cells needed to represent the computational domain,  $N_p$  is the number of processors used to run the simulator,  $CPU_t$  is the corresponding CPU simulation time and  $N_{it}$  is the number of iterations used in every simulation. One can observe that, even for the 3.5 GHz which is a relatively small frequency in the 5G band the CPU-time and memory requirements are very high. Repeating the same experiment a higher 5G frequency band

such as, 28 GHz ( $\epsilon_r \approx 16$ ,  $\sigma \approx 27$  S/m) [5] [7] means a mesh size less than 0.27 mm (1.46 billion cells, and 127 days with 42 processors).

	3.5 GHz	
	1 mm	0.667 mm
$N_c$	36750000	96768000
$N_p$	37	42
$CPU_t$	12h45min	37h41min
$N_{it}$	20000	30000

Table 1: Memory requirements, number of processors and iterations and the corresponding CPU-time (plane wave excitation)

#### 4.2 Duke' head excited by a half-wavelength dipole antenna

In figure 4 below, the Duke head is illuminated by a center-fed half-wavelength dipole antenna. The antenna is made of copper ( $\sigma = 5.96 \times 10^7$  S/m) with a length of 43 mm (43 cells in 1mm resolution and 64 cells in 0.667 mm) and a square cross section of 2 mm side length. An air gap of one cell-size at the center of the antenna is used to place a voltage source with a modulated Gaussian pulse temporal-profile. The antenna is located vertically next to the right-ear with around two cm distance from the skin.

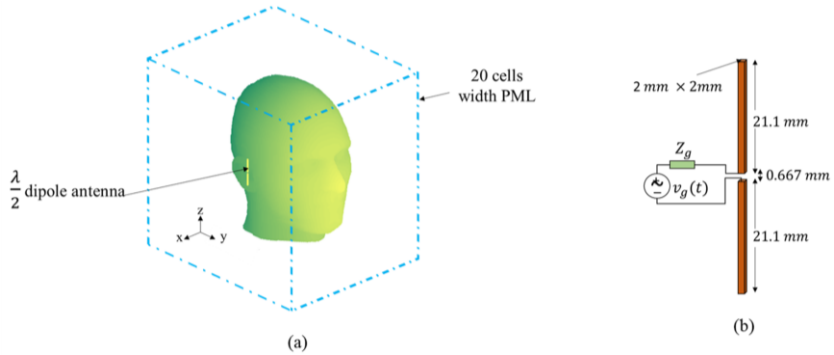


Figure 4: Duke voxel model illuminated by a half-wavelength dipole antenna at 3.5 GHz

Similar to the previous experiment, the SAR distributions were initially simulated at 1 mm resolution, and then were repeated at 0.667 mm resolution to test for convergence. As shown in figure 5 below the SAR distributions for both resolutions are in good matching.

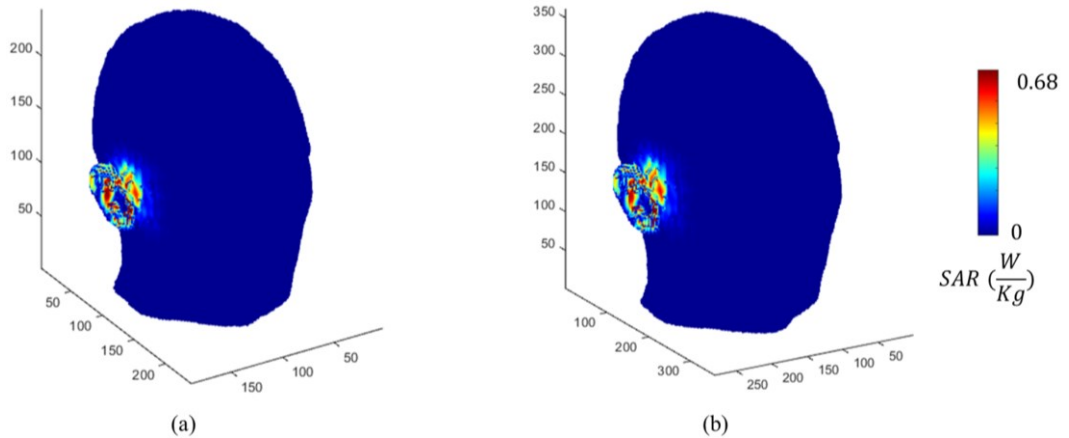


Figure 5: SAR distributions for a half-wavelength dipole antenna at 3.5 GHz, (a) resolution 1 mm, (b) resolution 0.667 mm.

Simulation times and memory requirements are shown in table 2 below, one can observe that the number of iterations is higher than what is used in the previous experiment, even though the same modulated Gaussian pulse temporal profile is used in both experiments. That is due to the high resonance phenomenon in the antenna structure; however, this high number of iterations allows us to compute the input impedance of the antenna.

	3.5 GHz	
	1 mm	0.667 mm
$N_c$	36750000	96768000
$N_p$	37	72
$CPU_t$	31h53min	55h04min
$N_{it}$	50000	75000

Table 2: Memory requirements, number of processors and iterations and the corresponding CPU-time (half-wavelength dipole antenna excitation)

One can observe in Figure 6 the high impact of human head presence in the proximity of the antenna on its input impedance (51.5  $\Omega$  difference in input resistance and 13.6  $\Omega$  in input reactance). That means the interaction between the head and the antenna modifies the operating setup of the latter. Note that to simplify our calculations we used a relatively thick wire antenna (square cross-section of side length of 2 mm, and 43 mm in length). However, if one is interested in using thin wire antennas a very fine resolution should be used to accurately discretize the cylindrical shape of the wire. This can be done by using block meshing approach, with fine meshing applied to the antenna and few cells in its proximity [8].

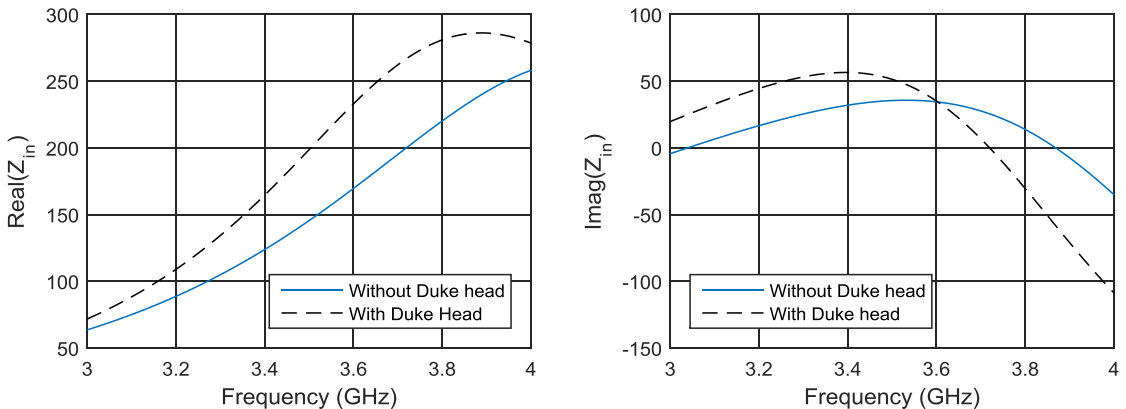


Figure 6: Input impedance of the dipole antenna vs. frequency, impact of Duke' head presence (results are shown for resolution  $\Delta x = 0.667\text{mm}$ )

#### 4.3 Duke' head vs. entire Duke' model excited by a plane wave

In this example, the objective is to study the effect of excluding the rest of Duke' body when computing the SAR in the head. The SAR was computed initially for the entire body as shown in figure 7a (figure 7b is the SAR distribution in the head cut from figure 7a for visualisation purposes). Then, the SAR distribution was computed for the head alone as in the first experiment. In both figure 7a and figure 7c a mesh-size of 2mm was used.

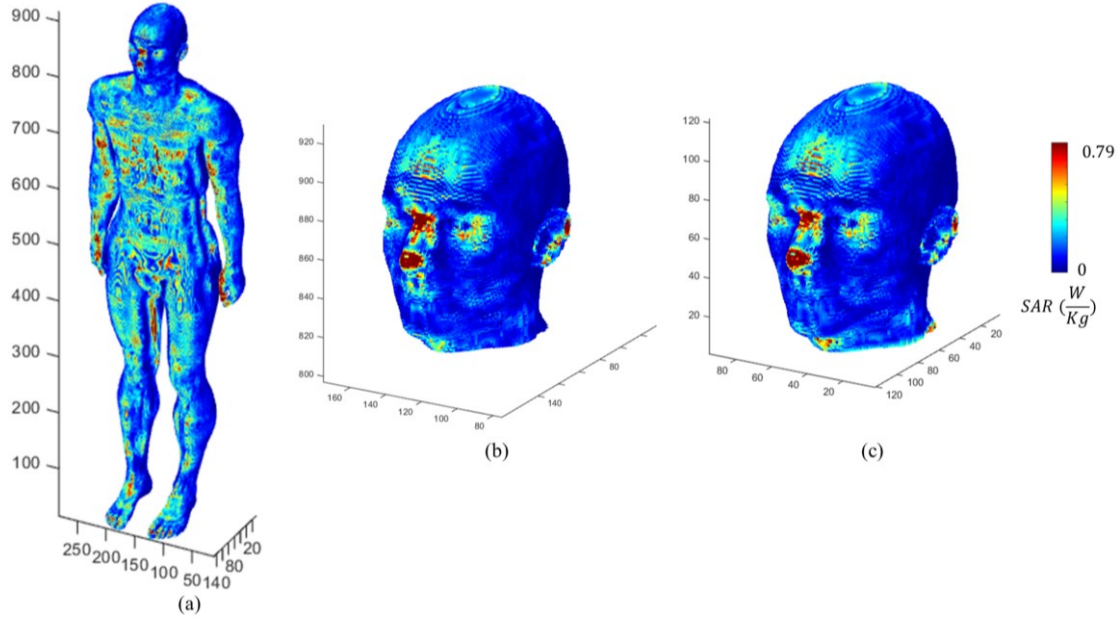


Figure 7: (a) SAR distribution in the entire Duke model illuminated by a plane wave at 3.5 GHz, (b) SAR distribution in the head of figure 7a, (c) SAR distribution in Duke head when head was simulated alone (the rest of the body was excluded from the computational domain)

Similar SAR distributions can be noticed in both figure 7b and figure 7c, with small differences can be observed in the neck region close to the cutting plane of Duke' head (this can be explained by the diffraction/scattering at the artificial discontinuity in the neck in figure 7c). Note that SAR distributions in figure 7b and figure 7c are in good agreement to SAR distributions in figure 3a and figure 3b in the first experiment. From figure 7 one can conclude that at 3.5 GHz the SAR can be computed with a reasonable accuracy in a specific region without the need to include the entire body. In table 3, one can notice big differences in simulation time and the number of TLM cells required to represent the computational domain for both the head alone, and the full Duke model, respectively.

	3.5 GHz (2mm)	
	Head	Full body
$N_c$	4593750	71319500
$N_p$	62	142
$CPU_t$	0h25min	7h40min
$N_{it}$	15000	15000

Table 3: Memory requirements, number of processors and iterations and the corresponding CPU-time (plane-wave excitation Duke' head vs. full Duke' model)

## 5 Conclusion

A numerical dosimetry procedure-based TD-TLM computational scheme was presented. This method allows for computing the EM-fields in arbitrary complex linear media such as human tissues. This allows for the calculations of SAR (up to 6-10 GHz) or PD (in the millimetric range of the 5G spectrum). Moreover, the possibility to simulate scenarios involving humans and EM-devices permits to evaluate the impact of human presence on their performance. The second objective of this article is to study the effect of considering only a part of the human model (ex. the head) vs. including the full human model in the computation domain. In addition, we study the impact of human tissues presence on the antenna performance in their proximity. Numerical experiments show that a good SAR distribution can be obtained in the head without considering the entire model with a huge memory and CPU-time gain as compared to the case of the entire model. Moreover, the input impedance of the dipole antenna was largely influenced by the presence of Duke head in their near field region.

## Acknowledgment

This work benefited from access to CINES computing resources through the 2019-A0060505122 resource allocation attributed by GENCI.

## References

- [1] Q. Abbasi et al. Advances in body-centric wireless communication: Applications and state-of-the-art. Institution of Engineering and Technology, 2016.
- [2] A. R. Guraliuc et al, "Near-Field User Exposure in Forthcoming 5G Scenarios in the 60 GHz Band," in IEEE Transactions on Antennas and Propagation, vol. 65, no. 12, pp. 6606-6615, Dec. 2017.
- [3] A. Farhat et al, "TLM Extension to Electromagnetic Field Analysis of Anisotropic and Dispersive Media: A Unified Field Equation." IEEE transactions on microwave theory and techniques 60.8 (2012): 2339-2351.
- [4] J. Włodarczyk, "New multigrid interface for the TLM method." Electronics Letters 32.12 (1996): 1111-1112.
- [5] <https://itis.swiss/virtual-population/virtual-population/vip2/duke/>
- [6] A. Ijjeh et al. "Solveur TLM multi-physique pour applications en dosimétrie." 2017.
- [7] D. Colombi et al. "RF energy absorption by biological tissues in close proximity to millimeter-wave 5G wireless equipment." IEEE Access. 2018 Jan 5:6:4974-81.
- [8] M. Ney et al. "Block Meshing TLM Based Approach for Low Frequency Antennas Characterization." 2019 International Conference on Electromagnetics in Advanced Applications (ICEAA). IEEE, 2019.

## Study of estimation accuracy of fast SAR measurement systems

Zicheng Liu<sup>1</sup> and Joe Wiart<sup>1</sup>

<sup>1</sup> Chaire C2M, LTCI, Télécom Paris, zicheng\_liu@hotmail.com, joe.wiart@telecom-paris.fr

**Keywords:** Human exposure, specific absorption rate, traditional SAR measurement system, fast SAR measurement system, estimation accuracy, field reconstruction

### Abstract:

With wireless devices, the specific absorption rate (SAR), which quantifies the human exposure by electromagnetic waves, is usually measured by a traditional measurement system where a probe measuring amplitude is intensively moved inside the phantom so that the peak spatial-averaged SAR is accurately estimated. However, such measurement process is time consuming considering varied configurations (device position, working mode, etc.) for the full-compliance test and massive production (e.g., mobile phones). Types of fast measurement systems have been developed to overcome this difficulty but estimation discrepancies are observed for different systems. Investigations are made on the estimation discrepancies by simulating the fast measurement system based on techniques of field reconstruction and comparing results from the traditional measurement system and the fast ones.

The electromagnetic exposure draws much public attention due to the wide usage of wireless devices in telecommunication systems. Specific absorption rate (SAR) [1] defined by

$$\text{SAR} = \frac{1}{V} \int_{\mathbb{V}} \frac{|\mathbf{E}(\mathbf{r})|^2 \sigma(\mathbf{r})}{\rho(\mathbf{r})} d\mathbf{r}, \quad (1)$$

is used to quantify the spatial-averaged power absorbed by the whole body or tissues. In (1),  $V$  is defined as the volume of region  $\mathbb{V}$ ,  $|\mathbf{E}(\mathbf{r})|^2$  the root-mean-square of electric field at the position  $\mathbf{r}$ , and  $\sigma$ ,  $\rho$  conductivity and density, respectively. While the density is set as  $1\text{g}/\text{cm}^3$  [2] and the conductivity is obtained from the database [2] in literature,  $|\mathbf{E}(\mathbf{r})|$  is measured by a probe, the position of which is controlled by a robot arm. The integral of (1) is computed with numerical methods based on sampled measurements by moving the probe. To reach a certain accuracy, high-density sampling is required and the measurement process becomes time consuming considering tests with different device positions and working modes.

Fast measurement systems have been developed and as an representative, the estimation of SAR based on techniques of field reconstruction is concerned here. Measuring the electric field (amplitude and phase) by vector probes on a plane surface inside the phantom, the electric field at other interested regions is obtained by a field-reconstruction algorithm [3]. Then, (1) is solved based on the reconstructed fields. Benefiting from the high efficiency of the reconstruction algorithm, the measurement speed can have a significant improvement.

Discrepancies are observed on the estimation by different fast measurement systems. However, no literature exists to investigate the reasons. Our contributions lies in simulating different fast measurement systems by applying two field-reconstruction algorithms and investigating the estimation accuracy with analytical functions (thus available reference value). In addition, comparisons between the traditional measurement system and fast ones are presented trying to conclude which measurement methodology is superior. Remark that the study is performed through simulating the concerned measurement systems based on analytical functions which generate the electric field inside the phantom. The uncertainty of the true instruments will not be considered, since no means to get the related parameters due to the security protection and the high complexity of the analysis of the whole system due to many uncertain variables.

### References

- [1] J. Wiart, *Radio-Frequency Human Exposure Assessment: From Deterministic to Stochastic Methods*. John Wiley & Sons, 2016.
- [2] *Measurement procedure for the assessment of specific absorption rate of human exposure to radio frequency fields from hand-held and body-mounted wireless communication devices - Part 1: Devices used next to the ear (Frequency range of 300 MHz to 6 GHz)*. International Electrotechnical Commission (IEC), 2016.
- [3] *Measurement procedure for the assessment of specific absorption rate of human exposure to radio frequency fields from hand-held and body-mounted wireless communication devices - Part 3: Vector measurement-based systems (Frequency range of 600 MHz to 6 GHz)*. International Electrotechnical Commission (IEC), 2019.

## Numerical modeling of downlink electromagnetic wave exposure generated by 5G beamforming antennas

---

*Nicolas Noé<sup>1</sup> and François Gaudaire<sup>2</sup>*

<sup>1</sup>Lighting and Electromagnetism Division, CSTB, Nantes, France, [nicolas.noe@cstb.fr](mailto:nicolas.noe@cstb.fr)

<sup>2</sup>Lighting and Electromagnetism Division, CSTB, Grenoble, France, [francois.gaudaire@cstb.fr](mailto:francois.gaudaire@cstb.fr)

---

**Keywords:** 5G, Antennas, Beamforming, Exposure

---

**Abstract:**

In this paper different scenarios were compared for the numerical modeling of electromagnetic wave exposure to beamforming antennas. These scenarios range from the simplest (using an averaged radiation pattern) to an almost realistic one (MU-MIMO beamforming taking into account users locations) with intermediate ones. The results underline the influence of the environment around the antennas on the distribution of the electric field.

### 1 Introduction

The issue of EMF exposure to smart antennas was addressed for the first time under the angle of the security perimeters. Indeed, to respect the sanitary standards of exposure of workers, a security perimeter is established around the antenna, in which it is prohibited to intervene when the antenna is in operation. Usually this perimeter is determined by calculating the minimum distance around the antenna beyond which the electric field is always lesser than the legal threshold. This distance is evaluated in free space and hence only depend of the Equivalent Isotropic Radiated Power (EIRP).

For beamforming antennas, the antenna gain can vary dynamically up to a maximum gain when a beam is formed in a given direction. Hence using EIRP to compute security perimeters would lead to very high distance.

### 2 Previous work

In [1, 2, 3] a statistical approach was used to obtain adapted distances of security. The method used consisted in defining exposure scenarios, depending on a very limited number of parameters: cell type (macro or micro), number of users served simultaneously  $K$  and duration of service  $D$ . Users are randomly distributed in the environment (80% indoor, 20% outdoor) and the antenna behavior is simulated (at full load) for a given time (6 minutes) in order to obtain the probability distribution function (pdf) of the effective maximum gain. The cumulative density function of the maximum gain therefore only depends on the chosen parameters. As a consequence this allows to estimate, with a given probability, a safety distance for a maximum level of exposure.

### 3 New approach

The previous approach is perfectly suited for security perimeters, but it seems insufficient for quantifying public exposure in real environments. The question of exposure is not limited to safety limits concerns. One might indeed try to know precise local exposure (for the search for atypical points in France for example, or for compliance with much more restrictive local laws on the level of exposure such as in the Brussels-Capital region in Belgium). The local exposure may vary greatly depending on the actual configuration of the environment (layout of buildings, construction materials, . . . ), even for the same type of cell (macro or micro).

With the previous approach, an averaged diagram could be determined (as a complement to the maximum gain alone). This diagram can be used as an input to a detailed exposure simulation in a given environment, but it is likely that the simulation with the averaged diagram will give results different from the one that could be obtained by averaging the exposure over time.

We therefore propose a new approach to modeling of exposure to beamforming antennas, by studying several antenna modeling scenarios, from the simplest one to more and more complex ones. The main objective of this study is to compare an *a priori* statistical analysis (with an average diagram) with an *a posteriori* statistical analysis on these different scenarios.

## 4 Antenna, environments and simulation method

### 4.1 Antenna

The input antennas can either be a single point with a far field radiation pattern or a set of radiating sub-elements with to model a Uniform Planar Array (UPA) antenna with its beamforming capacity. The characteristics of the theoretical UPA antenna used in this study are:

- a 3GPP base element [4] with a 12.6 dBi gain, with a  $65^\circ$  horizontal aperture and a  $20^\circ$  vertical aperture,
- an 8x8 array a elements with  $0.5\lambda$  horizontal spacing and  $0.6\lambda$  vertical spacing,
- beams that can be steered from  $-60^\circ$  to  $+60^\circ$  horizontally and from  $-20^\circ$  to  $+20^\circ$  vertically,
- a 24.8 dBi gain for a single beam and an input power of 52.04 dBm (160W).

Beamforming with this antenna is illustrated on figure 1. It must be noted that there are strong sides lobes for extreme azimuths (close to  $60^\circ$ ) since it is a purely analytical model and no side lobes suppression technique was applied.

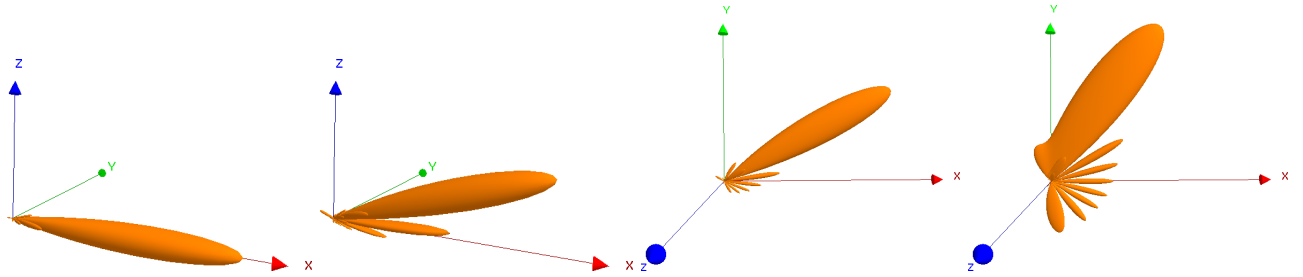


Figure 1 – Beamforming to azimuth & tilt (from left to right):  $0^\circ \& 0^\circ$ ,  $0^\circ \& 20^\circ$ ,  $30^\circ \& 0^\circ$ ,  $60^\circ \& 0^\circ$

## 5 Environments

Three environments have been studied. They are extract of a more complete Paris exposure simulation study and represent different configurations: one with mainly LOS exposure, one with other buildings reflections and a canyon street with indirect exposure. Only the buildings in the vicinity of the antenna have been kept (since only one antenna is used). The antenna is mechanically tilted  $3^\circ$  downward.

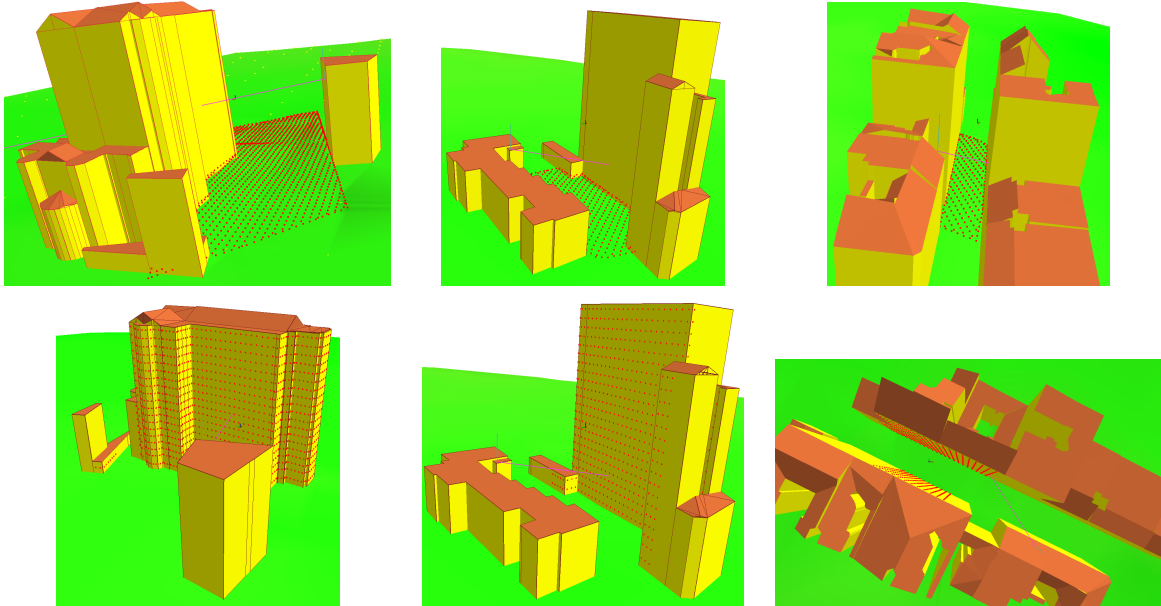


Figure 2 – First (left), second (middle) and third (right) environments: antenna with default main lobe direction, ground (top) and facade (bottom) maps

## 5.1 Simulation method

All simulations are performed using a 3D beam-tracing method [5]. This method computes paths between emitters and receivers, taking into account reflection, diffraction and transmission by obstacles, in order to get a complex electric field (with phase).

## 6 Scenarios

### 6.1 Scenario 0

For this scenario a single simulation is performed with an averaged (over all beam directions) far field diagram. This diagram has a 13.17 dBi gain and is illustrated on figure 3.

### 6.2 Scenario 0'

This scenario is related to the foreseen ANFR guidelines for 5G. It is a kind of envelop of all beams, made from the 3GPP base element with a 120° horizontal aperture and a 40° vertical aperture and an (artificial) gain of 24.3 dBi. Once again a single simulation if performed with this diagram and then a 13.5 dBi loss factor (from ANFR guidelines, to account for 5G usage) is applied to the final result. This diagram is illustrated on figure 3.

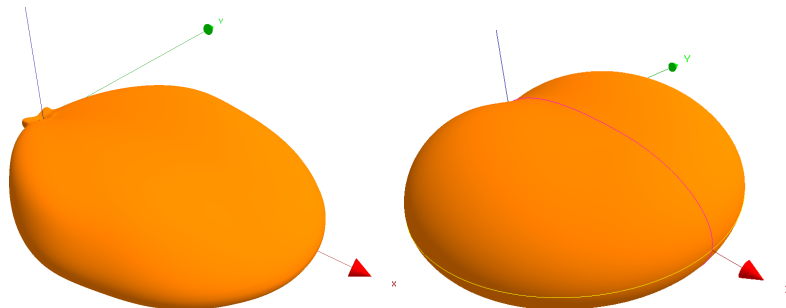


Figure 3 – Far field diagrams (linear) used for scenarios 0 (left) and 0' (right)

### 6.3 Scenario 1

In this scenario, beams are formed in every possible direction (whatever the environment is). One simulation is performed with a radiation pattern for each beam direction, with a 1° sampling (hence 4961 simulations and exposure maps) as illustrated on figure 4. Then an average exposure map is computed to compare to other scenarios.

### 6.4 Scenario 1'

With a smart antenna it is hinted that beams are formed only in directions where users really stand. A rough approximation is to consider only beams pointing to exposure points (either on the ground or on the building frontages) that are in line-of-sight of the antenna. As a matter of fact users are either in the streets or in the building, and not floating in air yet. The main point of this scenario is that it is easy to set up without any change in simulation tools, as it is only a sub-case of scenario 1. For the studied environments, LOS exposure points represent 10% of the ground surface and 20% of the facades (mainly the building in front of the antenna) as illustrated on figure 4.

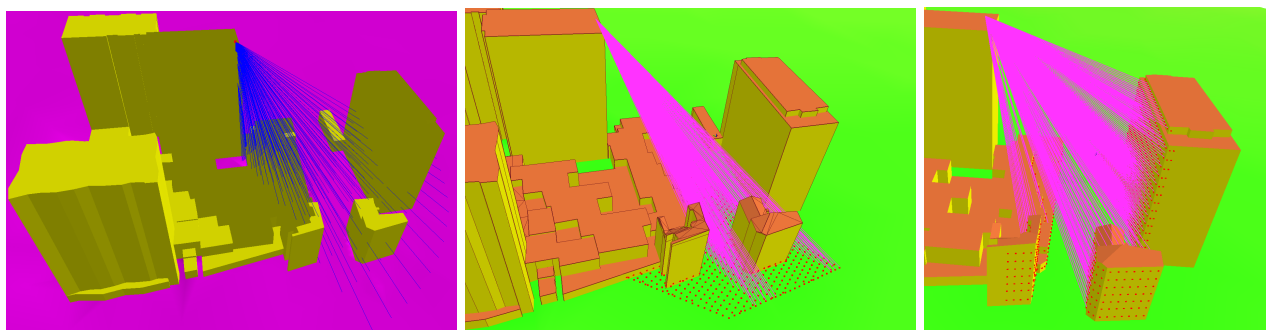


Figure 4 – Scenario 1 (left, beams in all possible directions), scenario 1' (middle and right, beams towards LOS exposure points on the ground and on the facades)

## 6.5 Scenario 2

In this scenario, users are taken into account and beamforming is dynamically computed depending on the channel between the antennas sub-elements and the users. It aims at reproducing the real behaviour of a MU-MIMO antenna.

### 6.5.1 Users

A pool of user equipments (UEs) is created. UEs are randomly distributed on the ground and inside the buildings with a ratio (for the same footprint) of 80% indoor UEs and 20% outdoor UEs. There are far more UEs in this pool than real users, in order to represent moving UEs and changing reception conditions. In this study 640 UEs were generated (540 indoor, 100 outdoor), see figure 5.

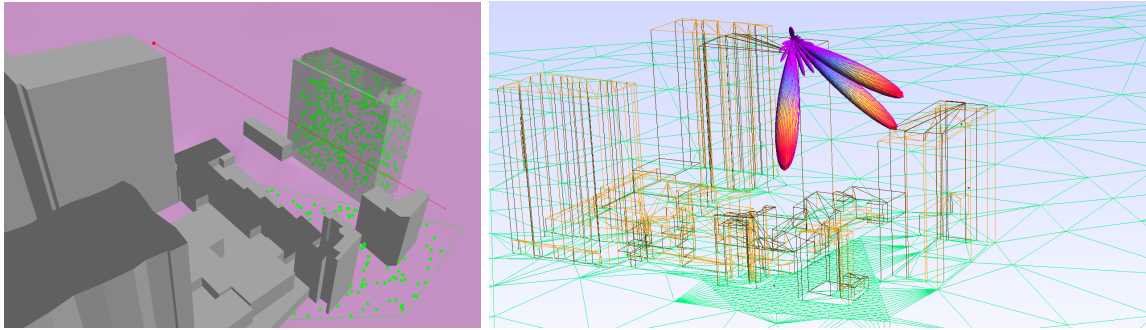


Figure 5 – Scenario 2': randomly generated UEs (left) and MU-MIMO beamforming for  $K=3$  served UEs (right)

### 6.5.2 Beamforming

In this study we used zero-forcing beamforming [6]. It aims at maximizing the SINR (signal to interference and noise ratio) so as to serve a maximum number of UEs simultaneously. The beamforming weights are obtained by computing the pseudo-inverse of the channel matrix between the 64 sub-elements of the antenna and a set of  $N$  UEs ( $N \leq 64$ ). The channel matrix is computed with the simulation method (each channel being the result of multiple paths contributions).

A greedy user selection is done to find the number  $K$  of UEs that can be served simultaneously amongst the  $N$  UEs with the overall higher rate with a given noise. Power allocation between users is done with a water-filling method. Actually  $K$  is not a parameter here, as it is automatically computed (usually 3 or 4).

### 6.5.3 Full algorithm

- UEs are handled by batches of 64 UEs. First these 64 UEs are removed from the pool of UEs (keeping the ratio between indoor and outdoor UEs, hence 50 indoor UEs and 14 outdoor UEs). Beamforming is performed on the 64 UEs by successive iterations, until every UE has been served (each UE has the same drop duration  $D$ ). Hence for each iteration  $i$  of beamforming,  $K_i$  UEs are served, with their allocated power. An exposure map is computed for each iteration, corresponding to the full antenna power.
- Once the 64 UEs have served, 64 others are extracted from the pool and so one, until the pool empties.
- When the pool is empty, an averaged (over the total number of iterations and also over time since  $D$  is constant) exposure map is computed.

The downlink rate for each UEs is computed but is not used yet.

## 7 Preliminary results

First we compare scenarios 0 (map with averaged diagram) and 1 (average of maps for each diagram). As expected the mean error between them is very close to zero. Nevertheless the error on some isolated points can be quite high. For instance the interference (either constructive or destructive) between direct and reflected field is amplified in scenario 0 due to the not very directional diagram. For instance on five highly exposed points (expressed in V/m):

point	#464	#100	#224	#202	#325
scenario 0	4.41	4.51	4.56	6.44	6.45
scenario 1	8.24	8.04	7.23	7.58	7.44

One obvious conclusion is that with an averaged diagram it is useless to perform an advanced simulation (with reflections for instance) since it introduces more error than precision (scenario 0 without reflection gives results closer to scenario 1).

## 8 Results

We compare cumulated density function of electric field (in V/m) in the final maps (after averaging) of each scenario. This allows to observe both the maximum value and the shape of the distribution.

### 8.1 On the ground (outdoor exposure)

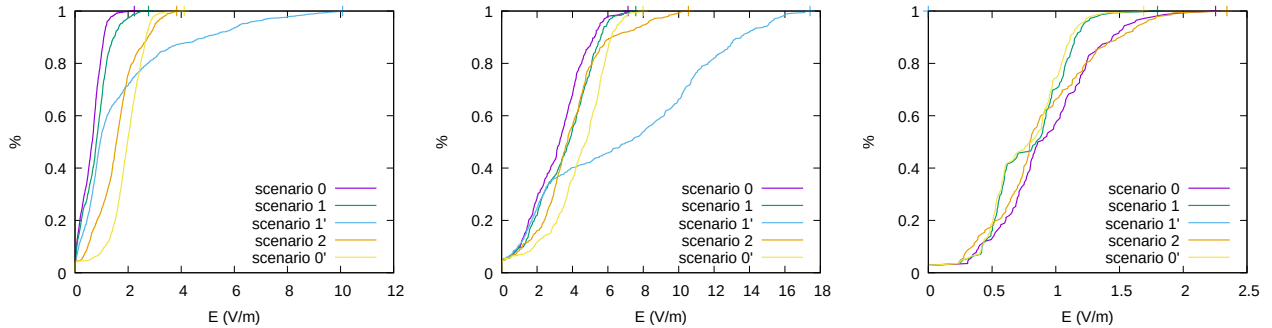


Figure 6 – Comparisons between scenarios 0, 0', 1, 1' and 2, on the ground for the three environments

### 8.2 On the facades (indoor exposure)

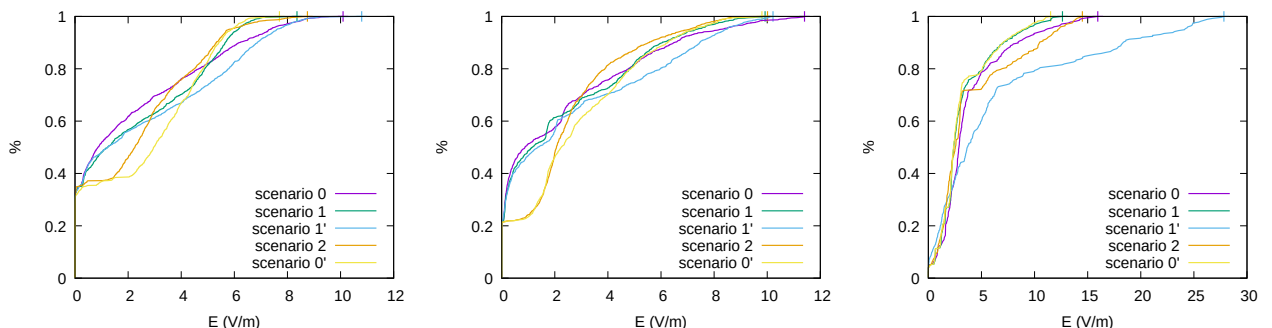


Figure 7 – Comparisons between scenarios 0, 0', 1, 1' and 2, on the facades for the three environments

### 8.3 Analysis

In all of the cases of this study, the differences between scenario 0 (*a priori* averaged diagram of all beams) and scenario 1 (*a posteriori* average of all maps, with one map per beam) are significant, both on the shape of the distribution function of the electric field, but also on the maximum exposure level. In some cases the difference can go up to 20%. The use of an average diagram, when there is a significant range of beam directions and especially changing beam shapes (with the appearance of non-negligible side lobes) has an influence on the characterization of the exposure levels. This result should be confirmed with manufacturer antenna diagrams for which attenuation values of the side lobes would be available.

Most of the time, scenario 1' (average of the maps for the beams in line of sight of the exposition areas) is a maximizing one. But it can be matched (for its maximum level) by scenario 2 in open range areas.

What mainly interests us in this study is the comparison between scenarios 0' (ANFR guidelines) and 2 (dynamic beamforming). In all the cases studied, scenario 2 gives maximum exposure levels higher or similar to scenario 0'. The usage assumptions of this study surely have a big influence on scenario 2: constant distribution of users at ground level and in buildings (this could depend on the time of day), equal service (in assigned time) among all users, continuous service (antenna at full load). However, the differences between scenarios highlight that the configuration of the antenna environment has a strong influence on the exposure levels, which is not reflected in the use of a scenario with a medium diagram as scenario 0 or 0'.

Finally this study should be carried out on a larger scale. This would make it possible to analyze the shadowed areas (exposure “behind” the buildings in line of sight), areas located at a greater distance from the antenna, and more complex environments with several antennas and base stations. It is important to note that the level of exposure on the facade is the level outside but that the channel was formed with users located inside buildings (taking into account attenuation by the building walls). It should be noted that the methodology implemented in this study can be deployed operationally on any site, and requires calculation resources similar to those of a conventional calculation of exposure levels (only the diagrams of antennas are changed dynamically).

## 9 Conclusion and future work

By comparing the scenarios based on the use of an average diagram (scenarios 0 and 0') with a scenario based on the average of the maps for all beams (scenario 1), it appears that, in the case of beamforming antennas, taking into account the side lobes is essential to obtain a relevant characterization of the exposure levels. This is particularly the case for an antenna having a wide horizontal angular steering capacity. This conclusion should be refined and confirmed with more complete information from the manufacturers on the diagrams of the 5G antennas that will be deployed in the field.

To make the calculation of exposure levels more precise and taking into account the antenna environment, it is possible and simple to implement in existing exposure tools a scenario which limits the focusing of the beams towards the points of exposure in line of sight of the antenna (scenario 1'). This scenario is, logically, very overestimating in the majority of the cases studied. This result justifies the use and analysis of a more advanced scenario such as the scenario integrating dynamic beamforming, taking into account the characteristics of the channel between the antenna and the users (scenario 2).

With regard to the statistical distribution of the electric field level, we also note that the scenarios based on an average diagram, including the scenario adopted for the ANFR guidelines, tend to overestimate the low electric field levels and under estimate the strong levels, compared to the scenario incorporating dynamic beamforming (scenario 2). Here again, the distribution of the electric field level shows the advantage of digital modeling which takes into account both the environment of the antenna and its realistic behavior in channel estimation. The corollary of this conclusion is that taking into account with precision the specific environment of the antenna (buildings, obstacles, etc.) for the numerical modeling of the exposure is of little interest with a simple hypothesis of a generic averaging antenna diagram.

This first study on a few sites therefore highlighted the limitations of an overly simplified statistical approach for modeling the exposure due to smart antennas. These conclusions should be supplemented by the study of larger sites, with more antennas and base stations and in larger-scale urban environments. The study could also be completed in the future with access to more complete manufacturer data, on antennas actually deployed by operators in the coming months.

## Acknowledgments

This work was partly funded by ANFR.

## 10 References

- [1] E. Degirmenci, B. Thors, and C. Törnevik, “Assessment of Compliance With RF EMF Exposure Limits: Approximate Methods for Radio Base Station Products Utilizing Array Antennas With Beam-Forming Capabilities,” *IEEE Transactions on Electromagnetic Compatibility*, vol. 58, pp. 1110–1117, Aug 2016.
- [2] B. Thors, D. Colombi, Z. Ying, T. Bolin, and C. Törnevik, “Exposure to RF EMF From Array Antennas in 5G Mobile Communication Equipment,” *IEEE Access*, vol. 4, pp. 7469–7478, 2016.
- [3] B. Thors, A. Furuskär, D. Colombi, and C. Törnevik, “Time-Averaged Realistic Maximum Power Levels for the Assessment of Radio Frequency Exposure for 5G Radio Base Stations Using Massive MIMO,” *IEEE Access*, vol. 5, pp. 19711–19719, 2017.
- [4] E. C. C. CEPT, “Analysis of the suitability of the regulatory technical conditions for 5G MFCN operation in the 3400-3800 MHz band,” tech. rep.
- [5] N. Noé, F. Gaudaire, and M. Diarra Bousso Lo, “Estimating and Reducing Uncertainties in Ray-Tracing Techniques for Electromagnetic Field Exposure in Urban Areas,” in *IEEE Conference on Antennas and Propagation in Wireless Communications*, 2013.
- [6] N. S. G. Dimic, “On Downlink Beamforming With Greedy User Selection: Performance Analysis and a Simple New Algorithm,” vol. 53, October 2015.

## Sur les procédures de mesure pour l'évaluation du débit d'absorption spécifique (DAS) des équipements cellulaires MIMO ayant des variations rapides des phases relatives

### *On the Measurement Procedures for the Assessment of the Specific Absorption Rate (SAR) from MIMO Cellular-Equipment of Fast Varying Relative Phases*

Mounir Teniou<sup>1</sup>, Mehdi Ramdani<sup>1</sup>, Ourouk Jawad<sup>1</sup>, Thomas Julien<sup>1</sup>, Stephane Pannetrat<sup>1</sup>, Lyazid Aberbour<sup>1</sup>

<sup>1</sup>ART-Fi: Orsay, France,

mounir.teniou,mehdi.ramdani,ourouk.jawad,thomas.julien,stephane.pannetrat,lyazid.aberbour@art-fi.eu

*Mots clés : DAS, MIMO, Mesures champ proche, Mesures vectorielles de champ.*

*Key words : SAR, MIMO, Near field measurements, Vector field measurements.*

#### Résumé/Abstract

**Résumé en français** Cet article propose une méthodologie de mesure pour l'évaluation du débit d'absorption spécifique (DAS) d'une classe de dispositifs de communication à entrées multiples et à sorties multiples (MIMO). Il est dédié aux systèmes MIMO spécifiques dans lesquels les phases relatives entre les antennes changent rapidement et dans des durées très courtes, telles que mises en œuvre à l'aide de la fonction STBC (Space-Time Block Code). En effet, un sujet particulier et nouveau dans ces mesures se pose lorsque l'on considère les systèmes SAR basés sur des mesures vectorielles, exploitant les principes d'équivalence de champ pour la reconstruction de la distribution de champ dans le volume à partir d'échantillons d'un sous-ensemble du champ électrique harmonique, indépendant du temps, et induit dans le milieu interne simulant du corps humain.

Cet article présente des méthodologies de mesure pour adresser ce nouveau cas de transmissions ainsi qu'à contribuer au développement des normes de la commission électrotechnique internationale (CEI) harmonisant les procédures de mesures de l'exposition aux rayonnements électromagnétiques, tout en prenant avantage des systèmes de mesures du DAS basés sur la mesure vectorielle et radiofréquence du champ électromagnétique.

**Résumé en anglais** This article introduces a measurement methodology for the evaluation of the specific absorption rate (SAR) of a class of multiple-input and multiple-output (MIMO) communication devices. It is dedicated to the specific MIMO systems in which the relative phases between the antennas are rapidly changing and in very courteous durations, as implemented using the STBC (Space-Time Block Code) function. Indeed, a particular and new subject in these measurements arises when we consider the SAR systems that use vector field measurements, and exploiting the principles of field equivalence for the reconstruction of the field distribution in the volume from samples of a subset of the time-independent harmonic-field that is induced in the internal media simulating the human body.

This article presents measurement methodologies to address this new case of transmissions as well as to contribute to the development of standards of the International Electrotechnical Commission (IEC) harmonizing the procedures for measuring the exposure to electromagnetic radiation, while taking advantage of SAR measurement systems that are based on vector and radiofrequency measurement of the electromagnetic fields.

#### 1 Introduction

Les systèmes de communication connaissent une évolution et une complexification qui augmentent de manière drastique, en particulier avec l'avènement du LTE-advanced et de la 5G. Ces technologies sont fondées, entre autres, sur l'introduction de techniques de communication complexes telle que la multiplication des antennes

d'émission et de réception ou MIMO (Multiple-Input Multiple-output) [1]. L'introduction de cette technologie MIMO dans les dispositifs de communications cellulaires soulève de nouveaux défis dans le domaine de l'évaluation expérimentale du débit d'absorption spécifique de l'exposition humaine aux champs radiofréquences [2]. Dans un dispositif MIMO, les niveaux d'exposition doivent être déterminés pour toutes les configurations de phase possibles [3-4]. En considérant par exemple un pas de  $10^\circ$ , cela correspond dans un système à deux antennes à 36 mesures. Plusieurs méthodes ont été proposées dans la littérature afin de déterminer plus rapidement le DAS dans des configurations MIMO [5-6]. Cependant, ces méthodes supposent un accès direct aux excitations des antennes du système, permettant ainsi d'avoir la même référence de phase pour les antennes d'émission et de mesure. Ceci n'est généralement pas possible dans les cas pratiques.

Dans [7], la notion de DAS local moyenné sur le temps est utilisée afin de déterminer le niveau d'exposition dans le cas des signaux MIMO à forte variation temporelle. Cette méthode de mesure est plus rapide que la méthode classique. Elle nécessite cependant d'intégrer la mesure sur des temps très longs afin de déterminer le DAS moyen. Il est également démontré dans [7], que le facteur déterminant du temps de mesure de cette nouvelle technologie MIMO est la fréquence d'échantillonnage de la mesure du champ-E. Avec une technologie de mesure à détecteur à diode, dont la fréquence d'échantillonnage typique est de quelques kHz, il en résulte une nécessité d'intégrer le signal sur une seconde à chaque point du scan volumique pour atteindre 2% de précision, alors qu'avec une instrumentation vectorielle et radiofréquences, telle qu'introduite dans [8] et dont la fréquence d'échantillonnage est de 250MHz et respectant le théorème de Shannon, le temps d'intégration pourrait être drastiquement réduit.

Dans ce papier, nous proposons une méthodologie de détermination du DAS moyen basée sur l'utilisation de systèmes de mesures vectorielles sur une matrice finie de capteurs du champ électrique et utilisant des méthodes de reconstruction du champ dans le volume. Cette méthodologie est l'extension des travaux présentés dans [9-10] aux cas de systèmes MIMO à forte variation temporelle.

## 2 Mesure du DAS des systèmes MIMO

### 2.1 Classification des signaux MIMO

Le taux de variation des phases relatives des signaux transmis par les antennes qui constituent un système MIMO a un impact significatif sur la variation du champ électromagnétique total ainsi que sur la valeur du DAS moyen qui en découle. De ce fait, il est pertinent de classifier les systèmes MIMO suivant la vitesse de variation de ces phases relatives. On définira alors deux classes principales de signaux MIMO des générations actuelles des systèmes de communications mobiles.

La première classe comprend les signaux ayant des phases relatives qui restent inchangées pendant une durée relativement longue. Le système MIMO reste alors dans une configuration stable tout au long de cette durée. Cela correspond par exemple au cas des réseaux d'antennes dans lesquels le déphasage est utilisé pour contrôler le diagramme de rayonnement et particulièrement la direction de rayonnement. Dans ce type de configurations, la méthode présentée dans [9-10] permet de déterminer rigoureusement, à partir de  $N+1$  mesures uniquement, la valeur de DAS pour toutes les configurations possibles du système MIMO (où  $N$  est le nombre d'antennes du système). La rapidité et rigueur de cette méthode, qui nécessite un nombre de mesures aussi réduit, est obtenue grâce à la mesure simultanée de l'amplitude ainsi que de la phase du vecteur du champ-E harmonique, combinée avec une analyse spectrale vectorielle des signaux radiofréquences, pour l'évaluation du SAR.

La seconde classe inclut quant à elle les signaux ayant une forte et rapide variation des phases relatives entre les antennes du système MIMO. Cela est par exemple le cas lors de l'utilisation d'un codage spatio-temporel des signaux (ex : codage STBC (Space-Time Block Code)). Dans ce type de configurations, et du fait de ces changements rapides, la valeur du DAS est très difficile à mesurer. Cependant, il a été démontré que la moyenne temporelle du DAS instantanée converge pour une durée d'intégration suffisamment longue [7], mais qui pourrait être de très courtes durées si le système de mesure du DAS exploite une acquisition dans le domaine temporel des signaux radiofréquences démodulés qui satisfait le théorème de Shannon. En se basant sur la méthodologie développée dans [9-10] ainsi que sur la convergence de la moyenne temporelle du DAS, nous proposons dans cet article une méthode de mesure efficace pour l'évaluation expérimentale du taux d'exposition dans le cas de signaux MIMO à forte variation de phase. Cette méthode est proposée pour le type de système de mesure du DAS qui utilisent un réseau de sondes de champ-E vectorielle, et qui opèrent avec sélectivité en fréquences et une acquisition dans le domaine temporel des signaux radiofréquences démodulés.

### 2.2 Convergence de la moyenne temporelle du DAS

Le DAS en un point donné  $(x, y, z)$  est défini de la manière suivante :

$$DAS(x, y, z) = \frac{\sigma |\mathbf{E}(x, y, z)|^2}{2\rho} \quad (1)$$

où  $\sigma$  et  $\rho$  sont la conductivité électrique [S/m] et la densité volumique [kg/m<sup>3</sup>] du milieu simulant le tissu humain.  $\mathbf{E}(x, y, z)$  est le phaseur complexe du champ électrique harmonique.

Considérons un système MIMO ayant deux antennes d'émission et qui génèrent chacune des champs  $\mathbf{E}_1$  et  $\mathbf{E}_2$  respectivement. En injectant les signaux  $s_1(t)$  et  $s_2(t)$  dans ces deux antennes, le champ total  $\mathbf{E}_t$  est obtenu tel que :

$$\mathbf{E}_t(x, y, z, t) = s_1(t) \mathbf{E}_1(x, y, z) + s_2(t) \mathbf{E}_2(x, y, z) \quad (2)$$

Le module au carré de l'équation (2) donne alors :

$$|\mathbf{E}_t(x, y, z, t)|^2 = |s_1(t) \mathbf{E}_1(x, y, z)|^2 + |s_2(t) \mathbf{E}_2(x, y, z)|^2 + 2|s_1(t)||s_2(t)| |\mathbf{E}_1(x, y, z)| |\mathbf{E}_2(x, y, z)| \cos(\phi(t)) \quad (3)$$

$$\text{où } \phi(t) = \arg(s_1(t)s_2(t) \mathbf{E}_1(x, y, z) \mathbf{E}_2(x, y, z))$$

En moyennant l'équation (3) dans le temps, on obtient :

$$\langle |\mathbf{E}_t(x, y, z, t)|^2 \rangle = \langle |s_1(t)|^2 \rangle |\mathbf{E}_1(x, y, z)|^2 + \langle |s_2(t)|^2 \rangle |\mathbf{E}_2(x, y, z)|^2 + 2 \langle |s_1(t)||s_2(t)| \cos(\phi(t)) \rangle |\mathbf{E}_1(x, y, z)| |\mathbf{E}_2(x, y, z)| \quad (4)$$

où  $\langle \cdot \rangle = \frac{1}{T} \int_0^T \cdot dt$  et  $T$  est le temps d'intégration.

Dans le cas de codage spatio-temporel, la phase relative des signaux  $s_1(t)$  et  $s_2(t)$  varie très vite, et le terme  $\langle |s_1(t)||s_2(t)| \cos(\phi(t)) \rangle$  tends vers zéro pour un temps d'intégration  $T$  suffisamment long. On obtient, à partir de l'équation (4), la moyenne temporelle du DAS instantané  $DAS(x, y, z, t)$  comme étant :

$$\langle DAS(x, y, z, t) \rangle = \langle |s_1(t)|^2 \rangle DAS_1(x, y, z) + \langle |s_2(t)|^2 \rangle DAS_2(x, y, z) \quad (5)$$

où  $DAS_1(x, y, z)$  et  $DAS_2(x, y, z)$  sont les DAS résultant respectivement des deux antennes lorsqu'elles sont excitées individuellement l'une après l'autre. Le résultat obtenu dans l'équation (5) pourra ensuite être généralisé au cas de N antennes MIMO.

### 2.3 Méthode de mesure proposée

Dans cette section, nous proposons une méthode afin de déterminer le DAS dans le cas de signaux MIMO à forte variation temporelle. A partir de l'équation (5), on remarque que la détermination de la moyenne temporelle du DAS d'un système MIMO revient à déterminer les DAS individuels, résultants des antennes excitées individuellement, ainsi que les moyennes  $\langle |s_i(t)|^2 \rangle$  des carrés des signaux d'excitation du système.

A la lumière de ces constatations, nous proposons une méthode de mesure composée de deux étapes, permettant de déterminer le DAS moyen d'un système MIMO à  $N$  antennes.

#### 1- Etape 1 - Configuration à faible variation temporelle :

- a. Forcer le DUT à opérer dans une configuration à faible variation temporelle.
- b. Suivre la méthode présentée dans [9-10] afin de déterminer, à partir de  $N+1$  mesures, les DAS individuels  $DAS_i(x, y, z)$  résultant de l'excitation séparée des antennes MIMO, et ce, en tout point  $(x, y, z)$  du domaine de mesure.

#### 2- Etape 2 - Configuration à forte variation temporelle :

- a. Mettre le DUT dans sa configuration nominale de forte variation temporelle des phases relatives et pour laquelle la mesure du DAS doit être effectuée.

- b. Mesurer le DAS local instantané  $DAS(x_k, y_k, z_k, t)$  en  $K$  points  $(x_k, y_k, z_k)$  ( $K \geq N$ ) de la grille du réseau de capteurs, et sur une durée  $T$  suffisamment longue afin d'atteindre la convergence de la moyenne temporelle  $\langle DAS(x_k, y_k, z_k, t) \rangle$ .
- c. A partir de ces moyennes de DAS  $\langle DAS(x_k, y_k, z_k, t) \rangle$  et des DAS individuels  $DAS_i(x, y, z)$  déterminés dans la phase 1, déterminer la valeur moyenne des carrés des signaux d'excitation  $\langle |s_i(t)|^2 \rangle = \alpha_i$ , et ce, en minimisant l'expression suivante :

$$\min_{\alpha_i} \sum_{k=1}^K \left| \langle DAS(x_k, y_k, z_k, t) \rangle - \sum_{i=1}^N \alpha_i DAS_i(x_k, y_k, z_k) \right| \quad (6)$$

- d. A partir des  $\alpha_i$ , déterminer la valeur de la moyenne temporelle du DAS en tout point de l'espace  $(x, y, z)$  à l'aide de l'équation suivante :

$$\langle DAS(x, y, z, t) \rangle = \sum_{i=1}^N \alpha_i DAS_i(x, y, z) \quad (7)$$

### 3 Validation numérique

Afin de valider la méthode de mesure proposée, une configuration MIMO composées de deux antennes dipôles est considérée, et ce, pour une fréquence de travail de 750MHz. Le champ E généré par un dipôle horizontal placé au-dessus d'un Phantom de paramètres diélectriques  $(\epsilon_r; \sigma) = (42.8; 0.85 \text{ S/m})$  a été simulé à l'aide du logiciel FDTD EMPIRE XPU [11], puis utilisé afin déterminer le champ généré par la configuration MIMO à 2 dipôles.

Afin d'avoir une forte variation temporelle de phase, des signaux temporels STBC ont été générés en suivant le schéma bloc décrit dans la *Figure 1*. Les signaux obtenus sont ensuite combinés avec les simulations des champs E afin de simuler le système de mesure dans une configuration MIMO à forte variation temporelle.

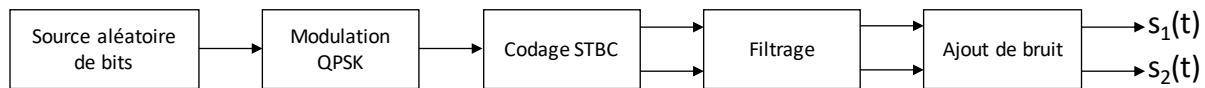


*Figure 1: Schéma bloc du système de transmission MIMO avec codage STBC.*

#### 3.1 Convergence de la moyenne temporelle du DAS

Une première étape de validation est dédiée à la vérification de la convergence de la moyenne temporelle du DAS ainsi que de la validité de l'équation (5). Cela permettra aussi de déterminer le temps d'intégration  $T$  nécessaire à la mesure. Pour cela, des signaux QPSK aléatoires sont générés en suivant le schéma bloc de la *Figure 1*. Le signal généré a les caractéristiques suivantes :

Débit symbole :  $10^6$  symbole/s (soit une durée symbole de  $1\mu\text{s}$ )

Modulation : QPSK

Codage : STBC

Filtre de mise en forme : Cosinus surélevé (Facteur de rolloff : 0.25)

SNR : 30 dB

La fréquence d'échantillonnage du bloc de numérisation des signaux démodulés du système de mesures de DAS est considérée égale à 50 MHz, soit 5 fois la fréquence maximale du signal. Il est à noter que dans la pratique, il est financièrement très abordable d'acquérir un convertisseur analogique-numérique de fréquences d'échantillonnage de plusieurs centaines de MHz.

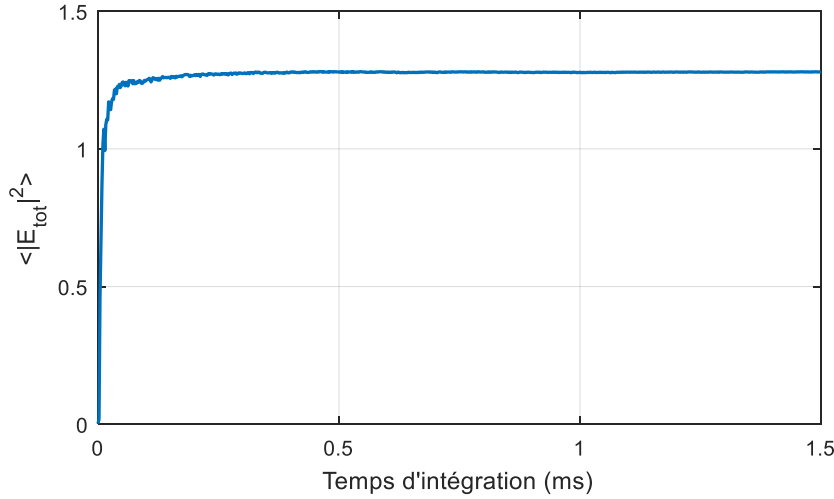


Figure 2: Variation de la moyenne temporelle du carré d'amplitude du champ en fonction du temps d'intégration en (ms).

Les signaux  $s_1(t)$  et  $s_2(t)$  générés à l'issue de cette étape sont combinés afin d'obtenir le champ total  $E_t(t) = c_1 s_1(t) + c_2 s_2(t)$  ( $c_1$  et  $c_2$  sont deux nombres complexes représentant les champs générés par les deux antennes). Le carré d'amplitude du champ total obtenu est ensuite moyené dans le temps en faisant varier le temps d'intégration. Les résultats obtenus sont représentés dans la Figure 2. On remarque à partir de cette dernière figure que la convergence de carré de l'amplitude du champ est atteinte après une durée d'intégration très courte de quelques fractions de la milliseconde.

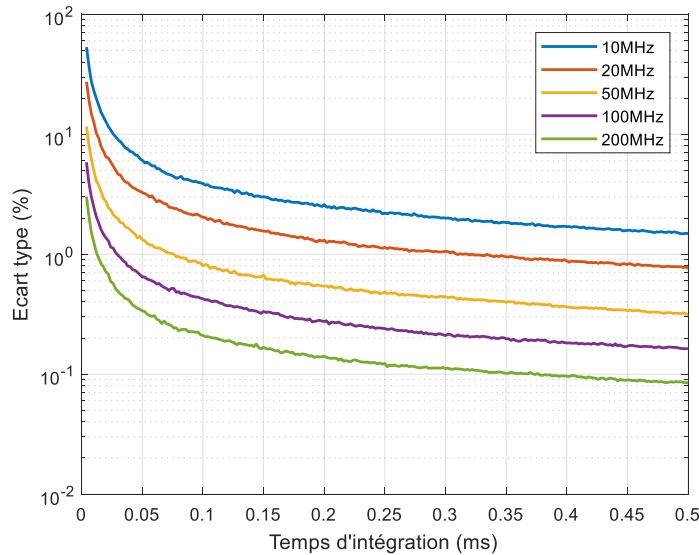


Figure 3: Variation de l'écart type de la moyenne du DAS local en fonction du temps d'intégration pour différentes fréquences d'échantillonnage avec 1000 réalisations par point.

L'opération est répétée un grand nombre de fois (1000 fois) pour différentes fréquences d'échantillonnage  $F_e$ , dont les résultats sont présentés en Figure 3. On y remarque que la fréquence d'échantillonnage du signal a un effet significatif sur la vitesse de convergence de la moyenne temporelle. Il est plus vrai pour les cas où le choix de la fréquence d'échantillonnage ne respecte pas le théorème de Shannon, tel que pour  $F_e = [10, 20, 50]$  MHz qui mènent à une augmentation drastique du temps d'intégration assurant moins de 1% d'erreur. À la fréquence d'échantillonnage considérée (50 MHz), l'écart type est inférieur à 1% pour un temps d'intégration supérieur à 80  $\mu$ s. C'est ce temps d'intégration qui sera utilisé pour la suite de cet article.

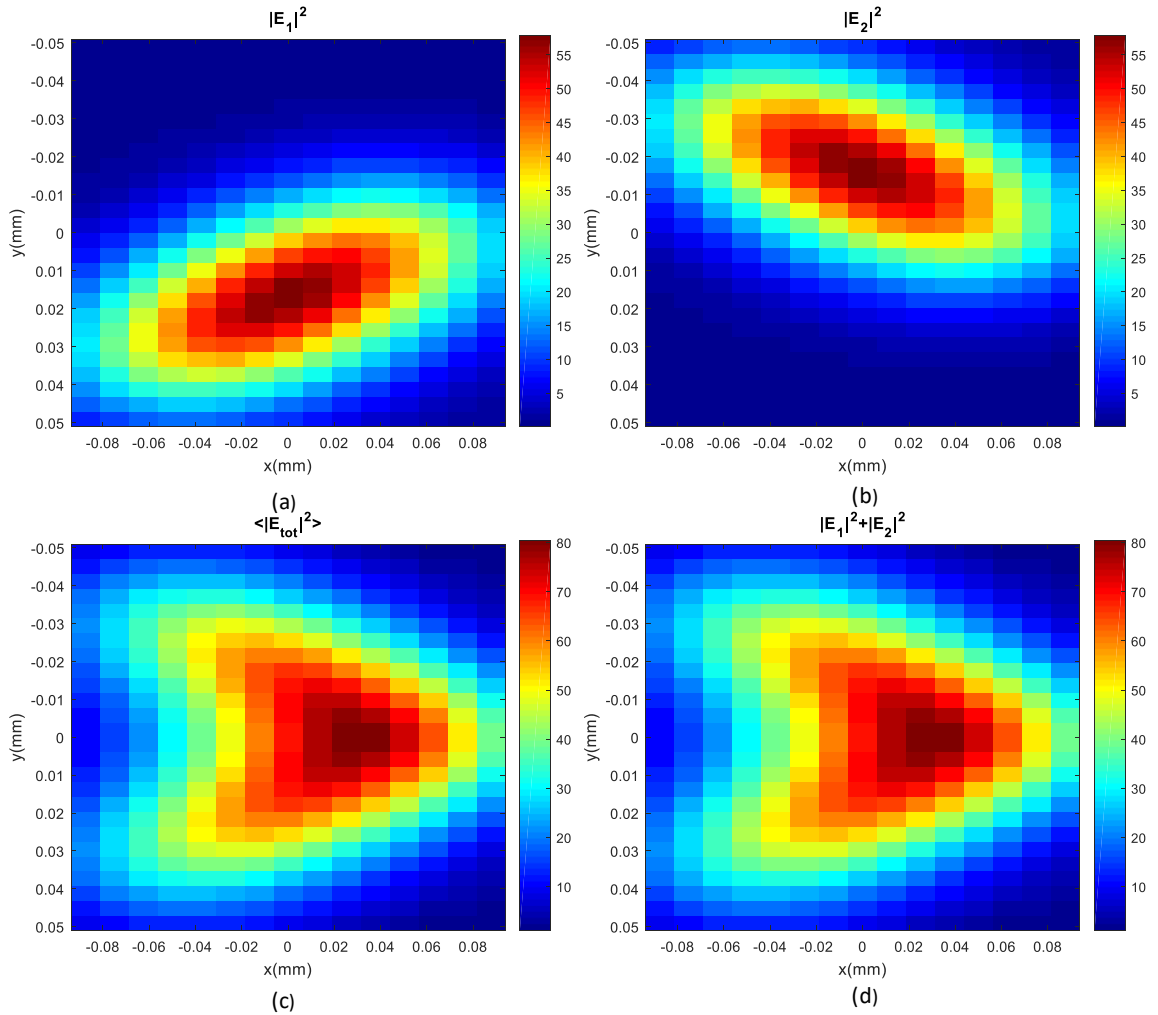


Figure 4: Variations de la moyenne temporelle des carrés d'amplitude des champs : (a)  $|E_1|^2$ . (b)  $|E_2|^2$ . (c)  $\langle |E_{tot}|^2 \rangle$ . (d)  $|E_1|^2 + |E_2|^2$ .

Les signaux STBC générés sont appliqués sur des champs-E internes au fantôme et calculés par simulations numériques de deux dipôles horizontaux, et ce, afin de simuler un système de mesure de DAS exploitant la mesure du champ vectoriel sur une grille finie et utilisant la reconstruction du champ dans le volume interne pour l'évaluation du DAS. Dans l'exemple considéré, les deux dipôles sont centrés à  $(x, y) = (0, 30)$  mm et  $(x, y) = (0, -30)$  mm et inclinés de  $+45^\circ$  et  $-45^\circ$  par rapport à l'axe  $y = 0$ , respectivement. Les signaux d'excitations utilisés sont d'amplitude unité de façon à avoir :  $\langle |s_1(t)|^2 \rangle = \langle |s_2(t)|^2 \rangle = 1$ . Les variations de la moyenne temporelle des carrés d'amplitude des champs sont représentées dans la Figure 4, où on remarque en Figure 4.(c) et Figure 4.(d) que les variations de  $\langle |E_t|^2 \rangle$  et de la somme  $|E_1|^2 + |E_2|^2$  sont pratiquement identiques, avec une erreur quadratique inférieure à 3%. Cela confirme que le terme  $\langle |s_1(t)||s_2(t)|\cos(\phi(t)) \rangle$  tends vers zéro pour un temps d'intégration suffisamment long et valide ainsi l'équation (5) sur laquelle se base la méthode de mesure proposée.

### 3.2 Validation numérique de la méthode proposée pour la mesure de DAS du MIMO rapide

Afin de valider la méthode de mesure proposée dans cet article, les étapes décrites dans la section 2.3 sont appliquées sur des distributions de champs similaires à celles utilisées dans les sections précédentes. Les dipôles considérés ont des orientations de  $-15^\circ$  et de  $45^\circ$  respectivement. Les amplitudes des signaux d'excitations générés sont paramétrées de manière à avoir  $\langle |s_1(t)|^2 \rangle = 0.5$  et  $\langle |s_2(t)|^2 \rangle = 0.75$ .

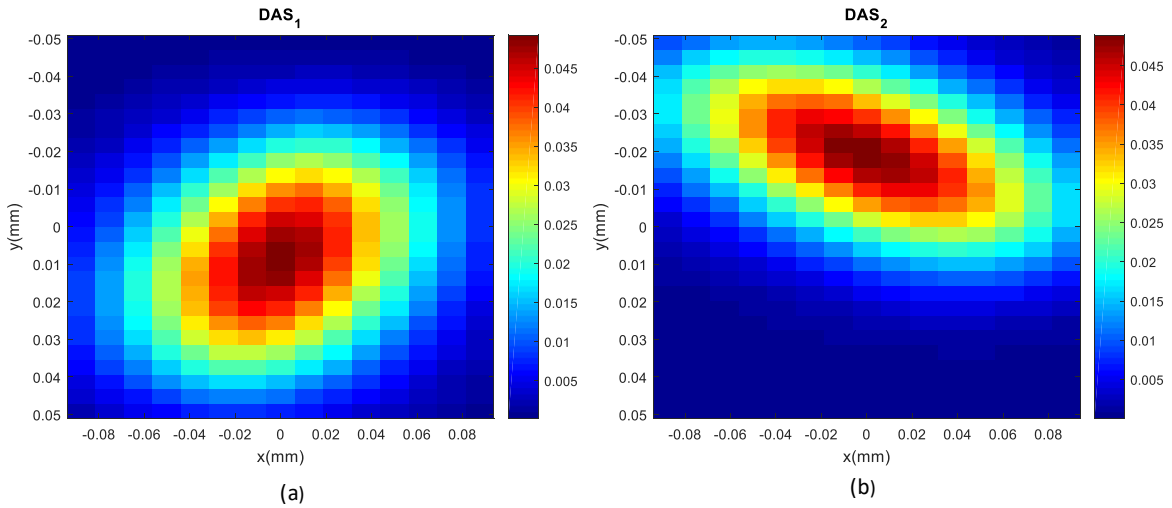


Figure 5: Variations du DAS local simulé. (a) antenne 1 seule. (b) antenne 2 seule.

L'étape 1 de la méthode de mesure ayant été validée dans [8-9], on supposera que les valeurs du DAS local  $DAS_1(x, y, z)$  et  $DAS_2(x, y, z)$  des deux antennes sont connues en tout point de l'espace de mesure. Les variations du DAS local correspondantes sont représentées dans la Figure 5.

A partir des signaux  $s_1(t)$  et  $s_2(t)$  ainsi que des simulations de champs E, la moyenne temporelle du DAS  $\langle DAS(x_k, y_k, z_k, t) \rangle$  est déterminée pour deux points de mesures  $(x_1, y_1, z_1)$  et  $(x_2, y_2, z_2)$  (par exemple les maximums des DAS locaux).

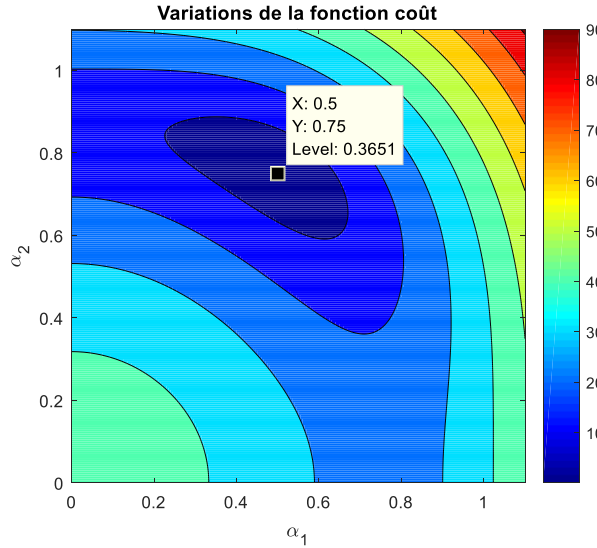


Figure 6: Variations de la fonction coût définie dans l'équation (8).

Une fonction cout  $f(\alpha_1, \alpha_2)$  est alors définie de la manière suivante :

$$f(\alpha_1, \alpha_2) = \sum_{k=1}^2 \left| \langle DAS(x_k, y_k, z_k, t) \rangle - (\alpha_1 DAS_1(x_k, y_k, z_k) + \alpha_2 DAS_2(x_k, y_k, z_k)) \right| \quad (8)$$

En faisant varier les valeurs des  $\alpha_i$ , les variations de la fonction coût définie dans l'équation (8) sont représentées dans la Figure 6. On remarque que le minimum de la fonction coût correspond aux valeurs  $(\alpha_1, \alpha_2) = (0.5, 0.75)$ . Cela correspond bien aux moyennes temporelles  $\langle |s_1(t)|^2 \rangle$   $\langle |s_2(t)|^2 \rangle$  initialement imposées. A partir de ces valeurs,

on pourra déduire les variations de la moyenne temporelle du DAS  $\langle DAS(x, y, z, t) \rangle$  en tout point de l'espace de mesure, et ce, à l'aide de l'équation (7). Les résultats obtenus sont représentés dans la *Figure 7*.

Pour résumer, la détermination du DAS moyen (en tout point de l'espace) dans le cas d'un système MIMO à 2 antennes aura nécessité trois mesures vectorielles de DAS (d'une durée moyenne de 15s chacune) ainsi que deux mesures de DAS moyenné dans le temps en deux points de l'espace (avec une durée de 80 $\mu$ s par mesure).

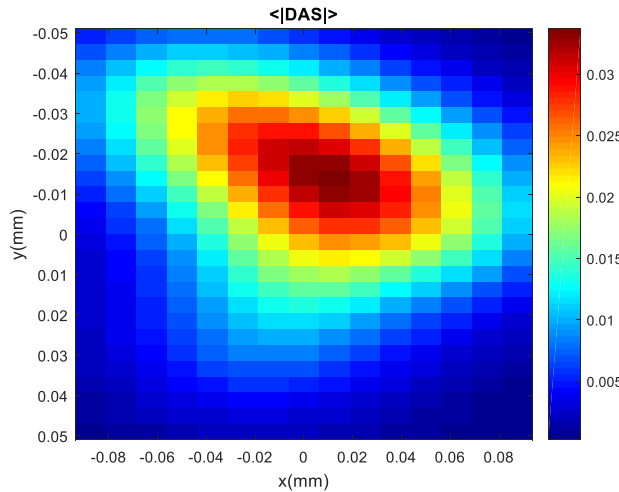


*Figure 7 : Distribution du DAS local moyenné dans le temps et retrouvées avec la méthode de mesure proposée.*

#### 4 Conclusion

Cet article présente une méthode innovante, pratique et rigoureuse pour l'évaluation expérimentale de l'exposition électromagnétique des dispositifs de communication sans fil qui exploitent la technologie MIMO utilisant la variation rapide des phases relatives entre les antennes du réseau MIMO. Pour un système à N antennes, la méthode proposée se base sur les mesures du champ-E vectoriel pour N+1 états d'interférences connus du réseau, couplées avec des mesures de moyennes temporelles, sur de très courtes durées de l'ordre de millisecondes, du DAS local en un nombre très limité de points sur le réseau de capteurs du champ E, permettant alors de s'affranchir de l'intégration temporelle du DAS instantané en tous points de l'espace d'évaluation du DAS.

En plus de sa rapidité et son caractère pratique, cette méthode est compatible avec le cas d'une distribution non aléatoire des phases d'excitation du réseau d'antennes ainsi qu'avec le cas de configurations MIMO à faible variation temporelle. On pourra alors traiter toutes les configurations possibles d'un système MIMO à partir du même jeu de mesures initiales.

Finalement, il est démontré dans ce papier que l'utilisation de la méthode proposée sur la nouvelle génération de systèmes de mesures vectorielles du DAS, qui intègrent une acquisition des signaux radiofréquences dans le domaine temporel avec une fréquence d'échantillonnage suffisamment élevée (quelques centaines de MHz pour un signal en bande de base ou en fréquence intermédiaire) permet d'envisager de ramener à quelques dizaines de secondes seulement la mesure du DAS MIMO-rapide, alors qu'il est de plusieurs dizaines de minutes sur un système de mesure utilisant une technologie traditionnelle de détecteur à diode qui souffre d'une limitation de fréquence d'échantillonnage à quelques kHz seulement.

#### 5 Remerciements

Nous tenons à remercier Joe Wiart, Directeur de la Chaire C2M, Telecom ParisTech, pour nos échanges très instructifs sur le sujet de la mesure du DAS MIMO.

#### Références bibliographiques

- [1] Z. Ying, "Antennas in cellular phones for mobile communications," *Proc. IEEE*, vol. 100, no. 7, pp. 2286-2296, Jul. 2012.

- [2] ICNIRP Guidelines Draft Ed. (2018). Draft Guidelines for Limiting Exposure to Time-Varying Electric, Magnetic, and Electromagnetic Fields (up to 300 GHz). [Online]. Available: <https://www.icnirp.org/en/activities/public-consultation/consultation-1.html>
- [3] "Guidance for evaluating exposure from multiple electromagnetic sources," IEC, Tech. Rep. 62 630, Oct. 2010.
- [4] Measurement procedure for the assessment of specific absorption rate of human exposure to radio frequency fields from hand-held and body-mounted wireless communication devices - Part 3: Vector measurement-based systems (Frequency range of 600 MHz to 6 GHz), 1st ed., Standard IEC 62209-3, 2019.
- [5] N. Perentos, S. Iskra, A. Faraone, R. J. McKenzie, G. Bit Babik and V. Anderson, "Exposure Compliance Methodologies for Multiple Input Multiple Output (MIMO) Enabled Networks and Terminals," IEEE Transactions on Antennas and Propagation, vol. 60, no. 2, pp. 644-653, Feb. 2012.
- [6] D. T. Le, L. Hamada, S. Watanabe and T. Onishi, "A Fast Estimation Technique for Evaluating the Specific Absorption Rate of Multiple- Antenna Transmitting Devices," in IEEE Transactions on Antennas and Propagation, vol. 65, no. 4, pp. 1947-1957, April 2017.
- [7] D. T. Le, and al. "Averaging time required for measuring the specific absorption rate of a MIMO transmitter." IEEE Electromagnetic Compatibility Magazine 3.1 (2014): 57-64.
- [8] B. Derat et al., "A novel technology for fast and accurate specific absorption rate measurement," 2013 International Workshop on Antenna Technology (iWAT), Karlsruhe, 2013, pp. 363-366.
- [9] L. Aberbour, O. Jawad, M. Ramdani, P. Giry and T. Julien, "Efficient Experimental Assessment of The Specific Absorption Rate (SAR) Induced by MIMO Wireless Communication Devices; Application of Vector Near-Field Measurement System," 2018 IEEE Conference on Antenna Measurements & Applications (CAMA), Vasteras, 2018, pp. 1-4.
- [10] M. Teniou, O. Jawad, S. Pannetrat and L. Aberbour, "A Fast and Rigorous Assessment of the Specific Absorption Rate (SAR) for MIMO Cellular Equipment Based on Vector Near-Field Measurements," 2018 IEEE Conference on Antenna Measurements & Applications (CAMA), Vasteras, 2018, pp. 1-4.
- [11] EMPIRE XPU : <https://www.empire.de/>

## Assessment of MaMIMO beamwidth using measurements and raytracing *Évaluation des ouverture de faisceau MaMIMO à l'aide de mesures et de raytracing*

**Maarten Velghe<sup>1</sup>, Sergei Shikhantsov<sup>1</sup>, Luc Martens<sup>1</sup>, Wout Joseph<sup>1</sup> and Arno Thielen<sup>1</sup>**

<sup>1</sup>*Department of Information Technology, Ghent University/IMEC, Technologiepark 126, 9052 Ghent, Belgium*

MaMIMO, beamwidth, RF-EMF exposure / *MaMIMO, ouverture de faisceau, exposition RF-EMF*

### Abstract/Résumé

The width of a beam produced by MaMIMO arrays will affect a user's exposure to RF-EMFs. We performed measurements in an anechoic chamber using a virtual arrays and successfully assessed this beamwidth. We validated our measurements with simulations.

L'ouverture d'un faisceau produit par les réseaux MaMIMO affectera l'exposition d'un utilisateur aux RF-EMF. Nous avons effectué des mesures dans une chambre anéchoïque avec des réseaux virtuels et évalué cette ouverture de faisceau. Nous avons validé nos mesures avec des simulations.

### 1 Introduction

In the fifth generation of telecommunication networks, Massive Multiple-input-multiple-output (MaMIMO, [1]) base stations (BSs) will produce narrow RF-EMF beams aimed at each specific user device they service. Knowledge on the widths of these beams is essential to evaluate a user's exposure to RF-EMFs. The aim of this study is to assess this beamwidth via measurements in an anechoic chamber and to validate the used setup with free-space simulations.

### 2 Materials and Method

#### 2.1 Measurement setup

Figure 1 shows a schematic top view of the measurement setup in the anechoic chamber. Two vertically polarized dipole dual cone broadband antennas, a transmitting (TX) and receiving (RX) antenna, are connected to a vector network analyser (VNA) performing measurements at 3.5 GHz. The TX antenna is fixed on a linear positioning system, moving along the y-axis. The RX antenna is placed on a 2D positioning system, consisting of two orthogonally oriented linear positioners moving along the y- and x-axis. Positioning systems are coplanar, such that the antennas stay in the same xy-plane as they move.

The TX grid has 17x1 locations, with the interspacing chosen to be  $\delta_{Tx}=4.28$  cm, which is about half the wavelength. This results in an array aperture L of 68 cm. The TX-RX distance D is chosen to be 68 cm as well. The RX grid has 33x17 locations (33 elements along the y-axis per 17 elements along the x-axis) with an interspacing half of the TX interspacing ( $\delta_{Rx}=2.14$  cm). We measure the channel transfer function  $h_{kn,\text{measured}}$  between each Tx-position k ( $k=1 \dots 17$ ) and each Rx-position n ( $n=1 \dots 561$ ), resulting in the channel matrix  $H_{\text{measured}}$ .

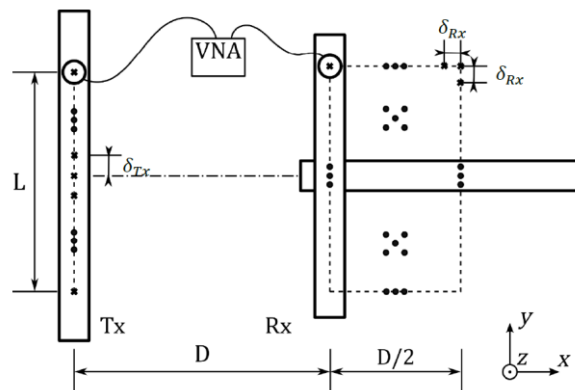


Figure 1: Schematic overview of the measurement setup.

To validate the measurement results, we estimate the wireless channel between the TX and RX virtual arrays using a Line-of-Sight (LOS) propagation model. This is suitable for calculating propagation in the anechoic chamber with virtual arrays, as it only takes into account direct propagation paths between TX-RX pairs and neglects mutual coupling effects of the arrays' antennas. This results in the simulated channel matrix  $\mathbf{H}_{\text{model}}$ .

## 2.2 Post processing

The channel correlation matrix (CM) is commonly used for the analysis of the performance of MaMIMO systems is defined as

$$\mathbf{G} = \mathbf{H}^* \mathbf{H}. \quad (1)$$

This results in two  $561 \times 561$  CMs:  $\mathbf{G}_{\text{measured}}$  and  $\mathbf{G}_{\text{model}}$  which are complex valued with real values on the main diagonal. To simplify the analysis we take the average of the results in each of the 17 Rx-rows along the x-axis. This way we calculate the average beamwidth over the distance  $x=[68\text{cm} \ 102\text{cm}]$ . This results in the  $33 \times 33$  averaged CMs  $\mathbf{G}_{\text{avg,measured}}$  and  $\mathbf{G}_{\text{avg,model}}$ . These are normalized to

To assess the beamwidth, we define the spatial correlation function (CF)  $\rho(\mathbf{G}_{\text{avg}}, i)$  as the average over the  $i^{\text{th}}$  diagonal of  $\mathbf{G}_{\text{avg}}$ :

$$\rho(\mathbf{G}_{\text{avg}}, i) = \frac{\sum_{k=1}^{33-i} |g_{k,k+i}|}{33 - i}, \quad (2)$$

with  $g_{lm}$  an element of  $\mathbf{G}_{\text{avg}}$ .  $\rho$  can be treated as a function of the distance in the y-direction between the receivers.

The average relative difference  $\sigma_{\text{avg}}$  between  $\mathbf{G}_{\text{avg,measured}}$  and  $\mathbf{G}_{\text{avg,model}}$  is calculated as

$$\sigma_{\text{avg,lm}} = \left| \frac{|g_{\text{avg,model,lm}}| - |g_{\text{avg,measured,lm}}|}{\frac{|g_{\text{avg,model,lm}}| + |g_{\text{avg,measured,lm}}|}{2}} \right|, \quad (3)$$

with  $\sigma_{\text{avg,lm}}$  an element of  $\sigma_{\text{avg}}$ .

## 3 Results and Discussion

Figure 2 compares  $\rho(\mathbf{G}_{\text{avg,model}})$  and  $\rho(\mathbf{G}_{\text{avg,measured}})$ . A very good agreement is observed. Both functions have maximum at  $\delta y=0$  and decrease rapidly within a 1-wavelength distance (8.57 cm). After minor oscillations they flatten-out at around 4% of their maximum value for  $\delta y > 0.5 \text{ m}$  ( $\approx 6*\lambda$ ). The distance between the maximum and half the maximum  $\delta_{\text{hm}}y=6.5 \text{ cm}$ , the beamwidth is thus  $2*\delta_{\text{hm}}y=13 \text{ cm}$ .

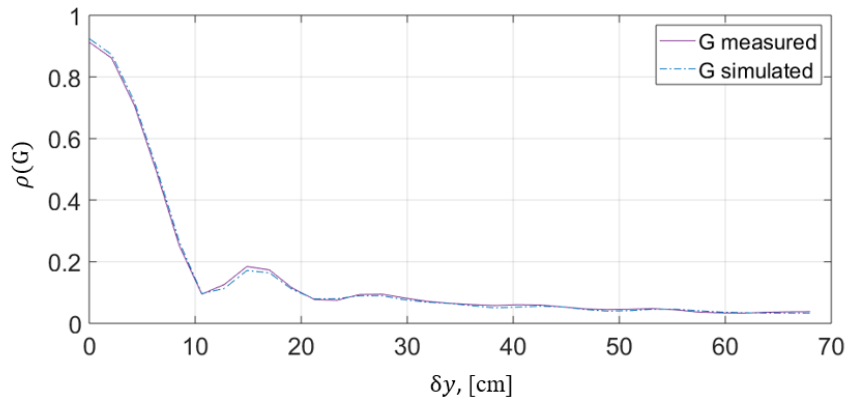


Figure 2: Spatial correlation function of  $G_{\text{avg,measured}}$  and  $G_{\text{avg,model}}$  in terms of the distance between their rows.

In Figure 3 the normalized CMs  $\mathbf{G}_{\text{avg,measured}}$  (3a),  $\mathbf{G}_{\text{avg,model}}$  (3b) and their difference  $\sigma_{\text{avg}}$  (3c) are shown. The main diagonal dominance is apparent in both averaged CMs. The same result has been obtained in measurement campaigns [2] and using geometry-based models [3].  $\sigma_{\text{avg}}$ , does not exceed 5% on the main diagonal. This implies a good agreement between measurements and simulations. However, some of the out-of-diagonal

elements exceed 30%. The reason for that are the low absolute correlation values observed at large RX separation distances, which are shown in the top-right corner of the CMs. Even a small variation of the received signal (due to e.g. reflections by the positioners and support structures, alignment errors, radiation pattern variation) results in a relatively high simulation error.

This measurement setup can now be used to evaluate exposure from MaMIMO systems in other environments, such as a room without absorbing materials, with obstructed line-of-sight conditions, etc.

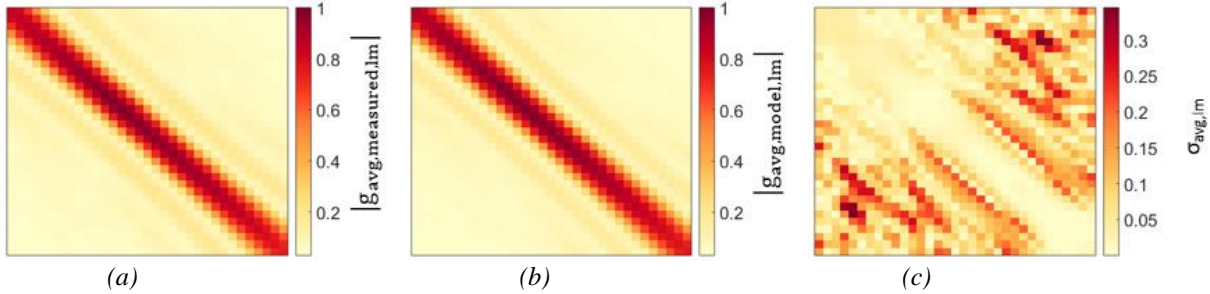


Figure 3: The normalized correlation matrices  $G_{avg,measured}$  (a),  $G_{avg,model}$  (b), and their relative difference  $\sigma_{avg}$  (c).

#### 4 Conclusion

We measured and simulated the beamwidth of a MaMIMO array and found  $2*\delta_{hmy}=13$  cm. A good agreement between measurements and simulations was observed.

#### References

- [1] Marzetta, et al. 2010. *IEEE Trans. Wirel. Commun.*, 9(11): 3590.
- [2] Claessens, et al. 2018. *IEEE International Workshop on SPAWC*, 19: 1–5.
- [3] Marzetta, 2016. *Fundamentals of Massive MIMO*. Cambridge University Press.

# Reconstruction of EMF Exposure in Cellular Networks from Sensor Measurements by Using Artificial Neural Network

---

**Shanshan Wang and Joe Wiart**

Télécom Paris - IP Paris, LTCI, C2M Chair, Palaiseau, France *{shanshan.wang, joe.wiart}@telecom-paris.fr}*

---

**Keywords:** Electromagnetic field, Exposure, Artificial Neural Network, Path Loss Model

---

**Abstract:**

This paper studies the electromagnetic field (EMF) exposure emitted by base stations (BSs) from cellular networks in the urban city environment. We reconstruct the EMF exposure by using artificial neural network (ANN) based on data measured by sensors. We take consideration of spatial locations of real BSs in 14th district of Paris, time variation and antenna orientation. And most importantly, we propose a new path loss model to capture the Light-of-Sight (LoS) and None-Light-of-Sight (NLoS) effects caused by complicated and varying blockages in urban cities. By applying the ANN, we are able to reconstruct EMF exposure for the locations of interest with  $R^2 = 0.755$ .

## 1 Introduction

The electromagnetic field (EMF) exposure has been a hot issue nowadays, especially with the fast development of wireless communication techniques, e.g. deployment of 5G equipment. The population risk perception linked to the emission of base station (BS) in urban cities become a spreading concern for both telecommunication regulators and citizens. In the present paper, radiofrequency exposure from 4G network is analyzed and reconstructed with the help of artificial neural network (ANN) based on the measurements recorded by sensors installed on the streetlamps, e.g., sensors installed in different cities by Observatoire des Ondes [1] and EXEM [2]. Sensors record the EMF exposure from certain frequencies, and those measurements are used to reconstruct and predict outdoor EMF exposure level.

However, there are several challenges, which prevent us from assessing an accurate spatial map of EMF exposure. Due to the complexity of building structure and material, it is difficult to capture the important features of channel information. Second, in the urban environment, the mobile objects in between transmitter and receiver would play an more important role, e.g., the Line-of-Sight (LoS) signal could be totally blocked by a passing-by bus. Furthermore, the usage of cellular network may experience peak and trough usage during different time of a day, which results in the time variation of exposure.

Conventional methods are used to assess EMF exposure of the network, like ray-based simulators [3] and Kriging [4]. While considering the complexity of analysis, ability to deal with high dimension data and accuracy of analysis, the mentioned methods are not feasible to cover all the aspects. Therefore, in the present paper, we present the reconstruction of EMF exposure using ANN approach, which captures important features in simulating network and also gives good over-all performance.

## 2 System Model

In this paper, a fully-loaded downlink cellular network where BSs operate at 2600 MHz with fixed transmit power is considered. The map of 14th district is shown in Fig 1, with real spatial locations of BSs (from ANFR) and street lamps (possible locations of sensors) are displayed in black and red dots respectively. The antenna equipped on each BS has uniformly distributed orientation. The aggregated exposure perceived by the receiver can be denoted as:

$$P_{exp}(x_j, t) = \sum_{i \in \Phi_{BS}}^{N_{BS}} P_{tx} G_{tx} PL(x_{ij}) f_t(t) \quad (1)$$

where  $G_{tx}$  is the gain of transmitting antenna, which depends on the orientation of antenna.  $PL(x_{ij})$  is the new block-based path loss attenuation function between receiver  $x_j$  and BS $_i$ .  $f_t(t) = -0.3\sin(t) + 2, 0 \leq t \leq 24$  gives the time variation function in a day, to model the rapidly changing traffic load in urban cities.

The block-based path loss model means different regions may have different reception ability depending on the surrounding environment, e.g., locations near a square, have a small value of path loss exponent (PLE). While locations among tall buildings are more likely to have high PLE value. We propose the path loss model as:  $PL = A + 10\alpha(x_j) \log_{10}(d/d_o); d \geq d_o$ , and  $A$  is the decibel path loss at distance  $d_o$ . Fig 1 shows a simple

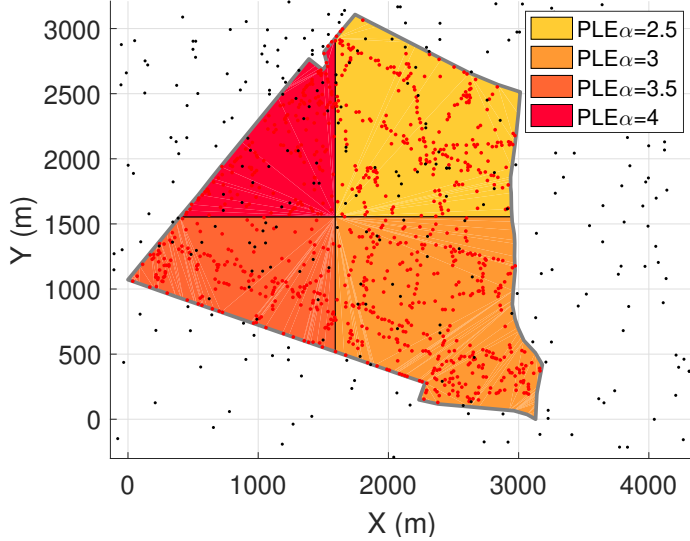


Figure 1 – Map of 14th district in Paris, different colors represent different regions covered by different PLE

example of  $\alpha(x_j)$  depending on locations of  $x_j$ . It should be noticed that, if given empirical city structure, the block-based model can also be extended and may not be in "blocks" only.

### 3 Construction of ANN

An ANN, aiming at solving regression problems are constructed. Inputs of the ANN are selected from possible influential factors in determining EMF exposure, which is, distance between receiver and BS, time of the measurement, azimuth of antennas and city structure in terms of blocked-based PLE.

In order to minimize the cost function, back propagation is performed by applying gradient descend method. And to better evaluate the performance of the ANN, two metrics are used in the present paper, mean square error (MSE) and  $R^2$  [5], where MSE approach is used to minimize residual sum of squares (RSS).  $R^2$  indicates how close two sets of data are. When  $R^2 \rightarrow 1$ , a large proportion of the variability in the response is explained by the ANN.

### 4 Results

We presented results of EMF exposure reconstructed by using ANN in this section. In total we use 1758 data sets generated from simulations in Matlab. Early stopping method is used to avoid over-fitting. Standardization approaches are used to pre-process inputs of ANN. With selection of 67% for training data, we are able to reconstruct the EMF exposure with  $R^2 = 0.755$  for testing data.

Fig 2 shows the scattering plot of target obtained from simulations and predictions generated by ANN. The closer the scattering points get to the black diagonal line, the more accurate predictions are. Both training and testing results, denoted by blue and red dots respectively, show good ability in reproducing the EMF exposure. Fig 3 illustrates cumulative distribution function (CDF) for targets and predictions of testing data, which shows a good overlap between predictions and targets as well.

### 5 Conclusion

In this work, we reconstruct EMF exposure from 4G networks given measurements recorded by sensors. We are able to take into account key factors as, distance to the BS, azimuth of antennas, time of measurement, and most importantly, the blockages in the urban environment. A new block-based model is proposed to capture LoS and NLoS links caused by complicated building structure. We are able to achieve that under a realistic scenario mentioned above, predictions from ANN has  $R^2 = 0.755$  compared with targets.

### 6 References

- [1] “Observatoire des ondes.” <https://observatoireondes.fr/>, 2019 (accessed December, 2019).

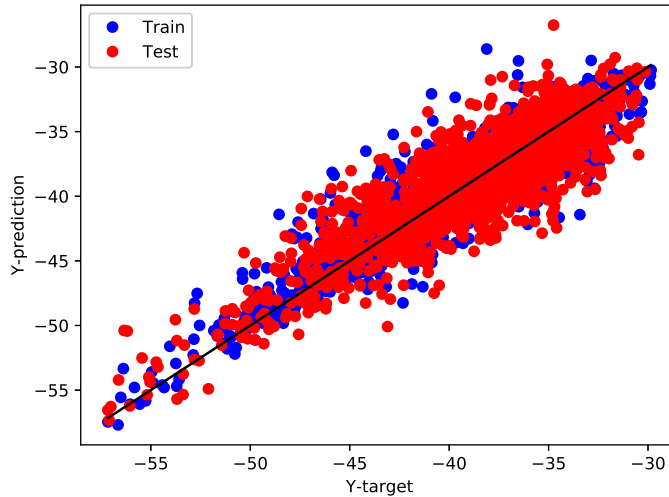


Figure 2 – Scattering plot of training and testing samples in ANN

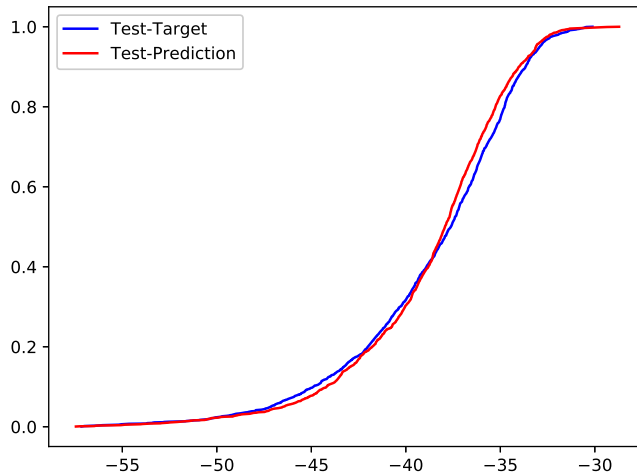


Figure 3 – Cumulative distribution function (CDF) comparison for targets and predictions from ANN.

- [2] “Exem.” <https://www.exem.fr/wp-content/uploads/2019/03/0bservatoire-des-Ondes-par-Exem.pdf>, 2019 (accessed December, 2019).
- [3] Y. Huang and J. Wiart, “Simplified assessment method for population rf exposure induced by a 4g network,” *IEEE Journal of Electromagnetics, RF and Microwaves in Medicine and Biology*, vol. 1, no. 1, pp. 34–40, 2017.
- [4] S. Aerts, D. Deschrijver, L. Verloock, T. Dhaene, L. Martens, and W. Joseph, “Assessment of outdoor radiofrequency electromagnetic field exposure through hotspot localization using kriging-based sequential sampling,” *Environmental research*, vol. 126, pp. 184–191, 2013.
- [5] I. Goodfellow, Y. Bengio, and A. Courville, *Deep learning*. MIT press, 2016.



## ORGANISATION

COMITÉ SCIENTIFIQUE, <i>SCIENTIFIC COMMITTEE</i>	
<ul style="list-style-type: none"><li>• <b>Président, Joe Wiart</b> (Telecom Paris) :</li><li>• <b>Joseph Achkar</b> (Observatoire de Paris)</li><li>• <b>Jean-Benoit Agnani</b> (ANFR)</li><li>• <b>Tahsin Akalin</b> (Université de Lille)</li><li>• <b>Francesco Andriulli</b> (Politecnico Di Torino)</li><li>• <b>Xavier Begaud</b> (Telecom Paris)</li><li>• <b>Sébastien Célestin</b> (CNRS Orléans)</li><li>• <b>Emmanuelle Conil</b> (ANFR)</li><li>• <b>Yoann Corre</b> (Siradel)</li><li>• <b>Raffaele D'Errico</b> (CEA-LETI)</li><li>• <b>Philippe De Doncker</b> (Université Libre de Bruxelles)</li><li>• <b>Mérouane Debbah</b> (Huawei)</li><li>• <b>Patrick Galopeau</b> (LATMOS, Université Versailles Saint-Quentin)</li><li>• <b>Azedine Gati</b> (Orange)</li><li>• <b>Christophe Grangeat</b> (Nokia)</li><li>• <b>Frédéric Grillot</b> (Telecom Paris)</li><li>• <b>Nicolas Gross</b> (MVG)</li><li>• <b>Florian Kaltenberger</b> (Eurecom)</li><li>• <b>Marco Klingler</b> (MPSA)</li><li>• <b>Jean-Marc Laheurte</b> (Université Paris Est Marne-La-Vallée)</li><li>• <b>Sébastien Lalléchère</b> (Université de Clermont Auvergne)</li></ul>	<ul style="list-style-type: none"><li>• <b>Quentin Lampin</b> (Orange)</li><li>• <b>Christophe Le Martret</b> (Thales)</li><li>• <b>Martine Liénard</b> (Université de Lille)</li><li>• <b>Yves Louët</b> (CentraleSupélec)</li><li>• <b>Lluis Mir</b> (Institut Gustave Roussy)</li><li>• <b>Claude Oestges</b> (Université de Louvain)</li><li>• <b>Allal Ouberehil</b> (TDF)</li><li>• <b>Patrice Pajusco</b> (IMT-Atlantique)</li><li>• <b>Christian Person</b> (IMT-Atlantique)</li><li>• <b>Dinh-thuy Phan Huy</b> (Orange)</li><li>• <b>Philippe Pouliquen</b> (DGA)</li><li>• <b>Yannis Pousset</b> (Université de Poitiers)</li><li>• <b>Christophe Roblin</b> (Telecom Paris)</li><li>• <b>Julien Sarrazin</b> (Sorbonne Université)</li><li>• <b>Alain Sibille</b> (Telecom Paris)</li><li>• <b>Tullio Tanzi</b> (Telecom Paris)</li><li>• <b>Smail Tedjini</b> (INP Grenoble)</li><li>• <b>Yann Toutain</b> (MVG)</li><li>• <b>Wim Van Driel</b> (Observatoire de Paris)</li><li>• <b>Maxim Zhadobov</b> (Université de Rennes)</li></ul>
COMITÉ D'ORGANISATION, <i>ORGANIZING COMMITTEE</i>	
<ul style="list-style-type: none"><li>• <b>Président Alain Sibille</b> (Telecom Paris)</li><li>• <b>Joël Hamelin</b> (URSI-France)</li></ul>	<ul style="list-style-type: none"><li>• <b>Hervé Sizun</b> (URSI-France)</li><li>• <b>Christophe Roblin</b> (Telecom Paris)</li></ul>

## INFORMATIONS COMPLÉMENTAIRES, MISCELLANEOUS

Toutes informations utiles relatives aux Journées scientifiques 2020 sur le site d'URSI-France :  
<http://www.ursi-france.org>

*All relevant information on 2020 Workshop on the site of URSI-France: <http://www.ursi-france.org>*





## AVEC LE SOUTIEN DE :



INSTITUT DE FRANCE  
Académie des sciences



ROHDE & SCHWARZ  
Make ideas real



## COMITÉ NATIONAL FRANÇAIS DE RADIOÉLECTRICITÉ SCIENTIFIQUE UNION RADIO SCIENTIFIQUE INTERNATIONALE

**Siège social** : Académie des Sciences, 23 quai de Conti, Paris 6<sup>ème</sup>  
**Site Internet** : <http://www.ursi-france.org>

**Adresse postale** : Alain Sibille, Secrétaire général d'URSI-France,  
Télécom ParisTech, 19 place Marguerite Perey, F-91120 Palaiseau  
Téléphone : + 33 1 75 31 93 13  
Courriel : [contact@ursi-france.org](mailto:contact@ursi-france.org)